Evaluation of the power performance of wind turbines in wind farms

Sebastiani, Alessandro

Link to article, DOI:
10.11581/DTU.00000269

Publication date:
2023

Document Version
Publisher's PDF, also known as Version of record

DTU Wind and Energy Systems

Evaluation of the power performance of wind turbines in wind farms

Alessandro Sebastiani

PhD Thesis

Summary

The International Electrotechnical Commission (IEC) describes the standard procedure to measure the power performance of a wind turbine. Manufacturers follow the IEC guidelines to assess the performance of their turbines, while wind farm operators conduct IEC-compliant power performance measurements to determine whether the turbines are performing properly. Since most operating wind turbines are in wind farms, the IEC standard describes the procedure to ensure that the measured power performance is not impacted by the neighbouring turbines. Most importantly, wind directions are restricted to make sure that both the tested turbine and the wind measurement equipment are not in wake.

When several wind turbines are clustered in a wind farm, upstream wake-free turbines might also be affected by flow disturbances caused by the other turbines. The IEC standard recommends to measure the wind speed at a minimum distance of two rotor diameter from the turbines to retrieve blockage-free wind speed measurements. However, wind farm blockage effects might still influence the flow field at that distance. Additionally, the turbine under test might be subject to blockage effects from the neighbouring turbines. This thesis evaluates the impact of blockage effects on power performance measurements and how to correct for them. Additionally, since numerous wind turbines operate under waked conditions for a substantial amount of time, it is investigated how to accurately measure the power performance of a waked wind turbine.

This thesis aims to advance the methods for the evaluation of the power performance of a wind turbine in a wind farm. To this purpose, nacelle lidar measurements are retrieved in front of the turbine under test. Several nacelle lidar configurations are tested for both wind speed and turbulence measurements under both waked and wake-free conditions. Specifically, it is tested whether nacelle lidar measurements can be used to improve the accuracy of power performance measurements relatively to the current standard procedure.

The impact of blockage on power performance measurements is evaluated through both simulations and measurements. Reynolds-averaged Navier-Stokes (RANS) simulations are performed with both a row of five turbines and a large wind farm with 100 turbines. Results are compared with simulations of a single isolated turbine operating under the same freestream conditions. Additionally, measurements are analyzed from a test site consisting of a single row of five turbines. The numerical results show consistent power performance deviations between the wind farm and the isolated cases, with C_P variations up to 4%. The measurements show that the power output of the turbine on one side of the row changes with the wind direction due to blockage effects from the neighbouring turbines. Specifically, compared to wind directions perpendicular to the row, the power

output varies of -1.8% and $+1.8\%$ when the turbine is the most upwind and downwind of the row, respectively.

A method is presented to correct for blockage effects on IEC-compliant power performance measurements. Two different approaches are presented to apply the correction: one based on numerical simulations and one based on short range nacelle lidar measurements. Both the approaches are tested numerically through RANS simulations, showing that they improve the evaluation of the power performance. Additionally, the method is used to correct power curves measured under waked conditions.

In addition to the correction method, lidar-based data-driven power curves are defined to evaluate the wind turbine power performance under waked conditions. Specifically, multivariate power curves are implemented as multivariable polynomial regressions, whose input variables are several wind speed and turbulence measurements obtained with nacelle lidars. A numerical framework is implemented to test the multivariate power curves under both waked and wake-free conditions using different nacelle lidar configurations. The same framework is also used to test nacelle lidar turbulence measurements. Furthermore, the numerical results are validated with lidar measurements from the field. Results show that the multivariate power curves are more accurate than the IEC standard power curve under both wake-free and waked conditions. The power output estimation improves when using nacelle lidar turbulence measurements in addition to wind speed measurements.

Several nacelle lidar scanning configurations are tested through both simulations and measurements. When measuring turbulence under nearly homogeneous conditions, at least six beams are needed, including one beam with a different opening angle, to retrieve all the six Reynolds stresses. Additionally, the Reynolds stresses estimation improves by increasing the opening angle, while no substantial improvement is obtained by increasing the number of beams beyond six. The optimal lidar configuration to implement the multivariate power curves is site-specific. However, both numerical and experimental results show that a circular scanning configuration provides similar accuracy to the optimal configuration, as long as the scanning pattern has a diameter equal to around 0.9 the turbine rotor diameter.

Preface

This thesis was prepared at the department of Wind and Energy Systems at the Technical University of Denmark partially in fulfillment of the requirements for acquiring a Ph.D. degree.

The research described in this thesis was conducted at the Meteorology and Remote Sensing section of DTU Wind and Energy Systems. This work has received funding from the European Union Horizon 2020 through the Innovation Training Network Marie Skłodowska-Curie Actions: Lidar Knowledge Europe (LIKE) [grant number 858358].

Risø campus, Roskilde, February 27, 2023

Alessandro Sebastiani

Acknowledgements

The publication of this thesis ends a three-year journey, which would not have been the same without the people who shared it with me. To those people I would like to express all my gratitude.

First of all, to my supervisors, Alfredo and Niels, for guiding and supporting me during the entire project. I consider myself lucky to have had the chance to learn from such talented and passionate scientists. To Niels, for getting me started with the initial numerical works and putting me in the best conditions to obtain my numerical results. To Alfredo, for allowing and helping me to pursue my own research ideas, for the constant involvement in the project and for building a great work environment.

I would also like to thank Rozenn, for initially shaping this project and giving me the chance to conduct it.

I would like to thank all the co-authors of my publications, who had a key role in this project. Alex, for sharing his deep knowledge of blockage and CFD. Nikolas, for providing the Tjæreborg measurements together with invaluable help to analyse them. Jakob, for supporting the turbulence-related part of this project. Jim, for showing great interest in the project and giving me the precious chance of collaborating with him. Wei, for the great collaboration and the good time, for making the PhD journey together.

To all my colleagues and friends at DTU Wind, for the great work and amazing time during these three years. For having such a great work environment where hard work goes together with ping pong games, beer in the Friday bar and freezing winter swimming in the fjord.

To all the colleagues and friends of the LIKE network, for the great work and much fun we have had during our trips. To Charlotte, for coordinating the LIKE network which has been such a memorable experience.

To all my friends in Italy, here in Copenhagen and elsewhere. For all our experiences during the past three years and before. For all the moments we have shared together.

To my parents, Mario and Cristina, and my brother, Francesco, for their endless love and support.

To my partner Cecilia, for her infinite support. For knowing me better than anyone else. For everything that we share.

Contents

CHAPTER 1

Introduction

1.1 Motivation

Wind energy is expected to play a key role in the energy system of the future. Forecasts predict a more than tenfold increase in wind energy production between 2020 and 2050 [21]. This means that the wind industry will be busy with the planning and development of numerous wind farms around the globe. Wind farm planning is not trivial, and one of the critical activities is estimating how much energy the wind farm is going to produce during its lifetime. This requires both the assessment of the wind resource at the designated location and the estimation of how much energy is produced out of that resource. The link between the estimated wind energy resource and the predicted energy production is provided by the wind turbine power performance, which indicates how much power is generated by the wind turbine in relation to the characteristics of the wind flow.

The International Electrotechnical Commission (IEC) describes the standard procedure to measure the power performance of a wind turbine [33]. Since its first publication in 1998 [34], the IEC standard is now widely accepted as the contractual guidance for wind turbine purchase agreements. Manufacturers follow the IEC standard to assess the performance of their turbines, while wind farm operators conduct on-site IEC-compliant power performance measurements to determine whether the turbines are performing at a level consistent with what predicted by the manufacturer. Since most operating wind turbines are in wind farms and these are nowadays in wind farm clusters, it is crucial to make sure that power performance measurements are not biased due to flow disturbances caused by neighbouring wind turbines.

According to the IEC standard, the wind turbine under test is not influenced by neighbouring wind turbines when it is not in the wake of upstream turbines and there is a distance of at least two rotor diameters (D) from all the neighbouring turbines, including those on the sides and downstream. Consequently, the wind turbine power performance is often measured in test centers consisting of a single row of wind turbines aligned perpendicularly to the prevailing wind direction, so that the turbines are most frequently not in wake. However, several numerical experiments and wind tunnel tests showed that the power performance is affected when several wind turbines are aligned perpendicularly to the incoming flow [53, 51, 46, 73], raising the question on whether power performance measurements might be biased when conducted at such sites. Additionally, power performance tests are also conducted within the upstream row of large operating wind farms, where the tested turbine might be subject to wind farm blockage effects, which consist of flow disturbances generated inside and around the wind farm by the wind farm itself [11, 68, 63, 70, 4].

Although growing evidence suggests that IEC-compliant power performance measurements might be influenced by wind farm blockage effects, these are still not accounted for by the IEC standard and there is not a generally accepted method to quantify and correct for such effects. Additionally, the IEC standard describes the procedure to measure the power performance of a wake-free wind turbine, and assessment of the power performance of a turbine in wake is not part of the standard yet. The lack of such procedure hinders the assessment of the power performance of most wind turbines, which operate inside wind farms and are in wake for a substantial amount of time [9, 8, 64]. Consequently, it is not possible to determine whether turbines inside wind farms are performing as specified by the manufacturer.

When in wake, wind turbines operate under a strongly inhomogeneous inflow, which causes large uncertainty in the determination of the power curve, here referred to as the relation between the power output and the wind speed at hub height, as specified by the IEC standard. Under waked conditions, even when using velocity measurements at several heights to estimate the rotor equivalent wind speed [79], horizontal wind speed gradients would cause high uncertainty in the power curve. In order to reliably evaluate the power performance of a waked turbine, several wind measurements are needed across the whole rotor swept area to accurately characterize the inflow to the turbine. Such measurements can be retrieved with nacelle-mounted lidars, which are able to measure across the rotor swept area and at several distances from the rotor [12, 58, 69].

Nacelle lidars provide accurate estimations of both wind speed and atmospheric turbulence [79, 81, 58, 25]. Moreover, they have been used to study wakes [18, 31]. They have also been used to improve the accuracy in load assessment [19, 17]. In the same manner, nacelle lidars could be used to improve the accuracy in the evaluation of the wind turbine power performance under both waked and wake-free conditions.

1.2 Objectives and hypotheses

The overall purpose of this thesis is to advance the methods for the evaluation of the power performance of a wind turbine in a wind farm, where the turbines influence each other through mainly wakes and blockage effects among others. The IEC standard accounts for the effect of wakes on the power performance by excluding waked wind turbines from power performance tests. Blockage effects are considered by recommending to measure the wind speed at a minimum distance of 2D from the turbine. However, wind farm blockage effects might still influence the flow field at that distance [47, 11, 68].

This thesis evaluates the impact of blockage effects on power performance measurements and how to correct for them. Additionally, it is investigated how to accurately measure the power performance of a waked wind turbine. To this purpose, nacelle lidar measurements are used to provide an accurate characterization of the inflow to the turbine. Therefore, the ability of nacelle lidars to provide both wind speed and turbulence measurements in wake is evaluated. The research activities are shaped by investigating the validity of three hypotheses:

- *Hypothesis I*: IEC power performance measurements do not provide a reliable

estimation of the power performance of the isolated wind turbine when conducted on wake-free turbines in a wind farm.

- *Hypothesis II*: Nacelle lidar measurements can be used to evaluate the wind turbine power performance with an accuracy of the same order under both waked and wake-free conditions.
- *Hypothesis III*: Nacelle lidar turbulence measurements improve the accuracy in power performance estimation under both wake-free and waked conditions compared to using mean wind speed measurements only.

On the basis of those three hypotheses, a number of research questions are formulated:

- Does the power performance measured in a single row of wind turbines differ from that of the isolated wind turbine? If yes, how to correct for that difference?
- Does the power performance measured at the edges of a large wind farm differ from that of the isolated turbine? If yes, how to correct for that difference?
- Can we use nacelle lidars to improve the accuracy of power performance measurements under both waked and wake-free conditions relatively to the current standard procedure? Moreover, can the power performance of the waked wind turbine be evaluated as accurately as that of the wake-free turbine?
- Do nacelle lidar turbulence measurements improve the accuracy of power performance estimations under both waked and wake-free conditions relatively to using mean wind speed measurements only?
- What is the optimal nacelle lidar configuration for turbulence measurements?
- What is the optimal nacelle lidar configuration to evaluate the wind turbine power performance?

In order to answer those research questions, a number of research activities are conducted, which aim at meeting the following objectives:

- To assess the blockage effects on power performance at a typical power performance test site through both simulations and field measurements.
- To define a method to correct for the effect of both blockage and wakes on power performance measurements.
- To investigate whether the correction method can be applied by relying on nacelle lidar measurements from the field.
- To implement a numerical framework to test both turbulence and power performance measurements with several nacelle lidar configurations under both wake-free and waked conditions.
- To use the previously defined numerical framework to test multivariate power curves, whose inputs are several wind speed and turbulence measurements retrieved with nacelle lidars.

- To validate the numerical findings regarding both turbulence estimation and multivariate power curves with nacelle lidar measurements from the field.

1.3 Thesis outline and list of publications

This thesis consists of two parts. In the first one, the overall motivation, scientific background and conclusions of the work are given, highlighting the main results from the related publications. The second part consists of a collection of the scientific peer-reviewed publications related to this PhD project.

The first part consists of six Chapters. Chapter 1 has introduced the motivation and objectives of this work. In Chapter 2, the wind turbine power performance is introduced by describing both the IEC standard power curve and data-driven approaches to model the power performance. Chapter 3 initially describes the main issues related to power performance measurements in wind farms and then discusses the research findings in relation to power performance measurements conducted on either a single row of wind turbines or a large wind farm. Chapter 4 presents the numerical framework developed to test nacelle lidar measurements and data-driven power curves, with a summary of the research findings from numerical investigations conducted with such framework. Chapter 5 describes the lidar measurements used to validate the main findings from the numerical evaluation of the data-driven power curves. Finally, conclusions are given in Chapter 6.

The second part of the thesis includes seven scientific peer-reviewed publications. Four articles are published (**Papers I, III, V** and **VI**), one is under review (**Paper IV**), one is about to be submitted (**Paper II**) and one manuscript is in preparation (**Paper VII**).

- **Paper I** [65]: Evaluation of the global-blockage effect on power performance in a single row of wind turbines. RANS simulations are performed of both a single isolated wind turbine and a row of five wind turbines operating under the same inflow conditions. Additionally, measurements are analyzed from a test site consisting of a single row of five turbines.
- **Paper II** []: Evaluation of the global-blockage effect on power performance in a large wind farms through RANS simulations. Additionally, a method is presented to correct for the effect of both blockage and wakes on wind turbine power performance measurements.
- **Paper III** [27]: Virtual turbulence measurements are retrieved by simulating several nacelle-lidar scanning geometries within synthetic wind fields. The lidars are simplified by neglecting their probe volume and the six Reynolds stresses are retrieved with a least-square procedure using the radial velocity variances from all beams.
- **Paper IV** [26]: The numerical investigation of **Paper III** is extended with more accurate simulations including the lidar probe volume. Additionally, numerical findings are validated with field measurements.

- **Paper V** [67]: The wind turbine power performance is modelled with multivariate power curves in the form of multivariable polynomial regressions, whose input variables are wind speed, turbulence and yaw misalignment. The analysis is conducted under homogeneous conditions with a numerical dataset of virtual power performance tests.
- **Paper VI** [66]: Data-driven multivariate power curves based on nacelle lidar measurements are tested under both waked and wake-free conditions. The analysis is conducted on a numerical dataset generated through aeroelastic simulations combined with both virtual nacelle lidars and the dynamic wake meandering model.
- **Paper VII** []: Measurements are retrieved with the DTU SpinnerLidar mounted in the spinner of a wind turbine inside a wind farm. Measurements are collected under both wake-free and waked conditions to test the multivariate power curves and validate the numerical findings of **Paper V** and **Paper VI**.

CHAPTER 2

Wind turbine power performance

The power performance of a wind turbine indicates how much power is generated by the turbine in relation to the characteristics of the wind flow. In the IEC standard, the power performance is quantified through the annual energy production (AEP) and the power curve, which indicates the relation between the wind speed and the wind turbine power output [33].

2.1 The IEC power curve

In the IEC standard for power performance measurements, the power curve is retrieved through simultaneous measurements of the turbine power output and a number of characteristics of the atmospheric flow [33]. Most importantly, the power output is defined in the standard as a direct function of the air density ρ and the horizontal wind speed at hub height U_{hub}. Other characteristics which are recognized to impact the turbine power output are the vertical variations of both wind speed and wind direction, which are referred to as vertical wind shear and vertical wind veer, respectively. Their effect on the power performance is evaluated with the rotor equivalent wind speed (U_{REWS}), which is defined by measuring the horizontal wind speed at several heights across the rotor swept area and combining those measurements in the expression defined by Wagner et al. [79]. In conditions of high shear and veer, U_{REWS} better characterizes the kinetic energy flux through the rotor and it is better correlated with the power output than U_{hub} [79].

Since the wind speed is a random non-stationary variable, the relation between the wind speed and the power output is based on 10-min realizations. The IEC power curve is derived as the relation between the 10-min means of the power output P and the wind speed evaluated as either U_{hub} or U_{REWS}. In order to get the curve, wind speed values are grouped within bins of 0.5 m/s to get the mean values of both P and U_{hub} (or U_{REWS}) within each bin.

The normalized IEC-compliant power curve obtained from measurements in **Paper I** is shown in Fig. 2.1, where two different turbine operating regions are highlighted. As illustrated, for wind speeds between the cut-in value U_{in} and the rated value U_{rated}, the turbine operates within the non-rated region, where the power output increases proportionally to the wind speed. Above U_{rated}, within the rated region of operation, the power output is nearly equal to the rated value P_{rated} for wind speeds up to the cut-out value U_{out}, which is the maximum operating wind speed. In addition to the measured

power curve, the IEC standard requires the evaluation of the power coefficient

$$C_P = \frac{P}{\frac{1}{2}\rho A U^3}\,, \tag{2.1}$$

where U is the measured wind speed evaluated as either U_{hub} or U_{REWS}, ρ is the measured air density and A is the rotor area. As seen in Fig. 2.1, the C_P curve typically presents the highest values within the non-rated region, where the aerodynamic efficiency of the turbine is maximized in order to extract as much energy as possible from the wind flow. During rated operation, the C_P gradually decreases as the aerodynamic efficiency is reduced to keep the power output constant.

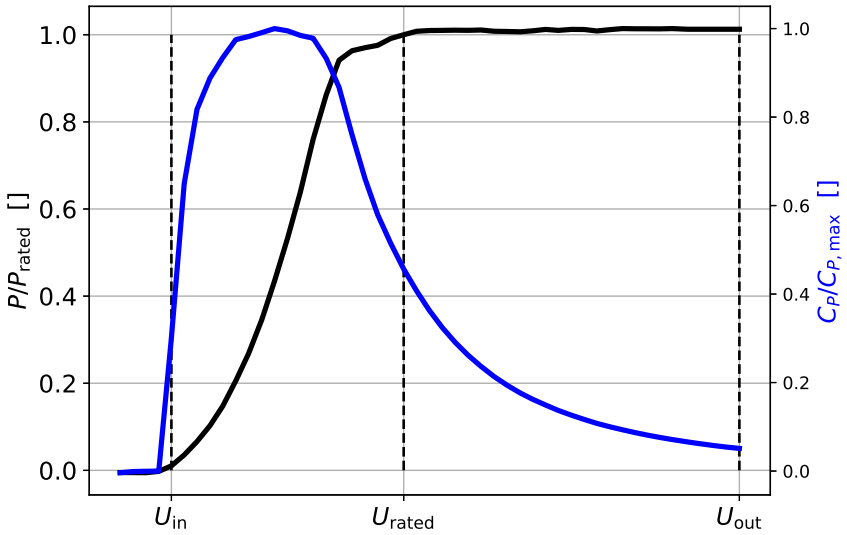

Figure 2.1: IEC-compliant power curve of the turbine analyzed in **Paper I**. Vertical dashed lines indicate the boundary of the two regions of operation: non-rated and rated.

According to the IEC, the uncertainty of the power curve is quantified by combining the standard uncertainty of the power output values within the bin with several Category B uncertainty components [35]. Therefore, the standard deviation of the power output values within each bin (σ_P^2) is one of the main contributors to the overall uncertainty of the power curve. Several factors contribute to increase σ_P^2, such as the spatial inhomogeneity of the wind flow and the turbulence-related wind speed variability within the 10-min intervals.

The turbulence-induced variations of the power performance can be qualitatively explained by the non-linearity of the power curve: the 10-min mean power output does not depend only on the mean wind speed, but also on the wind speed variance and therefore on the turbulence intensity (TI) [29]. Specifically, close to the cut-in wind speed, where the power curve is convex, the power output increases with the TI; close to the rated value, where the curve is concave, the power output decreases with the TI [15,

7]. The effect of turbulence is then negligible for wind speeds above rated, where the power output is constant.

In the IEC standard, the effect of turbulence is accounted for using a normalization method, which reduces the effect of turbulence on the measured power curve. Therefore, the IEC standard procedure includes the effect of atmospheric turbulence, vertical shear and vertical veer on the power performance, while, still, assuming horizontal homogeneity of the wind flow, so that horizontal shear and veer are not included. Consequently, IEC-compliant power performance measurements are not conducted under waked conditions, which are characterized by large horizontal wind-speed gradients.

In IEC-compliant power performance tests, the wind speed must be measured at distances between 2D and 4D from the rotor. The distance of 2D is defined as the closest distance to the rotor where the turbine blockage is negligible, while measuring closer to the rotor would result in an underestimation of the wind speed and consequently an overestimation of the power performance. On the other hand, farther than 4D from the rotor, the measured wind speed would be poorly correlated with the turbine power output. However, even when measuring at 2D, uncertainty is introduced in the power curve due to the distance between the wind measurement and the rotor.

By measuring closer to the rotor or, hypothetically, by retrieving the wind speed at the rotor, the measured velocity would be more highly correlated with the power output, reducing the scatter in the power curve. By hypothetically retrieving an 'effective' velocity across the rotor, the accuracy in the evaluation of the power performance would be nearly independent of the operating conditions, as the inhomogeneity of the inflow would not affect the correlation between the measured velocity and the power output. Consequently, power curves would present the same uncertainty when measured under waked and wake-free conditions.

Pedersen et al. [56] used a blade-mounted Pitot tube to estimate the velocity at the rotor plane, showing the complexity of such measurement procedure. They showed that the wind speed at the rotor plane is highly correlated with the power output, but also that the measurements are heavily influenced by the pitch angle of the blade, which introduces scatter in the power curve. A more viable option seems to retrieve nacelle lidar short-range measurements to accurately estimate both wind speed and turbulence in proximity of the rotor [12, 69, 20]. Such measurements are more highly correlated with the power output than IEC-compliant measurements at 2D from the rotor, and they could be used to improve the accuracy of power performance measurements in wind farms.

Nacelle lidar measurements could also be used to define data-driven power curves by modelling the relation between them and the power output. If properly trained, such models would be able to correctly predict the power output based on, e.g., nacelle lidar measurements. Consequently, the data-driven power curve could be used to evaluate the power performance of the wind turbine under a number of different operating conditions.

2.2 Data-driven power curves

Wind turbines are critically large rotating machines. They operate within the complex flow conditions of the atmospheric boundary layer (ABL), whose complexity is often increased by the turbines themselves through wakes and blockage effects. The combination of flow complexity and wind turbine size results in the large uncertainty of the IEC power curve, which is not reliable under a number of operating conditions, such as wake and complex terrain. Under those conditions, the IEC power curve cannot be used to conduct performance monitoring and fault detection, i.e. we cannot assess whether the wind turbine is under-performing. Therefore, data-driven power curves have been implemented with the primary scope of improving performance monitoring in wind farms, where the operating conditions are different from those of IEC power performance tests [14, 40, 82].

Data-driven power curves have been developed as both parametric and non-parametric models [40]. Parametric models absorb information through the definition of a finite number of parameters, which are then used for prediction, as in the case of linear and polynomial regressions. Non-parametric models do not consist of a finite set of parameters and they can capture a flexible amount of information, as in the case of neural networks and Gaussian processes. Additionally, data-driven power curves can be catalogued depending on the number of input variables.

In some cases, the sole input variable is the hub-height wind speed retrieved by the nacelle-mounted cup anemometer [28, 75, 45, 44, 84]. However, since the power performance does not only depend on the hub-height wind speed, those models leave margin for improvement and it is beneficial to include other atmospheric variables, such as turbulence, vertical wind shear and vertical wind veer [55, 62, 16, 13]. Pelletier, Masson, and Tahan [57] showed that the accuracy further improves when including yaw misalignment as an input to the model. Furthermore, when only hub-height wind measurements are available, data-driven power curves can be improved by including control variables, such as rotor rotational speed and blade pitch angle [36, 5].

Accurate data-driven power curves could be defined with nacelle lidar measurements, as they are able to retrieve several features of the inflow, such as hub-height wind speed [80], turbulence intensity [58, 25] and vertical wind shear [48, 12]. However, power curve modelling has so far been conducted by relying on mast measurements or nacelle-mounted cups and vanes. Additionally, no model has included several measurements at the same height in order to characterize horizontal velocity gradients, which are encountered under both waked and yaw-misaligned conditions. Nacelle lidars can be used to evaluate yaw misalignment [22] and to retrieve flow characteristics under waked conditions [32, 19, 17, 18]; therefore, it is possible to define data-driven power curves, which account for the effect of both wakes and yaw misalignment.

The performance monitoring of wind turbines would benefit enormously from the accurate evaluation of the power performance in wake, as most turbines within a wind farm operate under waked conditions. By having a clear reference of the power performance in wake, it would be possible to evaluate whether all the turbines in the farm are performing according to what specified by the manufacturer. On the contrary, nowadays, performance validation tests can be conducted only for those turbines which meet the IEC

standard requirements. Consequently, it is not possible to verify the turbine performance in the inner area of the wind farm, where the turbines are almost constantly in wake. Additionally, due to the development of the yaw-based wake steering control strategy [24, 23], there is an increasing need to accurately evaluate the effect of yaw misalignment on the power performance.

CHAPTER 3
Power performance inside a wind farm

The wind turbine power performance is hardly ever measured on a completely isolated turbine. Power performance test sites usually consist of a single row of wind turbines aligned perpendicularly to the prevailing wind direction, so that the turbines hardly operate under waked conditions [51]. Additionally, power performance tests are often conducted on the upstream turbines of an operating wind farm to evaluate whether the turbines perform accordingly to what the power curve specifies, i.e. to conduct production validation tests [11]. Consequently, it is important to evaluate whether turbine interactions affect power performance tests, resulting in a site-dependent estimation of the power performance.

Even a small bias of a few percentages in the measured power curve might cause large errors when that power curve is used to estimate the AEP of the wind farm. Therefore, it is crucial to make sure that power curves measured at a test site are not affected by blockage and that they are a reliable evaluation of the turbine performance. Additionally, power curves measured in operating wind farms should be also free of bias in order to assess whether the wind-farm turbines are performing according to the power curve specified by the manufacturer.

Inside a wind farm, most turbines operate in wake for a substantial amount of time and their performance cannot be compared with the reference power curve, which is assumed to be measured under wake-free conditions. Since there is not a generally accepted procedure to assess the power performance of a waked wind turbine, production validation tests cannot be conducted in the wind farm inner region. Therefore, the definition of a procedure for power performance tests in wake would give the chance to assess the power performance of all the turbines in the farm, reducing the uncertainty related to wind farm operation. Additionally it would allow wind farm operators to perform maintenance on turbines that do not operate properly, thus reducing power losses.

3.1 Blockage effects

In fluid mechanics, flow blockage is defined as the deflection of the flow due to an obstruction, which causes a deceleration of the incoming flow. In wind energy, the notion of turbine blockage refers to the deceleration of the wind flow upstream of the turbine rotor due to the turbine itself [47, 50]. The induction zone is the region upstream of the rotor where turbine blockage affects the wind speed, with maximum reduction at

the rotor position and an incremental wind speed recovery moving further upstream. Generally, the blockage effect is considered as negligible farther than 2.5D from the rotor [50], which is the recommended distance for wind speed measurements in power performance tests [33].

The concept of turbine blockage is of crucial importance for power performance tests, as a blockage-affected wind speed measurement would cause an underestimation of the wind velocity and, consequently, an overestimation of the power performance. Therefore, according to the IEC standard, the wind speed should be measured at a distance of at least 2D from the rotor. However, the IEC standard does not differentiate between the cases of a single isolated turbine and several turbines clustered together, only requiring to measure the performance of a wake-free wind turbine with a spacing of at least 2D from the neighbouring turbines [33].

In the IEC standard, the intensity of blockage is assumed to be the same in case of both a single isolated turbine and a wind farm. However, when several turbines are clustered together, blockage effects might be enhanced by the turbine interactions causing a deceleration of the incoming wind flow due to blockage from the whole wind farm, a phenomenon which is generally referred to as either global blockage or wind farm blockage [68, 63, 64, 74]. Because of the wind speed reductions due to global blockage, the wake-free wind-farm turbines produce less than a single isolated turbine under the same freestream conditions [11, 54].

Since global blockage affects both the power output of the wake-free wind turbines and the flow upstream of the wind farm, it most likely has an influence on power performance tests conducted in the upstream row of a wind farm. To the author's knowledge, whilst the wind energy community has paid much attention to the effects of wind farm blockage on the AEP, possible effects on power performance tests have not been thoroughly investigated.

Several studies evaluated blockage effects in a single row of wind turbines through both wind tunnel experiments and simulations [46, 53, 51, 73, 10], showing that the power performance changes relatively to the isolated turbine operating within the same freestream inflow. Specifically, the power output varies for the same freestream velocity depending on the wind direction, the inter-turbine spacing and the location of the turbine within the row, with variations up to 8% relatively to the isolated turbine [73]. Consequently, the question is raised on how strong the combined effect on the power output and the measured wind speed is in the context of power performance tests. Additionally, the power curve is retrieved by binning the power output values depending on the wind speed, so that measurements retrieved for different wind directions are averaged together. This might result in power variations observed for specific wind directions, which might be cancelling out when taking the bin average.

3.2 Single row of wind turbines

In **Paper I**, blockage effects at a typical test site are investigated through simulations of both an isolated wind turbine and a row of five turbines aligned perpendicularly to the

incoming flow. Specifically, several Reynolds-averaged Navier-Stokes (RANS) simulations are performed under neutral conditions (no buoyancy nor inversion) with a uniform wind profile (no vertical wind shear). The inter-turbine spacing L, the freestream velocity U_∞ and the inflow angle θ between the wind direction and the orthogonal line to the row are varied. Additionally, the simulations are compared to measurements from a turbine test site with five wind turbines aligned perpendicularly to the prevailing wind direction. The illustration in Fig. 3.1 describes the layout of both the numerical setup and the site.

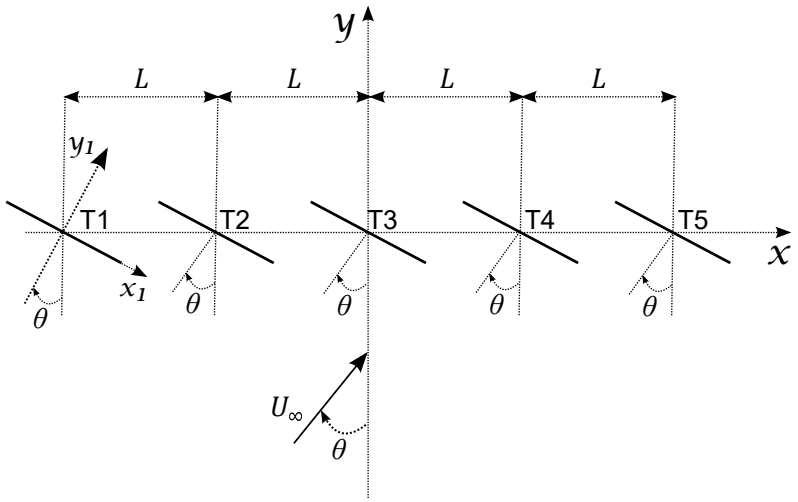

Figure 3.1: Layout of both numerical setup and site [Fig. 1 from **Paper I**].

The available field measurements comprise the operating data of turbine T1 together with the operational status of turbines T3-T5, while no information is available regarding turbine T2. The turbines are spaced with $L = 2.3$D, where D refers to the rotor of the reference turbine T1. Additionally, wind measurements are retrieved from both a meteorological mast and a ground-based lidar aligned with T1 along the orthogonal line to the row at distances of 2.3D and 2.5D, respectively. The met mast is equipped with, among others, a top-mounted cup anemometer at the turbine hub height and a side-mounted wind vane 4 m beneath the hub height. The ground-based lidar is a WindCube WLS7 from Vaisala Leosphere scanning at 11 different heights from -0.4 D to $+0.85$ D relatively to hub height.

The numerical results of **Paper I** show power variations among the row turbines due to blockage effects from the neighbouring turbines for all the tested inter-turbine spacings L (1.8D, 2D and 3D). The power variations increase with a closer spacing and vary with the free-stream velocity depending on the turbine thrust coefficient (C_T). In agreement with the findings from previous works [51, 46, 53], all the row turbines produce more than in isolation when the wind direction is perpendicular to the row ($\theta = 0°$), with increases in power up to 2%. For skewed inflows, the power output varies almost linearly across the row, with the lowest and highest productions from the most upstream and most downstream turbines, respectively. The highest and lowest power variations of nearly $+5\%$ and -3% are observed with $\theta = 45°$ for turbines T5 and T1, respectively.

Furthermore, due to the blockage effects from the neighbouring turbines, the relation between the power output and the measured wind speed at 2D changes relatively to the isolated turbine, with strong variations for the power coefficient C_P. When averaging over the whole inflow sector $[-45°, +45°]$, the measured C_P varies up to $+4\%$ relatively to the isolated turbine operating under the same freestream conditions.

The field measurements analyzed in **Paper I** corroborate the numerical results on the power variation with θ observed for T1 and T5 as a result of blockage effects from the neighbouring turbines. Specifically, compared to wind directions perpendicular to the row, the power output varies of $+1.8\%$ and -1.8% when the turbine is the most upwind and downwind of the row, respectively.

The IEC standard assumes that a reliable estimation of the power performance as function of the free-stream wind ($P = P(U_\infty)$) can be achieved by measuring the wind speed at around 2.5D from the turbine. **Paper I** shows the weakness of that assumption in the case of several turbines aligned perpendicularly to the wind direction. Specifically, different power outputs could be measured for the same free-stream velocity depending on the wind direction, the inter-turbine spacing and the location of the reference turbine within the row. As a consequence of the blockage effects from the neighbouring turbines, the relation between the power output and the IEC-compliant wind speed measurement changes relatively to what would be measured for a completely isolated wind turbine. Thus, the measured power curve is not the true estimation of the power performance of the isolated turbine, with variations of a few percentage points in both power output and C_P.

3.3 Multiple-row wind farm

Blockage effects on power performance measurements are evaluated in **Paper II** for the case of a large wind farm. RANS simulations are performed within a conventionally neutral ABL of a wind farm with five rows of twenty turbines, as shown in Fig. 3.2-(a). Simulations are also performed of a single isolated wind turbine operating within the same numerical domain under the same free-flow conditions, as shown in Fig. 3.2-(b). Simulations are performed for five different wind directions, from $-45°$ to $+45°$, where $\theta = 0°$ is the northerly wind direction shown in Fig. 3.2. Power performance measurements are simulated for all the upstream wind-farm turbines and the isolated turbine. The IEC-compliant wind speed measurements are simulated with both virtual nacelle lidars and mast-like measurements. As shown in Fig. 3.2, mast measurements are retrieved at 2D from the reference turbine along all the IEC-compliant measuring sector $[-45°, +45°]$.

Results from **Paper II** show that blockage effects cause consistent power deviations along the twenty upstream turbines (T81, T82,.., T100). When the wind direction is perpendicular to the rows, all the upstream turbines produce less than the isolated turbine under the same freestream conditions, with power variations down to -5%. For skewed inflows, similarly to the single-row case, the power output changes almost linearly along the row, with the downwind turbines producing more than the upwind ones. The

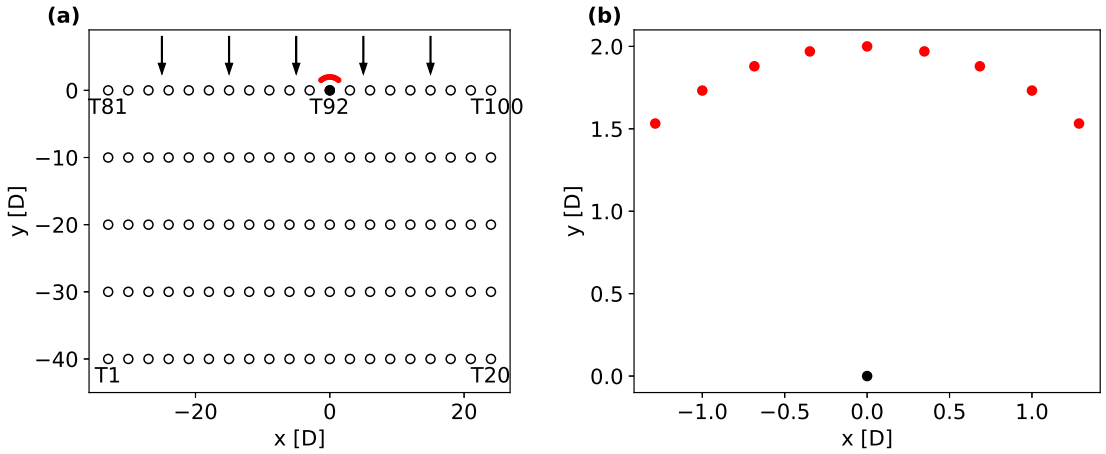

Figure 3.2: Schematics of the layout for the wind farm (a) and the isolated turbine (b), with both wind turbines (black circles) and met masts (red circles). Black arrows show the $\theta = 0°$ wind direction [Fig. 1 from **Paper II**].

strongest power deviations relatively to the isolated case are observed for $\theta = 45°$, with an increase of $+5\%$ for turbine T81 and a decrease of -9% for T100.

The power variations relatively to the isolated turbine are larger in the case of **Paper II** than in **Paper I**, as the wind farm blockage effects are stronger due to the higher number of turbines. The same is observed for the blockage effect on the wind speed measurements retrieved at 2D in front of the turbines, with variations down to -3% relatively to the isolated case. The power-velocity relation strongly differs from what would be measured for the isolated turbine. Consequently, power performance measurements conducted at the edge of a large wind farm are not a reliable estimation of the power performance of the isolated turbine. As shown in **Paper II**, the measured power performance vary with the wind direction, the location of the turbine within the row and the location of the met mast along the 2D arch. Those variations decrease the accuracy and increase the uncertainty of the power performance measurements relatively to the truly isolated case.

3.4 Correcting for the effect of blockage and wakes on power performance measurements

From the analyses of **Paper I** and **Paper II**, it is concluded that power performance tests do not provide a reliable evaluation of the isolated turbine performance when they are conducted either in a single row of wind turbines or at the edge of a large multi-row wind farm. However, the current practice is to assume that such power

performance tests provide a reliable estimation of the power curve, which is then used in AEP calculations or as a benchmark to evaluate the performance of operating wind turbines. Consequently, both the uncertainty and inaccuracy of AEP calculations are partially due to the unreliability of the utilized power curves. Furthermore, production validation tests might result in biased conclusions regarding whether the turbines are underperforming.

In **Paper II**, a method is presented to correct for the effect of blockage on power performance measurements. By applying such correction method, an accurate evaluation of the isolated turbine performance is retrieved from power performance tests conducted in wind farms, providing a nearly blockage-free power curve. The method relies on the numerical estimation of the power-velocity relation, which is modelled by retrieving the ratio $(U_{\text{disk}}/U_{\text{mast}})$, where U_{disk} is the rotor-averaged velocity extracted at the rotor plane and U_{mast} is the velocity retrieved at the IEC-compliant mast. The $(U_{\text{disk}}/U_{\text{mast}})$ ratio is numerically evaluated for both the isolated and the wind-farm cases, and it is then used to correct the wind speed measurements in order to retrieve the power performance of the isolated turbine from tests conducted within the wind farm.

In **Paper II**, the method is tested numerically with virtual power performance measurements conducted on the upstream turbines of Fig. 3.2. Results show both an increase in the accuracy and a reduction in the uncertainty of the power performance measurements. Specifically, the scatter in the power curve is reduced and the estimated C_P is closer to what would be measured for the isolated turbine. Furthermore, the method is applied to virtual power performance tests conducted on the downstream turbines (T1,.., T80), showing that reliable power curves can be retrieved from such measurements.

In order to apply the correction by relying on measurements only, the ratio $(U_{\text{disk}}/U_{\text{mast}})$ is replaced by $(U_{\text{disk,lidar}}/U_{\text{mast}})$, where $U_{\text{disk,lidar}}$ is derived from short-range nacelle lidar measurements within the turbine induction zone. Specifically, four different nacelle lidar configurations are used to retrieve the wind speed at 0.5D from the rotor. Results from **Paper II** show that the correcting method would be reliable with all the tested lidar configurations, providing accurate power performance measurements from the waked wind turbines.

CHAPTER 4

Numerical framework to test lidar configurations and power curve modelling

Numerical simulations are convenient to test engineering applications under specific conditions which are complicated to set up for an experiment. They can also be used for preliminary evaluations before planning an expensive measurement campaign. This chapter presents a numerical framework which can be used to test nacelle lidar configurations and power curve modelling approaches under both homogeneous and waked conditions. The framework consists in the combination of an aeroelastic code with virtual lidar measurements and a wake model.

The utilized aeroelastic code is the DTU in-house aeroelastic software HAWC2 [39]. The lidar simulations are performed with a Python code developed during this PhD project. The lidar simulator scans the same synthetic wind fields which are used as input to the aeroelastic simulations. Thus, from the same wind field, HAWC2 is used to retrieve the wind turbine outputs while the lidar simulator retrieves the wind measurements, similarly to what would happen in reality with a nacelle-mounted lidar on top of an operating wind turbine. The synthetic wind fields are generated with the turbulence spectral model by Mann, hereafter simply referred to as Mann model [41, 42]. When waked conditions are to be tested, the dynamic wake meandering (DWM) model is used to add wake characteristics to the homogeneous wind fields [2].

The choice of such framework aims to provide a relatively computationally inexpensive tool to perform simulations in time domain. The primary goal is to simulate power performance tests, which require the evaluation of the turbine performance during numerous 10-min realizations including a wide spectrum of wind characteristics. Specifically, IEC power performance tests require a database with a minimum of 1080 10-min intervals with at least three intervals within each velocity bin of 0.5 m/s.

4.1 Turbulence spectral model

The three-dimensional wind field can be described by the velocity vector field $\mathbf{u}(\mathbf{x})$, as time dependency is neglected because of the Taylor's frozen turbulence hypothesis [76]. The velocity vector field $\mathbf{u} = (u_1, u_2, u_3) = (u, v, w)$ refers to the right-hand coordinate system $\mathbf{x} = (x_1, x_2, x_3) = (x, y, z)$, where the x-axis is aligned with the direction of the mean horizontal wind vector. Assuming homogeneous turbulence and no vertical wind speed, the mean velocity field results in $\langle \mathbf{u}(\mathbf{x}) \rangle = (U(z), 0, 0)$, where

the wind speed variation with height depends on the vertical shear. Consequently, the turbulence-induced velocity fluctuations around the mean values are quantified as $\mathbf{u}' = \mathbf{u} - (U(z), 0, 0) = (u'_1, u'_2, u'_3) = (u', v', w')$.

Because of the assumption of homogeneity, the covariance of two velocity components between two different points in space is only function of the separation between the points: $R_{ij} = \left\langle u'_i(\mathbf{x})\, u'_j(\mathbf{x}+\mathbf{r}) \right\rangle = R_{ij}(\mathbf{r})$, where $\mathbf{r} = (r_1, r_2, r_3)$ is the separation vector. The covariance tensor of single-point statistics $\mathbf{R}(\mathbf{r}=0) = \mathbf{R}$ consists of the variances and covariances of the velocity components, and it is often referred to as the Reynolds stress tensor:

$$\mathbf{R} = \begin{bmatrix} u'u' & u'v' & u'w' \\ v'u' & v'v' & v'w' \\ w'u' & w'v' & w'w' \end{bmatrix} = \begin{bmatrix} \sigma_u^2 & u'v' & u'w' \\ v'u' & \sigma_v^2 & v'w' \\ w'u' & w'v' & \sigma_w^2 \end{bmatrix}. \tag{4.1}$$

The spectral tensor $\mathbf{\Phi}$ is defined as the Fourier transform of the covariance tensor:

$$\Phi_{ij}(\mathbf{k}) = \frac{1}{(2\pi)^3} \int_{-\infty}^{\infty} R_{ij}(\mathbf{r})\, \exp(-i\mathbf{k}\cdot\mathbf{r})\, \mathrm{d}\mathbf{r}, \tag{4.2}$$

where $\int \mathrm{d}\mathbf{r} \equiv \int_{-\infty}^{\infty}\int_{-\infty}^{\infty}\int_{-\infty}^{\infty} \mathrm{d}r_1 \mathrm{d}r_2 \mathrm{d}r_3$ and $\mathbf{k} = (k_1, k_2, k_3)$ is the vector field representing the wavenumbers along the (x, y, z) directions.

The Mann model describes the spectral tensor $\mathbf{\Phi}$ as function of three parameters: $\alpha\epsilon^{2/3}$ is the product between the Kolmogorov constant α and the turbulent energy dissipation rate ϵ, Γ is a parameter related to the anisotropy of the turbulence field, and L is a length scale related to the size of the turbulence eddies. From the spectral tensor, the spectra between two points located in the same y-z plane and separated by the vector $(0, \Delta y, \Delta z)$ can be retrieved as

$$\chi_{ij}(k_1, \Delta y, \Delta z) = \int_{-\infty}^{\infty}\int_{-\infty}^{\infty} \Phi_{ij}(\mathbf{k}, \alpha\epsilon^{2/3}, \Gamma, L) \exp(ik_2\Delta y + ik_3\Delta z)\, \mathrm{d}k_2\, \mathrm{d}k_3. \tag{4.3}$$

In case of $\Delta y = \Delta z = 0$, the single-point cross- and auto-spectra are given as

$$F_{ij}(k_1) = \int_{-\infty}^{\infty}\int_{-\infty}^{\infty} \Phi_{ij}(\mathbf{k}, \alpha\epsilon^{2/3}, \Gamma, L)\, \mathrm{d}k_2\, \mathrm{d}k_3, \tag{4.4}$$

from which the variances and covariances of the velocity components are retrieved as

$$u'_i u'_j = \int_{-\infty}^{\infty} F_{ij}(k_1)\, \mathrm{d}k_1. \tag{4.5}$$

4.2 Lidar simulator

Doppler wind lidar (light detection and ranging) is a remote sensing technology, which measures the wind speed by emitting a laser beam and detecting the light backscattered by aerosol particles in the air. The component of the wind velocity along the laser beam

direction, usually referred to as the radial velocity or line-of-sight velocity, is retrieved from the Doppler shift in the frequency of the backscattered light as

$$v_r = \frac{\lambda_l \, \Delta f}{2}, \tag{4.6}$$

where λ_l is the laser wavelength and Δf is the Doppler shift [60]. When the lidar is set to measure the wind speed at a certain focus distance f_d along the laser beam, light is still backscattered by aerosol particles lying along the beam trajectory closer or farther than the intended distance f_d. Consequently, lidar measurements are affected by a spatial sensitivity, also referred to as probe-volume effect, which is quantified with a weighting function φ, indicating the weighted contribution of the aeroesol particles along the beam trajectory.

The weighting function is modelled with different mathematical expressions depending on the lidar type:

- Continuous wave (CW) lidar [71]:

$$\varphi(s) = \frac{1}{\pi} \frac{l_z}{l_z^2 + s^2}, \text{ with } l_z = \frac{\lambda_l f_d^2}{\pi r_b^2}, \tag{4.7}$$

  where r_b is the lens aperture radius, s is the distance from the focus point along the beam direction and l_z is the Rayleigh length.

- Pulsed lidar [6, 49]:

$$\begin{aligned} \varphi(s) &= \frac{1}{2\Delta p} \left\{ \mathrm{Erf}\left[\frac{s + \Delta p/2}{r_p} \right] - \mathrm{Erf}\left[\frac{s - \Delta p/2}{r_p} \right] \right\} \\ \text{with } \mathrm{Erf}(x) &= \frac{2}{\sqrt{\pi}} \int_0^x \exp(-t^2) \mathrm{d}t \quad \text{and} \quad r_p = \frac{\Delta l}{2\sqrt{\ln(2)}}, \end{aligned} \tag{4.8}$$

  where Δp is the range-gate length and Δl the Gaussian lidar pulse full width at half maximum (FWHM).

As it can be noted from Eq. 4.7 and Eq. 4.8, the weighting function of a CW lidar changes with the distance of the focus point, while φ is independent of the measurement location for a pulsed lidar. Figure 4.1 shows the weighting functions given by Eq.s 4.7 and 4.8 using parameters of typical commercial lidars [49, 60].

The Doppler shift is retrieved by mixing the backscattered radiation with a reference laser beam in an optical mixer, where the frequency shift between the two radiations is determined through heterodyne detection. Then, the optically mixed beam is directed to a photodector which generates a digitised output. A digital Fourier transform is then applied to get a power spectrum from the detector output. Since the spectra are sampled at very high frequency (in the order of 100 MHz), several consecutive spectra are averaged to get a more reliable spectrum, resulting in a measurement frequency in the order of 100 Hz. Fig. 4.2 shows the normalized average power spectrum from the measurement campaign of **Paper VII**. In the case of a nacelle lidar scanning horizontally,

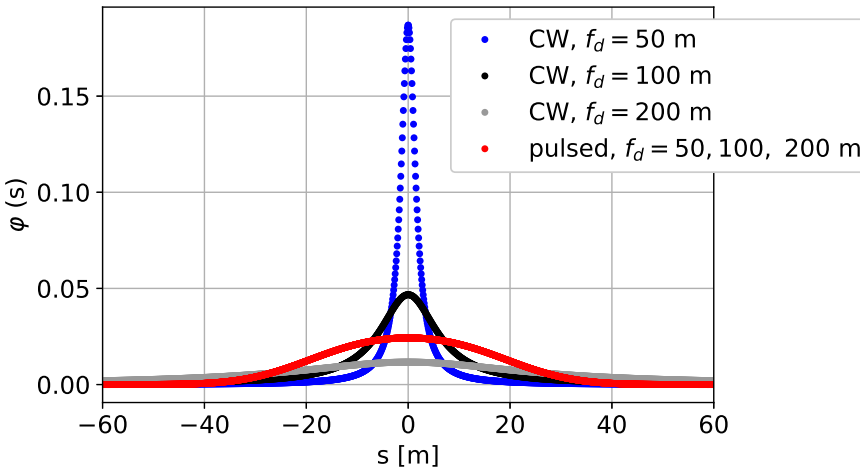

Figure 4.1: Weighting functions of a CW lidar ($r_b = 28$ mm and $\lambda_l = 1565$ nm) and a pulsed lidar ($\Delta p = 38.4$ m and $\Delta l = 24.75$ m) measuring at several distances.

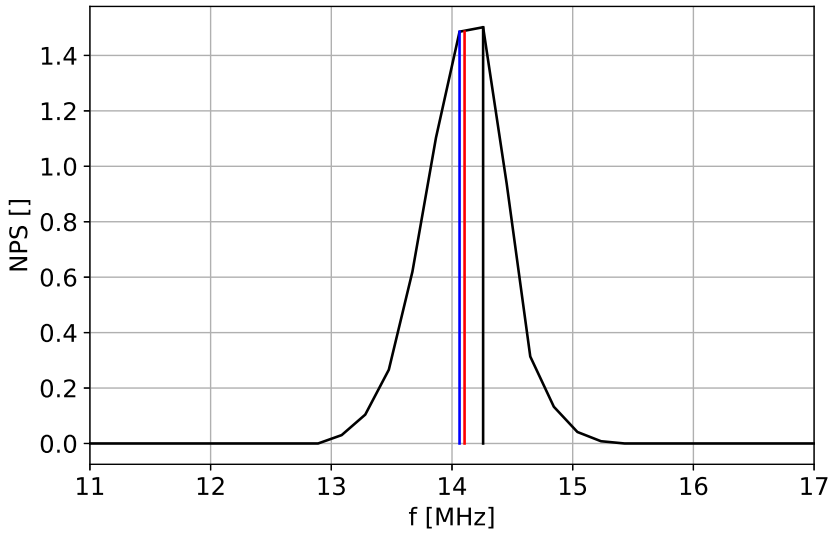

Figure 4.2: Normalized average power spectrum (NPS) from the measurement campaign of **Paper VII**. The vertical lines highlight the peak (*black*), median (*blue*) and centroid (*red*) frequencies.

the width of the power spectrum depends mainly on atmospheric turbulence and the weighting function. For a vertically-scanning ground-based lidar, the vertical wind shear also affects the width of the spectrum.

As highlighted in Fig. 4.2, the Doppler shift can be retrieved by estimating several frequency values from the power spectrum: the peak, the median or the centroid frequency [30]. Then, the radial velocity corresponding to such frequency is estimated with Eq. 4.6. Generally, the centroid method is most commonly used for wind speed estimations, while both the median and peak methods attenuate better the probe-volume effect on turbulence estimations [25, 30]. The power spectrum can also be seen as a distribution of radial velocities by converting the frequency axis of Fig. 4.2 to radial velocities through eq. 4.6.

In the lidar simulator, the radial-velocity power spectrum is retrieved as:

$$S(v_r) = \int_{s_{\min}}^{s_{\max}} \varphi(s)\, \delta(v_r - \mathbf{u}(s) \cdot \mathbf{n})\, \mathrm{d}s, \tag{4.9}$$

where δ is the Dirac delta function and $\mathbf{n} = (n_x, n_y, n_z)$ is the unit vector along the beam direction. $s_{\min}$ and $s_{\max}$ are the boundary of the modelled portion of the probe volume. From $S(v_r)$, the measured radial velocity can be retrieved as either the centroid, median or peak frequency. Specifically, when applying the centroid method, the radial velocity coincides with the first statistical moment of the spectrum:

$$v_r = \int_{s_{\min}}^{s_{\max}} \varphi(s) S(v_r)\, \mathrm{d}v_r. \tag{4.10}$$

The lidar-measurements time-series is retrieved by applying Eq. 4.9 along the whole length of the synthetic wind field. Because of the Taylor's assumption, time and space coincide along the direction of the x-axis. So, wind velocities are retrieved at subsequent focus points, whose locations depend on the lidar scanning geometry and the measurement frequency. Fig. 4.3 shows an illustration of the virtual measurements retrieved with a circular scanning lidar inside the turbulence box.

By neglecting the probe-volume effect and assuming the lidar measuring at a single point, the relation between the radial velocity and the wind speed vector can be written as

$$v_r = \mathbf{n} \cdot \mathbf{u} = n_x u + n_y v + n_z w. \tag{4.11}$$

This relation is used to reconstruct the wind speed vector from the radial velocity measurements through different wind-speed reconstruction methods, which depend on the lidar scanning geometry and the characteristics of the flow field [37, 12].

4.3 Nacelle lidar turbulence measurements

When referring to the coordinate system of Fig 4.3, the unit vector along the lidar beam direction can be defined as $\mathbf{n} = (n_x, n_y, n_z) = (-\cos\phi, \cos\theta \sin\phi, \sin\theta \sin\phi)$, where ϕ is the the angle between the beam direction and the negative x-axis (the lidar half-opening

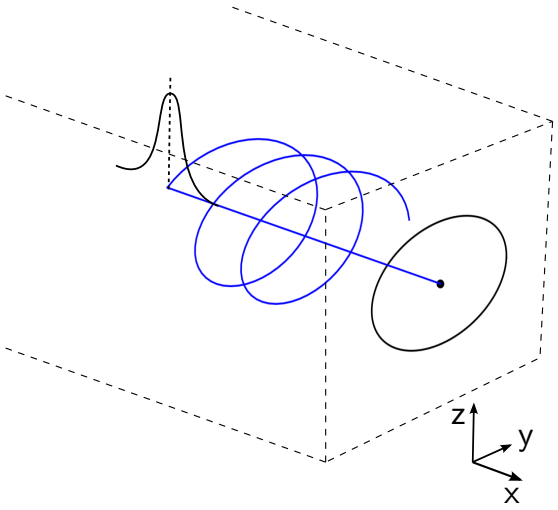

Figure 4.3: Schematics of the lidar simulator indicating the rotor, the lidar scanning pattern, the weighting function and the boundaries of the turbulence box.

angle) and θ is the angle between the y-axis and the projection of the beam onto the y-z plane. Consequently, by taking the variance of Eq. 4.11, the variance of the radial velocity is retrieved as [83]:

$$\begin{aligned}\sigma_{v_r}^2 =&\sigma_u^2 \cos^2\phi + \sigma_v^2 \cos^2\theta \sin^2\phi + \sigma_w^2 \sin^2\theta \sin^2\phi \\ &- 2\left\langle u'v'\right\rangle \cos\phi \cos\theta \sin\phi \\ &- 2\left\langle u'w'\right\rangle \cos\phi \sin\theta \sin\phi \\ &+ 2\left\langle v'w'\right\rangle \sin^2\phi \cos\theta \sin\theta.\end{aligned} \tag{4.12}$$

Due to the probe-volume effect, lidar measurements are not able to detect the velocity fluctuations at high frequency associated with small turbulence spatial structures. This results in an underestimation, or filtering, of the radial velocity variance $\sigma_{v_r}^2$. However, when the Doppler power spectra are available, the unfiltered radial velocity variance can be estimated as the second central statistical moment of the ensemble average spectrum [43]:

$$\sigma_{v_r,\mathrm{unf}}^2 = \int_{-\infty}^{\infty} \left\langle S(v_r)\right\rangle \left(v_r - \left\langle v_r\right\rangle\right)^2 \mathrm{d}v_r. \tag{4.13}$$

Then, same as for the estimation of the wind speed vector, reconstruction methods are needed to retrieve the Reynolds stresses from the measured $\sigma_{v_r,\mathrm{unf}}^2$.

In **Paper III**, several nacelle lidar configurations are simulated to retrieve turbulence measurements under homogeneous conditions. The lidar probe-volume effect is neglected by assuming point-wise measurements from the lidar. The Reynolds stresses are retrieved through a least-squares method which uses the radial velocity variances of each beam without reconstructing the wind components (u, v and w). The analysis is conducted with the implemented lidar simulator over 100 turbulence wind fields generated with the Mann model. Results show that at least six beams are needed, including one beam with

a different opening angle ϕ, to retrieve all the six Reynolds stresses. Additionally, both accuracy and uncertainty of the Reynolds stresses estimation improve by increasing ϕ, while no substantial improvement is obtained by increasing the number of beams beyond six.

In **Paper IV**, the results from **Paper III** are validated with both field measurements and more accurate lidar simulations, where the probe volume is modelled including both CW and pulsed lidars. Additionally, both numerical and experimental results show that, when the Doppler power spectrum $S(v_r)$ is available, all lidar configurations are able to accurately estimate the variance of the along-wind component σ_u^2, with variations up to 6.8% relatively to the mean value of σ_u^2 estimated with a sonic anemometer.

4.4 Dynamic wake meandering model

The DWM model is an efficient way of simulating wind turbine wakes in a time domain. It is based on the assumption of Taylor's frozen turbulence and it consists of three parts: a model for predicting the downstream evolution of the quasi-steady velocity deficit, a model for the meandering of the wake caused by large-scale turbulence structures and a model for the wake-generated turbulence [2].

The quasi-steady velocity deficit is defined according to the work of Ainslie [3]. In the near-wake region (within 2–3D) the wake deficit is function of the turbine's axial induction derived according to the blade element momentum (BEM) theory [2]. In the far-wake region (downstream distances larger than 2–3D), the flow field is defined with the thin-shear-layer form of the rotationally symmetric Navier-Stokes (N-S) equations: the pressure terms are neglected and turbulence closure is achieved with an eddy viscosity term [2]. The N-S equations consist of the following formulations for the momentum equation

$$U\frac{\partial U}{\partial x} + V_r\frac{\partial U}{\partial r} = \frac{1}{r}\frac{\partial}{\partial r}\left(\nu_t\, r\frac{\partial U}{\partial r}\right) \tag{4.14}$$

and the continuity equation

$$\frac{1}{r}\frac{\partial}{\partial r}\left(V_r\, r\right) + \frac{\partial U}{\partial x} = 0\,, \tag{4.15}$$

where U and V_r are the mean flow velocities in the axial and radial directions, respectively. ν_t represents the eddy viscosity term, which accounts for both atmospheric and shear layer generated turbulence [38, 18]:

$$\nu_t = F_1\, k_1\, \mathrm{TI}_{amb} + F_2\, k_2 \max\left(\frac{D_w^2}{2U_{\mathrm{hub}}\, D}\left|\frac{\partial U}{\partial r}\right|; \frac{D_w}{D}\left(1 - \frac{U_{\min}}{U_{\mathrm{hub}}}\right)\right), \tag{4.16}$$

where D_w is the wake diameter, TI_{amb} is the ambient turbulence intensity, $U_{\min}$ is the minimum wind speed in the wake. k_1 and k_2 are empirical constants. F_1 and F_2 are filter functions used to model the development of the turbulent stresses inside the wake.

The wake is assumed as a passive tracer driven by large-scale turbulence structures and the wake meandering is modelled by superimposing turbulence fluctuations with a cut-off frequency of $f_{cut} = U/2\mathrm{D}$, as the atmospheric turbulence structures responsible

for the wake meandering are in the order of 2D and larger [78]. The superimposed turbulence fluctuations are modelled with a turbulence box presenting a discretization of $\Delta y = \Delta z = D$, with the velocity vectors at each grid point evaluated as the average over the grid cube.

Additional turbulence is generated in the wake due to the velocity shear, as well as to trailing vortices generated at both tip and root of the blade. The additional wake turbulence is modelled by superimposing a turbulence box generated with $\Gamma = 0$ and a length scale L which is 10% of the atmospheric turbulence length scale, as wake-generated turbulence is nearly isotropic and characterized by smaller structures than atmospheric turbulence [1]. Additionally, wake turbulence is purely mechanically generated and rather inhomogenous. Such inhomogeneity is modelled by scaling the wake turbulence box with the factor

$$K_{mt}(\hat{r}) = |1 - \hat{U}_{\mathrm{def}}(\hat{r})|\, k_{m1} + \left| \frac{\partial \hat{U}_{\mathrm{def}}(\hat{r})}{\partial \hat{r}} \right| k_{m2}\,, \tag{4.17}$$

where $\hat{U}_{\mathrm{def}}$ is the mean velocity in the wake U_{def} nondimensionalized with U_{hub}. $\hat{r}$ is the radial distance normalized by the rotor radius. k_{m1} and k_{m2} are empirical constants [2].

The final three-dimensional velocity field is obtained through linear superposition of the quasi steady velocity deficit and the three fluctuating components related to the meandering turbulence, the ambient turbulence and the wake-generated turbulence:

$$u_{\mathrm{DWM}} = U_{\mathrm{def}} + u'_{\mathrm{amb}} + u'_{\mathrm{meandering}} + K_{mt}\, u'_{\mathrm{wake}}\,. \tag{4.18}$$

4.5 Multivariate power curves using nacelle lidars

In **Paper V** and **Paper VI**, datasets of synthetic power performance tests are generated by retrieving virtual lidar measurements from the same wind fields used as input to aeroelastic simulations of the Vestas V52 wind turbine [61]. The datasets are then used to implement and test multivariate power curves in the form of multivariable polynomial regressions, which consist of all the possible polynomial combinations of the N input variables with degree less than or equal to the specified degree β. For example, in the case of $\beta = 2$ and three input variables x_1, x_2 and x_3, the multivariable polynomial expression is defined as

$$y = c_1 + c_2x_1 + c_3x_2 + c_4x_3 + c_5x_1x_2 + c_6x_1x_3 + c_7x_2x_3 + c_8x_1^2 + c_9x_2^2 + c_{10}x_3^2, \tag{4.19}$$

where $c_1, .., c_{10}$ are the coefficients of the polynomial regression.

Since the same dataset is used to both train and test the multivariable polynomial regression, a k-fold cross-validation is performed to avoid overfitting. Specifically, the dataset is split into k folds (or subsets) of approximately equal size, $k - 1$ of which are used to train the regression, which is then tested on the one remaining fold. Such training-testing process is repeated k times with a different fold being used as the test set each time. The accuracy of the multivariate power curves is quantified with their error in power prediction, i.e. the deviation between the actual power output values given by the aeroleastic simulations and the power output predicted by the multivariate

power curves. The mean error in power prediction E_j is evaluated for each j^{th} iteration of the k-fold cross-validation. Then, by averaging the errors across all k iterations, the accuracy of the model is evaluated with the generalization error $E_{\text{gen}} = \frac{1}{k}\sum_{j=1}^{k} E_j$.

In **Paper V**, the multivariate power curves are tested under wake-free conditions including cases with yaw misalignment, i.e. the mean wind direction and the turbine rotor axis are skewed of an angle γ. The multivariable polynomial regressions define the power output as function of wind speed, turbulence and yaw misalignment: $P = P(U, \sigma_u^2, \gamma)$. The wind characteristics U and σ_u^2 are estimated with both a virtual sonic anemometer at hub height and simulations of the DTU SpinnerLidar [59]. The same reconstruction methods presented in **Paper III** and **Paper IV** are used to retrieve U and σ_u^2 from the v_r and $\sigma_{v_r}^2$ values. Results show that the multivariate power curves outperform the IEC standard power curve, with an error reduction of 48% when testing on a realistic dataset, which includes the same wind conditions of a test site on the west coast of Denmark. The multi-dimensional power curves are more accurate when using SpinnerLidar measurements than with mast-based anemometry, as nacelle lidars measure in front of the turbine in spite of the yaw misalignment, allowing for a better characterization of the inflow to the rotor. Additionally, it is shown that both turbulence and yaw misalignment improve the power output prediction relatively to using the wind speed only.

In **Paper VI**, multivariate power curves in the form of multivariable polynomial regressions are tested under both wake-free and waked conditions. Several nacelle lidar configurations are simulated, including both relatively simple commercial devices and complex configurations utilized in research projects, as, e.g., the DTU SpinnerLidar [59]. For the wake-free cases, the hub-height wind speed and the wind speed variance are used as input variables to the multivariate power curve $P = P(U_{\text{hub}}, \sigma_u^2)$, where U_{hub} and σ_u^2 are reconstructed from the lidar measurements using the methods presented in **Paper III** and **Paper IV**. When including waked conditions, due to the strong inhomogeneity of the flow field, the mean wind speed U and the radial velocity variance $\sigma_{v_r}^2$ retrieved from each lidar beam are considered as possible input variables, with U reconstructed by neglecting both the horizontal and vertical wind components: $v_r = n_x U$. Among all the measured values of U and $\sigma_{v_r}^2$, the input variables are selected with a feature-selection process. For example, in case of a lidar measuring along five beams, the input variables are selected among ten possible features (five values of both U and $\sigma_{v_r}^2$).

The feature selection is performed through a forward-selection algorithm: starting with an empty model, features are added iteratively by selecting the variable providing the greatest improvement in power prediction. The selection stops when the prediction error increases by adding one more variable. An illustration of the feature-selection process is shown in Fig. 4.4. At each step, the prediction error given by each model is evaluated with a k-fold cross-validation to ensure that the models are tested over all the observations of the dataset and that the selected features do not depend on which observations are used to train the model. Additionally, if the prediction accuracy was evaluated on the training data, the error would iteratively decrease until all the available features are selected. However, this results in overfitting over the training data: a larger error is obtained when testing the regression over new data, as the model is too closely related to the training data, with low capacity to describe the new data. Therefore, by

performing a cross-validation, the optimal number of features is spotted, allowing the most accurate modelling of the power-velocity relation without causing overfitting.

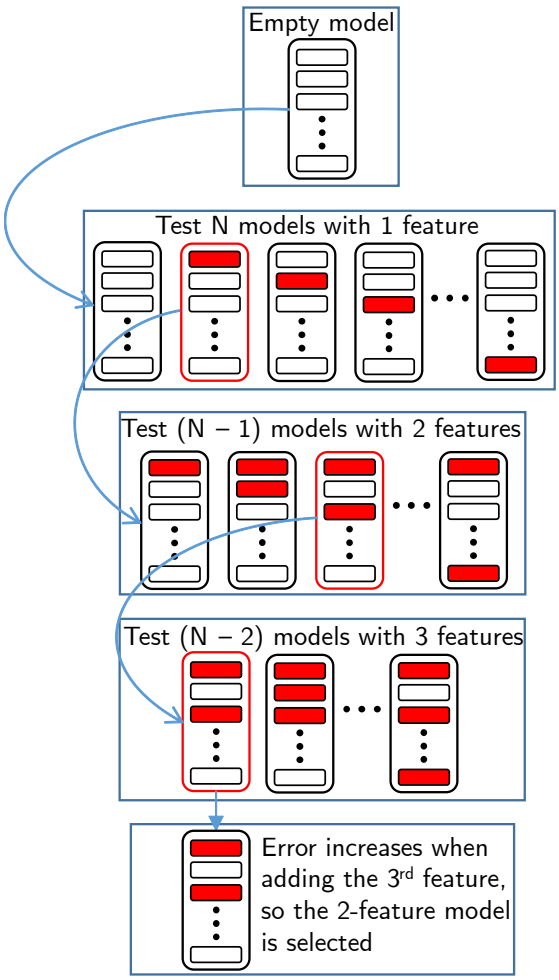

Figure 4.4: Schematics of the feature-selection process when two input variables are selected out of N available features.

Results from **Paper VI** show that the multivariate power curves are more accurate than the IEC standard power curve under both wake-free and waked conditions, with an error reduction of 88% for the in-wake cases. The feature-selection process shows the benefit of measuring wind characteristics at several locations, with error reductions of more than 50% compared to the case of a polynomial regression with a single wind speed measurement as the sole input variable. The feature selection also shows the importance of accounting for turbulence, which is selected as an input variable for all the tested lidar configurations. Moreover, the multivariate power curves evaluate the wind turbine power performance with accuracy of the same order under both homogeneous and waked conditions. When using SpinnerLidar-based multivariate power curves, the power output is predicted with mean absolute percentage error (MAPE) of 1.12% and 2.74% under wake-free and waked conditions, respectively. Results with different lidar configurations

show that, overall, the optimal multivariate power curve consists of a multivariable polynomial regression of the 4^{th} order ($\beta = 4$) with four selected input variables: three wind speed and one turbulence measurements. Furthermore, it is investigated what are the optimal scanning locations to retrieve those four measurements, showing that the lidar should scan along a line passing through the rotor centre rather than along a circular pattern to better characterize the radial velocity gradient of the waked flow. However, the multivariate power curve provides accurate power output estimations when using a circular scanning pattern with a diameter equal to 0.77D, with error reduction of 75% relatively to the IEC standard power curve.

CHAPTER 5
SpinnerLidar measurements from the Tjæreborg wind farm

5.1 Measurement campaign

The analyzed measurements were obtained in 2012 from an onshore wind farm located in Tjæreborg, western Denmark. As shown in Fig. 5.1, the site consists of eight Neg Micon (NM) 80 2.3 MW turbines with a rotor diameter of 80 m and hub height of 59 m. Turbine T2 was equipped with the SpinnerLidar, a CW Doppler wind lidar measuring at a high frequency along a rosette pattern, installed in the rotating spinner of the turbine. Additionally, Supervisory Control and Data Acquisition (SCADA) data are available from turbine T2, including measurements from a cup anemometer mounted on the turbine nacelle. The dataset comprise both SpinnerLidar measurements and SCADA data covering a period of nine days from 2 September 2012 to 11 September 2012.

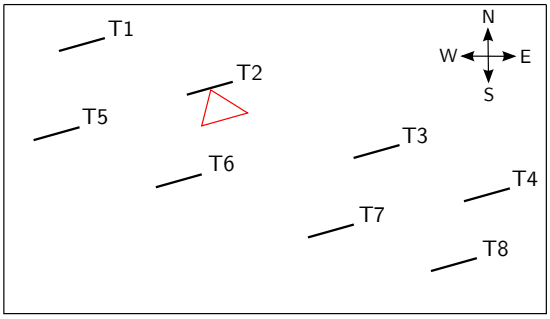

Figure 5.1: Layout of the Tjæreborg onshore wind farm [Fig. 1 from **Paper VII**].

Several measurement campaigns have been conducted to describe the characteristics of wakes using downwind-looking nacelle lidars [78, 77, 18, 72]. However, in order to evaluate the power performance of a waked turbine, an upwind-looking lidar must be installed on a waked turbine. Because of the scarcity of such measurements, the Tjæreborg SpinnerLidar dataset is still a very valuable and nearly unique dataset to investigate the power performance of a wind turbine under waked conditions.

The SpinnerLidar consists of a CW Doppler lidar equipped with two optical prisms in the scanner head. The prisms, also referred to as the Risley prism pair, rotate with a fixed velocity ratio of 13:7 and they are deflected of 15°. The lidar line-of-sight is redirected by the prism pair on a rosette pattern with half-opening angle from 0° to 30°, as shown in Fig. 5.2. More technical details can be found in the patent description [52].

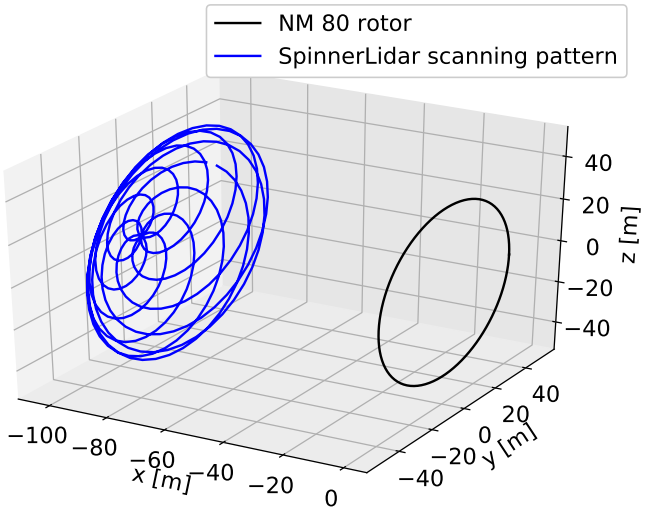

Figure 5.2: Illustration of the SpinnerLidar scanning pattern when focused at 100 m in front of an 80 m rotor.

During the field campaign, the SpinnerLidar was mounted in the rotating spinner of the turbine and it was focused to measure at 100 m, i.e. 1.25D, upstream of the turbine. Due to the configuration of the Risley prism pair, measurements are not retrieved within the same $y-z$ plane, with a maximum Δx of around 20 m between the measurements. The lidar system was set to cover the rosette pattern of Fig. 5.2 within 10 s with a measurement frequency of 100 Hz. Since the SpinnerLidar was mounted in the rotating spinner, the scanning pattern was rotating together with the rotor. Therefore, over longer periods, measurements were retrieved at many different points across the rotor swept area, as it can be seen in Fig. 5.3-(a) and Fig. 5.3-(b) for measurement periods of 10 s and 1 min, respectively.

5.2 SpinnerLidar measurements

After processing the Doppler spectra as described in **Paper VII**, all the spectra retrieved within the same 10-min period are grouped according to their measurement location. Specifically, the scanned area of the $y-z$ plane is gridded with squared cells of 3 m x 3 m, and 10-min ensemble average spectra are obtained by averaging the spectra within the same cell. Then, the 10-min mean radial velocity $\langle v_r \rangle$ is obtained as the median value of the ensemble average spectrum $\langle S(v_r) \rangle$, while the unfiltered radial velocity variance $\sigma^2_{v_r}$ is estimated according to Eq. 4.13. Only cells containing at least 30 Doppler spectra are considered for the estimation of both $\langle v_r \rangle$ and $\sigma^2_{v_r}$. Figure 5.4 shows the raw and processed Doppler spectra for the cell at $y = 0$ m and $z = 12$ m of the 10-min period 2012-09-04-08:40.

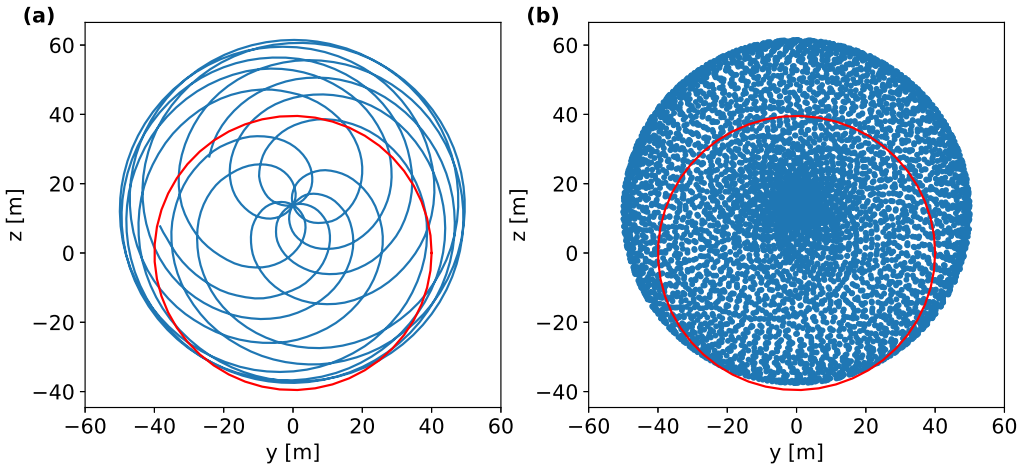

Figure 5.3: Scanning pattern covered by the SpinnerLidar every 10 s (*a*) and locations of measurements retrieved during 1 min (*b*). The *red* line indicates the rotor diameter.

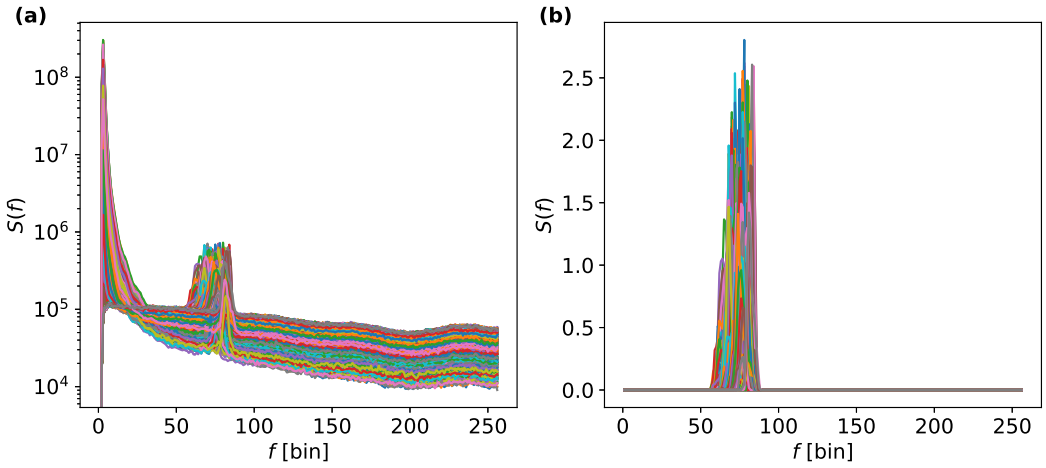

Figure 5.4: Raw (*a*) and cleaned (*b*) Doppler spectra from grid cell at $y = 0$ m and $z = 12$ m during the 10-min interval 2012-09-04-08:40.

Since most 10-min periods comprise measurements in wake, the strong inhomogeneity of the flow field does not allow to apply the wind speed reconstruction methods presented in **Paper III** and **Paper IV**. Therefore, by assuming no lateral nor vertical mean wind components ($V = W = 0$), and that the yaw misalignment is negligible, the 10-min mean wind speed is estimated as $U = \langle v_r \rangle / \langle n_x \rangle$, where $\langle n_x \rangle$ is obtained as the average of the $x-$axis components of the beam unit vectors within the grid cell. Information about turbulence is retrieved in the form of $\sigma^2_{v_r}$ as the combination of Eq. 4.13 with the strongly inhomogeneous conditions leaves no margin for the reconstruction of the Reynolds stresses.

The SpinnerLidar measurements are used to test the multivariate power curves defined as in Eq. 4.19 and validate the numerical findings from **Paper VI**. Therefore, a dataset is needed with N observations of n variables: $n/2$ measurements of both U and $\sigma^2_{v_r}$. In order to apply the feature-selection process described in Fig. 4.4, each i^{th} observation must contain the same n variables retrieved at the same $n/2$ cells. Since not all 10-min intervals comprise measurements at all cells, a filtering of both the 10-min intervals and the grid cells is applied in order to obtain a good trade-off between the number of selected intervals N and the number of available variables n, resulting in a dataset with 759 observations of 1424 variables: 712 values of both U and $\sigma^2_{v_r}$ retrieved within the cells shown in Fig. 5.5.

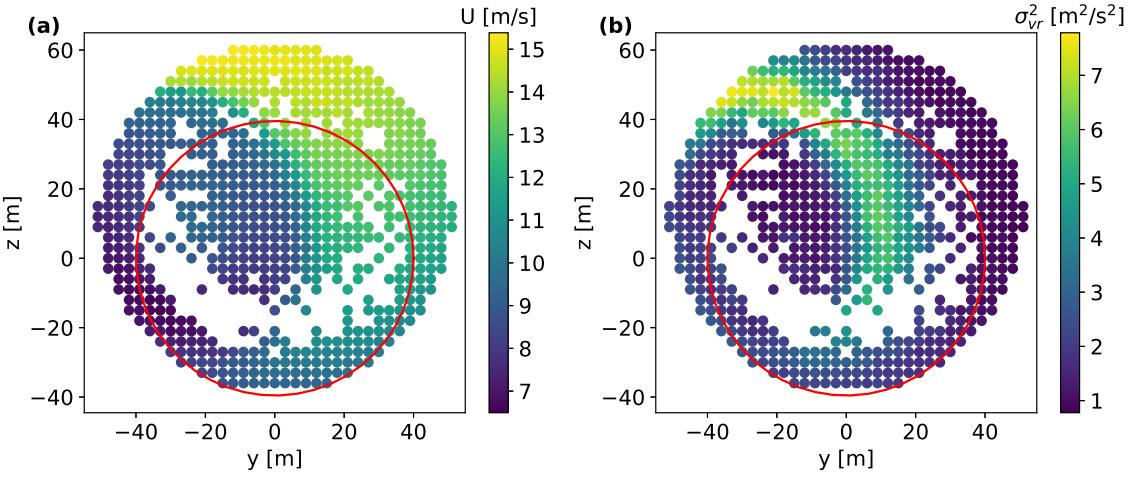

Figure 5.5: Wind speed (a) and radial velocity variance (b) at the 712 selected grid cells during the 10-min interval 2012-09-11-06:10. Turbine rotor is indicated in *red*.

The multivariate power curves are compared with IEC-similar power curves obtained by applying the IEC binning method using the SpinnerLidar measurements. Specifically, two different IEC-similar curves are obtained: one based on the wind speed U_{hub} from the central grid cell at hub height ($y = 0$ and $z = 0$ in Fig. 5.5), and one based on the rotor effective wind speed U_{rotor} obtained as the average weighted wind speed over the

rotor swept area. The IEC-similar power curves are derived using measurements under wake-free conditions, which are selected by relying on a wake detection method described in **Paper VII**. Both the multivariate and IEC-similar power curves are tested with a $k-$fold cross-validation and the generalization error is evaluated as both MAPE and root mean square error (RMSE).

5.3 Multivariate power curves: validation of the numerical results

As shown in **Paper VII**, when testing with the SpinnerLidar dataset, the multivariate power curve provides lower error in power prediction than both the IEC-similar power curves, with reductions in MAPE of 55.6% and 24.5% relatively to the U_{hub}- and U_{rotor}-based IEC curves, respectively. The input variables to the multivariate power curve are selected with the feature-selection algorithm of Fig. 4.4, resulting in 7 selected features in the optimal case: 6 wind speed and 1 turbulence measurements.

The multivariate power curve is also tested using measurements from a circular scanning lidar by selecting input variables along a circular pattern from the available cells shown in Fig. 5.5. Several circular scanning patterns are tested with diameter from 0.2D to 1.4D, with six wind speed measurements and one turbulence measurement retrieved along each circular pattern. Results show that the circular scanning pattern is suitable to implement the multivariate power curve when the scanning pattern has the proper diameter. In the optimal case, with a diameter of 0.9D, the multivariate power curve estimates the power output with a 52.5% lower MAPE than the U_{hub}-based IEC curve.

The analysis of the SpinnerLidar measurements from Tjæreborg validates some of the numerical results from **Paper VI**, showing that the multivariate power curves give a more accurate evaluation of the wind turbine power performance under waked conditions than the IEC binning method. When testing with measurements, more input variables are selected than when using the numerical dataset: 7 and 4 variables for measurements and simulations, respectively. This difference can be explained with the higher complexity of the inflow in the real case than in the simulations, where the only source of flow inhomogeneity is the DWM-generated wake field. In the field, the inflow is characterized by additional sources of inhomogeneity and complexity, such as atmospheric stability, yaw misalignment and terrain effects. However, in both simulations and measurements, one turbulence measurement is selected among the optimal features. This shows the utility and fitness of lidar-derived turbulence measurements for power curve modelling under both waked and wake-free conditions.

When selecting features rotated of an azimuth angle θ relatively to the optimal case, in both simulations and measurements, the error in power estimation increases up to twice that of the optimal case. However, in the numerical case, the multivariate power curve still performs much better than the IEC curve for all the tested values of θ. On the contrary, in the measurements, the accuracy of the multivariate power curve is slightly more accurate than the U_{hub}-based curve and less accurate than the U_{rotor}-based curve. This difference shows the low flexibility of the feature selection when working with field

measurements. This is probably due to the higher complexity of the inflow conditions in the field.

The circular scanning pattern is a robust lidar scanning configuration, which could be used independently of the turbine location and site characteristics. In both the analyses with measurements and simulations, when using features selected along a circular pattern of the proper dimension, the multivariate power curve is more accurate than the IEC binning method. Additionally, both numerical and experimental results show the same variation of the error with the diameter of the circular scanning pattern: starting from the lowest diameter, the accuracy of the multivariate power curve increases up to a maximum around 0.9D (0.77D and 0.9D for simulations and measurements, respectively) and decreases for larger circular patterns.

CHAPTER 6

Conclusions

The main objective of this thesis is to improve the methods for the evaluation of the power performance of wind turbines in wind farms. The shortcomings of the current IEC standard procedure are highlighted through both simulations and measurements. A method is presented to correct for the effect of both blockage and wakes on IEC power performance measurements. Additionally, data-driven multivariate power curves using nacelle lidar measurements are tested under both wake-free and waked conditions through both simulations and field measurements.

6.1 Main contributions

Both numerical and experimental results show that IEC-compliant power performance measurements are influenced by blockage effects, which cause the measured power performance to be different from that of a truly isolated turbine. The power-velocity relation changes depending on the wind farm layout and the wind direction, with C_P variations up to 4% relatively to the isolated turbine under the tested conditions. Results from this thesis highlight, in agreement with previous studies, that the influence of neighbouring turbines on IEC-compliant power performance measurements should not be neglected to avoid possible biases in power performance verification tests and energy yield analyses.

A method is presented to correct for blockage effects on IEC-compliant power performance measurements. The method relies on the assumption that the velocity reductions in the turbine induction zone are function of the turbine C_T. Two different approaches are presented to apply the correction: one based on numerical simulations and one based on short range nacelle lidar measurements. The two approaches are tested numerically under neutral conditions, showing that they improve the evaluation of the power performance. Additionally, the method can be used to correct power curves measured under waked conditions.

Lidar-based data-driven methods are presented to evaluate the wind turbine power performance. Specifically, multivariate power curves are defined in the form of polynomial regressions whose input variables are several wind speed and turbulence measurements retrieved with nacelle lidars. Numerical results show that the multivariate power curves are more accurate than the IEC standard power curve under wake-free conditions, with improved power output estimations when using nacelle lidar turbulence measurements in addition to wind speed measurements. Under waked conditions, the gap between the multivariate and the IEC power curves is enhanced, with further improvement provided by the multivariate power curves, as shown by both simulations and measurements. Additionally, numerical results show that the multivariate power curves can provide

accuracy of the same order under both waked and wake-free conditions. When retrieved under waked conditions, nacelle lidar turbulence estimations are still beneficial to estimate the wind turbine power output, as shown by both numerical and experimental results.

When using nacelle lidars to retrieve turbulence measurements under waked conditions, the strong inhomogeneity of the flow field does not allow to retrieve the Reynolds stresses. However, turbulence can be estimated in the form of radial velocity variance to improve the accuracy in power output prediction. On the contrary, under homogeneous conditions, all the six Reynolds stresses can be retrieved from the measurements of a six-beam lidar which includes one beam with a different opening angle. The accuracy in turbulence estimation improves by enlarging the lidar opening angles, while it is not beneficial to further increase the number of beams. For the estimation of the along-wind variance alone, all the tested nacelle lidar configurations provide good accuracy.

The optimal lidar configuration to implement the multivariate power curves is site-specific. However, both numerical and experimental results show that a circular scanning configuration provides similar accuracy to the optimal configuration, as long as the scanning pattern has a diameter equal to around 0.9 the rotor diameter. Furthermore, such configuration is the one which gives the highest accuracy when applying the correction method to IEC-compliant power performance measurements. However, for such correction, good accuracy is also obtained with a simple two-beam lidar.

6.2 Future work

The research work presented in this thesis should be extended by further testing the correction method for IEC power performance measurements. Simulations should be conducted under different atmospheric conditions and the method should be tested using nacelle lidar measurements from the field. The experiment could be conducted with a nacelle lidar measuring both at the IEC-compliant distance and in proximity of the rotor. The lidar should be mounted on a turbine located at the edge of a large wind farm, so that both wake-free and in-wake measurements can be retrieved. Ideally, two different power performance tests should be conducted at two different locations with the same turbine model to evaluate the site-dependency of the results.

The analysis of the multivariate power curves could be extended by using nacelle lidar measurements to implement different data-driven models than the polynomial regressions tested in this work. For example, artificial neural networks could be trained with nacelle lidar measurements retrieved in front of the same turbine model from different locations in order to decrease the site-dependency of the data-driven power curve.

Finally, it would be interesting to use both approaches presented in this thesis, i.e. the physics-based correction method and the data-driven multivariate power curves, for energy yield analyses and compare the results to traditional analyses conducted with the IEC power curve provided by the manufacturer.

Bibliography

[1] H. Aagaard Madsen, Gunner Chr. Larsen, and K. Thomsen. "Wake flow characteristics in low ambient turbulence conditions". English. In: Copenhagen Offshore Wind, 2005.

[2] Helge Aagaard Madsen et al. "Calibration and Validation of the Dynamic Wake Meandering Model for Implementation in an Aeroelastic Code". English. In: *Journal of Solar Energy Engineering* 132.4 (2010), 041014 (14 pages). ISSN: 0199-6231. DOI: 10.1115/1.4002555.

[3] JF Ainslie. "Calculating the flowfield in the wake of wind turbines". In: *Journal of Wind Engineering and Industrial Aerodynamics* 27.1-3 (JAN 1988), 213–224. ISSN: 0167-6105. DOI: {10.1016/0167-6105(88)90037-2}.

[4] D. Allaerts and J. Meyers. "Boundary-layer development and gravity waves in conventionally neutral wind farms". In: *Journal of Fluid Mechanics* 814 (2017), pp. 95–130. DOI: 10.1017/jfm.2017.11.

[5] D. Astolfi and R. Pandit. "Multivariate wind turbine power curve model based on data clustering and polynomial lasso regression". In: *Applied Sciences (Switzerland)* 12.1 (2022). DOI: 10.3390/app12010072.

[6] V.A. Banakh and I.N. Smalikho. "Estimation of the turbulence energy dissipation rate from the pulsed Doppler lidar data". In: *Atmos. Oceanic Opt* 10.12 (1997), pp. 957–965.

[7] Lars Morten Bardal and Lars Roar Sætran. "Influence of turbulence intensity on wind turbine power curves". In: *Energy Procedia* 137 (2017), pp. 553–558. DOI: 10.1016/j.egypro.2017.10.384.

[8] R. J. Barthelmie and L. E. Jensen. "Evaluation of wind farm efficiency and wind turbine wakes at the Nysted offshore wind farm". In: *Wind Energy* 13.6 (2010), pp. 573–586. DOI: https://doi.org/10.1002/we.408.

[9] R. J. Barthelmie et al. "Modelling and measuring flow and wind turbine wakes in large wind farms offshore". In: *Wind Energy* 12.5 (2009), pp. 431–444. DOI: 10.1002/we.348.

[10] J Bleeg and C Montavon. "Blockage effects in a single row of wind turbines". In: *Journal of Physics: Conference Series* 2265.2 (May 2022), p. 022001. DOI: 10.1088/1742-6596/2265/2/022001.

[11] James Bleeg et al. "Wind farm blockage and the consequences of neglecting its impact on energy production". In: *Energies* 11.6 (2018). ISSN: 19961073. DOI: 10.3390/en11061609.

[12] Antoine Borraccino et al. “Wind Field Reconstruction from Nacelle-Mounted Lidars Short Range Measurements”. English. In: *Wind Energy Science* 2 (2017), pp. 269–283. ISSN: 2366-7443. DOI: 10.5194/wes-2017-10.

[13] V. Bulaevskaya et al. “Wind power curve modeling in complex terrain using statistical models”. In: *Journal of Renewable and Sustainable Energy* 7.1 (January 2015). ISSN: 1941-7012. DOI: 10.1063/1.4904430.

[14] C. Carrillo et al. “Review of power curve modelling for windturbines”. In: *Renewable and Sustainable Energy Reviews* 21 (2013), pp. 572–581. DOI: 10.1016/j.rser.2013.01.012.

[15] A. Clifton and Rozenn Wagner. “Accounting for the effect of turbulence on wind turbine power curves”. English. In: *Journal of Physics: Conference Series* 524.1 (2014). ISSN: 1742-6588. DOI: 10.1088/1742-6596/524/1/012109.

[16] A. Clifton et al. “Using machine learning to predict wind turbine power output”. In: *Environmental Research Letters* 8.2 (April 2013). ISSN: 1748-9326. DOI: 10.1088/1748-9326/8/2/024009.

[17] D. Conti, N. Dimitrov, and A. Peña. “Aeroelastic load validation in wake conditions using nacelle-mounted lidar measurements”. English. In: *Wind Energy Science* 5.3 (2020), pp. 1129–1154. ISSN: 2366-7443. DOI: 10.5194/wes-5-1129-2020.

[18] D. Conti et al. “Probabilistic estimation of the Dynamic Wake Meandering model parameters using SpinnerLidar-derived wake characteristics”. English. In: *Wind Energy Science* 6.5 (2021), pp. 1117–1142. ISSN: 2366-7443. DOI: 10.5194/wes-6-1117-2021.

[19] D. Conti et al. “Wind turbine wake characterization using the SpinnerLidar measurements”. English. In: *Journal of Physics: Conference Series* 1618.6 (2020). ISSN: 1742-6588. DOI: 10.1088/1742-6596/1618/6/062040. URL: https://www.torque2020.org/.

[20] Nikolay Krasimirov Dimitrov et al. “Wind turbine load validation using lidar-based wind retrievals”. English. In: *Wind Energy* 22.11 (2019), pp. 1512–1533. ISSN: 1095-4244. DOI: 10.1002/we.2385.

[21] DNV. *Energy Transition Outlook 2022*. 2022.

[22] P. A. Fleming et al. “Field-test results using a nacelle-mounted lidar for improving wind turbine power capture by reducing yaw misalignment”. In: Journal of Physics Conference Series 524 (2014). ISSN: 1742-6588. DOI: 10.1088/1742-6596/524/1/012002.

[23] Paul Fleming et al. “Field test of wake steering at an offshore wind farm”. In: *Wind Energy Science* 2.1 (2017), pp. 229–239. DOI: 10.5194/wes-2-229-2017.

[24] Paul A. Fleming et al. “Evaluating techniques for redirecting turbine wakes using SOWFA”. In: *Renewable Energy* 70 (2014), pp. 211–218. DOI: 10.1016/j.renene.2014.02.015.

[25] W. Fu, A. Peña, and J. Mann. "Turbulence statistics from three different nacelle lidars". English. In: *Wind Energy Science* 7.2 (2022), pp. 831–848. ISSN: 2366-7443. DOI: 10.5194/wes-7-831-2022.

[26] W. Fu et al. "Dependence of turbulence estimations on nacelle-lidar scanning strategies". In: *Wind Energy Science Discussions* 2022 (2022), pp. 1–21. DOI: 10.5194/wes-2022-85.

[27] Wei Fu et al. "Influence of nacelle-lidar scanning patterns on inflow turbulence characterization". In: *Journal of Physics: Conference Series* 2265.2 (May 2022), p. 022016. DOI: 10.1088/1742-6596/2265/2/022016.

[28] Julia Gottschall and Joachim Peinke. "How to improve the estimation of power curves for wind turbines". In: *Environmental Research Letters* 3.1 (January 2008). ISSN: 1748-9326. DOI: 10.1088/1748-9326/3/1/015005.

[29] Emil Hedevang. "Wind turbine power curves incorporating turbulence intensity". In: *Wind Energy* 17.2 (2014), pp. 173–195. DOI: 10.1002/we.1566.

[30] Dominique Philipp Held and Jakob Mann. "Comparison of methods to derive radial wind speed from a continuous-wave coherent lidar Doppler spectrum". English. In: *Atmospheric Measurement Techniques* 11.11 (2018), pp. 6339–6350. ISSN: 1867-1381. DOI: 10.5194/amt-11-6339-2018.

[31] Dominique Philipp Held and Jakob Mann. "Detection of wakes in the inflow of turbines using nacelle lidars". English. In: *Wind Energy Science* 4.3 (2019), pp. 407–420. ISSN: 2366-7443. DOI: 10.5194/wes-4-407-2019.

[32] T. G. Herges et al. "High resolution wind turbine wake measurements with a scanning lidar: Paper". English. In: Journal of Physics: Conference Series 854 (2017). DOI: 10.1088/1742-6596/854/1/012021.

[33] IEC. *IEC 61400-12-1, Power performance measurements of electricity producing wind turbines*. 2017.

[34] IEC. *IEC 61400-12, Wind turbine power performance testing*. 1998.

[35] ISO/IEC. *Guide 98-3:2008, Uncertainty of measurement-Part 3: Guide to the expression of uncertainty in measurement (GUM:1995)*. 2008.

[36] O. Janssens et al. "Data-driven multivariate power curve modeling of offshore wind turbines". In: *Engineering Applications of Artificial Intelligence* 55 (2016), pp. 331–338. DOI: 10.1016/j.engappai.2016.08.003.

[37] Stefan Kapp. "Lidar-based reconstruction of wind fields and application for wind turbine control". In: *Ph.D. thesis* (2017).

[38] Rolf-Erik Keck et al. "Implementation of a Mixing Length Turbulence Formulation Into the Dynamic Wake Meandering Model". English. In: *Journal of Solar Energy Engineering* 134.2 (2012), p. 021012. ISSN: 0199-6231. DOI: 10.1115/1.4006038.

[39] Torben J. Larsen and Anders Melchior Hansen. "How 2 HAWC2, the user's manual". English. In: Denmark. Forskningscenter Risoe. Risoe-R 1597(ver. 3-1)(EN) (2007).

[40] M. Lydia et al. “A comprehensive review on wind turbine power curve modeling techniques”. In: *Renewable and Sustainable Energy Reviews* 30 (2014), pp. 452–460. DOI: 10.1016/j.rser.2013.10.030.

[41] J. Mann. “The spatial structure of neutral atmospheric surface-layer turbulence”. English. In: *Journal of Fluid Mechanics* 273 (1994), pp. 141–168. ISSN: 0022-1120.

[42] J. Mann. “Wind field simulation”. English. In: *Probabilistic Engineering Mechanics* 13 (1998), pp. 269–282. ISSN: 0266-8920.

[43] Jakob Mann et al. “Lidar Scanning of Momentum Flux in and above the Atmospheric Surface Layer”. English. In: *Journal of Atmospheric and Oceanic Technology* 27.6 (2010), pp. 959–976. DOI: 10.1175/2010JTECHA1389.1.

[44] Bartolomé Manobel et al. “Wind turbine power curve modeling based on Gaussian Processes and Artificial Neural Networks”. In: *Renewable Energy* 125 (2018), pp. 1015–1020. ISSN: 0960-1481. DOI: https://doi.org/10.1016/j.renene.2018.02.081.

[45] M. Marčiukaitis et al. “Non-linear regression model for wind turbine power curve”. In: *Renewable Energy* 113 (2017), pp. 732–741. DOI: 10.1016/j.renene.2017.06.039.

[46] S. McTavish et al. “An investigation of in-field blockage effects in closely spaced lateral wind farm configurations”. In: *Wind Energy* 18.11 (2015), pp. 1989–2011. DOI: 10.1002/we.1806.

[47] D. Medici et al. “The upstream flow of a wind turbine: blockage effect”. In: *Wind Energy* 14.5 (JUL 2011), 691–697. ISSN: 1095-4244. DOI: {10.1002/we.451}.

[48] J. Medley et al. “Evaluation of wind flow with a nacelle-mounted, continuous wave wind lidar”. English. In: (2014). URL: http://www.ewea.org/annual2014/.

[49] A. R. Meyer Forsting, N. Troldborg, and A. Borraccino. “Modelling lidar volume-averaging and its significance to wind turbine wake measurements”. In: *Journal of Physics: Conference Series* 854 (2017), p. 012014. DOI: 10.1088/1742-6596/854/1/012014.

[50] Alexander Raul Meyer Forsting. “Modelling Wind Turbine Inflow: The Induction Zone”. English. PhD thesis. Denmark, 2017. DOI: 10.11581/DTU:00000022.

[51] Alexander Raul Meyer Forsting, Niels Troldborg, and Mac Gaunaa. “The flow upstream of a row of aligned wind turbine rotors and its effect on power production”. English. In: *Wind Energy* 20.1 (2017), pp. 63–77. ISSN: 1095-4244. DOI: 10.1002/we.1991.

[52] Torben Mikkelsen, Jakob Mann, and Morten Nielsen. *Rotating prism scanning device and method for scanning*. English. Patent. EP 2304489. 2011.

[53] T. Nishino and S. Draper. “Local blockage effect for wind turbines”. In: *Journal of Physics: Conference Series* 625.1 (2015). DOI: 10.1088/1742-6596/625/1/012010.

[54] Nicolai Gayle Nygaard et al. “Modelling cluster wakes and wind farm blockage”. In: *Journal of Physics: Conference Series* 1618.6 (September 2020), p. 062072. DOI: 10.1088/1742-6596/1618/6/062072.

[55] R. Pandit, D. Infield, and M. Penas. “Accounting for environmental conditions in data-driven wind turbine power models”. In: *IEEE Transactions on Sustainable Energy* (2022), pp. 1–10. DOI: 10.1109/TSTE.2022.3204453.

[56] Mads M. Pedersen et al. “Using wind speed from a blade-mounted flow sensor for power and load assessment on modern wind turbines”. English. In: *Wind Energy Science* 2 (2017), pp. 547–567. ISSN: 2366-7443. DOI: 10.5194/wes-2-547-2017.

[57] Francis Pelletier, Christian Masson, and Antoine Tahan. “Wind turbine power curve modelling using artificial neural network”. In: *Renewable Energy* 89 (April 2016), pp. 207–214. ISSN: 0960-1481. DOI: 10.1016/j.renene.2015.11.065.

[58] A. Peña, J. Mann, and N.K. Dimitrov. “Turbulence characterization from a forward-looking nacelle lidar”. English. In: *Wind Energy Science* 2.1 (2017), pp. 133–152. ISSN: 2366-7443. DOI: 10.5194/wes-2-133-2017.

[59] Alfredo Peña, Jakob Mann, and Gunhild Rolighed Thorsen. *SpinnerLidar measurements for the CCAV52*. English. Vol. 0177. Denmark: DTU Wind Energy, 2019. ISBN: 978-87-93549-45-6.

[60] Alfredo Peña et al. *Remote Sensing for Wind Energy*. English. DTU Wind Energy E 0084(EN). Denmark: DTU Wind Energy, 2015.

[61] Jennifer M. Rinker, Morten H. Hansen, and Torben J. Larsen. “Calibrating a wind turbine model using diverse datasets”. In: *Journal of Physics: Conference Series* 1037 (2018). ISSN: 1742-6588. DOI: 10.1088/1742-6596/1037/6/062026.

[62] Yves-Marie Saint-Drenan et al. “A parametric model for wind turbine power curves incorporating environmental conditions”. In: *Renewable Energy* 157 (September 2020), pp. 754–768. DOI: 10.1016/j.renene.2020.04.123.

[63] J. Schneemann et al. “Offshore wind farm global blockage measured with scanning lidar”. In: *Wind Energy Science* 6.2 (2021), pp. 521–538. DOI: 10.5194/wes-6-521-2021.

[64] A. Sebastiani et al. “Data analysis and simulation of the Lillgrund wind farm”. In: *Wind Energy* 24.6 (2021), pp. 634–648. DOI: 10.1002/we.2594.

[65] A. Sebastiani et al. “Evaluation of the global-blockage effect on power performance through simulations and measurements”. In: *Wind Energy Science* 7.2 (2022), pp. 875–886. DOI: 10.5194/wes-7-875-2022.

[66] Alessandro Sebastiani, Alfredo Peña, and Niels Troldborg. “Numerical evaluation of multivariate power curves for wind turbines in wakes using nacelle lidars”. In: *Renewable Energy* 202 (2023), pp. 419–431. ISSN: 0960-1481. DOI: https://doi.org/10.1016/j.renene.2022.11.081.

[67] Alessandro Sebastiani, Alfredo Peña, and Niels Troldborg. "Wind turbine power performance characterization through aeroelastic simulations and virtual nacelle lidar measurements". In: *Journal of Physics: Conference Series* 2265.2 (May 2022), p. 022059. DOI: 10.1088/1742-6596/2265/2/022059.

[68] Antonio Segalini and Jan Åke Dahlberg. "Blockage effects in wind farms". In: *Wind Energy* 23.2 (2020), pp. 120–128. ISSN: 10991824. DOI: 10.1002/we.2413. URL: https://doi.org/10.1002/we.2413.

[69] C.W. Slinger, M. Harris, and M. Pitter. "Wind speed measurement for absolute power curve determination from induction zone lidar measurements". In: *Journal of Physics: Conference Series* 1618.3 (2020). DOI: 10.1088/1742-6596/1618/3/032027.

[70] R.B. Smith. "Gravity wave effects on wind farm efficiency". In: *Wind Energy* 13.5 (2010), pp. 449–458. DOI: 10.1002/we.366.

[71] C. M. Sonnenschein and F. A. Horrigan. "Signal-to-Noise Relationships for Coaxial Systems that Heterodyne Backscatter from the Atmosphere". In: *Appl. Opt.* 10.7 (July 1971), pp. 1600–1604. DOI: 10.1364/AO.10.001600.

[72] I. Sood et al. "Comparison of large eddy simulations against measurements from the Lillgrund offshore wind farm". In: *Wind Energy Science* 7.6 (2022), pp. 2469–2489. DOI: 10.5194/wes-7-2469-2022.

[73] J.M.I. Strickland and R.J.A.M. Stevens. "Effect of thrust coefficient on the flow blockage effects in closely-spaced spanwise-infinite turbine arrays". In: *Journal of Physics: Conference Series* 1618.6 (2020). DOI: 10.1088/1742-6596/1618/6/062069.

[74] Jessica M.I. Strickland and Richard J.A.M. Stevens. "Investigating wind farm blockage in a neutral boundary layer using large-eddy simulations". In: *European Journal of Mechanics - B/Fluids* 95 (2022), pp. 303–314. ISSN: 0997-7546. DOI: https://doi.org/10.1016/j.euromechflu.2022.05.004.

[75] E. Taslimi-Renani et al. "Development of an enhanced parametric model for wind turbine power curve". In: *Applied Energy* 177 (2016), pp. 544–552. DOI: 10.1016/j.apenergy.2016.05.124.

[76] G.I. Taylor. "The spectrum of turbulence". English. In: *Procedings of the Royal Society of London. Series A, Mathematical and Physical Sciences* 164 (1938), 476:490. DOI: https://doi.org/10.1098/rspa.1938.0032.

[77] Davide Trabucchi, Juan-José Trujillo, and Martin Kühn. "Nacelle-based Lidar Measurements for the Calibration of a Wake Model at Different Offshore Operating Conditions". In: *Energy Procedia* 137 (2017). 14th Deep Sea Offshore Wind RD Conference, EERA DeepWind'2017, pp. 77–88. ISSN: 1876-6102. DOI: https://doi.org/10.1016/j.egypro.2017.10.335.

[78] Juan-José Trujillo et al. "Light detection and ranging measurements of wake dynamics. Part II: two-dimensional scanning". English. In: *Wind Energy* 14.1 (2011), pp. 61–75. ISSN: 1095-4244. DOI: 10.1002/we.402.

[79] R. Wagner et al. “Accounting for the speed shear in wind turbine power performance measurement”. In: *Wind Energy* 14.8 (2011), pp. 993–1004. DOI: 10.1002/we.509.

[80] R. Wagner et al. “Power curve measurement with a nacelle mounted lidar”. English. In: *Wind Energy* 17.9 (2014), pp. 1441–1453. ISSN: 1095-4244. DOI: 10.1002/we.1643.

[81] Rozenn Wagner et al. “Uncertainty of power curve measurement with a two-beam nacelle-mounted lidar”. English. In: *Wind Energy* 19 (2015), pp. 1269–1287. ISSN: 1095-4244. DOI: 10.1002/we.1897.

[82] Yun Wang et al. “Approaches to wind power curve modeling: A review and discussion”. In: *Renewable and Sustainable Energy Reviews* 116 (2019). DOI: 10.1016/j.rser.2019.109422.

[83] Richard E. Cupp Wynn L. Eberhard and Kathleen R. Healy. “Doppler Lidar Measurement of Profiles of Turbulence and Momentum Flux”. English. In: *Journal of Atmospheric and Oceanic Technology* 6 (1989), pp. 809–819. DOI: https://doi.org/10.1175/1520-0426(1989)006<0809:DLMOPO>2.0.CO;2.

[84] Keyi Xu et al. “Quantile based probabilistic wind turbine power curve model”. In: *Applied Energy* 296 (2021). DOI: 10.1016/j.apenergy.2021.116913.

Publications

Paper I: Evaluation of the global-blockage effect on power performance through simulations and measurements

Wind Energ. Sci., 7, 875–886, 2022
https://doi.org/10.5194/wes-7-875-2022

eawe european academy of wind energy
Open Access
WIND ENERGY SCIENCE

Evaluation of the global-blockage effect on power performance through simulations and measurements

Alessandro Sebastiani, Alfredo Peña, Niels Troldborg, and Alexander Meyer Forsting

DTU Wind Energy, Frederiksborgvej 399 4000, Roskilde, Denmark

Correspondence: Alessandro Sebastiani (aseb@dtu.dk)

Received: 15 September 2021 – Discussion started: 21 October 2021
Revised: 11 January 2022 – Accepted: 22 March 2022 – Published: 14 April 2022

Abstract. Blockage effects due to the interaction of five wind turbines in a row are investigated through both Reynolds-averaged Navier–Stokes simulations and site measurements. Since power performance tests are often carried out at sites consisting of several turbines in a row, the objective of this study is to evaluate whether the power performance of the five turbines differs from that of an isolated turbine. A number of simulations are performed, in which we vary the turbine inter-spacing (1.8, 2 and 3 rotor diameters) and the inflow angle between the incoming wind and the orthogonal line to the row (from 0 to 45°). Different values of the free-stream velocity are considered to cover a broad wind speed range of the power curve. Numerical results show consistent power deviations for all five turbines when compared to the isolated case. The amplitude of these deviations depends on the location of the turbine within the row, the inflow angle, the inter-spacing and the power curve region of operation. We show that the power variations do not cancel out when averaging over a large inflow sector (from -45 to $+45°$) and find an increase in the power output of up to $+1\,\%$ when compared to the isolated case under idealised conditions (neutral atmospheric conditions, no vertical wind shear or ground effects). We simulate power performance "measurements" with both a virtual mast and nacelle-mounted lidar and find a combination of power output increase and upstream velocity reduction, which causes an increase of $+4\,\%$ in the power coefficient under idealised conditions. We also use measurements from a real site consisting of a row of five wind turbines to validate the numerical results. From the analysis of the measurements, we also show that the power performance is impacted by the neighbouring turbines. Compared to when the inflow is perpendicular to the row, the power output varies by $+1.8\,\%$ and $-1.8\,\%$ when the turbine is the most downwind and upwind of the line, respectively.

1 Introduction

It is well known that the performance of a wind turbine is highly affected by the wakes of upstream turbines (Crespo et al., 1999; Barthelmie et al., 2009; Göçmen et al., 2016; Sebastiani et al., 2021). Also well known is the blockage effect, which is the reduction of the velocity upstream of the turbine, due to the presence of the turbine itself (Medici et al., 2011; Meyer Forsting, 2017). Recently, the global-blockage effect has started to draw attention within the wind energy community. This is also characterised by a velocity decrease but upstream of a wind farm or cluster of wind turbines, due to the presence of the wind farm itself (Bleeg et al., 2018). In the latter study, the global-blockage effect was quantified by comparing wind speed measurements collected from meteorological masts before and after the operation of wind farms. Additionally, they showed, using Reynolds-averaged Navier–Stokes (RANS) simulations, that the velocity reduction upstream of wind farms causes the energy production of each of the turbines in the front row of the wind farm to be different from that of the same turbine in isolation. The velocity reduction upstream of a wind farm made up of several rows was also shown by Segalini and Dahlberg (2020) using wind tunnel experiments. Schneemann et al. (2021) showed how the global-blockage effect relates to the atmospheric stability for the case of an offshore wind farm. They used a long-range Doppler scanning lidar to measure the wind speed up-

stream of the wind farm and showed global blockage only under stable atmospheric conditions.

The global-blockage effect is not only due to the superposition of the induction from the single turbines, but is also the result of the interaction between the wind farm as a whole and the atmospheric boundary layer, which might generate an upstream reverse pressure gradient and thus a wind speed reduction (Smith, 2010; Allaerts and Meyers, 2017; Porté-Agel et al., 2020). In this work, with the term global blockage, we refer to all the alterations of the flow field (out of the wind turbine wakes) caused by the presence of a number of wind turbines, which would not occur for the case of an isolated turbine. Specifically, we do not specify whether we refer to the superposition of the rotor inductions, to the interaction between the rotors and the atmospheric boundary layer, or to the combination of both.

Some studies showed global blockage for a single row of turbines, where turbines are affected by those beside them rather than by downstream turbines (Nishino and Draper, 2015; McTavish et al., 2015; Meyer Forsting et al., 2017b; Strickland and Stevens, 2020). The power output of three wind turbines aligned perpendicularly to the wind was shown to be higher than that of an isolated turbine by means of both wind tunnel studies and simulations with the free-vortex code GENUVP (McTavish et al., 2015). They explained that the power increase is a consequence of in-field blockage occurring between adjacent turbines, which results in a region of relative increased wind speeds that extends up to three rotor diameters (D) upstream of the row. For the case with a spacing of 2 D, they found an increase in power output of the order of 3 % compared to the isolated turbine. Similarly, Nishino and Draper (2015) showed through RANS simulations that wind turbines produce up to 5 % more than what they would produce in isolation when they are aligned in a row of nine wind turbines with a spacing of 1.5 D. Strickland and Stevens (2020) performed large-eddy simulations of an infinite row of wind turbines with a spacing of 1.57 D, showing that the power enhancement relative to the isolated case increases with the thrust coefficient up to 8 %.

According to the IEC standard (IEC, 2017), power performance testing can be performed on a turbine within a row of turbines by considering a wind sector within the direction perpendicular to the row ($\pm 50°$ when the turbine inter-spacing is 2 D). Within these inflow conditions, turbines are assumed to be unaffected by neighbouring turbine wakes, and the measured power curve is assumed to be valid for the case of an isolated turbine. The study of McTavish et al. (2015) was perhaps the first that questioned these assumptions. Meyer Forsting et al. (2017b) analysed the power production of turbines in a row by using both RANS simulations and a simple inviscid vortex ring model with wake expansion. They considered a row of five turbines with a 3 D turbine spacing, a wind speed of $8\,\mathrm{m\,s^{-1}}$ (in the middle between cut-in and rated values), and wind directions of $+0$, $+15$, $+30$ and $+45°$ relative to the orthogonal line to the row. Results showed a difference in the power output when comparing each of the turbines in the row to the isolated case, which depended on the inflow angle and the location of the turbine in the row. The largest difference (2 %) was found for the turbine on the row edge for an inflow angle of 45°.

Ideally, a power curve relates the power output of the turbine with the wind speed that would be measured at the turbine's location without the turbine actually being there. The IEC standard assumes that blockage is negligible already at 2 D in front of the turbine and suggests measuring either the hub height wind speed or the rotor-equivalent wind speed (Wagner et al., 2011) in front of the turbine at a distance between 2 and 4 D. At these upstream distances, global blockage influences the flow field, with variations up to 3 % for the wind speed and up to 5 % for the power production (Meyer Forsting et al., 2017b; Bleeg et al., 2018; Segalini and Dahlberg, 2020), indicating that standard power performance tests, normally carried out on turbines at sites with at least a row of turbines, might be affected by global blockage. In this work, we use a similar numerical experiment to that of Meyer Forsting et al. (2017b) to further investigate this issue.

We analyse the power output of five wind turbines in a row and investigate the difference to their production in isolation. We extend the numerical work of Meyer Forsting et al. (2017b) by extracting velocities in front of the turbines using virtual met masts and nacelle-mounted lidars to further analyse the relation between global blockage and power performance measurements. Additionally, we analyse if and how deviations in the power output between the row and the isolated case are affected within a broad range of free-stream velocities and turbine inter-spacings. The inflow velocities cover a number of regions of the power curve from cut-in to rated, while the turbine inter-spacings represent typical values used at test sites. Further, this work includes the analysis of measurements from a real site consisting of a row of five wind turbines. This is the first time that the global-blockage effect for a single row of turbines is investigated using both simulations and measurements, which comply with the IEC standard for power curve measurements.

This paper is organised as follows. In Sect. 2, the numerical setup and the available measurements are introduced. In Sect. 2.2.1, possible numerical biases are analysed. The numerical results are reported in Sect. 3, the global-blockage effect on the power output is shown in Sect. 3.1, variations in the flow field around the row are shown in Sect. 3.2 and effects on power performance measurements are analysed in Sect. 3.3. The analysis of the measurements is described in Sect. 4. In Sect. 4.1, we explain how the measurements are filtered to assure compliance with the numerical setup. In Sect. 4.2 the power variations observed in the measurements are compared with those of the simulations. Finally, a discussion and conclusions are presented in Sects. 5 and 6, respectively.

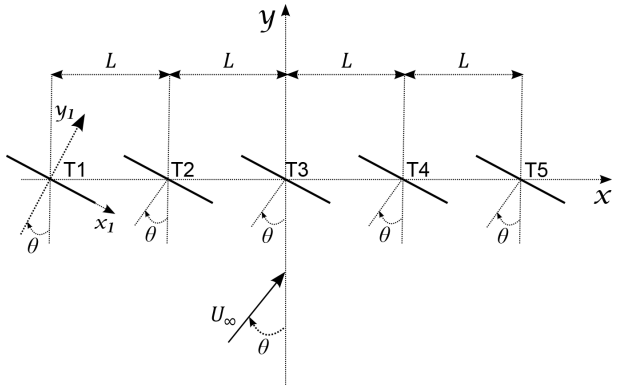

Figure 1. Schematics of the wind turbine rotors (T1–T5) in the numerical setup. Clockwise relative directions of θ are positive.

2 Methodology

2.1 Problem definition

The numerical setup consists of five turbines aligned in a row perpendicular to the prevailing wind, similar to power performance test sites. In addition to the case of the wind approaching perpendicular to the row, $\theta = 0°$, inflow angles between 5 and 45° are considered, as shown in Fig. 1. The modelled turbine is the NREL 5 MW with a diameter of 126 m (Jonkman et al., 2009), but any other turbine type could have been used as blockage is largely independent of turbine design (Meyer Forsting, 2017; Meyer Forsting et al., 2021). The effect of the turbine spacing (L) is evaluated by considering three different values: $L = 1.8$, 2 and 3 D. The 1.8 D case is tested to evaluate whether the global-blockage effect changes dramatically for a spacing lower than 2 D, which is the lowest value currently accepted by the IEC standard. To highlight the effects of the rotors on the power output, the inflow is simplified as much as possible. Therefore, the inflow is uniform without turbulence, purely neutral (no buoyancy) and assumed as time invariant. Additionally, the ground is not modelled, so the flow is completely unconstrained. Virtual measurements from meteorological towers are simulated by extracting point-wise velocity values in front of the rotors at hub height and at 2, 2.5 and 3 D upstream, which are the distances prescribed in the IEC standard. Lidar measurements are simulated with a two-beam pulsed lidar mounted on the nacelle and pointing upstream with a half-opening angle of 15°. The lidar is characterised by a range-gate length of 38.4 m and a full width at half maximum (FWHM) of 24.75 m. More details about the lidar simulator can be found in Meyer Forsting et al. (2017a). As can be seen in Fig. 1, the mast measurements are taken at fixed locations, while the nacelle-mounted lidars yaw together with the rotors and their point of measurement changes with θ.

2.2 Computational method

The numerical setup adopted here is the same as used and described in detail by Meyer Forsting et al. (2017b), so here we will only briefly describe the simulation setup. All simulations are performed using the in-house incompressible finite-volume flow solver EllipSys3D (Michelsen, 1992, 1994; Sørensen, 1995). The simulations are carried out with steady-state Reynolds-averaged Navier–Stokes (RANS) equations using the $k-\omega$ shear-stress transport (SST) turbulence model by Menter (1994). The numerical domain is an ellipse-shaped cylinder with $(L_x, L_y, L_z) = (95, 84, 25\,\mathrm{D})$, where L_x and L_y denote the major and minor axes of the ellipse and L_z is the height of the cylinder. The turbines are placed as shown in Fig. 1 with T3 located in the centre of the domain. In the vicinity of the turbines, the grid cells are cubic with a side length of $D/32$ within an inner box of dimensions $(15, 4, 2\,\mathrm{D})$. From there, the mesh grows hyperbolically outwards. The turbines are modelled as actuator discs (Réthoré and Sørensen, 2012; Troldborg et al., 2015) using the airfoil and blade data from the NREL 5 MW turbine (Jonkman et al., 2009). In contrast to Meyer Forsting et al. (2017b), who prescribed a constant rotational speed and blade pitch angle, we instead use a controller that set these based on the velocity averaged over the rotor area at the rotor position (Van Der Laan et al., 2015). The accuracy of the computational fluid dynamics (CFD) model (numerical setup and actuator disc) over the wind turbine induction zone was validated using measurements from three lidars (Meyer Forsting et al., 2017c).

2.2.1 Sensitivity to numerical domain and turbine location

As we need to assess the difference in both inflow and power output between a row of turbines and an isolated turbine, we need to verify that the difference between the two cases is only due to the number of turbines without being affected by numerical bias, not by the location of the turbine within the domain. Meyer Forsting and Troldborg (2015) already showed that this numerical setup guarantees results free of tunnel blockage due to either grid resolution or domain size.

Here, we further simulate an isolated turbine placed at the location of turbine 5, and these results are compared with the reference case, i.e. an isolated turbine placed at T3, for $U_\infty = 8\,\mathrm{m\,s^{-1}}$ and $\theta = 0, 30$ and 45°. The difference in power output is found to be negligible compared to the deviations caused by the whole row (we show these deviations in Sect. 3.1). Specifically, for $\theta = 45°$, when the turbine is placed at T5, the power output is only 0.15 % higher than when it is placed at T3.

The results might also be biased due to numerical sensitivity to the inflow angle, as the effective grid resolution changes when the flow is aligned or misaligned with the grid direction. Even though the grid refinement is unchanged,

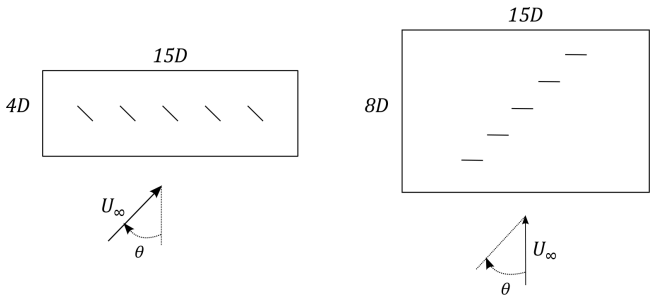

Figure 2. Standard and staggered configurations with boundaries of the refined area.

these variations in the effective resolution affect the power output of the isolated turbine, which changes with θ while it should be dependent on U_∞ alone. However, this effect causes only small variations in power. The difference with the case $\theta = 0°$ is 0.02 % for $\theta = 30°$ and 0.15 % for $\theta = 45°$.

The sensitivity of the results to the extension of the refined area is evaluated by replicating some of the results from Fig. 3 with the same layout and an enlarged refined area (from $y = -4$ D to $y = +4$ D). However, enlarging the refined area results in differences of the order of 0.3 % for both the isolated turbine and the five turbines, so that no difference is found for the results of Fig. 3. Therefore, we assume that there is no need to enlarge the refined area and that our results are reliable, at least when evaluated in terms of normalised power output.

Simulations are also performed with a staggered configuration, where the same layout of Fig. 1 is achieved not by yawing the rotors, but by moving the turbines along the y direction, as is shown in Fig. 2. In this way, the main flow direction is aligned with the grid direction regardless of the inflow angle. In the staggered configuration, the equispaced box mesh in the centre of the domain is enlarged ($y = -4$ D to $y = +4$ D), as T1 and T5 would otherwise be out of the refined area. Results show a much larger dependency of the power output on the turbine location, with variations for the power of the isolated turbine when it is placed at different locations. This is probably due to differences in the fraction of the wake that rests inside the refined mesh region, causing variations for the induction of the single rotors. The power output of the isolated turbine decreases 1.2 % when the turbine is moved from T3 to T1, while it increases 0.71 % when moved from T3 to T5. These results suggest that the staggered configuration should be avoided for studies that require high accuracy and, thus, not used in this study.

2.3 Measurements

Measurements are available for a period of approximately 21 months from a site consisting of five turbines aligned perpendicularly to the predominant wind direction. The area is flat, and the surface characteristics within the analysed directions are the same for each of the turbines in the row (and rather homogeneous). The name of the site can not be disclosed due to proprietary reasons, but the layout is very similar to that in Fig. 1. The available dataset comprises the operational data from a turbine on one edge of the row (T1) together with measurements from "its power-performance" meteorological mast and a ground-based wind lidar aligned with the turbine along the predominant wind direction at distances of 2.3 and 2.5 D, respectively. The lidar is a WindCube WLS7 from Vaisala Leosphere. Additionally, the data include the operational status of the turbines T3–T5 (T2 operation and status are unknown). The five turbines are placed with a mutual distance $L = 2.3$ D, with D being the diameter of T1. Although we do not know specifics on the turbines standing on the other four positions, considering the size of modern wind turbines, the spacing is likely to be lower than 3 D when normalised with the rotor diameters of the other turbines at the site.

Data from T1 are used to validate the numerical results. If the asymmetry due to wake rotation is neglected, the turbine can represent either turbine T1 or T5 from the simulations, as it is either the most upwind or downwind turbine of the row for $\theta > 0°$ and $\theta < 0°$, respectively.

Measurements from both the turbine and the mast are sampled at 35 Hz, while the wind lidar provides measurements at 11 different heights every 4 s, covering a vertical distance from −0.4 to +0.85 D relative to the wind turbine hub height. The analysis is performed by considering 10 min means for all examined variables.

3 Numerical results

3.1 Power output

In Fig. 3, the power output P of the five turbines is normalised by that of the isolated turbine P_{ref} under the same inflow conditions. The normalised power varies with the free-stream velocity U_∞ for different values of θ. At $U_\infty \approx 8\,\mathrm{m\,s^{-1}}$, the turbine is within the region of the power curve where the turbine controller keeps a constant tip speed ratio and an optimal power output, i.e. a constant power coefficient (C_{P}) and thrust coefficient (C_{T}). We also show results for 7 and 11 $\mathrm{m\,s^{-1}}$ as they are the first two integer values out of this region (Jonkman et al., 2009). The highest variation from the reference case is found for the side turbines (T1 and T5) with an inflow angle $\theta = 45°$. Although not shown, the difference between the power output of the five turbines and the isolated turbine decreases for 12 $\mathrm{m\,s^{-1}}$ (above the C_{P}-constant interval), while it increases for 7 $\mathrm{m\,s^{-1}}$. The power output increases for all five turbines when $\theta = 0°$, with the highest gain, when compared to the reference case, for T3 and $U_\infty = 7\,\mathrm{m\,s^{-1}}$ reaching nearly 2 %.

Figure 4 shows the normalised power output for cases with the same free-stream velocity (8 $\mathrm{m\,s^{-1}}$) and a number of turbine inter-spacings (1.8, 2 and 3 D). The normalised

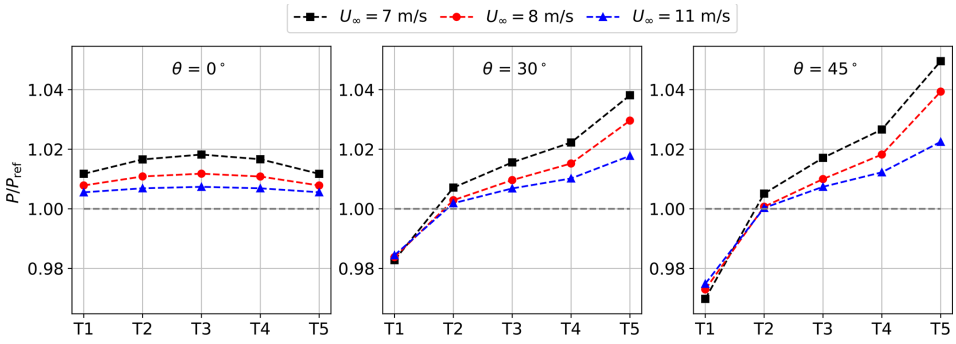

Figure 3. Power output of the five turbines normalised by that of an isolated turbine (placed at T3) for the cases with an inter-spacing of 2 D predicted by RANS–CFD.

power varies with turbine inter-spacing for all five turbines and decreases the larger the turbine inter-spacing. For the largest turbine inter-spacing (3 D), the normalised power is still larger than 2 % for the side turbines when $\theta = 30$ and 45°. The reduction of the turbine inter-spacing from 2 to 1.8 D results in small variations in the power output; the highest variation (0.75 %) is for turbine T5 when $\theta = 45°$.

3.2 Global blockage and induced velocities

The higher power output of the five turbines relative to that of the isolated case cannot be explained with upstream velocity measurements. The upstream induction on the row of turbines is higher than that of the single turbine, so that there is a higher velocity reduction in front of the rotors, as expected because of the global-blockage effect. This is shown in Fig. 5, where the vertical velocity profile in front of T1 and T3 is compared to that of an isolated turbine for $U_\infty = 8\,\mathrm{m\,s^{-1}}$ and $\theta = 0°$. Lower velocities correspond to higher power production, with T3 producing the most despite the lowest incoming wind speed at both 2 and 1 D. It is only very close to the rotor (closer than 0.2 D) that the incoming wind speed in front of T3 is higher than in the isolated case. Although not shown, the same trend is found for all values of U_∞ and θ.

Meyer Forsting et al. (2017b) already showed that these counter-intuitive power deviations of the turbines on the row relate to the downstream induced velocity caused by the neighbouring turbines. Particularly, a positive downstream induced velocity results in faster advection of the wake and lower induction upstream of the turbine. The "local" blockage at the rotor is thus lower compared to the isolated case, which results in higher power output. Likewise, a negative downstream induced velocity results in lower power output compared to the isolated case.

Figure 6 shows the velocity induced by the isolated turbine at T3 along the rotor axis at the locations T2 and T4 (but without other rotors than T3) for $\theta = 45°$ and $U_\infty = 7$, 8 and 11 $\mathrm{m\,s^{-1}}$. For $-1.3 \lessapprox y_i \lessapprox 1.5$, the induction is positive along y_4 and negative along y_2. This explains the results in Fig. 3, where the downstream turbines (T4 and T5) produce more than the upstream ones (T1 and T2). It should be noted that a velocity increase of ≈ 1 % at the rotor (case with $U_\infty = 8\,\mathrm{m\,s^{-1}}$ in Fig. 6) is not negligible and it could definitely be enough to explain the power variations observed in Figs. 3 and 4. For example, assuming the same air density and power coefficient values, such a velocity increase can result in a power increase of ≈ 3 %. Additionally, the magnitude of the induction decreases the higher the wind speed, also in agreement with the results in Fig. 3, where the power variation decreases for higher wind speeds. Furthermore, as shown in Fig. 7, the magnitude of the induced velocities varies with the turbine inter-spacing so that stronger inductions are observed for an inter-spacing of 2 D compared to those of the 3 D case, which is in agreement with the power variations in Fig. 4. The variation in induced velocities with both turbine inter-spacing and wind speed further confirms the relation between downstream induced velocities and power variations.

3.3 Effects on power performance measurements

From the previous results, one might expect biases in power performance measurements carried out for non-isolated turbines. Particularly, we would like to quantify whether the effects shown for specific θ values in Figs. 3 and 4 cancel out when averaging over an inflow sector typical for power performance measurements.

A series of simulations are performed for both the reference case and the turbine row with an inter-spacing of 2 D for a number of U_∞ and θ values. The free-stream velocity varies from 7 to 11 $\mathrm{m\,s^{-1}}$ with a step of 1 $\mathrm{m\,s^{-1}}$, while θ varies from -45 to $+45°$ with a step of 5°. A normal distribution $N_\theta(\mu_\theta, \sigma_\theta^2)$ (with μ_θ and σ_θ as mean and standard deviation) is assumed for the wind direction, and the mean power output is calculated for each free-stream velocity as $\bar{P} = \int P(U_\infty, \theta)\, N_\theta(\mu_\theta, \sigma_\theta^2)\, \mathrm{d}\theta$. The effect of averaging over the whole inflow sector is shown in Fig. 8 for a distribution given by $\mu_\theta = 0°$ and $\sigma_\theta = 41°$. A standard deviation value of 41° is chosen in order to get a nearly uniform dis-

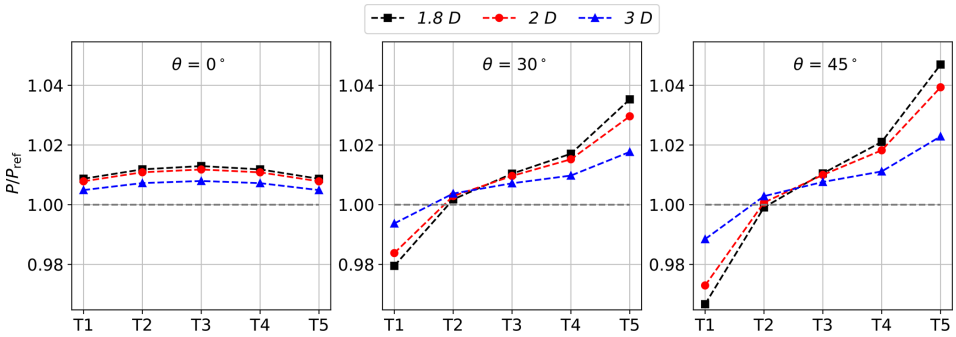

Figure 4. Power output of the five turbines normalised by that of an isolated turbine (placed at T3) for $U_\infty = 8\,\mathrm{m\,s^{-1}}$ and a number of θ values and turbine inter-spacings.

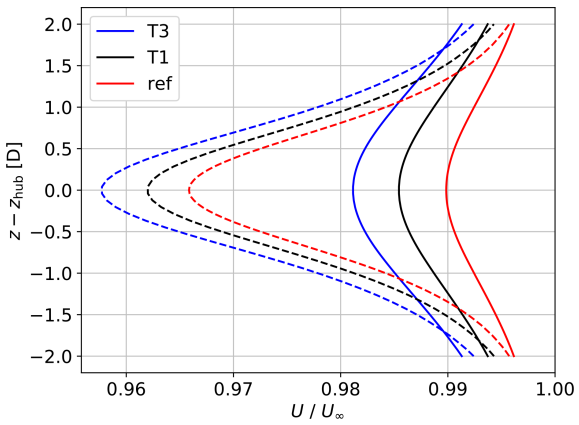

Figure 5. Upstream vertical velocity profiles extracted from RANS–CFD at 1 D (dashed lines) and 2 D (continuous lines) of the isolated case, T1 and T3 for $U_\infty = 8\,\mathrm{m\,s^{-1}}$ and $\theta = 0°$.

tribution of wind directions within the interval $[-45, 45°]$. Although not shown here, a narrower Gaussian distribution would enhance the increase in power for T3, and the results would not be representative of power performance tests in general, but rather of tests conducted with that specific and narrow wind direction distribution. As illustrated in Fig. 8, there is a difference with respect to the reference case; the five turbines in the row produce more than in isolation for all values of U_∞. Since $N_\theta(\mu_\theta, \sigma_\theta^2)$ is symmetric and centred in $\theta = 0°$, the power output of T5 is exactly the same as T1, and the same applies to T2 and T4. The central turbine T3 shows the largest increase in power relative to the reference case, with a power gain higher than 1 % for most wind speeds. Furthermore, the highest and lowest power variations are observed for $U_\infty = 7$ and $11\,\mathrm{m\,s^{-1}}$, respectively. The power variations are nearly constant for free-stream velocities within the range 8–10 $\mathrm{m\,s^{-1}}$. These results further confirm that the global-blockage-related power variations depend on the power curve region of operation of the wind turbines; they are C_T-dependent and consequently steady in the constant-C_P region of the power curve, while they decrease for U_∞ closer to the rated wind speed and increase for U_∞ closer to the cut-in value.

Due to the increase in power and reduction of the upstream wind speed, the differences in power coefficient C_P compared to the isolated case are higher than those of the power output. Results for C_P are shown in Fig. 9 for the same case of Fig. 8. The estimated free-stream velocity U_∞ is extracted at hub height and 2.5 D upstream of the rotor by both the virtual met mast and the virtual nacelle-mounted lidar. $C_\mathrm{P}s$ for the turbines of the row are up to 4 % higher than that of the reference when measuring with a mast and higher when measuring with the nacelle lidar. This is due to the masts measuring at fixed locations, while the nacelle-mounted lidars yaw together with the turbine. The volume-averaging effect of the lidar is considered negligible due to the nearly uniform velocity within the probe volume.

4 Analysis of the measurements

4.1 Data filtering

To compute the power variation $P(\theta)$ observed at the site, the inflow sector $\theta = 0° \pm 50°$ is divided into three different intervals $\theta = 0° \pm 16.5°$, $+33° \pm 16.5°$ and $-33° \pm 16.5°$. These are selected to characterise the three conditions of operation ("upwind", "downwind" and inflow perpendicular to the row) and obtain the largest possible amount of data within each interval. The wind direction is taken from measurements of a wind vane installed on the met mast 4 m below hub height. Additionally, the data are filtered according to the wind speed measured by the hub height cup anemometer (U_HH) and corrected for air density, even though the correction leaves the data nearly unchanged due to the flat and sea level terrain. Only wind speeds within the constant-C_P range are considered, as this is also the range providing a constant C_T (the manufacturer's C_T curve is not available). Therefore, after determining the C_P curve of the turbine, the interval $U_\mathrm{HH} = [5.5, 8.5]\,\mathrm{m\,s^{-1}}$ is selected.

After selecting the data according to 10 min mean values of both θ and U_HH, other meteorological conditions are im-

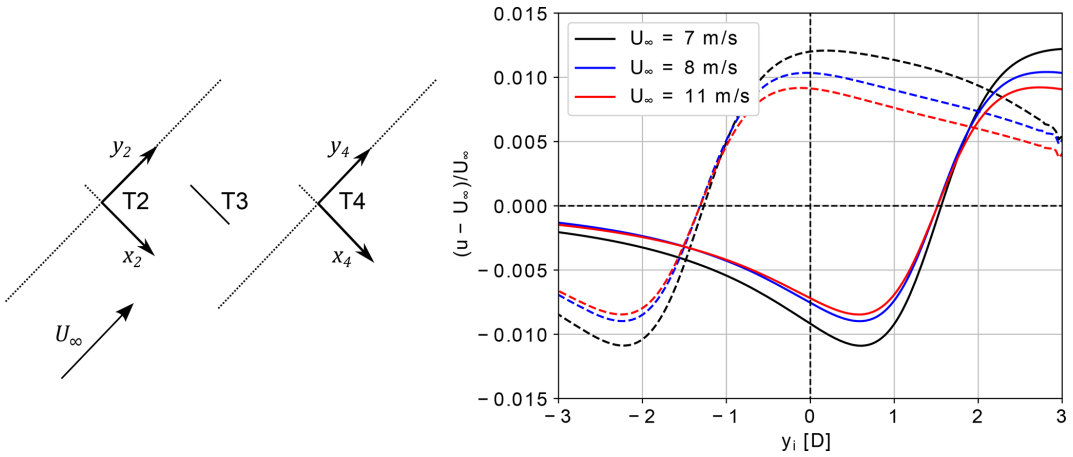

Figure 6. Velocities induced by the central turbine (T3) on the rotor axis of T2 (solid line) and T4 (dashed line), for different values of U_∞, turbine inter-spacing of 2 D and $\theta = 45°$.

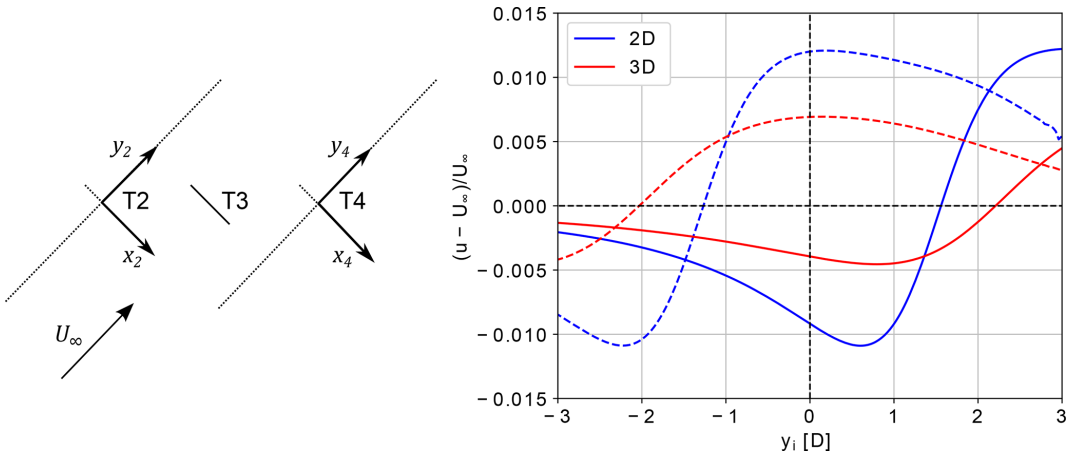

Figure 7. Velocities induced by the central turbine (T3) on the rotor axis of T2 (solid line) and T4 (dashed line), for $U_\infty = 7\,\mathrm{m\,s^{-1}}$, $\theta = 45°$ and different turbine inter-spacings.

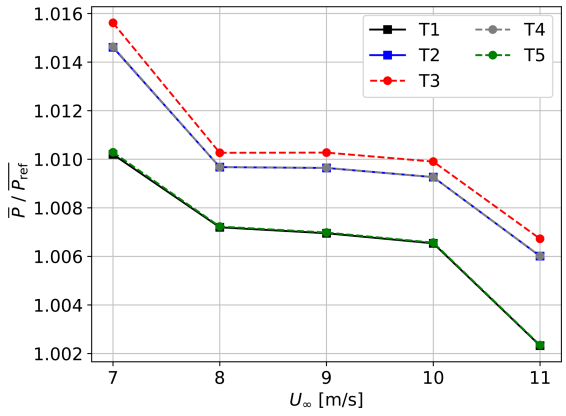

Figure 8. Power output of the five turbines in the row averaged over an inflow sector and normalised by the average power output of the isolated turbine for several values of U_∞ and a normal distribution $N_\theta(\mu_\theta = 0°, \sigma_\theta = 41°)$ for θ.

posed to both increase the compliance with the numerical setup and avoid biases due to extreme conditions. Conditions of both very low and very high turbulence are filtered out by considering only 10 min intervals where the turbulence intensity at hub height is between 2 % and 10 %. Additionally, thresholds are set for both the wind veer (γ) and the wind direction standard deviation (σ_θ). Measurements with either $\gamma > 10°$ or $\sigma_\theta > 10°$ are filtered out. γ is the difference between the 10 min mean wind directions given by the WindCube at heights of -0.4 and 0.85 D relative to hub height.

We also consider only power-law-like wind profiles to avoid biases due to different profiles among different wind directions. For all the 10 min intervals, the power law $U(z)/U_{\mathrm{ref}} = (z/z_{\mathrm{ref}})^\alpha$ is fitted to the WindCube measurements at the 11 different heights via a least-squares fit. Then, the mean absolute error (MAE) between the measured wind speeds and the values estimated by the power law is calculated. Only the profiles providing a MAE lower than 0.03 are

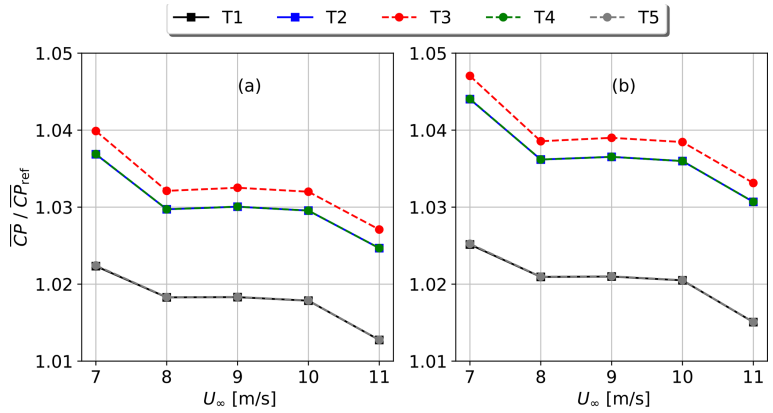

Figure 9. Power coefficient C_P of the five turbines in the row averaged over the inflow sector and normalised by the average C_P of the isolated turbine for several values of U_∞ and a normal distribution $N_\theta(\mu_\theta = 0°, \sigma_\theta = 41°)$ for θ. The free-stream velocity U_∞ is extracted by a virtual met mast **(a)** and a virtual lidar **(b)** at a distance of 2.5 D from the rotor.

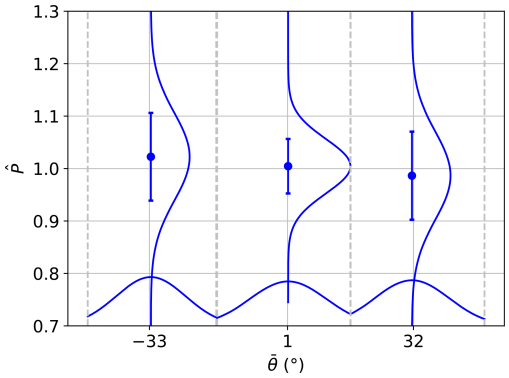

Figure 10. Power output normalised by the power derived from the power curve for different wind directions. Dots and error bars represent means and standard deviations within each bin, while the continuous lines represent the distributions of $\hat{P}$ and θ within each bin.

taken for the analysis to avoid reducing the amount of data excessively. Additionally, to avoid conditions of very strong shear, profiles with a shear exponent α higher than 0.35 are discarded. Finally, to increase the amount of data, we select all the intervals when at least two of the other four turbines are operating.

4.2 Power variations

Due to the substantial differences between the numerical setup and the real site, the objective of the inter-comparison with the measurements is to evaluate the trends of power variations. Thus, we evaluate the power output for each of the three wind direction bins ($\theta = 0° \pm 16.5°$, $\theta = +33° \pm 16.5°$ and $\theta = -33° \pm 16.5°$) and make sure that the same meteorological conditions are in place in all three bins, so that the power differences are mainly explained by the effect of the other four turbines. However, we could have different wind speed distributions among the bins, since the wind speed interval is relatively large ($3\,m\,s^{-1}$). Therefore, we normalise the 10 min mean power values P_i with the power value derived from the power curve for the related 10 min mean wind speed measured at hub height, resulting in the normalised power values $\hat{P}$. The power curve is derived from the dataset filtered for meteorological conditions, without including the operational status of the other turbines. Different atmospheric stability conditions might be associated with different wind directions. To decrease the effect of stability, data are sampled so that the three bins present the same number of measurements within each interval $\alpha = \bar{\alpha} \pm 0.02$, for $\bar{\alpha} = 0.01, 0.03, 0.05, \ldots, 0.33, 0.35$. This sampling assures that all the inflow sectors have the same distribution of α values, and it results in 534 10 min mean data for each of the three sectors. The distributions for the normalised power $\hat{P}$ are shown in Fig. 10. Additionally, the sampling for α is repeated for 50 random seeds, and the results are nearly constant (standard deviations lower than 0.1 % of the means), proving that the findings are not affected by the random sampling.

The highest mean power output is observed for $\bar{\theta} = -33°$ ($\bar{\theta}$ stands for the mean of all the 10 min wind directions), i.e. when the turbine is the most downwind in the row. The lowest power output is observed for $\bar{\theta} = 32°$, when the wind turbine is the most upwind. The comparison between measurements and simulations is shown in Fig. 11, where the numerical results, indicated as red squares, represent the means of the power distributions obtained for the same wind direction distribution of the measurements and a free-stream velocity of $8\,m\,s^{-1}$. To ease the comparison, as the simulations do not correspond to the same turbine, the means and uncertainties are normalised by the mean power output for the central sector ($\bar{\theta} = 1°$). As illustrated, both simulations and observations show the same trend. Also, the measurements show that the differences among mean power values for different

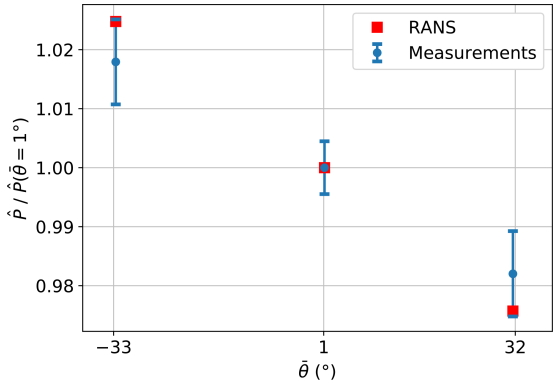

Figure 11. Normalised power output variation with wind direction based on measurements and simulations. Error bars represent 95 % confidence intervals.

inflow angles are larger than the uncertainties, which represent 95 % confidence intervals. The statistical significance of the results is also tested through null hypothesis significance testing, resulting in p values below 0.05 for all the inflow angles.

5 Discussion

The RANS simulations show that the power output of five turbines in a row is higher than what they would produce in isolation when the incoming wind is perpendicular to the line along the rotors. This is in agreement with the study of McTavish et al. (2015) for a line of three turbines, with that of Meyer Forsting et al. (2017b) for a row of five turbines and with that of Van der Laan et al. (2019) for a multi-rotor configuration. Additionally, the RANS simulations show that the power difference between the reference and the five aligned turbines changes when the wind is not perpendicular to the row. Specifically, the downwind turbines produce more power than the upwind turbines, with a difference that increases for larger inflow angles. For the cases with $\theta = 30$ and 45°, the most upwind turbine produces less than the isolated turbine for all simulated turbine inter-spacings (1.8, 2 and 3 D). These results agree with those by Meyer Forsting et al. (2017b) for the case with $U_\infty = 8\,\mathrm{m\,s^{-1}}$ and a turbine inter-spacing of 3 D, despite the addition of a wind turbine controller. However, adding the controller results in a different outcome for the cases with $U_\infty = 7$ and $11\,\mathrm{m\,s^{-1}}$, as we are not within the constant-C_P region of operation of the turbine any longer.

The power variations are due to positive and negative velocities induced in the wakes of the neighbouring rotors, which depend on θ. In this study, we show how these induced velocities vary with both the turbines' inter-spacing and the free-stream velocity. Furthermore, wind profiles extracted upstream of the rotors show that the row's global blockage causes a reduction of the upstream velocity relative to the isolated case, as expected. However, it has the opposite effect on the power output, which might be counter-intuitive. When averaging over the whole inflow sector ($-45° < \theta < 45°$), an increase relative to the isolated case of more than 1 % for the power and more than 4 % for the power coefficient C_P further confirms our results. This might cause a bias for power performance measurements conducted on a row of wind turbines, as they would result in a higher power performance than what would be measured for the same turbine in isolation.

Analysis of field and supervisory control and data acquisition (SCADA) measurements confirms that the power performance changes with the inflow angle due to the global-blockage effect. Due to differences between the numerical setup and the conditions of the measurements, we cannot expect a one-to-one agreement between measurements and simulations. We expected the global-blockage effect at the site to be lower than in the simulations, since the turbine inter-spacing is larger at the site and since we also consider cases where three, four or five turbines are in operation. Nevertheless, measurements show a very good agreement with the numerical results. This might be due to an increase in the global-blockage effect due to wind shear and terrain effects. The terrain represents an additional boundary to the flow, deflecting greater amounts to the sides and above the wind farm. This effect, usually simulated with mirror rotors (Meyer Forsting et al., 2021), is not accounted for in our setup and causes an additional source of blockage in the real site. In sheared inflow conditions, the wind speed in the lower part of the rotor can be substantially lower than that in the higher part, which causes a non-optimal selection of the pitch angle for the blades and consequently a non-optimal aerodynamic performance of the wind turbine. As shown by Meyer Forsting et al. (2018), the blade forces in the lower half of the rotor are stronger than what would be the optimal value according to the local velocity. This results in a higher local C_T and stronger induction in the lower half of the rotors.

The measurements confirmed the relation between power and wind direction $P(\theta)$, with an increased power output when the side turbine is the most downwind and a decreased power output when it is the most upwind relative to the case for $\theta = 0°$. This might cause a bias for power performance tests conducted on a single row of wind turbines, as a different power output could be obtained from the same turbine depending on the wind direction distribution and the number of turbines in the row. The filtering procedures applied to the measurements try to guarantee that the power variation $P(\theta)$ is driven by blockage effects as is the case in the simulations. Additionally, it must be noted that the measurements analysed in this work cover only the constant-C_P region of the power curve, so only a small portion of the power curve is subjected to the power increase. Numerical results show that the power rise is higher for wind speeds below that re-

gion, while it is lower, although still present, for wind speeds above it.

One might argue that the power performance of a wind turbine within a wind farm is better represented by the turbine in the row than by the turbine in isolation. Consequently, energy yield assessments would be more accurate when the power performance is estimated in a row of wind turbines. However, according to our results, the power performance of the turbine in the row depends, among others, on both the wind direction and the C_T of all turbines in the row. This suggests that power performance tests do not result in generic power curves when carried out in a non-isolated situation. Therefore, due to the lack of a validated methodology to assess the power performance of a wind turbine inside a wind farm, we should aim at minimising the influence of other turbines.

Ideally, power curves define the relation between the wind turbine power output and the wind speed that would be measured at the turbine's location without the turbine actually being there. Therefore, the procedure outlined in the IEC standard (IEC, 2017) is seriously questioned by our numerical results, which show how the wind speed measured at 2 D in front of the rotor would be affected by global blockage, increasing the difference between the measured wind speed and the "ideal" value when compared to the case of an isolated wind turbine. However, an accurate evaluation of the bias on the wind speed measurements is out of the scope of this work, and it will be considered when extending this study.

6 Conclusions

The power output of five wind turbines in a row is computed through RANS simulations and compared with the power output of the same turbine in isolation. The flow field is also analysed both upstream and downstream to understand the global-blockage effect (as it is defined in this work) resulting from the wind farm orientation. All the simulations are performed under purely neutral conditions, without ground effects and with a uniform inflow. Several cases are considered, with variations to the free-stream velocity, the turbine inter-spacing and the inflow angle.

Our results show that the power output varies according to the above three factors, with changes relative to the isolated case from $-3\,\%$ to $+5\,\%$. We find an increase of more than $1\,\%$ for the mean power output when averaging over the whole inflow angle ($-45° < \theta < 45°$) for a turbine inter-spacing of 2 D and several values of the free-stream velocity. Due to the upstream velocity reduction caused by global blockage, the difference with the reference increases up to $4\,\%$ for the mean power coefficient.

Measurements from a site are analysed in order to validate the numerical findings. The site consists of five turbines in a row, and the available dataset comprises the operational data from one of the side turbines together with measurements from both a met mast and a ground-based WindCube lidar located in front of the turbine. The analysis confirms the variation in power with inflow angle observed in the simulations. Compared to the case with a flow perpendicular to the row, the power output changes $+(1.8 \pm 0.7)\,\%$ and $-(1.8 \pm 0.7)\,\%$ when the turbine is the most downwind and upwind of the line, respectively.

Our numerical results show that wind turbine power output can be enhanced when wind turbines are aligned on a row. Therefore, power performance tests might be biased when conducted on such an array, resulting in a better power performance than what would be measured for the same turbine in isolation. Additionally, the measurements show that, in a single row of wind turbines, the power output changes with the wind direction due to the global-blockage effect. This suggests that a different power output could be obtained depending on the wind direction distribution, resulting in possible biases for power performance tests conducted at such turbine arrays.

Code and data availability. Data from the turbines, the meteorological mast and the WindCube are not publicly available due to a non-disclosure agreement between the authors and the provider of the data. Results from the simulations and codes to generate Figs. 3–9 can be accessed at https://doi.org/10.11583/DTU.17263163 (Sebastiani et al., 2022). The source code of the simulations is licensed and not publicly available, but it can be requested by contacting the authors.

Author contributions. AS, AP, NT and AMF participated in the conceptualisation and design of the work. NT and AMF implemented the numerical setup for the CFD simulations. AP was responsible for the acquisition of the dataset. AS performed the CFD simulations, conducted the data analysis and wrote the draft manuscript. AP, NT and AMF supported the whole analysis and reviewed and edited the manuscript.

Competing interests. The contact author has declared that neither they nor their co-authors have any competing interests.

Disclaimer. Publisher's note: Copernicus Publications remains neutral with regard to jurisdictional claims in published maps and institutional affiliations.

Acknowledgements. We would like to thank Andrea Vignaroli for discussions on the analysis of the wind turbine measurements.

Financial support. This work has received funding from the European Union Horizon 2020 through the Innovation Training Network Marie Skłodowska-Curie Actions: Lidar Knowledge Europe (LIKE (grant no. 858358)).

Review statement. This paper was edited by Horia Hangan and reviewed by Bleeg James and one anonymous referee.

References

Allaerts, D. and Meyers, J.: Boundary-layer development and gravity waves in conventionally neutral wind farms, J. Fluid. Mech., 814, 95–130, https://doi.org/10.1017/jfm.2017.11, 2017.

Barthelmie, R. J., Hansen, K., Frandsen, S. T., Rathmann, O., Schepers, J. G., Schlez, W., Phillips, J., Rados, K., Zervos, A., Politis, E. S., and Chaviaropoulos, P. K.: Modelling and measuring flow and wind turbine wakes in large wind farms offshore, Wind Energy, 12, 431–444, https://doi.org/10.1002/we.348, 2009.

Bleeg, J., Purcell, M., Ruisi, R., and Traiger, E.: Wind farm blockage and the consequences of neglecting its impact on energy production, Energies, 11, 1609, https://doi.org/10.3390/en11061609, 2018.

Crespo, A., Hernández, J., and Frandsen, S.: Survey of modelling methods for wind turbine wakes and wind farms, Wind Energy, 2, 1–24, 1999.

Göçmen, T., Van der Laan, P., Réthoré, P.-E., Peña, A., Larsen, G., and Ott, S.: Wind turbine wake models developed at the technical university of Denmark: A review, Renew. Sust. Energ. Rev., 60, 752–769, https://doi.org/10.1016/j.rser.2016.01.113, 2016.

IEC: 61400-12-1, Power performance measurements of electricity producing, 2017.

Jonkman, J., Butterfield, S., Musial, W., and Scott, G.: Definition of a 5-MW Reference Wind Turbine for Offshore System Development, National Renewable Energy Lab (NREL), Golden, CO, USA, tech. rep., https://doi.org/10.2172/947422, 2009.

McTavish, S., Rodrigue, S., Feszty, D., and Nitzsche, F.: An investigation of in-field blockage effects in closely spaced lateral wind farm configurations, Wind Energy, 18, 1989–2011, https://doi.org/10.1002/we.1806, 2015.

Medici, D., Ivanell, S., Dahlberg, J.-A., and Alfredsson, P. H.: The upstream flow of a wind turbine: blockage effect, Wind Energy, 14, 691–697, https://doi.org/10.1002/we.451, 2011.

Menter, F.: Two-equation eddy-viscosity turbulence models for engineering applications, AIAA J., 32, 1598–1605, https://doi.org/10.2514/3.12149, 1994.

Meyer Forsting, A.: Modelling Wind Turbine Inflow: The Induction Zone, PhD thesis, Denmark, https://doi.org/10.11581/DTU:00000022, 2017.

Meyer Forsting, A. and Troldborg, N.: The effect of blockage on power production for laterally aligned wind turbines, J. Phys. Conf. Ser., 625, 012029, https://doi.org/10.1088/1742-6596/625/1/012029, 2015.

Meyer Forsting, A., Troldborg, N., and Borraccino, A.: Modelling lidar volume-averaging and its significance to wind turbine wake measurements, J. Phys. Conf. Ser., 854, 012014, https://doi.org/10.1088/1742-6596/854/1/012014, 2017a.

Meyer Forsting, A., Troldborg, N., and Gaunaa, M.: The flow upstream of a row of aligned wind turbine rotors and its effect on power production, Wind Energy, 20, 63–77, https://doi.org/10.1002/we.1991, 2017b.

Meyer Forsting, A., Troldborg, N., Murcia Leon, J., Sathe, A., Angelou, N., and Vignaroli, A.: Validation of a CFD model with a synchronized triple-lidar system in the wind turbine induction zone, Wind Energy, 20, 1481–1498, https://doi.org/10.1002/we.2103, 2017c.

Meyer Forsting, A., Van Der Laan, M., and Troldborg, N.: The induction zone/factor and sheared inflow: A linear connection?, J. Phys. Conf. Ser., 1037, 072031, https://doi.org/10.1088/1742-6596/1037/7/072031, 2018.

Meyer Forsting, A., Rathmann, O., Van Der Laan, M., Troldborg, N., Gribben, B., Hawkes, G., and Branlard, E.: Verification of induction zone models for wind farm annual energy production estimation, J. Phys. Conf. Ser., 1934, 012023, https://doi.org/10.1088/1742-6596/1934/1/012023, 2021.

Michelsen, J. A.: Basis3D – a platform for development of multiblock PDE solvers, Tech. Rep. AFM 92-05, Dept. of Fluid Mechanics, Technical University of Denmark, https://backend.orbit.dtu.dk/ws/portalfiles/portal/272917945/Michelsen_J_Basis3D.pdf (last access: 11 April 2022), 1992.

Michelsen, J. A.: Block structured multigrid solution of 2 D and 3 D elliptic PDEs, AFM 94-06, Dept. of Fluid Mechanics, Technical University of Denmark, 1994.

Nishino, T. and Draper, S.: Local blockage effect for wind turbines, J. Phys. Conf. Ser., 625, 012010, https://doi.org/10.1088/1742-6596/625/1/012010, 2015.

Porté-Agel, F., Bastankhah, M., and Shamsoddin, S.: Wind-Turbine and Wind-Farm Flows: A Review, Bound.-Lay. Meteorol., 174, 1–59, https://doi.org/10.1007/s10546-019-00473-0, 2020.

Réthoré, P.-E. and Sørensen, N. N.: A discrete force allocation algorithm for modelling wind turbines in computational fluid dynamics, Wind Energy, 15, 915–926, 2012.

Schneemann, J., Theuer, F., Rott, A., Dörenkämper, M., and Kühn, M.: Offshore wind farm global blockage measured with scanning lidar, Wind Energ. Sci., 6, 521–538, https://doi.org/10.5194/wes-6-521-2021, 2021.

Sebastiani, A., Castellani, F., Crasto, G., and Segalini, A.: Data analysis and simulation of the Lillgrund wind farm, Wind Energy, 24, 634–648, https://doi.org/10.1002/we.2594, 2021.

Sebastiani, A., Peña Diaz, A., Troldborg, N., and Meyer Forsting, A.: Data from simulations of five wind turbines in a row to evaluate the global-blockage effect on power performance, Technical University of Denmark [data set], https://doi.org/10.11583/DTU.17263163, 2022.

Segalini, A. and Dahlberg, J. Å.: Blockage effects in wind farms, Wind Energy, 23, 120–128, https://doi.org/10.1002/we.2413, 2020.

Smith, R.: Gravity wave effects on wind farm efficiency, Wind Energy, 13, 449–458, https://doi.org/10.1002/we.366, 2010.

Sørensen, N. N.: General Purpose Flow Solver Applied to Flow over Hills, PhD thesis, Risø National Laboratory, https://backend.orbit.dtu.dk/ws/portalfiles/portal/12280331/Ris_R_827.pdf (last access: 11 April 2022), 1995.

Strickland, J. and Stevens, R.: Effect of thrust coefficient on the flow blockage effects in closely-spaced spanwise-infinite turbine arrays, J. Phys. Conf. Ser., 1618, 062069, https://doi.org/10.1088/1742-6596/1618/6/062069, 2020.

Troldborg, N., Sørensen, N., Réthoré, P.-E., and van der Laan, P.: A consistent method for finite volume discretization of body forces on collocated grids applied to flow through an actuator disk, Comput. Fluids, 119, 197–203, https://doi.org/10.1016/j.compfluid.2015.06.028, 2015.

Van Der Laan, M., Sørensen, N., Réthoré, P.-E., Mann, J., Kelly, M., and Troldborg, N.: The k-ϵ-f_p model applied to double wind turbine wakes using different actuator disk force methods, Wind Energy, 18, 2223–2240, https://doi.org/10.1002/we.1816, 2015.

Van der Laan, M. P., Andersen, S. J., Ramos García, N., Angelou, N., Pirrung, G. R., Ott, S., Sjöholm, M., Sørensen, K. H., Vianna Neto, J. X., Kelly, M., Mikkelsen, T. K., and Larsen, G. C.: Power curve and wake analyses of the Vestas multi-rotor demonstrator, Wind Energ. Sci., 4, 251–271, https://doi.org/10.5194/wes-4-251-2019, 2019.

Wagner, R., Courtney, M., Gottschall, J., and Lindelöw-Marsden, P.: Accounting for the speed shear in wind turbine power performance measurement, Wind Energy, 14, 993–1004, https://doi.org/10.1002/we.509, 2011.

Paper II: A method to correct for the effect of blockage and wakes on power performance measurements

A method to correct for the effect of blockage and wakes on power performance measurements

Alessandro Sebastiani[1], James Bleeg[2], and Alfredo Peña[1]

[1]DTU Wind and Energy Systems, Frederiksborgvej 399, 4000 Roskilde, Denmark
[2]DNV, One Linear Park, Avon St, Temple Quay, Bristol BS2 0PS, UK

Correspondence: Alessandro Sebastiani (aseb@dtu.dk)

Abstract. Wind turbine power performance measurements are often conducted in the upstream row of a wind farm, where the wind flow is affected by blockage effects, which might impact the measured power performance relatively to the turbine performance in isolation. We perform Reynolds-averaged Navier-Stokes simulations within a conventionally neutral atmospheric boundary layer of a wind farm with five rows of twenty turbines to evaluate whether the power performance measured on turbines on the upstream row would differ from that of the isolated turbine operating under the same inflow conditions. We simulate power performance measurements with both meteorological masts and nacelle-mounted lidars. Results show that blockage effects have an impact on the power performance of the turbines; for the turbines on the upstream row of the wind farm the scatter of the power curve increases causing a variation of more than 1% in the power coefficient relatively to that of the isolated turbine. Furthermore, we suggest a method to correct for the effect of blockage on power performance measurements. The method reduces the scatter in the power curve and can be used to derive the power performance of the isolated turbine from measurements conducted on the wind farm turbines. Additionally, the method accounts for blockage effects from the single isolated turbine, which results in the power as function of the undisturbed freestream wind speed. The method relies on the numerical modelling of the turbine induction zone, but we show that it can be applied using nacelle lidar measurements retrieved very close to the turbine rotor. Finally, the numerical results show that by applying the method, we can derive reliable power curves from nacelle lidar measurements mounted on downstream waked wind turbines as these measurements are highly correlated with the power output despite the strong inhomogeneity of the waked flow.

1 Introduction

Wind turbine power curve measurements play an important role in the wind industry. Manufacturers use them to better understand the performance of their fleet of operating turbines, and also to refine their power predictions for new, untested designs. Wind farm owners use on-site power performance measurements to determine whether their turbines are performing at a level consistent with the predicted, theoretical power curves provided by the manufacturer. The vast majority of power performance measurements are conducted in wind farms for this purpose. Any assessment of discrepancies between actual wind farm energy production and the pre-construction estimate is not complete without verification of turbine power performance.

In an energy yield analysis (EYA), theoretical turbine power curves are the key link between the expected freestream wind resource and the predicted energy production of a planned wind farm. As such, theoretical power curves are traditionally defined as functions of hub-height freestream wind speed. When running a power performance verification test, it is straightforward to measure the power; however, the freestream wind speed—i.e. the horizontal wind speed that would prevail at the turbine location if the wind turbine was not there—is not a measurable quantity. Instead, power performance measurement campaigns are designed to measure a wind speed that is expected to be very close to what the hub-height freestream wind speed would be if we could measure it. The IEC standard for power performance measurements (IEC, 2017) requires the mast or lidar to measure between two and four rotor diameters (D) upstream of the test turbine, close enough for the flow to be well correlated with conditions at the turbine, but far enough, ostensibly, for the influence of turbine induction on the measured wind speed to be negligibly small. In addition, the measurement location and valid wind directions are restricted to avoid upstream wakes. The IEC standard states the purpose of these requirements clearly (IEC, 2017): "The WME (wind measurement equipment) shall not be influenced by the wind turbine under test. The wind turbine under test and the WME shall not be influenced by neighbouring operating wind turbines."

Despite these restrictions, there is growing evidence that turbine-related disturbances materially influence power performance measurements. The most compelling evidence involves field observations. Nacelle-mounted lidar measurements at eight different offshore wind farms reported by Nygaard and Brink (2017) showed that the wind speeds measured 2.5D upstream of the test turbines were below freestream, an average of 1.0% below according to the authors' estimate. Based on this finding, the authors recommended applying an "induction correction factor" when calculating energy yield using a measured power curve or similarly productive theoretical curve. Using meteorological mast measurements taken before and after the start of operation at three onshore wind farms, Bleeg et al. (2018) found that wind speeds measured 2D upstream the wind farms decreased by 3.4%, on average, relative to wind speeds measured farther away after the turbines started operating. The observed slowdowns were well in excess of what could be attributed to induction of a single turbine, which in part led to the conclusion that the other wind farm turbines also contributed to these slowdowns. Based on additional analysis, the authors further concluded that wind farm blockage not only reduces the wind speed upstream of the wind farm, but it also reduces the wind speed experienced by the turbines on the upstream perimeter of the wind farm, causing them to generally produce less than they would operating in isolation. An analysis of power performance measurements conducted in a row of five turbines, along with a complementary set of Reynolds-Averaged Navier-Stokes (RANS) simulations, showed that wind farm blockage materially influences the measurements (Sebastiani et al., 2022). Specifically, wind farm blockage appears to affect the wind speed relationship between the mast location and the rotor in these results. Beyond field observations, there are also simulation-based studies (Allaerts and Meyers, 2017; Meyer Forsting et al., 2017; Nishino and Draper, 2015; Strickland and Stevens, 2022) and wind tunnel studies (Medici et al., 2011; Ebenhoch et al., 2017; Segalini and Dahlberg, 2020; McTavish et al., 2015) that highlight flow disturbances that likely affect power performance measurements.

The IEC standard largely explains how to correct for flow distortions caused by terrain, but there is no information on flow disturbances/distortions caused by wind turbines themselves. This omission can no longer be ascribed to a lack of evidence that these disturbances exist in IEC-compliant measurements. We lack a generally accepted method to quantify the impact of

these flow disturbances and thereby correct for them. Specifically, although several models have been developed to account for blockage effects on turbine interaction loss (Nygaard et al., 2020; Branlard and Meyer Forsting, 2020; Segalini, 2021; Bleeg, 2020), accounting for blockage effects on power performance measurements is still a rather unexplored topic.

Here, we propose a method to correct for the impact of turbine-related disturbances on power performance measurements. The methodology, which applies to both mast- and lidar-based measurements, is designed to yield power curves that are consistent with how theoretical curves are defined. After describing the correction method in detail, including the reasoning behind it, we test the method using RANS simulations of a notional wind farm. Finally, we explore whether the correction can be completed, at least partly, using nacelle lidar measurements rather than flow simulations alone.

The work is organized as follows. In Sect. 2, the correction method is explained. In Sect. 3, the numerical model is presented with descriptions of the computational fluid dynamics (CFD) model (Sect. 3.1), the simulation set-up (Sect. 3.2) and the virtual lidar measurements (Sect. 3.3). Results from power performance measurements conducted on the first upstream row of a wind farm are shown in Sect. 4, while in Sect. 5 we show how short-range nacelle lidar measurements can be used to apply the correction method. In Sect. 6, the correction method is applied to all turbines in the wind farm, including downstream waked turbines. Finally, discussion and conclusions are presented in Sects. 7 and 8, respectively.

2 Correction method

Common practice, when estimating the energy yield of a planned wind farm, is to combine the expected freestream wind resource at each turbine location with the manufacturer-provided theoretical power curve to calculate the so-called gross energy. This is the total of the energy that each turbine would produce absent the presence of the other wind turbines and other loss sources. The net energy is obtained after turbine interaction and other losses are accounted for. Thus, the power curve used in an EYA should faithfully represent the power production of the turbine as function of freestream wind speed when the turbine is operating in isolation. We refer to this power curve definition as a freestream power curve, P(U_∞).

A power curve measured according to IEC standards, P(U_{mast}), is not a freestream power curve as defined above. The test turbine affects the measured wind speed via induction, and the other wind farm turbines affect the relationship between that wind speed and conditions at the rotor face, via blockage and sometimes wakes. The impact of these effects on the measured power curve should be quantified and corrected. The objective of the correction method described in this section is to convert the measured power curve to a freestream curve that can defensibly be compared with a theoretical power curve. In our approach, we only alter the wind speed column in the tabular power curve. Specifically, for a given measured power vs. wind speed pair in the table, we correct to the freestream mean wind speed that would prevail if the test turbine were producing the same amount of power while operating in isolation. The correction can be thought of a two-step process:

- Convert the measured curve to what would be measured if the test turbine were operating in isolation and producing the same amount of power measured in the test.
- Correct for the impact of induction from the isolated turbine on the mast wind speed.

When measuring the power performance of a turbine inside a wind farm, the measured power curve$P^{\mathrm{WF}} = P(U^{\mathrm{WF}}_{\mathrm{mast}})$ differs from the power curve that would be measured if the turbine were operating in isolated condition $P^{\mathrm{I}} = P(U^{\mathrm{I}}_{\mathrm{mast}})$, since both P and U_{mast} are affected by the turbine interactions. Consequently, since both power and wind speed are different ($P^{\mathrm{WF}} \neq P^{\mathrm{I}}$ and $U^{\mathrm{WF}}_{\mathrm{mast}} \neq U^{\mathrm{I}}_{\mathrm{mast}}$), both $U^{\mathrm{WF}}_{\mathrm{mast}}$ and P^{WF} should be corrected in order to retrieve the power performance of the isolated turbine from wind farm measurements. However, if we consider the case with the isolated and the wind farm turbines producing the same amount of power $P = P^{\mathrm{I}} = P^{\mathrm{WF}}$, we would only need to correct the wind speed measurement, retrieving $U^{\mathrm{I}}_{\mathrm{mast}}$ from $U^{\mathrm{WF}}_{\mathrm{mast}}$.

Although wind turbine power is commonly formulated as a function of freestream wind speed, it is more directly a function of the velocity across the rotor face, which, along with air density and rotor speed, determines most of the aerodynamic loads on the blades. In this paper, we use average axial velocity across the rotor face as a power-equivalent wind speed, U_{disk}. In other words, if two turbines experience the same U_{disk}, they are assumed to produce the same amount of power regardless of the respective U_{mast} and U_∞ values. Thus, if $P^{\mathrm{I}} = P^{\mathrm{WF}}$, then $(U^{\mathrm{I}}_{\mathrm{disk}}/U^{\mathrm{WF}}_{\mathrm{disk}}) = 1$, and $U^{\mathrm{I}}_{\mathrm{mast}}$ can be reconstructed from $U^{\mathrm{WF}}_{\mathrm{mast}}$ as

$$U^{\mathrm{I,rec}}_{\mathrm{mast}} = U^{\mathrm{WF}}_{\mathrm{mast}} \left(\frac{U_{\mathrm{disk}}}{U_{\mathrm{mast}}}\right)^{\mathrm{WF}} \left(\frac{U_{\mathrm{mast}}}{U_{\mathrm{disk}}}\right)^{\mathrm{I}}, \tag{1}$$

where $U^{\mathrm{I,rec}}_{\mathrm{mast}}$ is the reconstructed velocity at the mast of the isolated turbine, $U^{\mathrm{WF}}_{\mathrm{mast}}$ is the velocity measured at the wind-farm mast, and the ratios $(U_{\mathrm{disk}}/U_{\mathrm{mast}})^{\mathrm{WF}}$ and $(U_{\mathrm{mast}}/U_{\mathrm{disk}})^{\mathrm{I}}$ are computed from numerical simulations of the wind farm and the isolated turbine, respectively.

The ratio $(U_{\mathrm{mast}}/U_{\mathrm{disk}})^{I}$ relates to the turbine blockage/induction and can be assumed to be nearly constant with small changes in wind speed over the plateau of the thrust-coefficient curve $C_T = C_T(U_\infty)$. Therefore, Eq. (1) is still valid in the case of $U^{\mathrm{WF}}_{\mathrm{disk}} \neq U^{\mathrm{I}}_{\mathrm{disk}}$, as long as the turbine is operating at nearly the same thrust coefficient $C_T = C^{\mathrm{WF}}_T = C^{\mathrm{I}}_T$ and at a similar wind speed.

When $U^{\mathrm{I}}_{\mathrm{mast}}$ is retrieved at a distance of 2 D upstream of the rotor, it might be affected by turbine blockage. Therefore, a similar approach as that used to derive Eq. (1) can be applied to reconstruct the freestream velocity:

$$U^{\mathrm{rec}}_{\infty} = U^{\mathrm{I,rec}}_{\mathrm{mast}} \left(\frac{U_\infty}{U_{\mathrm{mast}}}\right)^{\mathrm{I}}, \tag{2}$$

where $U^{\mathrm{I,rec}}_{\mathrm{mast}}$ is given by Eq. (1) and $(U_\infty/U_{\mathrm{mast}})^{\mathrm{I}}$ is computed from simulations of both the isolated turbine and the undisturbed free flow.

Some variations are expected for both $(U_{\mathrm{mast}}/U_{\mathrm{disk}})^{\mathrm{I}}$ and $(U_\infty/U_{\mathrm{mast}})^{\mathrm{I}}$ depending on the wind direction, as the degree of blockage at the mast depends on turbine yaw. Therefore, we also simulate IEC-compliant measurements with a 2-beam nacelle-mounted lidar, which yaws with the turbine. In those cases, we refer to the IEC wind speed measurement as either $U^{\mathrm{I}}_{\mathrm{lidar}}$ or $U^{\mathrm{WF}}_{\mathrm{lidar}}$.

3 Numerical model

3.1 CFD model

The numerical simulations were run using a CFD model based on STAR-CCM+, a general-purpose CFD software. The model solves the steady-state RANS equations along with a transport equation for potential temperature. The turbulence model is standard $k-\epsilon$ with modified coefficients. Buoyancy effects are captured through the addition of a gravity term in the vertical momentum equation, which is formulated using a shallow Boussinesq approximation. Buoyancy source terms are also included in the turbulence equations. More details about the flow model may be found in Bleeg et al. (2015b) and Bleeg et al. (2015a).

The turbines are represented via a simple actuator disk model. The disk volumes are discretised with cubic mesh cells with edge lengths equal to 5% of the rotor diameter (20 cells across the rotor diameter and 5 cells across the disk thickness). The axial and tangential body forces applied to the disk are modelled as a function of the disk-averaged axial velocity at the rotor face when the turbine is operating (U_{disk}). Since manufacturer-provided curves for power and thrust coefficient (C_T) are functions of freestream wind speed (U_∞), the curves used in the simulations need to be reformulated to be functions of U_{disk}. The conversion of the manufacturer-provided C_T and power curves follows a procedure similar to that reported by van der Laan et al. (2015). The procedure involves running a series of single-turbine simulations, each corresponding to a different hub-height wind speed. In these simulations, the U_∞ values are known, and actuator disk forces are thereby set according to theoretical curves specified as functions of U_∞. After each simulation finishes, we record U_{disk}. The outcome of the conversion is a set of curves ($P'(U_{\mathrm{disk}})$, $C_T'(U_{\mathrm{disk}})$, and rotor speed) specified as a function of U_{disk}.

All simulations correspond to a conventionally neutral boundary layer with a thickness of approximately 1000 m. The maximum potential gradient in the capping inversion is +10 K/km, and the free atmosphere above is stably stratified with a vertical potential temperature gradient of +3.3 K/km. In this numerical experiment, three types of simulations were run: full wind farm, turbines in isolation, and freestream. As the labels imply, the full wind farm simulations include all the wind turbines, the isolated turbine simulations only include one turbine, and the freestream simulations have no turbines/actuator disks. The three types of simulations are run with the same mesh and boundary conditions.

3.2 Simulation set-up

We perform RANS simulations of a wind farm with five rows of 20 turbines, as shown in Fig. 1-(a). The turbines have a rotor diameter of 136 m and are distributed with spacings of 3 and 10 D along x and y, respectively. We simulate five different wind directions, covering the sector from -45° to $+45^\circ$ with respect to the orthogonal wind direction $\theta = 0^\circ$ as shown in Fig. 1-(a). The turbines are numbered starting from the most downwind row, so that turbines from T81 to T100 are wake-free for all the simulated wind directions.

Simulations are also performed with a single turbine operating within the same domain and under the same free-flow conditions of the wind farm. We simulate four different single-turbine cases in order to evaluate whether numerical effects cause different results for different locations of the isolated turbine. We simulate the single turbine located at the spot of T28, T81, T92 and T100 and, although not shown, we find that the location of the isolated turbine does not change the conclusions re-

garding the blockage effect on power performance: the variations in both power and wind speed between the upstream turbines (T81,.., T100) and the isolated turbine do not change, i.e. results shown in Fig. 4 are independent of the location of the isolated turbine. Therefore, in the following analysis, we refer to the case with the isolated turbine located at T92 spot, as shown in Fig. 1-(b).

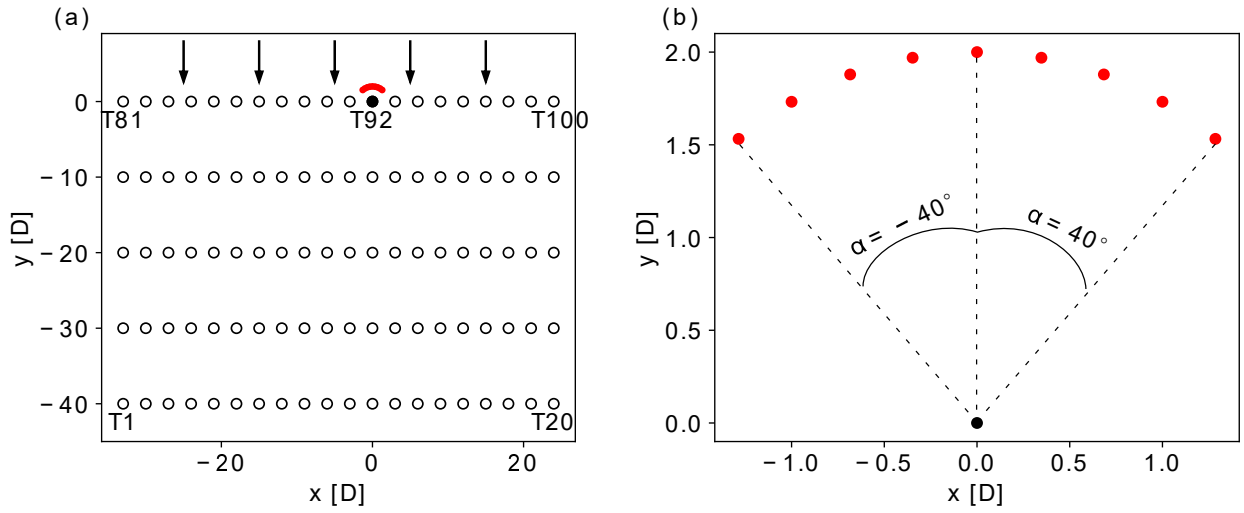

Figure 1. Illustrations of the wind farm layout (a) and the isolated turbine (b), with both wind turbine (*black circles*) and mast (*red circles*) locations. The arrows show the $\theta = 0^\circ$ wind direction.

To test the correction method, i.e., Eqs. (1) and (2), we extract the wind speed at hub height in front of all the first-row turbines and the isolated turbine. To test all the possible IEC-compliant wind speed measurements, we simulate nine masts located on the 2D-radius circle around each turbine and distributed every 10° from $\alpha = -40^\circ$ to $\alpha = 40^\circ$ relatively to the north, as shown in Fig. 1-(b). It should be noted that, according to the IEC standard, the available sector for power performance tests would be larger than $[-40^\circ, +40^\circ]$ for the isolated turbine, T81 and T100, as there are not neighbouring turbines on one or both sides of the turbine. However, to keep consistency in the comparison between the 20 upstream turbines and the isolated turbine, we consider the same sector of -40° to 40° for all the turbines.

We aim to simulate five wind directions regularly distributed over the $[-45^\circ, +45^\circ]$ interval. However, the simulated flow field is characterized by vertical veer due to the combination of surface friction and Coriolis force, so the wind direction varies around 4° from bottom to top of the rotor swept area, as shown in Fig. 2-(b), with wind directions at hub height of -46°, -23°, -1°, 20° and 44°. Additionally, Fig. 2-(a) shows the vertical velocity profiles, which are all characterized by an horizontal wind speed of around 7.1 m/s at hub height, with variations from $\sim$5.9 to $\sim$7.8 m/s across the rotor swept area. The wind speed was chosen so that the wake-free turbines operate on the plateau of the C_T curve.

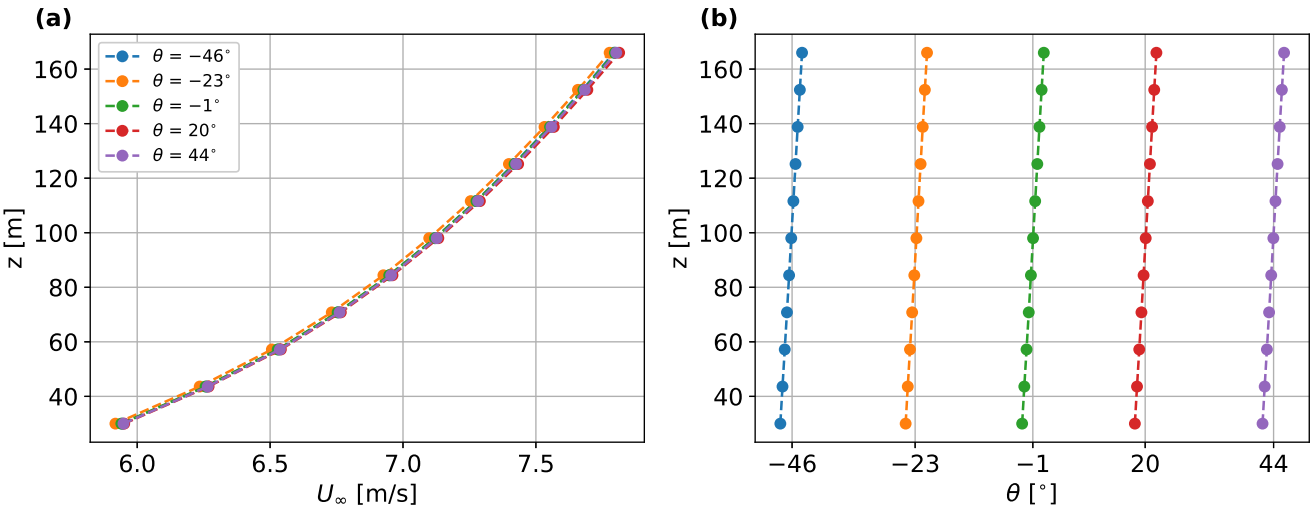

Figure 2. Vertical profiles of the horizontal wind speed (a) and wind direction (b) extracted at the location of T92 from the freestream simulations.

3.3 Virtual lidar measurements

The correction method is based on the combination of measurements (U_{mast} or U_{lidar}) with the numerically computed value of U_{disk}, which is hard to estimate out in the field. Therefore, we investigate whether U_{disk} can be replaced with a measurable velocity quantity: we simulate short-range nacelle lidar measurements in the induction zone and derive a velocity quantity $U_{\mathrm{disk,lidar}}$ that is tested as a proxy for U_{disk} in Eq. (1). Furthermore, we simulate IEC-compliant nacelle lidar measurements to evaluate the performance of the correction method when replacing U_{mast} with U_{lidar} in Eq. (1).

We retrieve the IEC-compliant wind speed measurements with a 2-beam nacelle-mounted lidar measuring at 2 D upstream of the rotor with a half-opening angle $\varphi = 15°$. Additionally, as shown in Fig. 3, we retrieve wind speed values at 0.5 D upstream of the rotor with four different nacelle lidars: the same 2-beam lidar used to measure at 2 D; a 4-beam lidar with $\varphi = 18°$ and the measurement points at the four vertices of a square; a 50-beam circularly scanning lidar with $\varphi = 15°$; and an additional 50-beam ideal lidar which scans along the circular pattern of radius equal to three quarters of the rotor radius. The choice of the 50-beam ideal lidar scanning pattern is based on the work by Sebastiani et al. (2023), who showed that, among several circular scanning patterns, the one scanning at around a three quarter of the radius provided the highest accuracy in power prediction.

We assume horizontal homogeneity of the flow field to reconstruct the horizontal wind speed at hub height from the 2-beam lidar measurements by inverting the linear system

$$\begin{pmatrix} n_x^1 & n_y^1 \\ n_x^2 & n_y^2 \end{pmatrix} \cdot \begin{pmatrix} u_x \\ u_y \end{pmatrix} = \begin{pmatrix} v_r^1 \\ v_r^2 \end{pmatrix}, \tag{3}$$

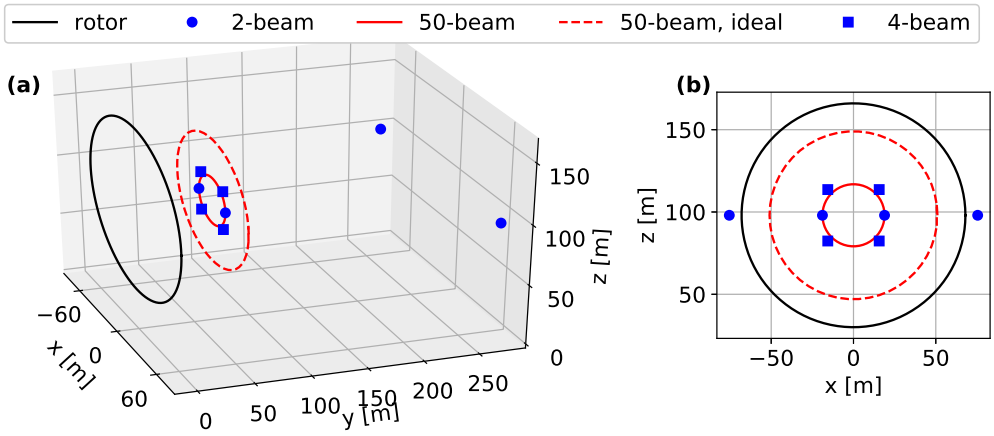

Figure 3. Illustrations of the rotor and lidar measurement points at both 2 and 0.5D with three- and two-dimensional views in (a) and (b), respectively.

where n_j^i is the j-th component of the unit vector n^i indicating the direction of the i-th beam, v_r^i is the radial velocity retrieved from the i-th beam and u_j is the j-th component of the horizontal wind velocity, whose magnitude is $U_{\text{lidar}} = \sqrt{u_x^2 + u_y^2}$. We do not simulate the lidar probe volume, so the radial velocities are retrieved as point measurements with a three-dimensional linear interpolation from the flow solution.

When using lidars with more than 2 beams, i.e., the two 50-beam and the 4-beam, we neglect both the lateral and vertical components of the wind speed vector by assuming $u_x = u_z = 0$ m/s, so that the horizontal wind speed at each beam location is retrieved as $u_y = v_r/n_y$. Then, the lidar-estimated disk velocity is obtained as the mean of the beam measurements: $U_{\text{disk,lidar}} = 1/n_{\text{beam}} \sum_{i=1}^{n_{\text{beam}}} u_y^i$. When using the 2-beam lidar focused at 0.5 D, the horizontal wind speed value reconstructed with Eq. (3) is used as $U_{\text{disk,lidar}}$.

4 Power performance measurement of the first-row turbines

Wind farm blockage affects the flow upstream of the wind farm, changing velocity relative to the flow upstream of the isolated turbine. Figure 4-(a) shows the difference between the wind speed $U_{\text{mast}}^{\text{I}}$ measured in front of the isolated turbine and the wind speed $U_{\text{mast}}^{\text{WF}}$ measured in front of the i^{th} wind-farm turbine for the same j^{th} wind direction:

$$\Delta U_{ij} = 100\,\frac{U_{\text{mast}}^{\text{WF}}(T_i,\theta_j) - U_{\text{mast}}^{\text{I}}(\theta_j)}{U_{\text{mast}}^{\text{I}}(\theta_j)}. \tag{4}$$

The error bars of Fig. 4-(a) indicate mean and standard deviations associated with the mast orientation α. For most of the first-row turbines, the measured wind speed is lower than in the isolated case for all the simulated wind directions, with

velocity reductions of more than 3% in the centre of the row. However, in cases of highly skewed inflow, the wind speed is increased around the most downwind turbines. For $\theta = 44°$, $U^{\mathrm{WF}}_{\mathrm{mast}}$ at T81 is more than 1% higher than $U^{\mathrm{I}}_{\mathrm{mast}}$. The same trend of wind speed variations for a skewed inflow was found by Sebastiani et al. (2022) for a single row of wind turbines, where the downstream turbines are in the speed-up region formed at the edge of the wakes from the upstream turbines (Sebastiani et al., 2022; Meyer Forsting et al., 2017). In our case, due to the larger scale of the wind farm, the wind speed increase might be also due to the speed-up at the edge of the wind-farm induction region. The asymmetry in global-blockage effect between cases with almost symmetric inflow angles, such as $-46°$ and $44°$, is probably due to the asymmetry introduced by the vertical wind veer, and perhaps also wake rotation.

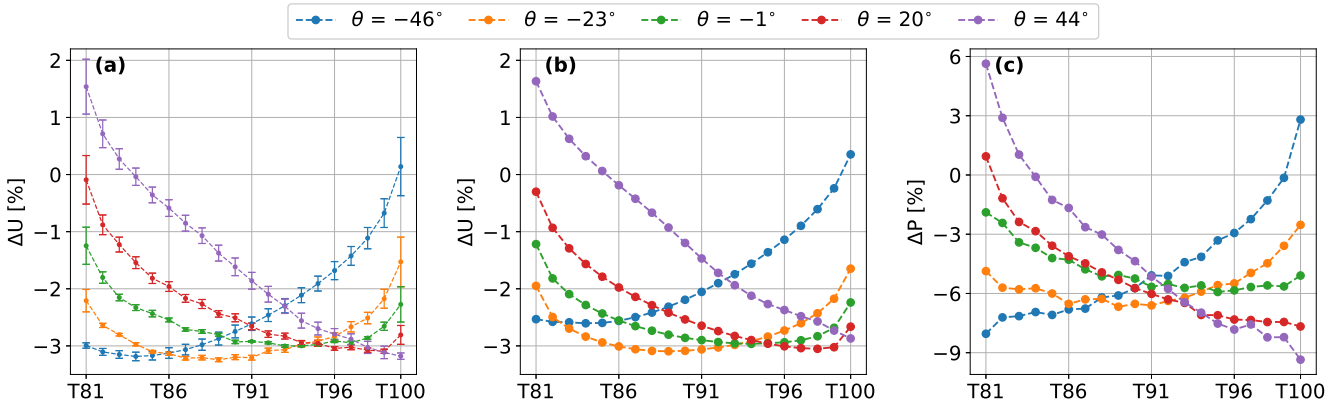

Figure 4. Variations in wind speed (a,b) and power output (c) relatively to the isolated turbine for all the simulated wind directions, when measuring the wind speed at 2D in front of the turbines with either masts (a) or the 2-beam lidar (b). Error bars (a) indicate the standard deviations with the α values.

The blockage-induced velocity variations do not change much when replacing the masts with a 2-beam nacelle-mounted lidar, as shown in Fig. 4-(b). However, the nacelle lidars measure the wind speed along the rotor axis irrespective of θ, removing the variation associated with α.

Similarly to the wind speed variations shown in Fig.s 4-(a) and 4-(b), Fig. 4-(c) shows the power deviations of the first-row turbines relatively to the isolated turbine:

$$\Delta P_{ij} = 100\,\frac{P^{\mathrm{WF}}(T_i,\theta_j) - P^{\mathrm{I}}(\theta_j)}{P^{\mathrm{I}}(\theta_j)}. \tag{5}$$

Since the power output is related to the velocity raised to the power of 2–3, power variations are larger in magnitude than the velocity ones, with variations from -9.4% to $+5.6\%$ with respect to the isolated turbines. Additionally, the largest power losses are not found for the central turbines as for the wind speed, but for the most upstream turbines in the case of strongly skewed inflows, i.e., T81 for $\theta = -46°$ and T100 for $\theta = 44°$.

Since $U^{\mathrm{WF}}_{\mathrm{mast}}$ and P are not perfectly correlated, their blockage-induced variations cause uncertainty in the power curve, as shown in Fig. 5-(a) with a scatter plot of the power output from the first-row turbines against the wind speed measured by their

mast for all wind directions. When applying the correction in Eq. (1) to $U_{\mathrm{mast}}^{\mathrm{WF}}$, the scatter in the power curve does not decrease much, as shown in Fig. (5)-(b). On the other hand, when further correcting $U_{\mathrm{mast}}^{\mathrm{I,rec}}$ with Eq. (2), the scatter in the power curve decreases substantially to a much lower level as shown in Fig. 5-(c).

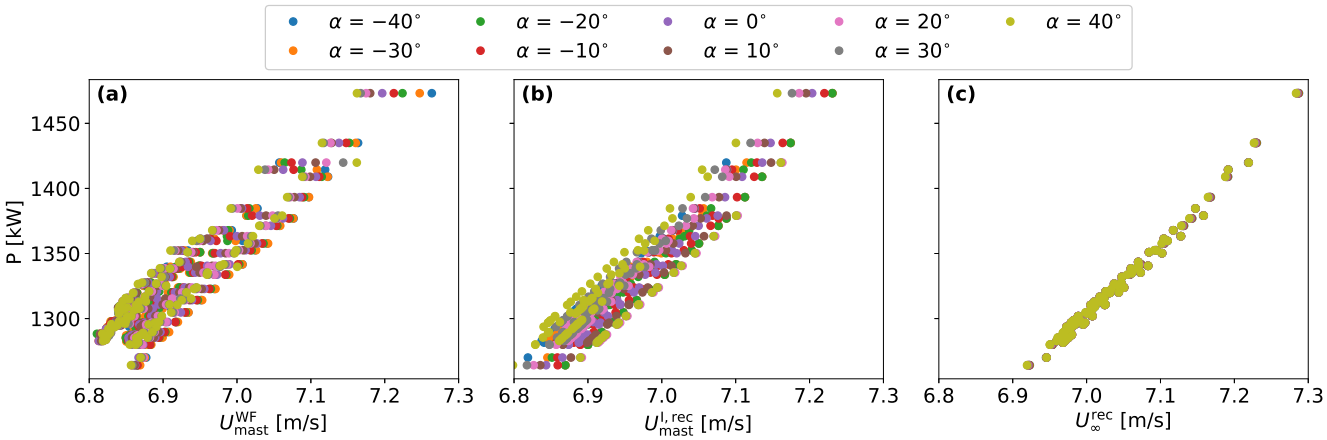

Figure 5. Power output against the mast-measured wind speed of all the first-row turbines for all wind directions and mast locations. (a): no correction applied on the measured wind speed. (b): wind speed corrected with Eq. (1). (c): wind speed corrected with Eq. (2).

The scatter shown in Fig. 5-(a) is not only due to global blockage, but also to turbine blockage, whose effect is not accounted for using Eq. (1), which reconstructs the wind speed that would be measured around the isolated turbine that is producing the same amount of power as the wind-farm turbine. Since the blockage-induced velocity field is not spatially uniform, the ratio $(U_{\mathrm{mast}}/U_{\mathrm{disk}})^{\mathrm{I}}$ varies with both θ and α as shown in Fig. 6, where error bars represent the standard deviations of the values obtained for different mast orientations α.

When applying Eq. (2), we are correcting for the turbine blockage, relating the power output to the freestream velocity that would be measured at the isolated turbine location if the turbine was not there. The power curves retrieved from different masts collapse onto each other, as the freestream velocity does not vary substantially with either α or θ due to the nearly homogeneous velocity field. As shown in Fig. 6, the variation of $(U_{\infty}/U_{\mathrm{disk}})^{\mathrm{I}}$ with α is almost non-existing while a maximum variation of 0.25 % is observed with θ. The larger variation with θ is partly due to tiny variations in the wind profiles among different simulations, as U_{∞} is evaluated at hub height while U_{disk} depends on the wind speed along the entire rotor swept area. Additionally, other factors might cause the discrepancy in $(U_{\infty}/U_{\mathrm{disk}})^{\mathrm{I}}$ between different simulations, such as slight variations in the wake diffusion or number of cells across the disk.

Figure 7 shows scatter plots of the power output against the lidar-retrieved wind speeds for the first-row turbines. When using nacelle lidars, α can be disregarded and the power performance variations are due to the turbine location and wind direction only. The scatter is almost completely reduced by using Eq. (1), as nacelle lidars measure the wind along the rotor axis regardless of θ so that the measurements are equally affected by turbine blockage for different values of θ. When using

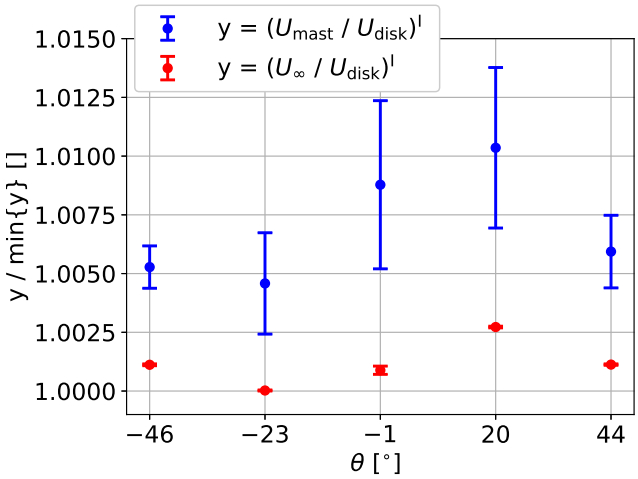

Figure 6. Wind speed variations in the induction zone of the isolated turbine when using mast measurements. Error bars represent the standard deviations of the values obtained for different mast orientations α and same wind direction θ.

Eq. (2) to correct for turbine blockage, the scatter does not decrease and the only effect is the shifting towards higher velocity values.

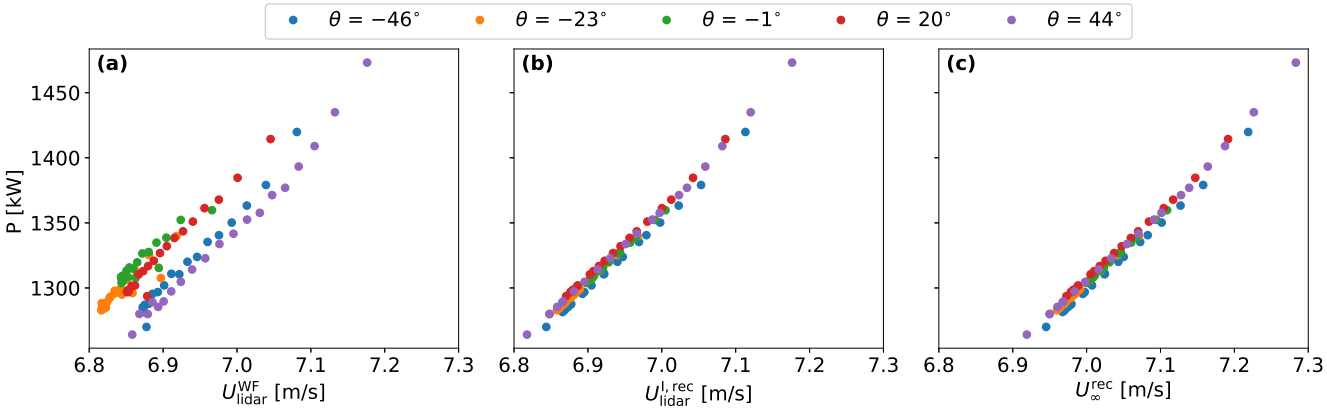

Figure 7. Power output against the lidar-measured wind speed of all the first-row turbines for all wind directions. (a): no correction applied on the measured wind speed. (b): wind speed corrected with Eq. (1). (c): wind speed further corrected with Eq. (2).

245 Figure 8 shows the variations with θ of the ratios $(U_{\mathrm{lidar}}/U_{\mathrm{disk}})^{\mathrm{I}}$ and $(U_{\infty}/U_{\mathrm{disk}})^{\mathrm{I}}$. Both ratios show almost the same dependency on θ, which demonstrates that the differences in $U^{\mathrm{I}}_{\mathrm{lidar}}$ values are due to the variation of the freestream flow rather than to turbine blockage. This also explains the similarity in the scatter of the power curve when using either $U^{\mathrm{I,rec}}_{\mathrm{lidar}}$ or $U^{\mathrm{rec}}_{\infty}$. When measuring power curves with nacelle lidars, Eq. (1) can be used to correct wind-farm effects and retrieve the power performance of the isolated turbine. However, Eq. 2 is still needed to get the power output as function of the freestream

velocity and avoiding an overestimation of the power performance, as it can be noticed in Fig. 7-(c), where power values are shifted to the right compared to Fig. 7-(b).

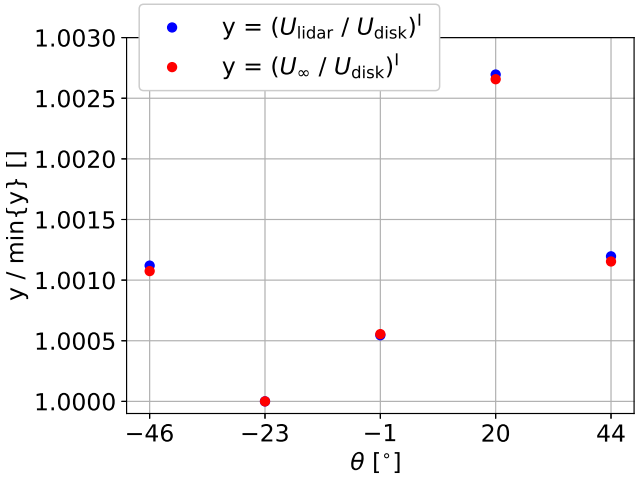

Figure 8. Wind speed variations in the induction zone of the isolated turbine when using nacelle lidars

Figure 9 shows the distributions of the C_P values estimated using the different wind speed definitions. When looking at the C_P of the isolated turbine, we notice lower variation using lidar than mast measurements, as we avoid dependencies on α variations, so that the spread of the C_P values is lower when using $U^{\mathrm{WF}}_{\mathrm{lidar}}$, $U^{\mathrm{I,rec}}_{\mathrm{lidar}}$ and $U^{\mathrm{I}}_{\mathrm{lidar}}$ than with $U^{\mathrm{WF}}_{\mathrm{mast}}$, $U^{\mathrm{I,rec}}_{\mathrm{mast}}$ and $U^{\mathrm{I}}_{\mathrm{mast}}$, respectively. If we assume $C_P = C_P(U^{\mathrm{I}}_{\mathrm{lidar}})$ as the reference value, the C_P estimation is both inaccurate and imprecise when using either $U^{\mathrm{WF}}_{\mathrm{lidar}}$ or $U^{\mathrm{WF}}_{\mathrm{mast}}$. The C_P mean values are 1.5% and 1.4% higher than $C_P(U^{\mathrm{I}}_{\mathrm{lidar}})$ for $U^{\mathrm{WF}}_{\mathrm{mast}}$ and $U^{\mathrm{WF}}_{\mathrm{lidar}}$, respectively, whereas the interquartile range (IQR) is 600% and 700% higher for $U^{\mathrm{WF}}_{\mathrm{mast}}$ and $U^{\mathrm{WF}}_{\mathrm{lidar}}$, respectively. By correcting with Eq. (1), the term $U^{\mathrm{I,rec}}_{\mathrm{mast}}$ provides higher accuracy than $U^{\mathrm{WF}}_{\mathrm{mast}}$ with both median and mean values closer to the reference, but the values are still highly spread due to the variations in $(U_{\mathrm{mast}}/U_{\mathrm{disk}})^{\mathrm{I}}$, as shown in Fig. 6. On the other hand, we observe both an increase in accuracy and reduction in the spread when using $U^{\mathrm{I,rec}}_{\mathrm{lidar}}$, with differences with the reference of 0.4% and 19.8% for the mean value and IQR, respectively. However, without applying Eq. 2, the C_P values are not an accurate estimation of the power performance as $C_P = C_P(U_\infty)$. As shown in Fig. 9, the C_P is overestimated relative to $C_P(U_\infty)$ of 4.1% and 4.5% when using $U^{\mathrm{I}}_{\mathrm{mast}}$ and $U^{\mathrm{I}}_{\mathrm{lidar}}$, respectively. On the other hand, the C_P estimation is very accurate when using Eq. 2, with deviations of 0.4% from $C_P(U_\infty)$ for both $U^{\infty,\mathrm{rec}}_{\mathrm{mast}}$ and $U^{\infty,\mathrm{rec}}_{\mathrm{lidar}}$.

It should be noted that the overestimation of C_P observed with both $U^{\mathrm{WF}}_{\mathrm{mast}}$ and $U^{\mathrm{WF}}_{\mathrm{lidar}}$ might have strong implications on the accuracy of AEP estimations. Additionally, the wind speeds corresponding to the high C_T values assumed in this work are usually among the most frequent wind speed values at the wind farm site. Therefore, results of Figs. 5, 7 and 9 show the need to correct for the effect of blockage on power performance measurements.

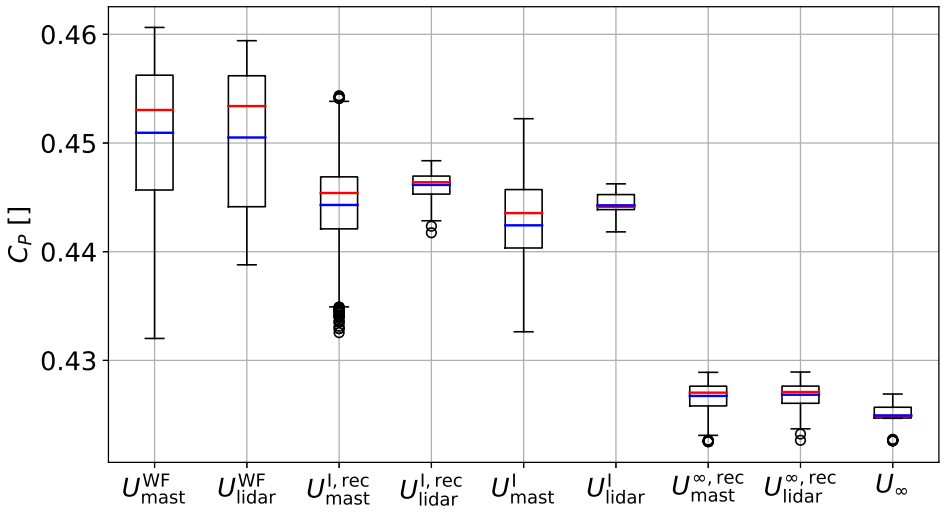

Figure 9. Box plots of the C_P distributions for the first-row and isolated turbines. Box plot features: quartiles $q1$ and $q3$ (*box limits*); lowest and highest values within [$q1 - 2$ IQR, $q3 + 2$ IQR] (*whiskers*); values outside the range [$q1 - 2$ IQR, $q3 + 2$ IQR] are shown as outliers (*circles*); median (*red line*) and mean (*blue line*).

5 Lidar-based estimation of the disk velocity

We simulate the 2-beam lidar focused at 19 different distances from the rotor, as shown in Fig. 10-(a). Specifically, we simulate measurements from the rotor plane up to 1.875 D, and we compute $U_{\mathrm{disk,lidar}}$ from the radial velocities of the two beams at each distance. We then model the relationship between the terms $U_{\mathrm{disk,lidar}}$ and U_{disk} with least-square linear regressions using the ($U_{\mathrm{disk,lidar}}$,U_{disk}) values from all the 20 upstream turbines, whose coefficients of determination R^2 are shown in Fig. 11.

As it can be noted in Fig. 11, R^2 is low when measuring closer than 0.2 D to the rotor and reaches its maximum at 0.25 D, with a smooth decreasing trend for further distances. The value at $\Delta y = 0.625$ D appears as an outlier due to numerical biases because the focus point of the beams is at the edge of the highly discretized region, as shown in Fig. 10-(b).

The correlation between U_{disk} and $U_{\mathrm{disk,lidar}}$ decreases very close to the rotor. This is due to a combination of discretisation and interpolation error. As shown in Fig. 10-(a), the flow field close to the rotor ($y \lessapprox 0.2$D) does not appear as smooth as it does far from the rotor. Strong velocity gradients near the rotor, caused by the applied turbine forces, increase discretisation and interpolation errors here.

We use the distance of $\Delta y = 0.5$ D for testing the correction method based on the work by Troldborg and Meyer Forsting (2017), who showed that the induction zone is self-similar beyond 0.5 D upstream of the rotor, i.e., that the induced velocity field is only function of the total C_T with no dependency on the distribution of loads across the rotor. When measuring $U_{\mathrm{disk,lidar}}$ at 0.5 D, the results are representative of all wind turbine rotors, while using closer measurements might provide results which are representative of the simulated rotor only.

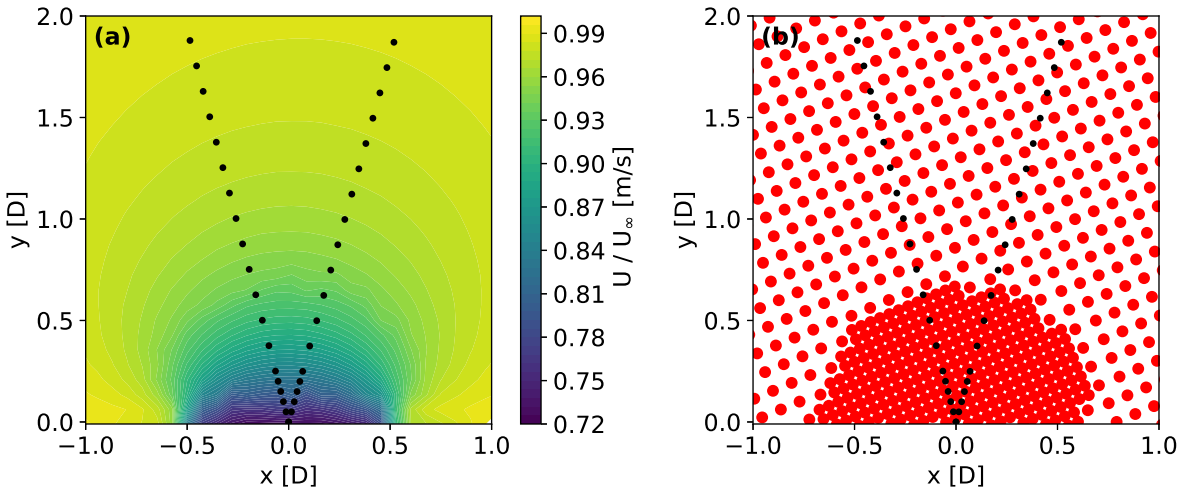

Figure 10. Normalized velocity field at hub height in front of the isolated turbine (a) and grid discretization within the same area (b).

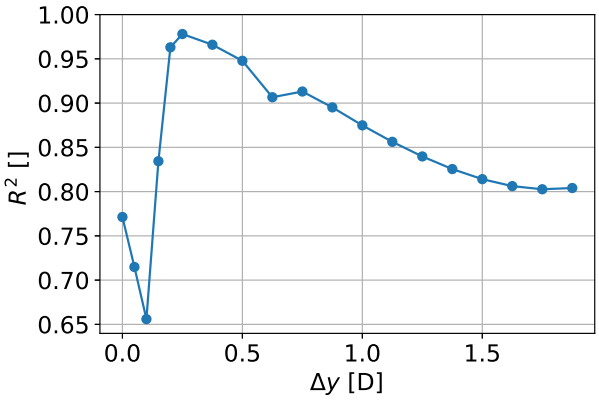

Figure 11. Coefficient of determination of the least-square linear regression between U_{disk} and $U_{\mathrm{disk,lidar}}$ estimated at several upstream distances.

6 Power performance measurements in wakes

The correction method is not limited to blockage effects. In theory, it can be used to correct for any turbine-related disturbances, including wakes. Figure 12 shows the relation between wind speed and power output for all the 100 turbines in the farm and for all the simulated wind directions. Since it is not common to erect masts in the inner region of the wind farm, we only consider nacelle lidars for power performance measurements of turbines T1, .., T80. As shown in Fig. 12-(a), the power output is very poorly correlated with the hub-height wind speed measured at 2 D in front of the rotor, as this does not represent well U_{disk}. This is due to the complex inflow conditions faced by the downstream turbines (T1, T2, ..., T80), with both axial and lateral velocity gradients affecting the relationship between the measured wind speed and U_{disk}. Additionally, for skewed wind directions, the measurement location might be in wake, while the rotor is not, or the rotor might be partially in wake, further decreasing the correlation between the power output and the measured wind speed.

When applying Eq. (1), as shown in Fig. 12-(b), the corrected wind speed is highly correlated with the power output, as the correlation between U_{disk} and P is not affected by the complexity of the flow field in the model. When further correcting with Eq. (2), as shown in Fig. 12-(c), the scatter in the power curve is not further decreased, and a shift towards slightly higher wind speed values is observed due to the correction of the turbine blockage. When comparing to the freestream power curve values (U_∞, P^I) given by the combination of the isolated and freestream simulations (black squares in Fig 12), we notice an overestimation of the power performance when correcting with Eq. (1) only, and strong agreement when further correcting with Eq. (2).

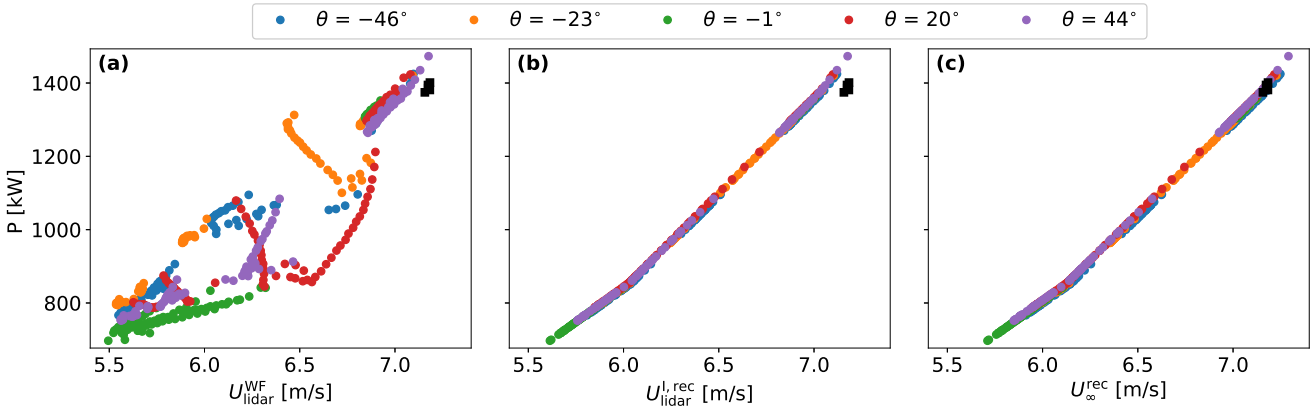

Figure 12. Power output against the lidar-measured wind speed of all the wind-farm turbines for all wind directions. (a): no correction applied on the measured wind speed. (b): wind speed corrected with Eq. 1. (c): wind speed corrected with Eq. 2. Black squares indicate the (U_∞, P^I) points given by the combination of the isolated and freestream simulations.

The correction method also works well when replacing the term U_{disk} in Eq. (1) with $U_{\mathrm{disk,lidar}}$ retrieved at 0.5 D in front of the rotors, as shown in Fig. 13. Although the scatter is slightly larger than when using U_{disk}, all lidar configurations allow

for large improvements in the power curve. The results for the three commercial lidars in Figs.13-(a,b,c) are quite similar with no significant improvements when increasing the number of beams, while keeping the same opening angle ($\varphi = 15°, 18°$). However, when increasing φ to 37°, the correction results in significant less scatter, as shown in Fig. 13-(d). This is because the lidar-estimated U_{disk} is closer to the true value when increasing the scanned area.

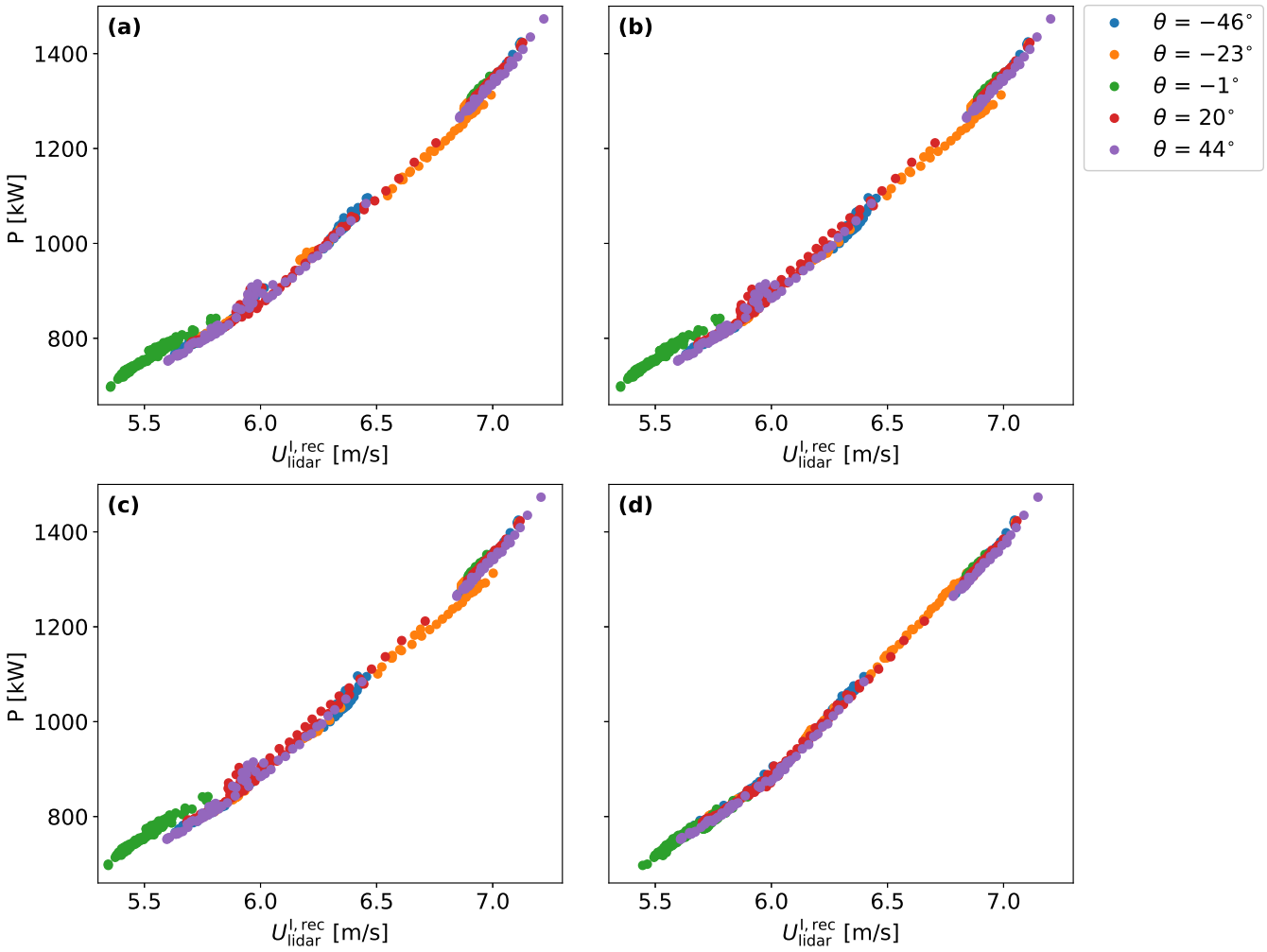

Figure 13. Power output against the lidar-measured wind speed of all the wind-farm turbines and all wind directions. Wind speed measurements are corrected with Eq. (1), where U_{disk} is replaced with the term $U_{\mathrm{disk,lidar}}$, which is estimated using measurements at 0.5D from the 2-beam lidar (a), the 4-beam lidar (b), the 50-beam (c) and the 50-beam ideal lidar (d).

The short-range lidar measurements at 0.5 D in front of the rotor cannot be used as a proxy of U_{disk}. However, the correction method can be applied with these measurements as they are highly correlated with the velocity at the disk, as shown in Fig. 14. Since the lidar measures very close to the rotor, the correlation between $U_{\mathrm{disk,lidar}}$ and U_{disk} is less affected by the velocity

gradients in the wakes and the measurements and the rotors have a higher probability of being both either inside or outside the wake. In agreement with the results of Fig. 13, the highest correlation is shown by the circular scanning lidar with $\varphi = 37°$ with a coefficient of determination $R^2 = 0.998$.

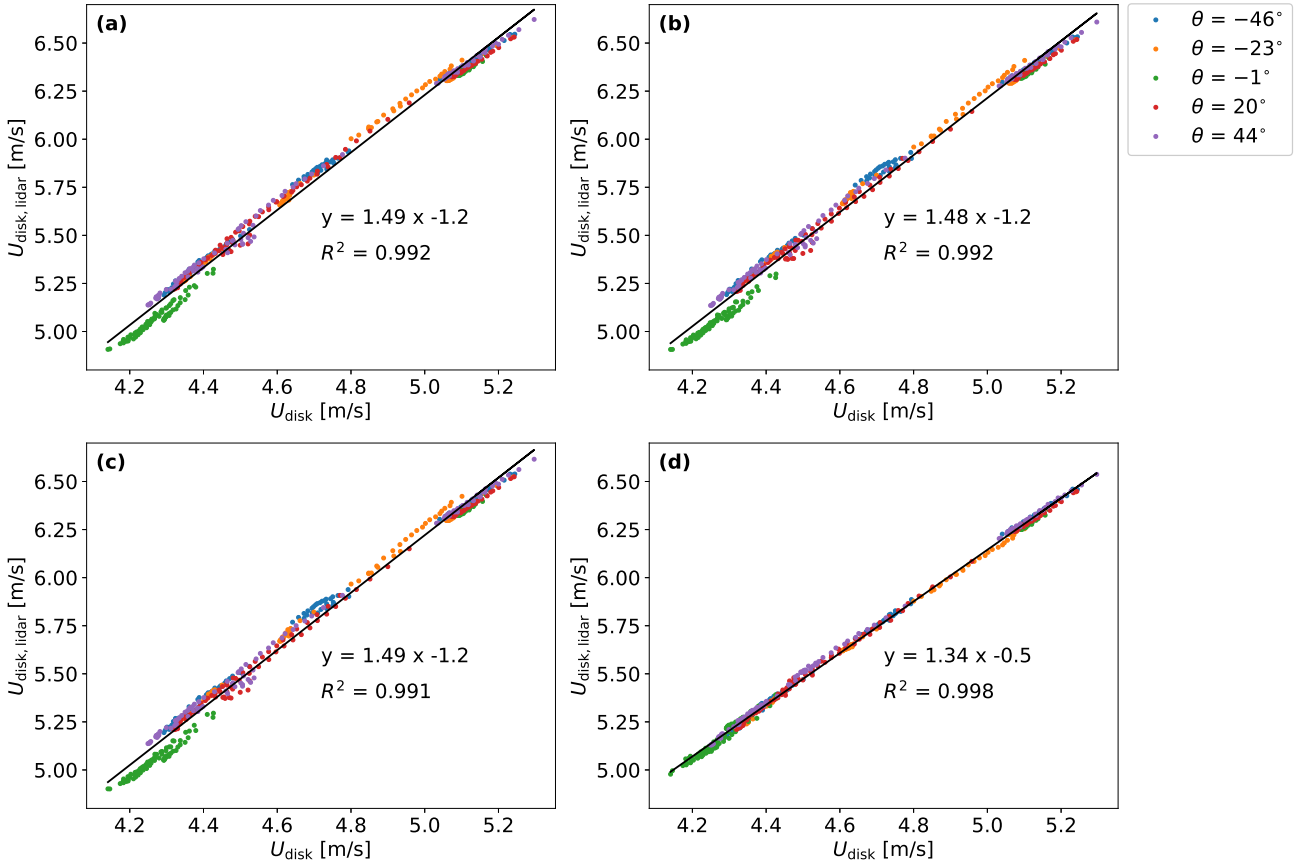

Figure 14. Scatter plots and related linear regressions between U_{disk} and $U_{\text{disk,lidar}}$ estimated with measurements at 0.5D from the 2-beam lidar (a), the 4-beam lidar (b), the CSL (c) and the 50-beam lidar (d).

7 Practical application and limitations

In this work, a method is presented to correct for the effect of turbine-induced flow distortions on power performance measurements. Our results show that the correction method can potentially reduce both bias and uncertainty of power performance measurements. However, the approach relies on the accuracy of the flow model, which might introduce errors when applying the correction to field measurements. In addition, the ratio $(U_{\text{disk}}/U_{\text{lidar}})^{\text{WF}}$ is likely sensitive to the wind direction and, especially out of the constant-C_T region of the C_T curve, the correction factors change with the wind speed; as a result, many

numerical simulations might be required to account for different wind speed and wind directions. Additionally, it would be necessary to evaluate the uncertainty introduced in the measurements by the numerical correction.

The drawbacks of relying exclusively on numerical simulations to make the corrections could be mitigated by complementing the flow model with nacelle lidar measurements. Our numerical results indicate that short range nacelle lidar measurements can be used to reduce the impact of turbine-induced flow disturbances on power performance measurements, improving both accuracy and precision of the power curve. However, when using nacelle lidar measurements to apply Eq. 1, the power performance would be still overestimated because of the difference between $U^{\mathrm{I}}_{\mathrm{lidar}}$ and U_∞. In order to retrieve the freestream power curve $P = P(U_\infty)$, the lidar measurements must be further corrected with Eq. 2, which can only be applied through numerical simulations of both the isolated turbine and the freestream flow field. Thus, as shown in this work, nacelle lidar measurements can be used to correct for the effect of neighbouring turbines on the measured power performance, but simulations are needed in order to further correct for the blockage effect of the single isolated rotor.

During the power performance testing of an isolated turbine, nacelle lidar measurements could be retrieved at both 0.5 D and 2 D in order to estimate $(U_{\mathrm{disk}}/U_{\mathrm{lidar}})^{\mathrm{I}}$. Then, when testing the power performance of the same turbine model in a wind farm, the ratio $(U_{\mathrm{disk}}/U_{\mathrm{lidar}})^{\mathrm{WF}}$ would be retrieved with the same procedure and the measured power curve can be corrected with Eq. 1. However, $(U_{\mathrm{disk}}/U_{\mathrm{lidar}})^{\mathrm{I}}$ might be sensitive to the atmospheric conditions at the isolated-turbine test site, which might be different from those of the wind farm site. In our numerical tests, both the isolated turbine and the wind farm operate under the same atmospheric conditions. This might improve the results compared to the case where $(U_{\mathrm{disk}}/U_{\mathrm{lidar}})^{\mathrm{I}}$ and $(U_{\mathrm{disk}}/U_{\mathrm{lidar}})^{\mathrm{WF}}$ are obtained from sites presenting significantly different atmospheric conditions.

A viable procedure could be using the short range nacelle lidar measurements to validate the flow model. Numerical and experimental investigations (Meyer Forsting, 2017; Simley et al., 2016) showed that the induction factor $a = (U_\infty - U_{\mathrm{disk}})/U_\infty$ is not affected by moderate shear, while strong variations of both a and C_T have been observed under extreme shear conditions (power law exponent of 0.5) (Meyer Forsting et al., 2018). On the basis of such results, the variation of $(U_{\mathrm{disk}}/U_{\mathrm{lidar}})^{\mathrm{I}}$ among different sites is likely small when measuring under neutral or nearly-neutral conditions, while variations might be observed under stable conditions characterized by strong vertical shear. However, further investigation is needed to evaluate the sensitivity of the correction method to different vertical wind profiles and atmospheric conditions.

Separately, but still on the subject of further investigation, the reliability of the correction method under waked conditions could be tested by conducting power performance measurements at the wind farm edge using nacelle lidar measurements. Depending on the wind direction, the reference turbine would be either the most upwind or downwind of the farm. So, $(U_{\mathrm{disk}}/U_{\mathrm{lidar}})^{\mathrm{I}}$ and $(U_{\mathrm{disk}}/U_{\mathrm{lidar}})^{\mathrm{WF}}$ could be retrieved from wake-free and waked measurements, respectively. Eq. 1 would be then applied to the waked measurements to evaluate whether they provide a power curve which is consistent with that obtained from the IEC-compliant wake-free measurements.

8 Conclusions

We perform RANS simulations that include both a wind farm and an isolated wind turbine operating within a conventionally neutral ABL. The simulations aim to analyze the influence of wind farm blockage effects on power performance tests, assessing whether the measured power performance differs from that of the isolated wind turbine. Furthermore, we suggest a method to correct for blockage effects on the power performance. The method corrects the power curves of the wind farm turbines so that they become closer to that of the isolated turbine. Additionally, we correct for the blockage effect of the single isolated wind turbine, retrieving the power performance as function of the undisturbed freestream velocity. Finally, we use the correcting method to evaluate the power performance of all the wind turbines in the farm, including downstream turbines in wake.

The numerical results show that wind farm blockage affects the power performance of the turbines in the upstream row of the wind farm, with variations up to 3% in IEC-compliant wind speed measurements and up to 9% in power output depending on both the location of the turbine in the row and the wind direction. Wind farm blockage increases the uncertainty of power performance measurements conducted on the wind-farm turbines, with high scatter in the power curve and large spread of the C_P values. When considering all wind directions and upstream turbines, variations up to 1.5% are observed for the mean power coefficient C_P relatively to the isolated turbine. Additionally, single-turbine blockage causes an overestimation of C_P up to 4.5% due to the difference between the measured wind speed and the undisturbed freestream velocity.

We show that the influence of blockage effects on power performance measurements can be reduced by performing numerical simulations of the frestream flow field, the isolated wind turbine and the wind farm. The method reduces the scatter in the power curve and decreases the difference in C_P between the wind farm and the isolated turbines. Additionally, the method accounts for blockage effects from the single isolated turbine, retrieving the power performance of the turbine in isolation as a function of the freestream wind speed. Furthermore, the correction method is used to derive reliable power curves from power performance measurements conducted on waked wind turbines.

The correction method is also tested by replacing the numerical estimation of the rotor velocity with virtual nacelle lidar measurements retrieved close to the rotor. Results show that the nacelle lidar measurements are highly correlated with the power output; therefore, they can likely be used to perform power performance measurements for wind turbines inside the wind farm. However, further investigation is needed to assess to what extent the lidar-based correction is affected by the atmospheric conditions during the measurements.

Code and data availability. Code and data related to this work can be obtained by contacting the authors.

Acknowledgements. This work has received funding from the European Union Horizon 2020 through the Innovation Training Network Marie Skłodowska-Curie Actions: Lidar Knowledge Europe (LIKE) [grant number 858358].

References

Allaerts, D. and Meyers, J.: Boundary-layer development and gravity waves in conventionally neutral wind farms, Journal of Fluid Mechanics, 814, 95–130, https://doi.org/10.1017/jfm.2017.11, 2017.

Bleeg, J.: A Graph Neural Network Surrogate Model for the Prediction of Turbine Interaction Loss, Journal of Physics: Conference Series, 1618, https://doi.org/10.1088/1742-6596/1618/6/062054, 2020.

Bleeg, J., Digraskar, D., Horn, U., and Corbett, J.: Modelling stability at microscale, both within and above the atmospheric boundary layer, substantially improves wind speed predictions, In Proceedings of the EWEA Conference, Paris, France, 2015a.

Bleeg, J., Digraskar, D., Woodcock, J., and Corbett, J.-F.: Modeling stable thermal stratification and its impact on wind flow over topography, Wind Energy, 18, 369 – 383, https://doi.org/10.1002/we.1692, 2015b.

Bleeg, J., Purcell, M., Ruisi, R., and Traiger, E.: Wind farm blockage and the consequences of neglecting its impact on energy production, Energies, 11, https://doi.org/10.3390/en11061609, 2018.

Branlard, E. and Meyer Forsting, A.: Assessing the blockage effect of wind turbines and wind farms using an analytical vortex model, Wind Energy, 23, 2068–2086, https://doi.org/10.1002/we.2546, 2020.

Ebenhoch, R., Muro, B., Dahlberg, J.-, Berkesten Hägglund, P., and Segalini, A.: A linearized numerical model of wind-farm flows, Wind Energy, 20, 859 – 875, https://doi.org/10.1002/we.2067, 2017.

IEC: 61400-12-1, Power performance measurements of electricity producing wind, turbines, 2017.

McTavish, S., Rodrigue, S., Feszty, D., and Nitzsche, F.: An investigation of in-field blockage effects in closely spaced lateral wind farm configurations, Wind Energy, 18, 1989–2011, https://doi.org/10.1002/we.1806, 2015.

Medici, D., Ivanell, S., Dahlberg, J.-A., and Alfredsson, P. H.: The upstream flow of a wind turbine: blockage effect, Wind Energy, 14, 691–697, https://doi.org/10.1002/we.451, 2011.

Meyer Forsting, A.: Modelling Wind Turbine Inflow: The Induction Zone, Ph.D. thesis, Denmark, https://doi.org/10.11581/DTU:00000022, 2017.

Meyer Forsting, A., Troldborg, N., and Gaunaa, M.: The flow upstream of a row of aligned wind turbine rotors and its effect on power production, Wind Energy, 20, 63–77, https://doi.org/10.1002/we.1991, 2017.

Meyer Forsting, A., Van Der Laan, M., and Troldborg, N.: The induction zone/factor and sheared inflow: A linear connection?, Journal of Physics: Conference Series, 1037, https://doi.org/10.1088/1742-6596/1037/7/072031, 2018.

Nishino, T. and Draper, S.: Local blockage effect for wind turbines, Journal of Physics: Conference Series, 625, https://doi.org/10.1088/1742-6596/625/1/012010, 2015.

Nygaard, N. and Brink, F.: Measurements of the wind turbine induction zone, vol. 26-29 June 2017, 2017.

Nygaard, N. G., Steen, S. T., Poulsen, L., and Pedersen, J. G.: Modelling cluster wakes and wind farm blockage, Journal of Physics: Conference Series, 1618, https://doi.org/10.1088/1742-6596/1618/6/062072, 2020.

Sebastiani, A., Peña, A., Troldborg, N., and Meyer Forsting, A.: Evaluation of the global-blockage effect on power performance through simulations and measurements, Wind Energy Science, 7, 875–886, https://doi.org/10.5194/wes-7-875-2022, 2022.

Sebastiani, A., Peña, A., and Troldborg, N.: Numerical evaluation of multivariate power curves for wind turbines in wakes using nacelle lidars, Renewable Energy, 202, 419–431, https://doi.org/https://doi.org/10.1016/j.renene.2022.11.081, 2023.

Segalini, A.: An analytical model of wind-farm blockage, Journal of Renewable and Sustainable Energy, 13, https://doi.org/10.1063/5.0046680, 2021.

Segalini, A. and Dahlberg, J. Å.: Blockage effects in wind farms, Wind Energy, 23, 120–128, https://doi.org/10.1002/we.2413, 2020.

Simley, E., Angelou, N., Mikkelsen, T., Sjöholm, M., Mann, J., and Pao, L. Y.: Characterization of wind velocities in the upstream induction zone of a wind turbine using scanning continuous-wave lidars, Journal of Renewable and Sustainable Energy, 8, https://doi.org/10.1063/1.4940025, 2016.

Strickland, J. M. and Stevens, R. J.: Investigating wind farm blockage in a neutral boundary layer using large-eddy simulations, European Journal of Mechanics, B/Fluids, 95, 303 – 314, https://doi.org/10.1016/j.euromechflu.2022.05.004, 2022.

Troldborg, N. and Meyer Forsting, A.: A simple model of the wind turbine induction zone derived from numerical simulations, Wind Energy, 20, 2011–2020, https://doi.org/10.1002/we.2137, 2017.

van der Laan, P., Sørensen, N., Réthoré, P.-E., Mann, J., Kelly, M., and Troldborg, N.: The k-ϵ-fP model applied to double wind turbine wakes using different actuator disk force methods, Wind Energy, 18, 2223–2240, https://doi.org/10.1002/we.1816, 2015.

Paper III: Influence of nacelle-lidar scanning patterns on inflow turbulence characterization

Influence of nacelle-lidar scanning patterns on inflow turbulence characterization

Influence of nacelle-lidar scanning patterns on inflow turbulence characterization

Wei Fu, Alessandro Sebastiani, Alfredo Peña, Jakob Mann

Department of Wind Energy, Technical University of Denmark, Frederiksborgvej 399, 4000 Roskilde, Denmark

E-mail: weif@dtu.dk

Abstract. Nacelle lidars with different number of beams, scanning configurations and focus distances are simulated for characterizing the inflow turbulence. Lidar measurements are simulated within 100 turbulence wind fields described by the Mann model. The reference wind turbine has a rotor diameter of 52 m. We assume homogeneous frozen turbulence over the lidar scanning area. The lidar-derived Reynolds stresses are computed from a least-square procedure that uses radial velocity variances of each of the beams and compared with those from a simulated sonic anemometer at turbine hub height. Results show that at least six beams, including one beam with a different opening angle, are needed to estimate all Reynolds stresses. Enlarging the beam opening angle improves the accuracy and uncertainty in turbulence estimation more than increasing the number of beams. All simulated lidars can estimate the along-wind variance accurately. This work provides guidance on designing and utilizing nacelle lidars for inflow turbulence characterization.

1. Introduction

Characteristics of inflow turbulence are crucial for wind turbine load validation [1], power performance assessment [2] and wind turbine control [3]. In-situ anemometers installed on meteorological masts, such as cup and sonic anemometers, have been used to measure inflow turbulence. Nevertheless, with the increasing size of modern wind turbines, installing a meteorological mast that reaches the height of the blade tips has becoming more and more unaffordable, especially in offshore conditions. In recent years, lidars of different types and configurations have been mounted on the nacelle of wind turbines to scan the inflow [2; 4]. These forward-looking nacelle lidars have the advantage that they yaw with the wind turbine and scan towards the main wind direction. Compared to the point-wise anemometers, lidars measure over an area in front of the rotor, which gives the possibility to derive rotor-averaged turbulence characteristics.

Turbulence can be characterized by the second-order moments (variances and covariances) of the wind field components u, v and w in typically 10 min or 30 min assuming statistical stationarity. A matrix containing these six second-order moments $\langle u_i' u_j' \rangle$ is known as the Reynolds stress tensor, which is frequently used to describe atmospheric flow. The along-wind variance is widely used in wind energy as it is part of the definition of the turbulence intensity, which is an important turbulence parameter for turbine structural loads [5]. The momentum fluxes (i.e., two covariances $\langle u'w' \rangle$ and $\langle v'w' \rangle$) are used to calculate the friction velocity, which is closely connected to the vertical wind profile [6; 7]. The turbulence kinetic energy, i.e., half

the sum of the variances of the three velocity components, is a key parameter for studying wind turbine wake structure [8]. The Reynolds stresses are also useful for evaluating the three-dimensional turbulence models for e.g., load simulations.

Compared to turbulence estimates from sonic anemometers, lidar-derived turbulence characteristics can be biased due to the lidar scanning patterns, the spatial and temporal resolutions intrinsic to the lidar systems and the characteristics of atmospheric turbulence. [1; 9] studied the application of lidar measurements from different scanning patterns for load validation. [10] optimized the scanning trajectory of nacelle lidars based on a coherence model for the rotor-effective wind speed for control applications. Only a few works have investigated the influence of lidar scanning pattern on turbulence characterization. [11] proposed an optimized six-beam configuration using an objective function for a ground-based lidar to minimize the sum of the random errors of the Reynolds stresses. [12] showed that turbulence estimates from ground-based lidars can be improved by using the variance from the vertical beam.

Here, we compare the estimates of the Reynolds stress tensor from nacelle lidars with different scanning patterns through numerical simulations. The Reynolds stresses are computed via a least-square procedure that uses radial velocity variances for each of the lidars' beams without the need to reconstruct the wind components. We summarize how the number of beams, the half-cone opening angle and focus distance influence the accuracy and the uncertainty of turbulence estimates. This work provides guidance on designing and utilizing nacelle lidars for inflow turbulence characterization.

This paper is organized as follows. Section 2 describes the simulated turbulence wind fields and the methodology to estimate the Reynolds stresses. Section 3 provides information on the simulated lidar scanning patterns and the simulation setup. Section 4 shows the comparison of Reynolds stress estimation between the virtual lidars and sonic anemometer. Conclusion and outlook are given in Section 5.

2. Methodology

2.1. Turbulence wind fields

Assuming homogeneous frozen turbulence [13], the wind fields can be described by a vector field $\boldsymbol{u}(\boldsymbol{x}) = (u, v, w)$, where u is the horizontal along-wind component, v the horizontal lateral component, w the vertical component, and $\boldsymbol{x} = (x, y, z)$ the position vector defined in a right-handed coordinate system. The mean value of the homogeneous velocity field is $\langle \boldsymbol{u}(\boldsymbol{x}) \rangle = (U, 0, 0)$, so the coordinate x is in the mean wind direction. We simulate lidar measurements on the nacelle of a wind turbine with a rotor diameter (D) of 52 m using 100 randomly generated turbulence fields described by the Mann model [14; 15]. The wind fields have typical values of the model parameters: $\alpha\varepsilon^{2/3} = 0.05$ m$^{4/3}$ s^{-1}, which is related to the turbulent energy dissipation rate; $L = 61$ m, which is a turbulent length scale; and $\Gamma = 3.2$, which describes the anisotropy of the turbulence. The turbulence boxes have lengths of 30 min in the along-wind direction assuming a mean wind $U = 10$ m s^{-1}. We add a linear shear $\mathrm{d}U/\mathrm{d}z = 0.0288$ s^{-1} to the u components in each box. The lengths are 128 m both in the vertical and lateral directions. The number of grid points in the three directions are $(N_x, N_y, N_z) = (8192, 64, 64)$. Sonic anemometer statistics are taken at the location of the turbine rotor (i.e., center of the turbulence boxes) as the reference for evaluation of the lidar-derived turbulence characteristics.

2.2. Estimation of the Reynolds stresses

The Reynolds stress tensor $R_{ij}(\boldsymbol{x}) \equiv \langle u_i' u_j' \rangle$, where u_i are the fluctuations around the mean, contains the variances $\sigma^2_{u,v,w}$ and the covariances of the velocity components:

$$\boldsymbol{R} = \begin{bmatrix} \sigma_u^2 & \langle u'v' \rangle & \langle u'w' \rangle \\ \langle v'u' \rangle & \sigma_v^2 & \langle v'w' \rangle \\ \langle w'u' \rangle & \langle w'v' \rangle & \sigma_w^2 \end{bmatrix}. \tag{1}$$

The unit vector $\boldsymbol{n}$ describing the beam orientation of a nacelle lidar can be expressed as [4]:

$$\boldsymbol{n}(\phi, \theta) = (-\cos\phi, \cos\theta \sin\phi, \sin\theta \sin\phi), \tag{2}$$

where θ is the angle between the y axis and $\boldsymbol{n}$ projected onto the y-z plane and ϕ is the angle between the beam and the negative x-axis (the half-cone opening angle). If we assume the lidar probe volume can be negligible and u, v, and w do not change over the scanned area, the radial velocity can be expressed as

$$v_\mathrm{r}(\phi, \theta) = -u\cos\phi + v\cos\theta\sin\phi + w\sin\theta\sin\phi. \tag{3}$$

The radial velocity variance can be derived by taking the variance of Eq. (3), as shown in [16]:

$$\begin{aligned} \sigma^2_{v_\mathrm{r}}(\phi, \theta) = \sigma_u^2\cos^2\phi + \sigma_v^2\cos^2\theta\sin^2\phi + \sigma_w^2\sin^2\theta\sin^2\phi - 2\langle u'v' \rangle\cos\phi\cos\theta\sin\phi \\ - 2\langle u'w' \rangle\cos\phi\sin\theta\sin\phi + 2\langle v'w' \rangle\sin^2\phi\cos\theta\sin\theta. \end{aligned} \tag{4}$$

To compute the Reynolds stress tensor $\boldsymbol{R}$, we use the simulated lidar radial velocity variance from all beams over the scanning pattern. Assuming statistical homogeneity, we apply a least-square fit to all radial velocity variances $\sigma^2_{v_\mathrm{r}}$ and the beam unit vectors $\boldsymbol{n}$:

$$\Delta^2 = \int (\boldsymbol{n} \cdot \boldsymbol{R}\boldsymbol{n} - \sigma^2_{v_\mathrm{r}})^2 \mathrm{d}\mu. \tag{5}$$

The matrix $\boldsymbol{R}_{ij}$ that minimizes the integral must fulfill

$$\frac{\partial \Delta^2}{\partial R_{ij}} = 0 \Rightarrow \int (\boldsymbol{n} \cdot \boldsymbol{R}\boldsymbol{n} - \sigma^2_{v_\mathrm{r}}) n_i n_j \mathrm{d}\mu = 0. \tag{6}$$

This can be written as

$$R_{kl} \int n_k n_l n_i n_j \mathrm{d}\mu = \int \sigma^2_{v_\mathrm{r}} n_i n_j \mathrm{d}\mu, \tag{7}$$

where (k, l) and (i, j) go through the six combinations of indices. More details are given in [17].

Equation (7) implies that we need at least six radial velocity variances from different beam directions to compute the six Reynolds stresses. If the nacelle lidar has fewer than six beams, only σ_u^2 (R_{uu}) can be determined well and the stresses involving the lateral component will be more noisy [18]. For lidars that have fewer than six beams, we use another two ways to retrieve only σ_u^2 from the simulated measurements under different assumptions. The first is to correct all radial velocity variances $\sigma^2_{v_\mathrm{r}}$ with a factor of $\cos^2\phi$, which is the same as solving Eq. (4) assuming that all Reynolds stresses apart from σ_u^2 are zero (denoted as 'σ_u^2-LSP' method). The second is to assume that turbulence is isotropic, which gives σ_u^2 as the mean of all $\sigma^2_{v_\mathrm{r}}$ (denoted as 'σ_u^2-isotropy' method).

3. Lidar scanning patterns

Figure 1 shows the considered lidar scanning patterns. The SpinnerLidar (SL in short) scans in a rosette-curve pattern and generates 400 radial velocities in one full scan. In practice, the SpinnerLidar streams out radial velocities at a rate of 200 Hz so it takes 2 s to finish one full scan. It has half-cone opening angles between $0-30^\circ$ and measures with a focus distance $f_d = 52$ m ($1D$) in front of the rotor. Other lidars have $\phi = 15^\circ$ and measure further away (at the focus distance of 98 m) to cover the whole rotor plane. Furthermore, we simulate all considered lidars with multiple measurement planes at $f_d = 49, 72, 98, 121$ and 142 m. We use the simulated radial velocity variances at all measurement levels to compute the turbulence statistics. Figure 2 illustrates the scanning trajectories of the 4-beam and 50-beam lidars with multiple planes as examples. To investigate the influences of the lidar opening angle and the focus distance on turbulence estimation, we simulate the 6-beam configuration [11] with a fixed focus distance of 52 m and increasing opening angles (Fig. 3(a)), and a fixed opening angle of 15° and increasing focus distances (Fig. 3(b)). We neglect the lidar probe volume and assume that the lidar can measure at a point in the simulation.

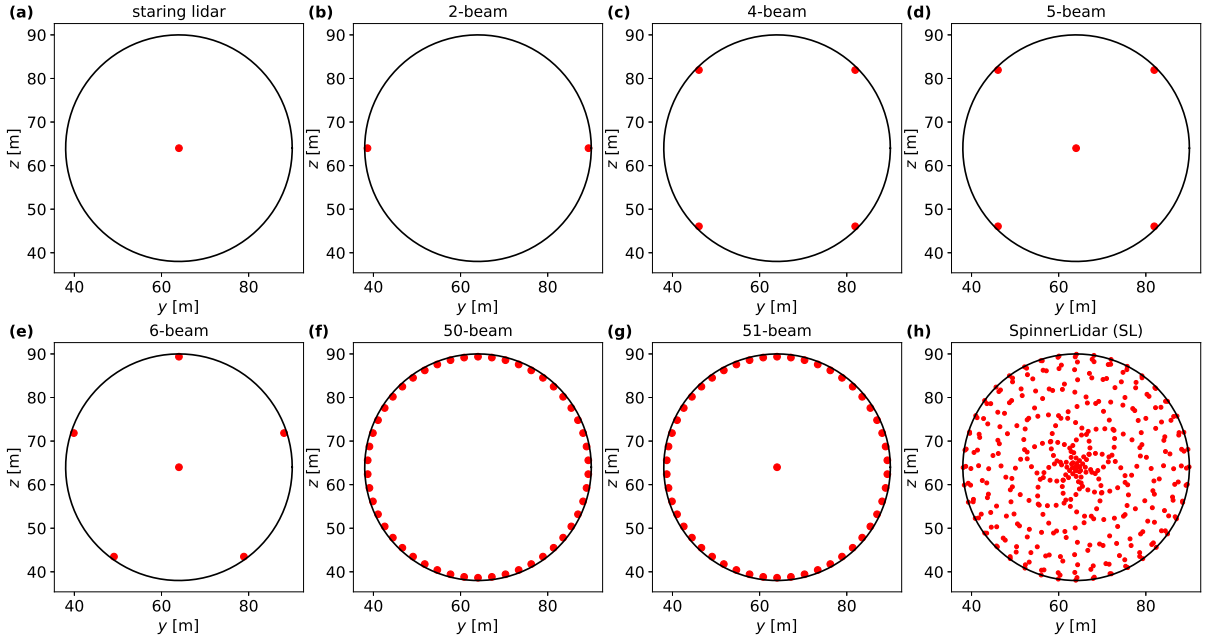

Figure 1: Scanning patterns of the simulated lidars. The SpinnerLidar (h) has $\phi = 0 - 30^\circ$ and scans at $f_d = 52$ m, while other lidars (a-g) have $\phi = 15^\circ$ and scan at $f_d = 98$ m to cover the whole rotor plane. Red dots represent the lidar beam scanning locations. The wind turbine rotor is indicated in a black circle.

4. Results

We compare the six Reynolds stresses computed from the simulated measurements of lidars, which have more than six beams and measure with a single plane, with those from a sonic anemometer at hub height, as shown in Fig. 4. The SpinnerLidar gives the best estimation for all six components, which is closely related to the maximum ϕ of the lidar. The 6-beam and 51-beam lidar provide very similar results, with larger errors and higher uncertainties than the SpinnerLidar. However, the 50-beam configuration cannot estimate the v- and w-variances accurately. This is because the least-squares problem can lead to infinite solutions if we have

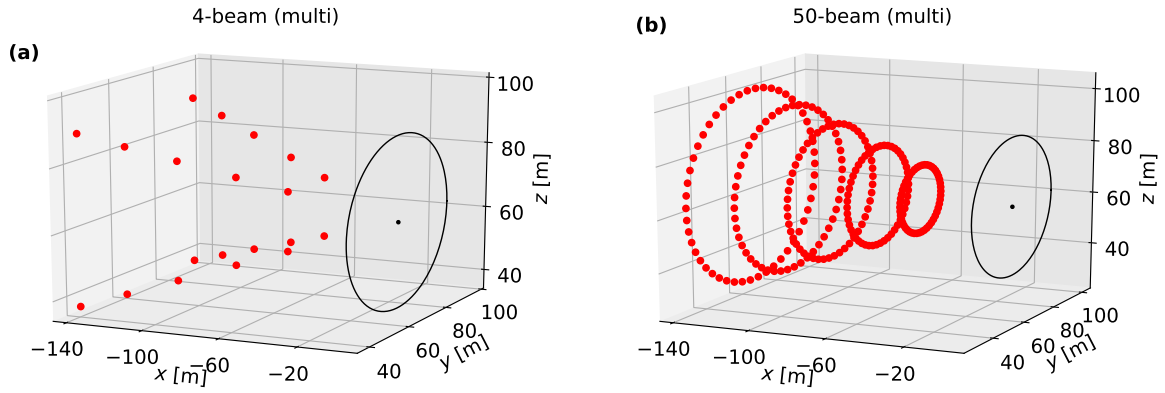

Figure 2: Scanning trajectories of the 4-beam and the 50-beam lidars with multiple measurement planes at $f_d = 49, 72, 98, 121$ and 142 m. Red dots represent the lidar beam scanning locations. The wind turbine rotor is indicated in a black circle. The turbine nacelle is marked in a black dot on the rotor plane.

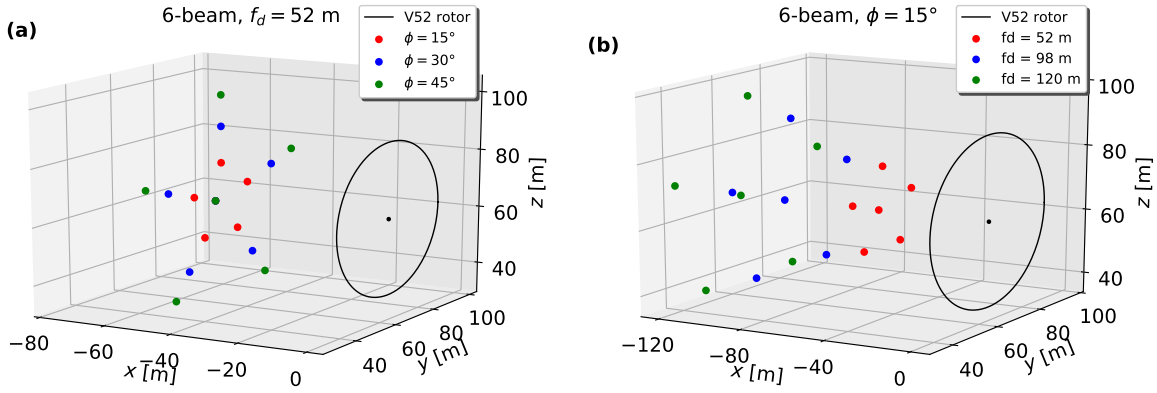

Figure 3: Scanning patterns of the 6-beam lidar with (a) a fixed focus distance and various half-cone opening angles, and (b) a fixed half-cone opening angle and various focus distances. The wind turbine rotor is indicated in a black circle. The turbine nacelle is marked in a black dot on the rotor plane.

only one ϕ value. Comparing the results from 50-beam and 51-beam lidar, we can see that adding one central beam is very beneficial for measuring all variances.

We show the performances of 50-beam and 51-beam lidar with multiple measurement planes on the Reynolds stresses estimation in Fig. 5, where the estimates using a single plane (marked in green and blue) are the same as those in Fig. 4. The comparison shows that if the measurements at a single plane are not sufficient to retrieve all Reynolds stresses, measuring at multiple planes with the same beam configuration does not help in the turbulence reconstruction. Results from the 51-beam lidar suggest that using multiple measurement planes does not improve the results much in our simulations; it only reduces slightly the uncertainty of the estimations.

Figure 6 shows the four Reynolds stresses retrieved from the 4-beam and 5-beam lidars assuming that the $\langle u'v' \rangle$ and $\langle v'w' \rangle$ covariances are negligible in Eq. (7). The Reynolds stress estimates are very noisy so that some of them are out of the limit of the axis. In all cases, the determinants of the matrix that results when expanding Eq. (7) are close to zero, which

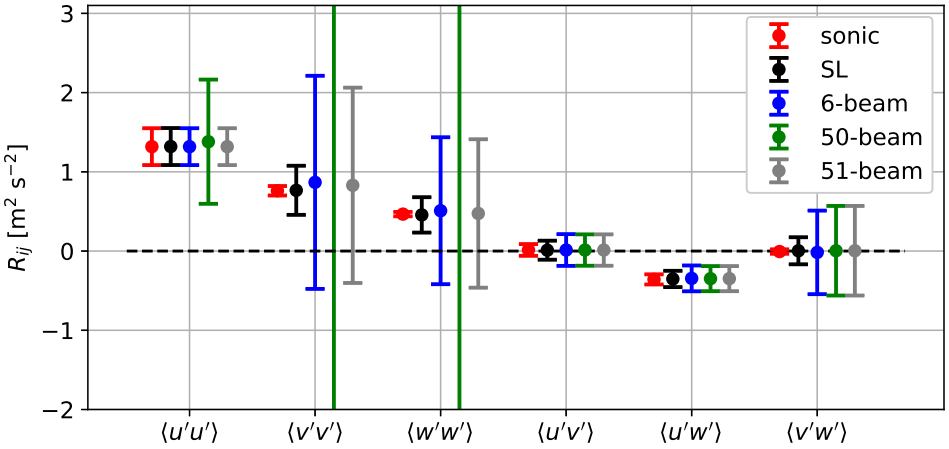

Figure 4: Reynolds stresses derived from the virtual sonic anemometer and lidars, which have more than six beams and measure at a single distance, from 100 simulated wind fields. The markers are the means and the error bars are ± one standard deviation.

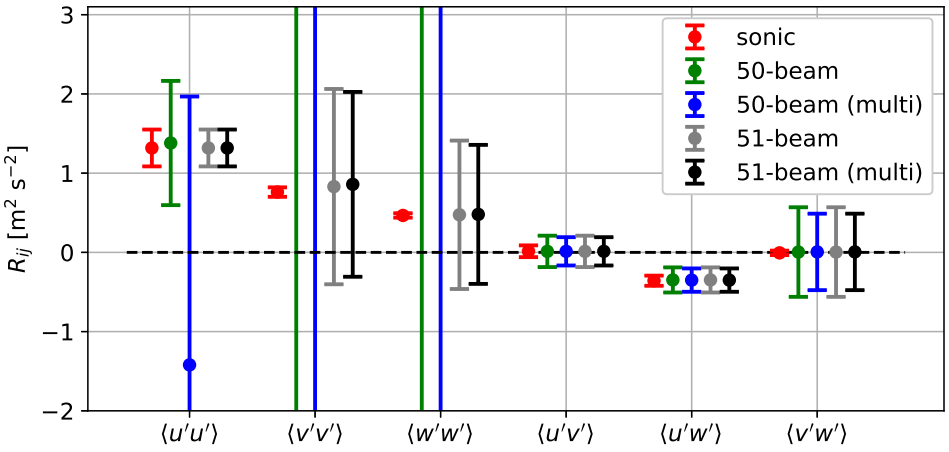

Figure 5: Reynolds stresses derived from the virtual sonic anemometer, the 50-beam and 51-beam lidars measuring at a single plane and at multiple planes from 100 simulated wind fields. The markers are the means and the error bars are ± one standard deviation.

indicates that the four Reynolds stresses cannot be estimated accurately using the least-square procedure with the 4-beam and 5-beam configurations. Again, the comparison suggests that using multiple measurement planes does not improve the results much in our simulations.

In Fig. 7, we analyze how the accuracy and the uncertainty of the Reynolds stresses estimation change when increasing ϕ and f_d of the 6-beam lidar. We compare them with those from the sonic anemometer and the SpinnerLidar. Both the error and the uncertainty decrease as the opening angle increases. Specifically, for $\phi = 45°$, the six-beams configuration provides lower uncertainty than the SpinnerLidar despite having much fewer beams. Increasing the focus distance has an opposite effect as increasing the beams' opening angles due to the random error on the variances of the radial velocity. The radial velocity variances of the beams are less correlated when the lidar scans over a larger area. We performed the same analysis with the 51-beam lidar and observed the same trends (not shown here).

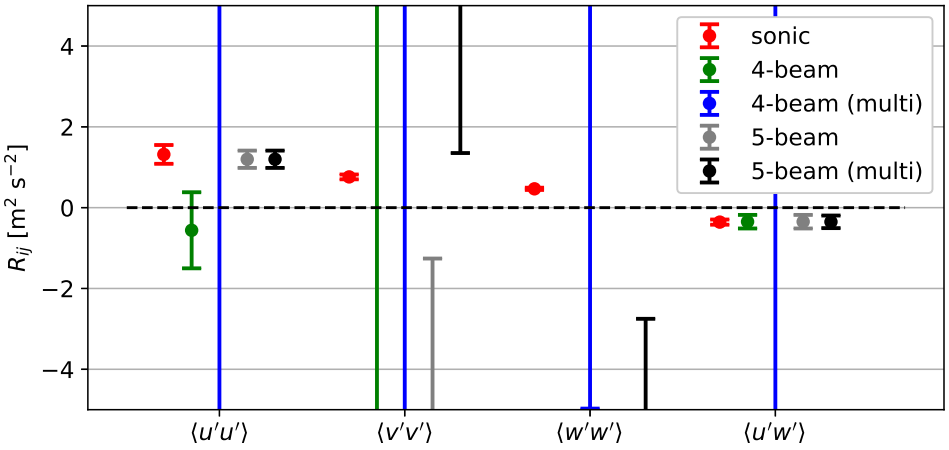

Figure 6: Reynolds stresses derived from the virtual sonic anemometer, the 4-beam and 5-beam lidars measuring at a single plane and at multiple planes from 100 simulated wind fields. The markers are the means and the error bars are ± one standard deviation.

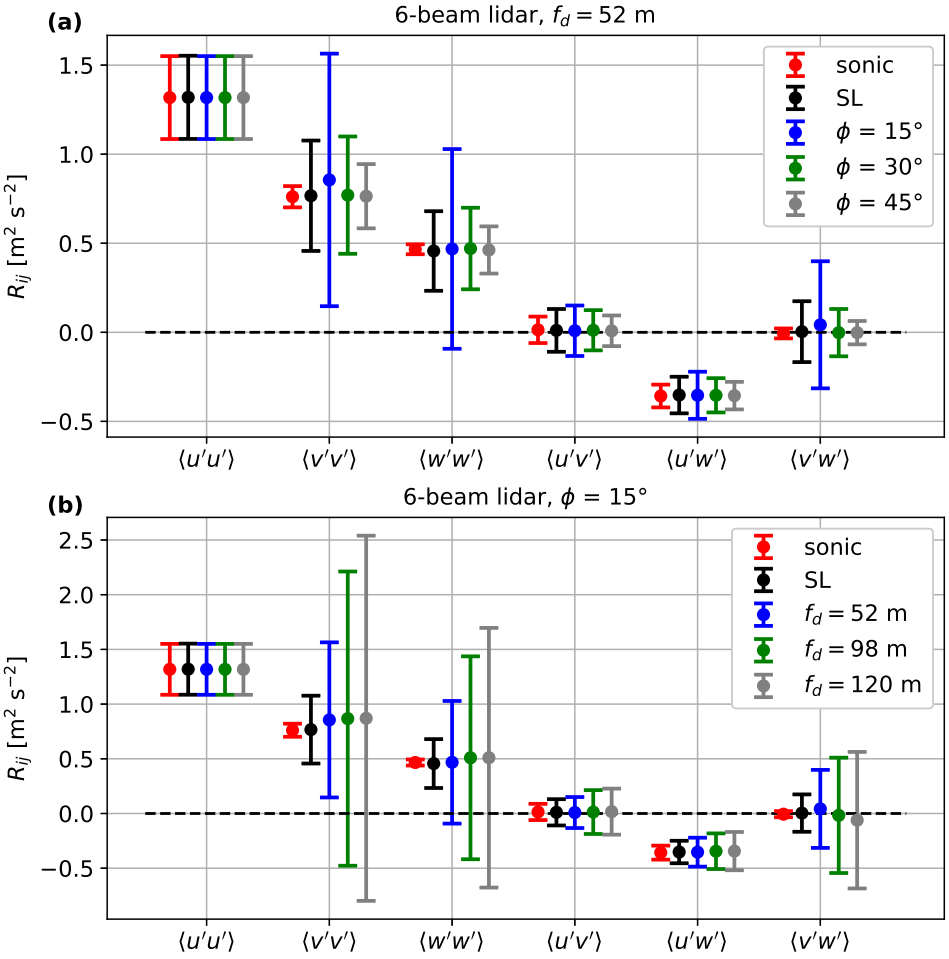

Figure 7: Influence of increasing opening angle ϕ and focus distance f_d on the Reynolds stresses estimation for the virtual sonic anemometer, the SpinnerLidar, and all 6-beam lidar configurations from 100 simulated wind fields.

We also simulate the nacelle lidars with all considered scanning patterns at the five measurement planes mentioned above, and retrieve the along-wind variance using the 'σ_u^2-LSP' and 'σ_u^2-isotropy' methods, respectively. The results are shown in Fig. 8. Table 1 summarizes the relative errors of the lidar-derived estimates compared to the one from the sonic anemometer. The results in first row are computed solving Eq. (7), from which we get perfect estimations of the along-wind variance using lidars with more than six beams. Furthermore, we find as an overall trend that lidar-derived σ_u^2 are overestimated using the 'LSP' method, when compared to the estimate from the sonic anemometer, while they are slightly underestimated using the 'isotropy' method. The biases are in general smaller when σ_u^2 are computed using the 'isotropy' method. Overall, all simulated lidars are able to estimate σ_u^2 well, despite of their different number of beams. The staring lidar acts like a sonic anemometer in our simulation and achieves zero relative error since no probe volume is considered and the beam is perfectly aligned with the along-wind component.

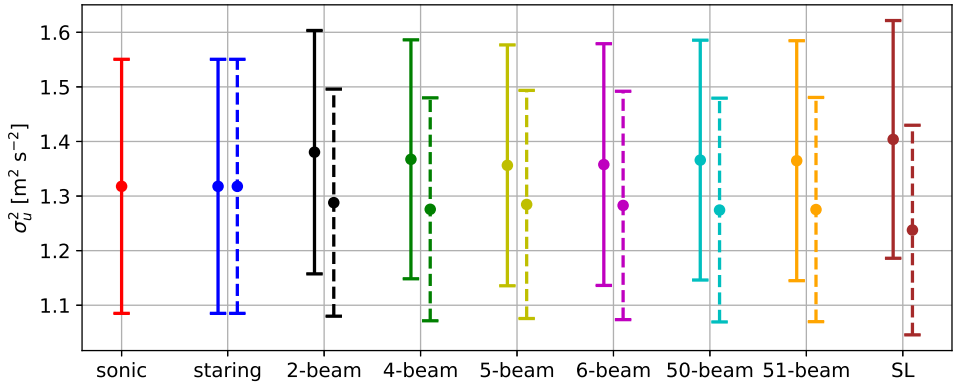

Figure 8: The along-wind variance derived from simulated lidars using the 'σ_u^2-LSP' method (in solid lines) and 'σ_u^2-isotropy' method (in dashed lines). All lidars measure at multiple planes.

Table 1: Relative error of the mean value of the lidar-derived along-wind variance using 100 simulated wind fields, when compared to the one from the sonic anemometer. All lidars measure at multiple planes. Negative values indicate that the along-wind variance is underestimated.

	staring	2-beam	4-beam	5-beam	6-beam	50-beam	51-beam	SL
$\langle u'u' \rangle$ [%]	—	—	—	—	0.00	—	0.00	0.17
σ_u^2-LSP [%]	0	4.75	3.76	2.92	3.03	3.65	3.56	6.53
σ_u^2-isotropy [%]	0	-2.27	-3.91	-2.52	-2.66	-3.30	-3.23	-6.07

5. Conclusion and Outlook

Our results show that at least six beams, including one beam with a different opening angle, are needed to estimate all the six Reynolds stresses accurately. The accuracy and uncertainty in turbulence characterization are better improved by enlarging the opening angle than by increasing the number of beams. Enlarging the measurement area of the nacelle lidars with the same beam orientation reduces the accuracy and increases the uncertainty. Compared to the point-wise sonic anemometer, all considered lidars can estimate the along-wind variance with

a relative error lower than 7%. All in all, the lidar with a 6-beam configuration and a large opening angle gives the best estimates of all Reynolds stresses.

This study should be extended by modelling the lidar probe volume in the simulation, which can cause turbulence attenuation. For continuous-wave lidar, the focus distance is closely related to the impact of the probe volume. Further studies on the lidar scanning pattern should also consider the inhomogeneity of the inflow. Modern wind turbines are often operating inside a wind farm or have large vertical span among the rotor area. Under those conditions, the turbulence homogeneity assumption is violated. Therefore, there is a need to investigate the scanning strategy for characterizing inhomogeneous inflows.

Acknowledgement
This study is funded by the European Union's Horizon 2020 research and innovation program under the Marie Sklodowska-Curie grant agreement No. 858358 (LIKE – Lidar Knowledge Europe, H2020-MSCA-ITN-2019).

References

[1] Conti D, Pettas V, Dimitrov N and Peña A 2021 *Wind Energy Science* **6** 841–866
[2] Wagner R, Courtney M, Pedersen T F and Davoust S 2015 *Wind Energy* **19** 1269–1287
[3] Schlipf D, Guo F and Raach S 2020 *Journal of Physics: Conference Series* **1618** 032053
[4] Peña A, Mann J and Dimitrov N 2017 *Wind Energy Science* **2** 133–152
[5] IEC 2019 IEC 61400-1. Wind turbines – Part 1: Design guidelines International standard International Electrotechnical Commission Geneva, Switzerland
[6] Wyngaard J 2010 *Turbulence in the Atmosphere* (Cambridge University Press) ISBN 9781139485524
[7] Peña A, Floors R, Sathe A, Gryning S E, Wagner R, Courtney M S, Larsén X G, Hahmann A N and Hasager C B 2016 *Boundary-Layer Meteorology* **158** 1–26
[8] Kumer V M, Reuder J, Dorninger M, Zauner R and Grubišić V 2016 *Renewable Energy* **99** 898–910
[9] Dimitrov N and Natarajan A 2017 *Wind Energy* **20** 79–95
[10] Schlipf D, Fürst H, Raach S and Haizmann F 2018 *Journal of Physics: Conference Series* **1102** 012014
[11] Sathe A, Mann J, Vasiljevic N and Lea G 2015 *Atmospheric Measurement Techniques* **8** 729–740
[12] Newman J F, Klein P M, Wharton S, Sathe A, Bonin T A, Chilson P B and Muschinski A 2016 *Atmospheric Measurement Techniques* **9** 1993–2013
[13] Taylor G I 1938 *Proceedings of the Royal Society of London. Series A - Mathematical and Physical Sciences* **164** 476–490
[14] Mann J 1994 *Journal of Fluid Mechanics* **273** 141–168
[15] Mann J 1998 *Probabilistic Engineering Mechanics* **13** 269–282
[16] Eberhard W L, Cupp R E and Healy K R 1989 *Journal of Atmospheric and Oceanic Technology* **6** 809–819
[17] Fu W, Peña A and Mann J 2021 *Wind Energy Science Discussions* **2021** 1–29 URL `https://wes.copernicus.org/preprints/wes-2021-149/`
[18] Peña A, Mann J and Thorsen G 2019 Spinnerlidar measurements for the ccav52 Tech. Rep. DTU Wind Energy E Vol. 0177 DTU Wind Energy

Paper IV: Dependence of turbulence estimations on nacelle-lidar scanning strategies

Dependence of turbulence estimations on nacelle-lidar scanning strategies

Wei Fu, Alessandro Sebastiani, Alfredo Peña, and Jakob Mann
Department of Wind and Energy Systems, Technical University of Denmark, Frederiksborgvej 399, 4000 Roskilde, Denmark
Correspondence: Wei Fu (weif@dtu.dk)

Abstract. Through numerical simulations and the analysis of field measurements, we investigate the dependence of the accuracy and uncertainty of turbulence estimations on the main features of the nacelle lidars' scanning strategy, i.e., the number of measurement points, the half-cone opening angle, the focus distance and the type of the lidar system. We assume homogeneous turbulence over the lidar scanning area in front of a Vestas V52 wind turbine. The Reynolds stresses are computed via a least-squares procedure that uses the radial velocity variances of each lidar beam without the need to reconstruct the wind components. The lidar-retrieved Reynolds stresses are compared with those from a sonic anemometer at turbine hub height. Our findings from the analysis of both simulations and measurements demonstrate that to estimate the six Reynolds stresses accurately, a nacelle lidar system with at least six beams is required. Further, one of the beams of this system should have a different opening angle. Adding one central beam improves the estimations of the velocity components' variances. Assuming the relations of the velocity components' variances as suggested in the IEC standard, all considered lidars can estimate the along-wind variance accurately using the least-squares procedure and the Doppler radial velocity spectra. Increasing the opening angle increases the accuracy and reduces the uncertainty on the transverse components, while enlarging the measurement distance has opposite effects. All in all, a 6-beam continuous-wave lidar measuring at a close distance with a large opening angle provides the best estimations of all Reynolds stresses. This work gives insights on designing and utilizing nacelle lidars for inflow turbulence characterization.

1 Introduction

Inflow turbulence characteristics are important for wind turbine load validation (Conti et al., 2021), power performance assessment (Gottschall and Peinke, 2008; Wagner et al., 2014) and wind turbine control (Dong et al., 2021). The traditional way to measure inflow turbulence uses the in-situ anemometers installed on meteorological masts, such as cup and sonic anemometers. However, rotor planes of the modern wind turbines have large vertical span that can reach 250 m above the ground. It is more and more costly to install a meteorological mast that reaches the height of the blade tips, especially under offshore conditions. Recently, nacelle lidars of different types and configurations have been used to scan the inflow (Harris et al., 2006; Mikkelsen et al., 2013; Wagner et al., 2015; Peña et al., 2017; Fu et al., 2022a). Compared to the point-wise, mast-mounted anemometers, forward-looking nacelle lidars yaw with the wind turbine and measure at different points in front of the rotor, which can potentially better characterize the inflow that actually interacts with the wind turbine.

Assuming statistical stationarity, turbulence can be represented by the variances and covariances of the wind field components u, v and w (u_1, u_2, u_3) averaged typically over 10 or 30 min. The homogeneous velocity field can be decomposed into the mean U_i and the fluctuating part u_i'. The Reynolds stress tensor, a matrix containing the six second-order moments $\langle u_i' u_j' \rangle$, describes the variability of the atmospheric flow in some detail. The terms in the Reynolds stress tensor are frequently used in wind energy and meteorology. The square root of the along-wind variance is a part of the definition in the turbulence intensity, which is a key turbulence parameter for the structural loads assessment and the design of wind turbines (IEC, 2019). However, this is not the only component that is important for loads (Petersen et al., 1994). The two covariances $\langle u'w' \rangle$ and $\langle v'w' \rangle$ form the momentum fluxes, which are used to calculate the friction velocity and are closely connected to the vertical wind profile (Wyngaard, 2010; Peña et al., 2016). The half the sum of the variances of the three velocity components is the turbulence kinetic energy, which is an important parameter for investigating wind turbine wake structures (Kumer et al., 2016). Also, the Reynolds stresses are needed to determine the parameters of the three-dimensional turbulence models for, e.g., load simulations (Mann, 1994).

Compared to turbulence estimates from traditional anemometry, the accuracy and the uncertainty of lidar-derived turbulence characteristics can be affected by not only the spatial and temporal resolutions intrinsic to the lidar systems and the characteristics of atmospheric turbulence but also the lidar scanning strategies (Sathe et al., 2011; Smalikho and Banakh, 2017). Dimitrov and Natarajan (2017) and Conti et al. (2021) applied lidar measurements using different scanning strategies for load validation. Schlipf et al. (2018) optimized the scanning trajectory of nacelle lidars based on a coherence model for the rotor-effective wind speed to improve control performance. Only a few works investigated the dependence of turbulence estimations on lidar scanning strategies. Sathe et al. (2015) explained that at least six radial velocity variances are needed to compute all six Reynolds stresses, and proposed for a ground-based lidar an optimized six-beam configuration using an objective function which minimizes the sum of the random errors of the Reynolds stresses. Newman et al. (2016) showed that using the variance from the vertical beam improves the turbulence estimates from ground-based lidars. Fu et al. (2022a) investigated the benefit of using multiple-beam nacelle lidars by comparing the accuracy of turbulence estimations from a SpinnerLidar (a lidar measuring the inflow at 400 positions) with two- and four-beam lidars.

Lidars measure the radial velocity (also known as the line-of-sight velocity) along the laser beam. Sathe and Mann (2013) and Fu et al. (2022a) showed that the variance along a single beam can be higher or lower than the u-variance measured by sonic anemometers depending on the beam orientation. This is due to the correlation between different velocity components, which can be described in the three-dimensional spectral velocity tensor model by Mann (1994) (hereafter Mann model). We need to assume homogeneity when combining the radial velocity variances along different laser beam directions to reconstruct the Reynolds stresses. Compared to the in-situ anemometers, the lidar's measurement volume is generally larger, which leads to turbulence attenuation.

There are two main types of nacelle lidar systems, namely continuous-wave (CW) and pulsed. They mainly differ on the working principle and the way they probe the atmosphere within their measurement volume. The probe volume of a CW system increases with the square of the focus distance, while the one of a pulsed system remains constant with measurement range (Peña et al., 2015). The 'unfiltered' radial velocity variances (in which the volume-averaging effect is compensated) can be

retrieved from the Doppler radial velocity spectra, which are normally available in CW systems (Mann et al., 2010; Branlard et al., 2013).

This work investigates the dependence of the accuracy and the uncertainty of the turbulence estimations on the main features of the nacelle lidars' scanning strategy, i.e., the number of measurement positions within a full scan, the half-cone opening angle, the focus distance and the type of the lidar system. We select eight scanning patterns, which are commonly known or widely used in the wind energy industry. Homogeneous frozen turbulence is assumed throughout our analysis. The Reynolds stresses are estimated via a least-squares procedure using radial velocity variances instead of computing from the reconstructed mean wind velocities. Estimates from a sonic anemometer at turbine hub height are used as reference. Compared to Fu et al. (2022b), here we study the topic using not only numerical simulations with turbulence boxes but also the SpinnerLidar measurements collected at DTU Risø test site. We select measurements at certain beam scanning locations of the SpinnerLidar to imitate lidars with different scanning configurations. Another main difference to Fu et al. (2022b) is that we consider the probe volume of both a CW and a pulsed lidar system in our simulations, which plays an important role, especially when studying the influence of the focus distance on the turbulence estimation.

This paper is organized as follows. Section 2 introduces the turbulence spectral model and the modeling of nacelle lidars. Section 3 describes how the unfiltered radial velocity variance and the Reynolds stresses are estimated. It also gives details about the setup of the numerical simulations, the considered lidar scanning strategies and the field experiment. Section 4 compares the Reynolds stress estimations between the lidars and the sonic anemometer at turbine hub height from both numerical simulations and measurements. Discussions are given in Section 5. Section 6 concludes the work and provides the outlook.

2 Theoretical background

2.1 Turbulence spectral model

Assuming Taylor's frozen turbulence (Taylor, 1938), the wind field can be described by $\boldsymbol{u}(\boldsymbol{x}) = (u, v, w)$, where $\boldsymbol{x} = (x, y, z)$ is the position vector defined in a right-handed coordinate system, u the horizontal along-wind component, v the horizontal lateral component, and w the vertical component. The homogeneous wind field $\boldsymbol{u}(\boldsymbol{x})$ can be decomposed into the mean value $\langle \boldsymbol{u}(\boldsymbol{x}) \rangle = (U, 0, 0)$, where $\langle\ \rangle$ denotes ensemble averaging, and the fluctuating part $\boldsymbol{u'}(\boldsymbol{x}) = (u', v', w')$. U is the mean wind velocity along the x-direction. The one-dimensional single point (co-)spectra of any component of the wind field are given as (Mann, 1994)

$$F_{ij}(k_1) = \frac{1}{(2\pi)} \int_{-\infty}^{\infty} R_{ij}(x_1, 0, 0) \exp(-ik_1 \cdot x_1) \mathrm{d}x_1, \tag{1}$$

where k_1 is the first component of the wave vector $\boldsymbol{k}$, $R_{ij}(\boldsymbol{r}) \equiv \langle u_i'(\boldsymbol{x}) u_j'(\boldsymbol{x} + \boldsymbol{r}) \rangle$ is the Reynolds stress tensor, $\boldsymbol{r}$ is the separation vector, and u_i' are the fluctuations around the mean of the wind field. The wave number can, via Taylor's hypothesis, be related to the frequency f through $k_1 = 2\pi f / U$. The auto-spectra of the three wind components $F_{u,v,w}$ ($= F_{11,22,33}$) can

be evaluated using Eq. (1). The velocity components' variances are

$$\sigma^2_{u,v,w} = \int_{-\infty}^{\infty} F_{u,v,w}(k_1)\mathrm{d}k_1. \tag{2}$$

We assume that the Mann model well describes the spatial structure of the turbulent flow. Besides k_1 and the other two components of the wave vector $\boldsymbol{k}$, the Mann model contains three parameters: $\alpha\varepsilon^{2/3}$, which is related to the turbulent energy dissipation rate, L to a turbulence length scale, and Γ to the anisotropy of turbulence. This model is chosen because it describes the correlations between different velocity components, which play an important role in deriving turbulence statistics from measurements of multiple-beam lidars pointing at different directions.

2.2 Nacelle lidar and modeling of the probe volume

The unit vector $\boldsymbol{n}$ describes the beam orientation of a nacelle lidar, which can be expressed as (Peña et al., 2017):

$$\boldsymbol{n}(\phi,\theta) = (-\cos\phi, \cos\theta\sin\phi, \sin\theta\sin\phi), \tag{3}$$

where θ is the angle between the y axis and $\boldsymbol{n}$ projected onto the y-z plane and ϕ the angle between the beam and the negative x-axis (also known as the half-cone opening angle), as shown in Fig.1.

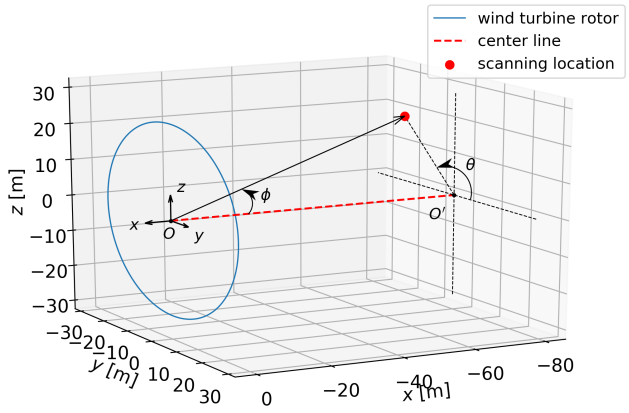

Figure 1. Definition of the coordinate system and beam angles for nacelle lidar modeling.

The radial velocity of a lidar can be written as the convolution of the weighting function φ and the radial velocity sampled along the beam in the probe volume (Mann et al., 2010):

$$v_\mathrm{r}(\phi,\theta) = \int_{-\infty}^{\infty} \varphi(s)\boldsymbol{n}(\phi,\theta)\cdot\boldsymbol{u}[\boldsymbol{n}(\phi,\theta)(f_d+s)]\mathrm{d}s, \tag{4}$$

where s is the distance from the focus point along the beam and f_d the focus or measurement distance. The relation assumes that the velocity is determined from the Doppler spectrum as the center of gravity, see Held and Mann (2018). We use the following weighting functions to approximate the probe volume of different types of lidar:

- CW lidar (Sonnenschein and Horrigan, 1971):

$$\varphi(s) = \frac{1}{\pi} \frac{z_\mathrm{R}}{z_\mathrm{R}^2 + s^2} \quad \text{with } z_\mathrm{R} = \frac{\lambda f_d^2}{\pi r_\mathrm{b}^2}, \tag{5}$$

  where z_R is the Rayleigh length, λ the laser wavelength and r_b the beam radius at the output lens.

- pulsed lidar (Meyer Forsting et al., 2017):

$$\varphi(s) = \frac{1}{2\Delta p} \left\{ \mathrm{Erf}\left[\frac{s + \Delta p/2}{r_p} \right] - \mathrm{Erf}\left[\frac{s - \Delta p/2}{r_p} \right] \right\}$$

$$\text{with the error function } \mathrm{Erf}(x) = \frac{2}{\sqrt{\pi}} \int_0^x \exp(-t^2)\mathrm{d}t \quad \text{and} \quad r_p = \frac{\Delta l}{2\sqrt{\ln(2)}}, \tag{6}$$

  where Δp is the range-gate length and Δl the Gaussian lidar pulse Full Width at Half Maximum (FWHM).

Variances calculated from the centroid-derived radial velocities are attenuated by the lidar probe volume, which acts like a low-pass filter to the wind velocity fluctuations. Therefore, we refer to them as the 'filtered' radial velocity variances. If we assume that the lidar probe volume can be negligible and that u, v, and w are constant over the scanned area, the radial velocity can be expressed as

$$v_\mathrm{r}(\phi, \theta) = -u\cos\phi + v\cos\theta\sin\phi + w\sin\theta\sin\phi. \tag{7}$$

The 'unfiltered' radial velocity variance can be derived by taking the variance of Eq. (7), as shown in Eberhard et al. (1989):

$$\begin{aligned}\sigma^2_{v_\mathrm{r},\mathrm{unf}}(\phi, \theta) = {} & \sigma_u^2 \cos^2\phi + \sigma_v^2 \cos^2\theta \sin^2\phi + \sigma_w^2 \sin^2\theta \sin^2\phi - 2\langle u'v' \rangle \cos\phi\cos\theta\sin\phi \\ & - 2\langle u'w' \rangle \cos\phi\sin\theta\sin\phi + 2\langle v'w' \rangle \sin^2\phi\cos\theta\sin\theta.\end{aligned} \tag{8}$$

3 Methodology

3.1 Estimation of the unfiltered radial velocity variance

In practice, the unfiltered radial velocity variance $\sigma^2_{v_\mathrm{r},\mathrm{unf}}$ in Eq. (8) can be estimated from the Doppler radial velocity spectrum. When the nacelle lidar measures at a small opening angle over a relatively homogeneous inflow and the wind shear is not very strong, the effect of radial velocity gradient within the lidar probe volume can be negligible (see Mann et al., 2010, for a detailed discussion). In this case, one can estimate $\sigma^2_{v_\mathrm{r},\mathrm{unf}}$ as the second central statistical moment of the ensemble-averaged Doppler spectrum of the radial velocity within typically a 10- or 30-min period. Each Doppler spectrum is area-normalized

before computing the ensemble-averaged Doppler spectrum $p(v_\mathrm{r})$. The mean radial velocity can be estimated as

$$\mu_{v_\mathrm{r}} = \int_{-\infty}^{\infty} v_\mathrm{r} p(v_\mathrm{r}) \mathrm{d}v_\mathrm{r}, \tag{9}$$

and its variance as

$$\sigma^2_{v_\mathrm{r}} = \int_{-\infty}^{\infty} (v_\mathrm{r} - \mu_{v_\mathrm{r}})^2 p(v_\mathrm{r}) \mathrm{d}v_\mathrm{r}. \tag{10}$$

Assuming that all contributions of the radial velocity to the Doppler spectrum are because of turbulence, $\sigma^2_{v_\mathrm{r}}$ in Eq. (10) provides an estimate of $\sigma^2_{v_\mathrm{r},\mathrm{unf}}$. This assumption is reasonable when beams are close to horizontal.

3.2 Estimation of the Reynolds stresses

The Reynolds stress tensor $\boldsymbol{R} \equiv \boldsymbol{R}(\boldsymbol{x} = \boldsymbol{0})$ contains the variances and covariances of the velocity components:

$$\boldsymbol{R} = \begin{bmatrix} \sigma_u^2 & \langle u'v' \rangle & \langle u'w' \rangle \\ \langle v'u' \rangle & \sigma_v^2 & \langle v'w' \rangle \\ \langle w'u' \rangle & \langle w'v' \rangle & \sigma_w^2 \end{bmatrix}. \tag{11}$$

To compute $\boldsymbol{R}$, we use the radial velocity variances from all beams over the lidar scanning trajectory. Assuming spatial homogeneity, we apply a least-squares fit to the radial velocity variances $\sigma^2_{v_\mathrm{r}}$. This can be done since the variance in any direction $\boldsymbol{n}$ can be written as $\boldsymbol{n} \cdot \boldsymbol{R}\boldsymbol{n}$ or $n_i R_{ij} n_j$ using the index notation and assuming summation over repeated indices. We then sum the squared differences between the measured radial variances $\sigma^2_{v_\mathrm{r}}$ and $\boldsymbol{n} \cdot \boldsymbol{R}\boldsymbol{n}$ for any given Reynolds stress tensor $\boldsymbol{R}$. In order to avoid too many indices, we express this sum as integral $\int \mathrm{d}\mu$ such that the sum we are going to minimize can be written as

$$\Delta^2 = \int (\boldsymbol{n} \cdot \boldsymbol{R}\boldsymbol{n} - \sigma^2_{v_\mathrm{r}})^2 \mathrm{d}\mu. \tag{12}$$

The matrix R_{ij} that minimizes the integral must fulfill

$$\frac{\partial \Delta^2}{\partial R_{ij}} = 0 \Rightarrow 2 \int (\boldsymbol{n} \cdot \boldsymbol{R}\boldsymbol{n} - \sigma^2_{v_\mathrm{r}}) n_i n_j \mathrm{d}\mu = 0. \tag{13}$$

This can be written as

$$R_{kl} \int n_k n_l n_i n_j \mathrm{d}\mu = \int \sigma^2_{v_\mathrm{r}} n_i n_j \mathrm{d}\mu, \tag{14}$$

where (k,l) and (i,j) are each of the indices combinations $(1,1),(1,2),(1,3),(2,2),(2,3),(3,3)$, $n_1 = -\cos\phi$, $n_2 = \cos\theta \sin\phi$ and $n_3 = \sin\theta \sin\phi$ (as given in Eq. 3), i.e. Fu et al. (2022a),:

$$\begin{bmatrix} \sum n_1^4 & \sum n_1^2 n_2^2 & \sum n_1^2 n_3^2 & \sum 2n_1^3 n_2 & \sum 2n_1^3 n_3 & \sum 2n_1^2 n_2 n_3 \\ \sum n_1^2 n_2^2 & \sum n_2^4 & \sum n_2^2 n_3^2 & \sum 2n_1 n_2^3 & \sum 2n_1 n_2^2 n_3 & \sum 2n_2^3 n_3 \\ \sum n_1^2 n_3^2 & \sum n_2^2 n_3^2 & \sum n_3^4 & \sum 2n_1 n_2 n_3^2 & \sum 2n_1 n_3^3 & \sum 2n_2 n_3^3 \\ \sum n_1^3 n_2 & \sum n_1 n_2^3 & \sum n_1 n_2 n_3^2 & \sum 2n_1^2 n_2^2 & \sum 2n_1^2 n_2 n_3 & \sum 2n_1 n_2^2 n_3 \\ \sum n_1^3 n_3 & \sum n_1 n_2^2 n_3 & \sum n_1 n_3^3 & \sum 2n_1^2 n_2 n_3 & \sum 2n_1^2 n_3^2 & \sum 2n_1 n_2 n_3^2 \\ \sum n_1^2 n_2 n_3 & \sum n_2^3 n_3 & \sum n_2 n_3^3 & \sum 2n_1 n_2^2 n_3 & \sum 2n_1 n_2 n_3^2 & \sum 2n_2^2 n_3^2 \end{bmatrix} \begin{bmatrix} R_{uu} \\ R_{vv} \\ R_{ww} \\ R_{uv} \\ R_{uw} \\ R_{vw} \end{bmatrix} = \begin{bmatrix} \sum n_1^2 \sigma^2_{v_\mathrm{r}} \\ \sum n_2^2 \sigma^2_{v_\mathrm{r}} \\ \sum n_3^2 \sigma^2_{v_\mathrm{r}} \\ \sum n_1 n_2 \sigma^2_{v_\mathrm{r}} \\ \sum n_1 n_3 \sigma^2_{v_\mathrm{r}} \\ \sum n_2 n_3 \sigma^2_{v_\mathrm{r}} \end{bmatrix}. \tag{15}$$

To solve the six Reynolds stresses from Eq. (15), two requirements of the nacelle lidar scanning pattern need to be fulfilled (see Sathe et al., 2015, for a detailed discussion):

- the lidar has at least six beams or measures at six different locations within one full scan;
- the lidar beams have at least two different opening angles.

If a lidar has less than six beams, or the opening angles of all beams are identical and some of the six equations are linearly dependent, we have fewer knowns than unknowns in Eq. (15), which leads to infinite solutions. In those cases, only the along-wind variance σ_u^2 can be estimated well (Peña et al., 2019). To solve σ_u^2 from Eq. (15), assumptions of some Reynolds stresses terms are needed to reduce the number of unknowns. Here, we use three different assumptions, as introduced in Fu et al. (2022a):

- All Reynolds stresses apart from σ_u^2 are zero (denoted as 'LSP-σ_u^2' method). For lidars with only one half-cone opening angle, this means $\sigma_u^2 = \sum \sigma_{v_\mathrm{r}}^2 / \sum \cos^2 \phi$.
- Turbulence is isotropic, i.e., $\sigma_u^2 = \sigma_v^2 = \sigma_w^2$ and that other terms are negligible (denoted as 'LSP-isotropy' method). This method is the same for lidars with only one half-cone opening angle as taking the mean of all radial velocity variances.
- The relations between velocity components' standard deviation $\sigma_v = 0.7\sigma_u$ and $\sigma_w = 0.5\sigma_u$, as recommended in IEC (2019), and all covariances are negligible (denoted as 'LSP-IEC' method).

3.3 Numerical simulations

We simulate lidar measurements on the nacelle of a wind turbine with a rotor diameter (D) of 52 m using 100 randomly generated turbulence boxes. The boxes contain the fluctuations of the three wind components. The turbulence boxes are described by the Mann model with typical values of the model parameters $\alpha\varepsilon^{2/3} = 0.05$ m$^{4/3}$ s^{-1}, $L = 61$ m and $\Gamma = 3.2$. The selected three parameters are adopted from Mann (1994) and characterize a neutral atmospheric stratification on a typical offshore site. The dissipation rate $\alpha\varepsilon^{2/3}$ is a scaling factor on the turbulence intensity. The number of grid points in the three directions are $(N_x, N_y, N_z) = (8192, 64, 64)$. The lengths of the turbulence boxes in the vertical and lateral directions are both 128 m. The boxes have lengths of 30 min in the along-wind direction assuming a mean wind $U = 10$ m s^{-1}. We add a linear shear $\mathrm{d}U/\mathrm{d}z = 0.0288$ s^{-1} on top of the along-wind velocity component u in each box:

$$u = U + \frac{\mathrm{d}U}{\mathrm{d}z}(z - z_\mathrm{rotor}) + u', \tag{16}$$

where z_rotor is the turbine hub height in the turbulence box, i.e., the middle grid point in the z-coordinate.

We simulate eight lidars with different scanning patterns, as shown in Fig. 2. Statistics of the sonic anemometer are taken at the location of the turbine rotor center (which is also the center of the turbulence boxes) as the reference for evaluating the lidar-derived turbulence characteristics. The SpinnerLidar scans in a rosette-curve pattern and has half-cone opening angles in the range $0 - 30°$. It generates 400 radial velocities in one full scan. The SpinnerLidar is simulated with a focus distance of

52 m ($1D$) in front of the rotor, while other lidars are simulated with the focus distance of 98 m due to their smaller opening angles ($\phi = 15°$) to cover the whole rotor plane. We also simulate all considered lidars with multiple measurement planes at $f_d = 49,\ 72,\ 98,\ 121$ and 142 m, which are arbitrarily selected. As examples, Fig. 3 shows the scanning trajectories of the 4-beam and 50-beam lidars measuring at the five planes. We then use the radial velocity variances at all measurement levels to compute the turbulence statistics. Furthermore, to study the dependence of the turbulence estimations on the opening angle and the focus distance, we simulate the 6-beam configuration, proposed by Sathe et al. (2015), with extra setups: a fixed focus distance of 52 m and increasing opening angles (see Fig. 4(a)), as well as a fixed opening angle of 15° and increasing focus distances (see Fig. 4(b)).

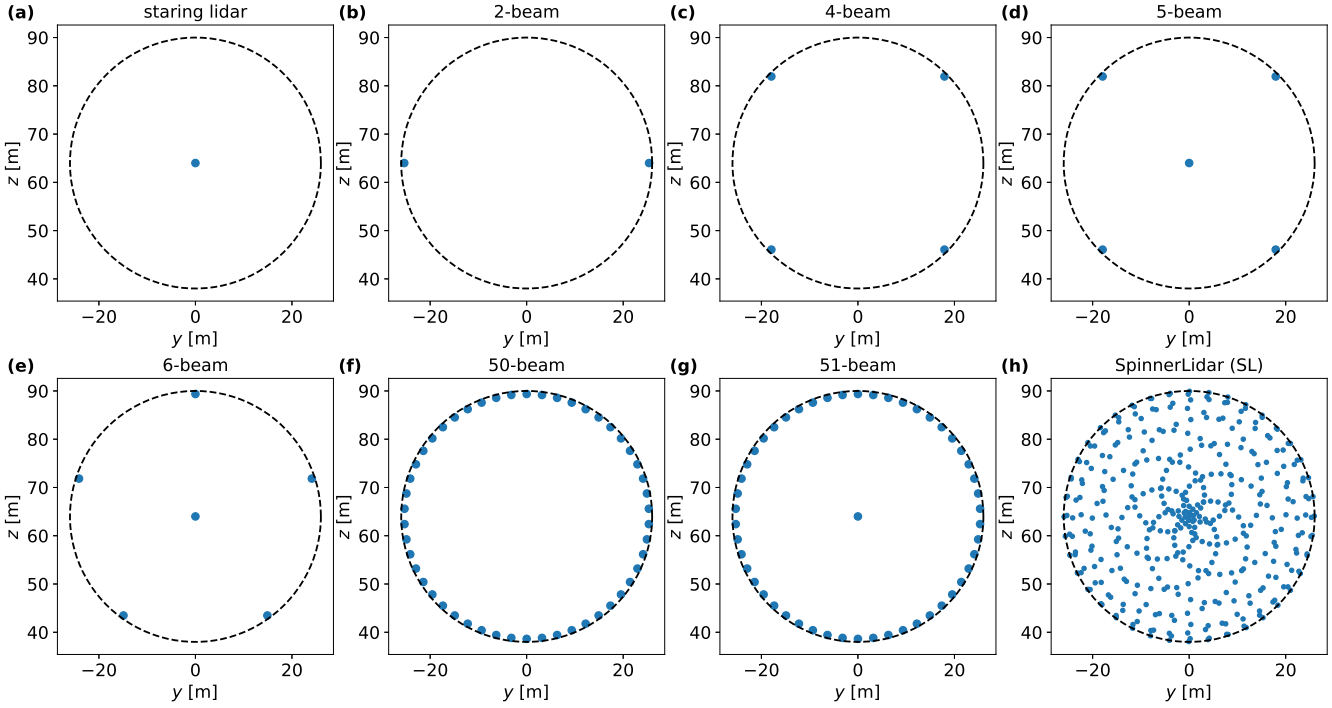

Figure 2. Selected lidar scanning patterns for numerical simulations. The SpinnerLidar (h) has $\phi = 0 - 30°$ and scans at $f_d = 52$ m, while other lidars (a-g) have $\phi = 15°$ and scan at $f_d = 98$ m to cover the whole rotor plane. The lidar beam scanning locations are marked in blue dots. The wind turbine rotor is represented in a black dashed circle.

We consider the lidar probe volume when we investigate the dependence of the Reynolds stresses estimation on ϕ and f_d. The Doppler radial velocity spectrum $S(v_\mathrm{r}, t)$ is simulated as (Held and Mann, 2018)

$$S(v_\mathrm{r}, t) = \int_{-M}^{M} \varphi(s)\delta(v_\mathrm{r} - \boldsymbol{u}(\boldsymbol{n}s - \boldsymbol{U}t) \cdot \boldsymbol{n})\mathrm{d}s, \tag{17}$$

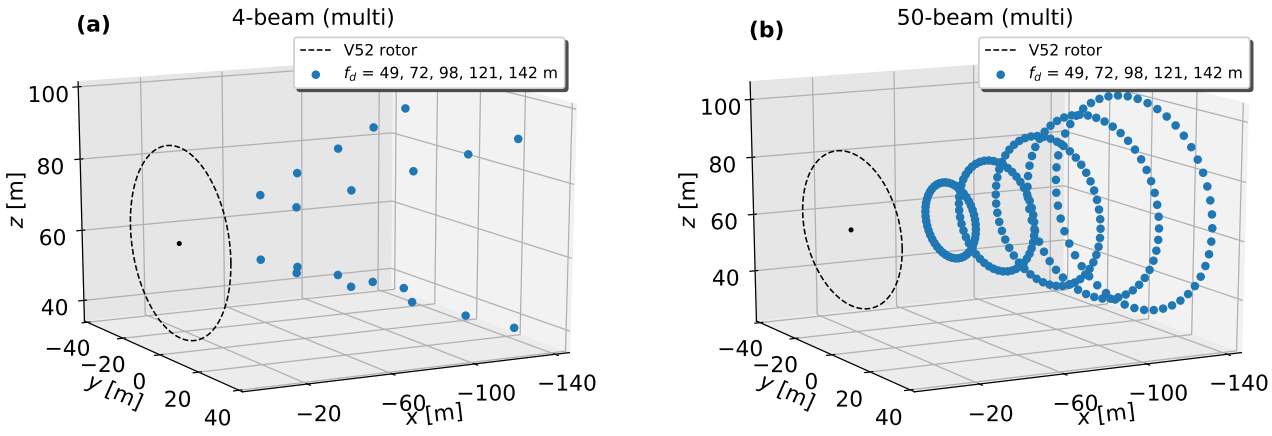

Figure 3. Scanning trajectories of the 4-beam and the 50-beam lidars measuring at $f_d = 49, 72, 98, 121$ and 142 m. Features regarding the blue dots and the dashed circle as in Fig. 2. The turbine nacelle is marked in a black dot on the rotor plane.

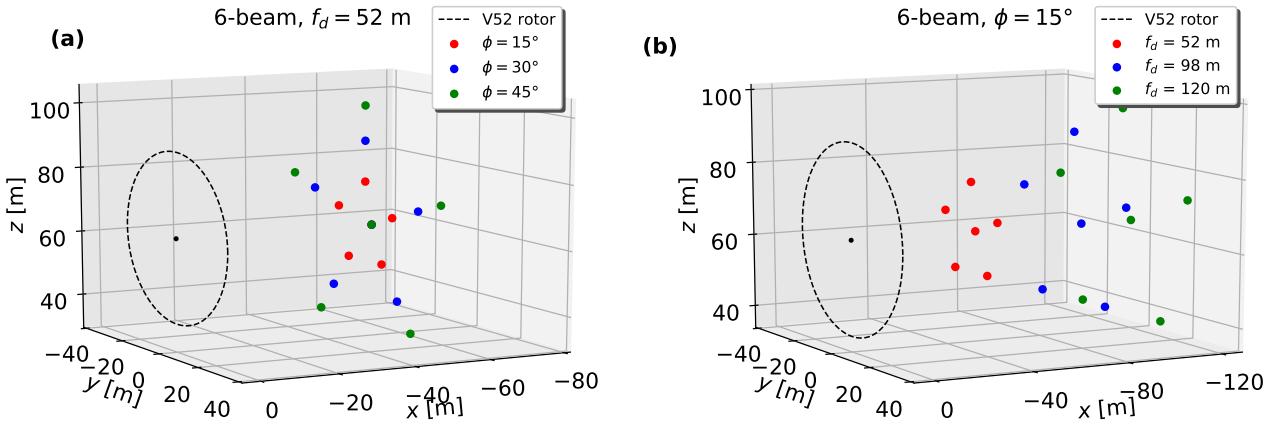

Figure 4. Scanning strategies of the 6-beam lidar with (a) a fixed focus distance and various half-cone opening angles, and (b) a fixed half-cone opening angle and various focus distances. Features regarding the dashed circle and the black dot as in Fig.3.

where δ represents the Dirac delta function, the integral is truncated with the distance M along the beam, and $\varphi(s)$ can be described by Eq. (5) or (6) depending on the type of the lidar system. The resolution of the Doppler radial velocity spectrum is 0.1 m s^{-1} per velocity bin, which is hereafter always used. Parameters used for modelling the probe volume are summarized in Table 1 (Meyer Forsting et al., 2017). We select M as shown in Table 1 so that 95% of the area under both weighting functions is covered. Figure 5 compares the modelled lidar probe volume for CW and pulsed lidars at focus distances $f_d = 52,\ 98$ and 120 m. The size of the probe volume for CW lidars increases with the square of the focus distance (see Eq. 5), while it remains the same for pulsed lidars.

CW	$\lambda = 1.565 \times 10^{-6}$m
	$r_b = 2.8 \times 10^{-2}$ m
	$M = 8z_{\mathrm{R}}$
pulsed	$\Delta l = 24.75$ m
	$\Delta p = 38.4$ m
	$M = 1.2\Delta l$

Table 1. Parameters for modelling the CW and pulsed lidar probe volume in numerical simulations.

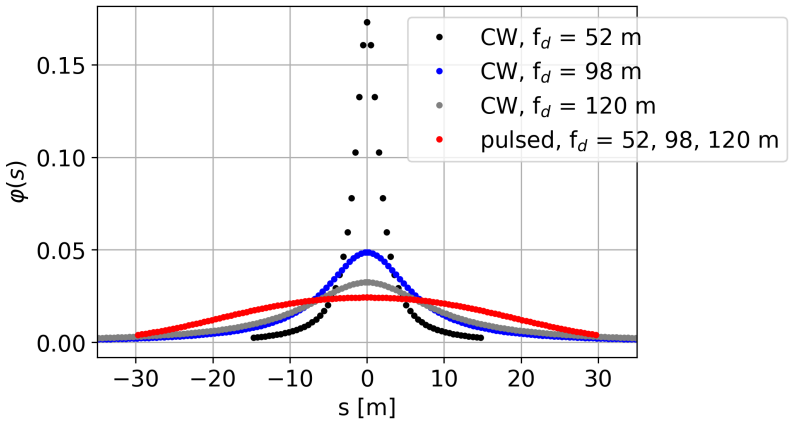

Figure 5. Comparison of the modelled lidar probe volume for CW and pulsed lidars at three different focus distances.

The time lag between each measurement within a full scan is not considered but assumed that measurements are taken at the same time. In the numerical simulations neglecting lidar probe volume (see results in Sections 4.1 and 4.2), the time resolution of the wind field is used as the lidar scan rate, i.e., lidars complete one full scan in $\mathrm{d}t = \mathrm{d}x/U = 0.22$ s. In the simulations considering lidar probe volume (see results in Section 4.3), the lidars are assumed to finish a full scan in 2 s.

3.4 Field measurements

During the period from 1 October 2020 to 30 April 2021, a SpinnerLidar was deployed on the nacelle of a Vestas V52 wind turbine at DTU Risø campus in Roskilde, Denmark, measuring the flow in front of the turbine. The V52 wind turbine has a rotor diameter of 52 m and a hub height of 44 m. Between the scan head of the SpinnerLidar and the turbine rotation axis, there is a vertical displacement of 2.47 m. A test site layout is shown on a digital surface elevation model in Fig. 6. The terrain is slightly hilly and its surface is characterized by a mix of cropland, grassland and coast. The dominant wind directions during this period at this site are west and south-west. The V52 wind turbine (marked with a red circle) stands at the northernmost position of a row of wind turbines (marked in black circles). There is also a meteorological mast (marked as a red square) mounted at 120 m ($\approx$ 2.3D) upstream from the V52 wind turbine at 291° from the north. One of the Metek USA-1 3D sonic anemometers on the mast is located at 44 m above the ground, and its turbulence statistics is used as references to be compared with the estimations from the nacelle-based lidars. A cup anemometer is located at the same height as the sonic anemometer on the mast. There are also a wind vane at 41 m and a Thies precipitation opto sensor at 2 m on the mast.

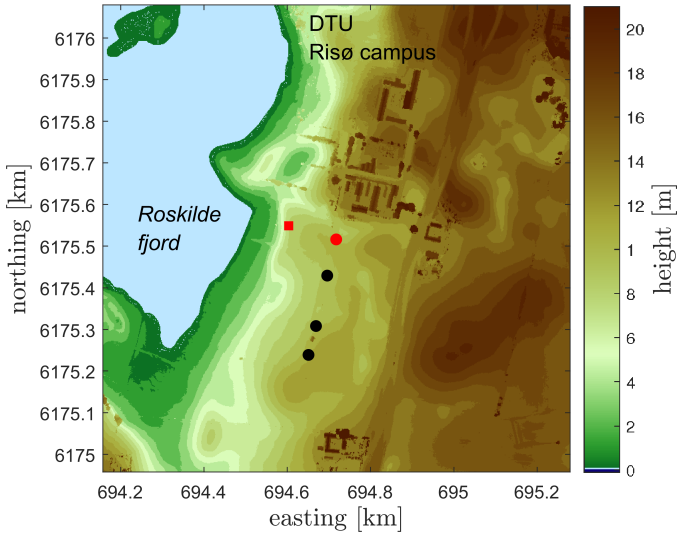

Figure 6. A digital surface elevation model (UTM32 WGS84) showing the Risø test site in Roskilde, Denmark. The height above the mean sea level is indicated by the color bar (in meters). A row of wind turbines are marked in circles (in red the reference V52 wind turbine). The meteorological mast is shown in a red square.

The SpinnerLidar (Peña et al., 2019) is based on a CW system and it was set up to scan the inflow at a focus distance of 62 m ($\approx 1.2D$, see Fig. 7). The Rayleigh length z_{R} of the SpinnerLidar at this focused distance is 2.44 m. It reported 400 radial velocities at a rate of 200 Hz, so it took 2 s to finish one full scan. The system also stored the instantaneous Doppler spectrum of the radial velocity, which allows us to estimate the unfiltered radial velocity variance.

The measurements used for the analysis are from the wind sectors, which are relatively aligned with the mast-turbine direction (i.e., the 10-min averaged wind direction measured by the vane is within $291° \pm 30°$). The yaw misalignment of the V52

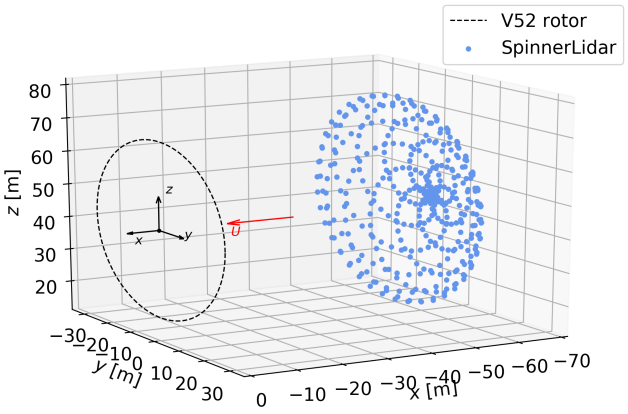

Figure 7. The scanning trajectory of the SpinnerLidar in the measurement campaign.

turbine is below $5°$, thereby minimizing the influence of nearby wind turbine wakes. We use a 10-min period, when the lidar and the V52 wind turbine are concurrently operating, and the averaged wind speed from the cup anemometer at 44 m is higher than 3 m s^{-1}. No precipitation was detected during the analyzed 10-min periods. After filtering, 2348 10-min periods are used for the analysis.

The SpinnerLidar measurements are post-processed to remove the signals reflected by the wind turbine blades, the telescope lens (the beam can hit the lens perpendicularly) or other hard targets. Such a procedure filters out some measurements close to the middle of the pattern. To compensate for the nacelle movement, we rotate the system-reported beam scanning coordinates using the 10-min averaged azimuthal and inclination angles of the SpinnerLidar, which are typically around $0.3°$ and $3°$, respectively. Taking the motion of the turbine and the slack of the SpinnerLidar into consideration, we divide the y–z plane into grids of 1-m resolution to aggregate the corrected scan locations. In the given 10-min, all Doppler radial velocity spectra lying within each grid cell are accumulated, and only measurements within the grid cells, where there are more than 30 instantaneous Doppler spectra, are used for the reconstruction. At least 900 grid cells should satisfy the criterion in the 10-min periods for our analysis. The light-grey dots in Figs. 8 and 9 represent the grid cells (for this particular case we have 1127 grid cells) satisfying the criterion in one arbitrary 10-min period. Other details about the measurement campaign and how the SpinnerLidar measurements are selected, filtered and processed can be found in Fu et al. (2022a). The post-processing of the measurements leaves us 1294 time periods for the final comparison.

To imitate lidars with different scanning strategies, we select SpinnerLidar measurements at certain grid cells to estimate the Reynolds stresses, as marked in red in Fig. 8. Due to the rotation of the system-reported lidar unit vectors, the corresponding half-cone opening angles of the grid cells are typically higher in the upper circle than those in the lower circle of the pattern, e.g., the ϕ of the top beam reaches $32°$ while the ϕ of the bottom beam is $27°$. To mimic the simulation setup of the 6-beam lidar in Fig. 4(a), we select 6 grid cells with different levels of opening angle (see Fig. 9), in which the central grid is always used. The mean half-cone opening angles of the 5 grid cells forming the circles are $12°$, $19°$ and $30°$, respectively. We estimate

the unfiltered radial velocity variance $\sigma^2_{v_r,\mathrm{unf}}$ using the Doppler radial velocity spectra collected in each selected grid cell. The Doppler spectra processing and usage are described in detail in Fu et al. (2022a).

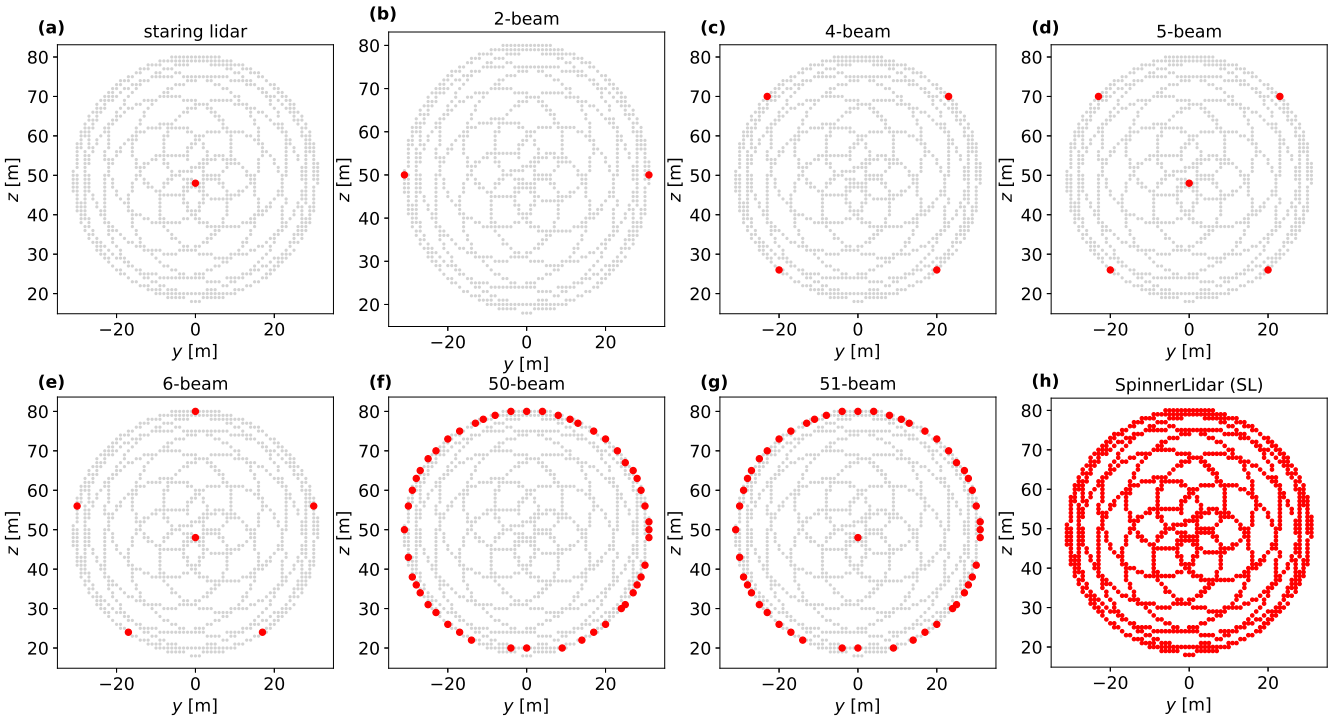

Figure 8. Selected lidar scanning patterns (in red) from the gridded SpinnerLidar scans (in light grey), which are at the focus distance of 62 m.

4 Results

In this section, we show comparisons of the Reynolds stresses computed from the considered lidars against those from the sonic anemometer at turbine hub height in bar plots. In the plots, markers correspond to the means of the estimations from 100 turbulence fields and the error bars are $\pm$ one standard deviation indicating the uncertainty of the estimation. The Reynolds stresses estimated from the measurements are normalized by the square of the mean along-wind velocity estimated by the lidar U^2 as we analyze a wide range of observed turbulence conditions. The mean wind velocity is computed by applying a least-square fit to the lidar radial velocities from all beams (Fu et al., 2022a). Results in Sections 4.1 and 4.2 neglect the lidars' probe volumes to study the influence of the number of beams. Nevertheless, for the CW lidar system, the probe volume increases with the square of the focus distance. Also, for pulsed lidar systems, the probe volume effect cannot be easily compensated since the Doppler spectra are usually not accessible. Therefore, the probe volumes are considered in Section 4.3 to show how different factors are altogether influencing the turbulence estimations.

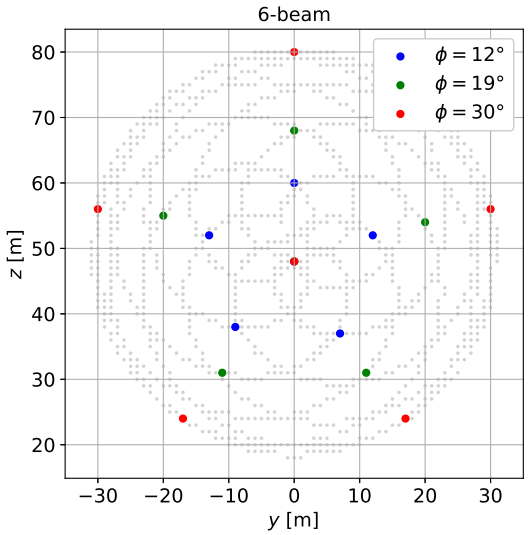

Figure 9. Selected grid cells for the 6-beam lidar with three different levels of the half-cone opening angle. The central grid coincides in the three cases. The gridded SpinnerLidar scans are shown in light grey.

4.1 Estimation of Reynolds stresses by multiple-beam lidars

We show in Fig. 10 the estimations of the six Reynolds stresses by the lidars, which have more than six beams and measure at a single plane, as well as those of the sonic anemometer. Results in Fig. 10(a) are from simulations that assume the lidars measure at the focus point only, i.e., no probe-volume averaging is accounted for. Results from both the simulations and the measurements show that the SpinnerLidar gives the best estimation for all six components. The results for the 6-beam and 51-beam lidars are very similar with larger errors and higher uncertainties than those of the SpinnerLidar. The 50-beam lidar can estimate the covariances accurately, while it shows large errors and uncertainties for $\langle v'v' \rangle$ and $\langle w'w' \rangle$; these are so noisy that some of them are out of the limit of the figure's axis. This is because the least-squares problem as formulated in Eq. (14) can lead to infinite solutions if we have only one opening angle ϕ. By comparing the results from the 50- and 51-beam lidar, we can see that the addition of a central beam is very beneficial for the computation of the variances of the velocity components, because the central beam provides an additional opening angle to the 50-beam lidar making the matrix on the left side of Eq. (15) not singular. In principle, adding an extra beam in any different opening angle than the others in the 50-beam scanning pattern will improve the estimations. The central beam is the best option for improving the estimation of the $\langle u'u' \rangle$ since the beam aligns with the along-wind velocity component and can fully capture its variation when the probe volume is neglected.

Results in Fig. 10 (a) indicate that nacelle lidars are able to characterize inflow turbulence as accurate as the sonic anemometer with reasonable uncertainties, when the lidar has at least six beams and two different opening angles. We see the similar trends from the measurements shown in Fig. 10 (b). The unfiltered Reynolds stresses estimated from all lidar measurements

are generally close to those from the sonic anemometer but biased. What unexpected and rare are the negative values of $\langle v'v' \rangle$ and $\langle w'w' \rangle$ observed in some periods of the measurements, as shown and discussed in Fu et al. (2022a).

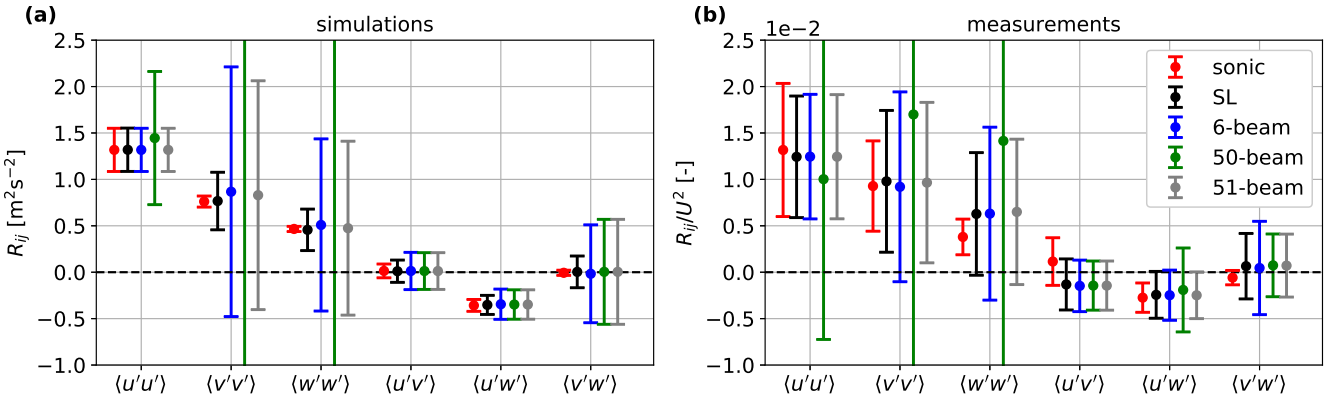

Figure 10. Reynolds stresses derived from the sonic anemometer and lidars, which have more than six beams and measure at a single distance. (a) simulated with 100 virtual wind fields. The lidars' probe volumes are neglected. (b) computed from the unfiltered radial velocity variance of the measurements. The markers are the means and the error bars are ± one standard deviation indicating the uncertainty of the estimation.

Figure 11 shows four of the Reynolds stresses retrieved from the 4- and 5-beam lidars. $\langle u'v' \rangle$ and $\langle v'w' \rangle$ are neglected in Eq. (15). In all cases, the determinants of the matrix in Eq. (15) are close to zero, which indicate that the 4- and 5-beam configurations cannot estimate these four Reynolds stresses accurately using the least-square procedure. Results from multiple-plane cases show that measuring at several planes with the same beam orientations does not aid much in the Reynolds stress reconstruction, as the determinant of the matrix in Eq. (15) does not change. For the 5-beam lidar, adding measurement planes only slightly reduces the uncertainty of the $\langle u'u' \rangle$ and $\langle u'w' \rangle$ components. This lack of sensitivity is partly due to Taylor's frozen hypothesis, as we do not account for evolution in the turbulence fields. We observe the same trend by comparing the estimation of these stresses from a 50-beam lidar measuring at a single and multiple planes (not shown here).

4.2 Estimation of the along-wind variance by all considered lidars

In case the nacelle lidar has fewer than six beams, not all six Reynolds stresses can be solved from Eq. (15). We focus our estimations on the along-wind variance and retrieve σ_u^2 from all considered lidars using the 'LSP-σ_u^2', 'LSP-isotropy' and 'LSP-IEC' methods, respectively, as introduced in Section 3.2. Results are shown in Fig. 12. All lidars are simulated to measure at a single plane (same as in Fig. 2) without accounting for the probe volume. Results from measurements are computed using the unfiltered radial velocity variances.

Both simulation and measurement results show, as a general trend, that lidar-derived σ_u^2 values are overestimated using the 'LSP-σ_u^2' method when compared to those from the sonic anemometer, while they are underestimated using the 'LSP-isotropy' method. The 'LSP-IEC' method gives the most accurate estimates among the three methods, as it assumes relations between the

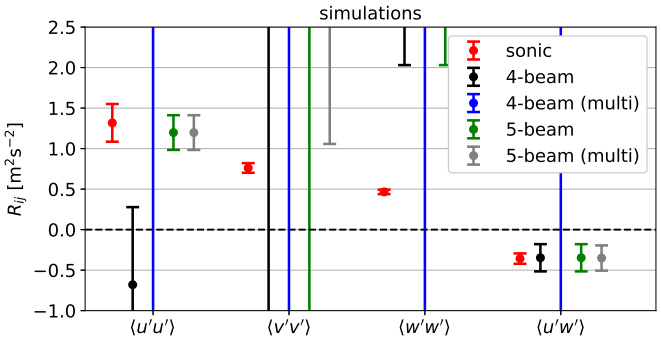

Figure 11. Reynolds stresses derived from the virtual sonic anemometer, the 4- and 5-beam lidars measuring at a single and multiple (multi) planes from 100 simulated wind fields. The lidars' probe volumes are neglected.

variances of the velocity components that might be close to those we can find within the atmospheric surface layer. The staring lidar performs like a sonic anemometer in our simulations as the beam is perfectly aligned with the along-wind component and the effect of lidar probe volume is not considered. Overall, all considered lidars are able to estimate σ_u^2 very well, despite of their different number of beams.

Table 2 summarizes the relative errors of the means of lidar-derived estimates compared to the one from the sonic anemometer. A negative value indicates that the along-wind variance is underestimated and vice-versa. The results in the first row of the table are computed solving the full matrix of Eq. (15) (same as $\langle u'u' \rangle$ showed in Fig. 10, here denoted as 'LSP-6Re' method), from which we get perfect estimations of σ_u^2 using the 6- and the 51-beam lidars, and the SpinnerLidar without the effect of the probe volume in the simulations. Furthermore, for lidars that have at least six beams and two different opening angles, the method 'LSP-6Re' is the best option to compute σ_u^2 among others, because it does not assume any relations between the six Reynolds stresses. While for lidars with fewer than six beams or only one opening angle, the 'LSP-6Re' does not work well and the 'LSP-IEC' gives the best estimation of σ_u^2. These results are aligned with one of the main findings in Fu et al. (2022a). In this work, the 'LSP-IEC' gives even smaller errors because we are able to compensate for the probe volume effect and use the 'unfiltered' radial velocity variances. In addition, comparing the relative errors between the 4- and 5-beam lidars, and those between the 50- and 51-beam lidars, we find again that the addition of a central beam can sometimes improve the estimation of the along-wind variance.

4.3 Dependence of Reynolds stresses estimations on the opening angle, focus distances and the type of lidar

The results shown in this section include the averaging effect of the lidar probe volume. In Fig. 13, we analyze how the accuracy and the uncertainty of the Reynolds stresses estimations change when increasing the half-cone opening angle ϕ for the 6-beam lidar. The simulation setup has been shown in Fig. 4(a). We compare these estimations with those from the sonic anemometer and the SpinnerLidar. The lidar probe volumes are modelled as in a CW system. Simulation and measurement results show that both the error and the uncertainty decrease as the opening angle increases. Specifically, the 6-beam lidar with $\phi = 45°$

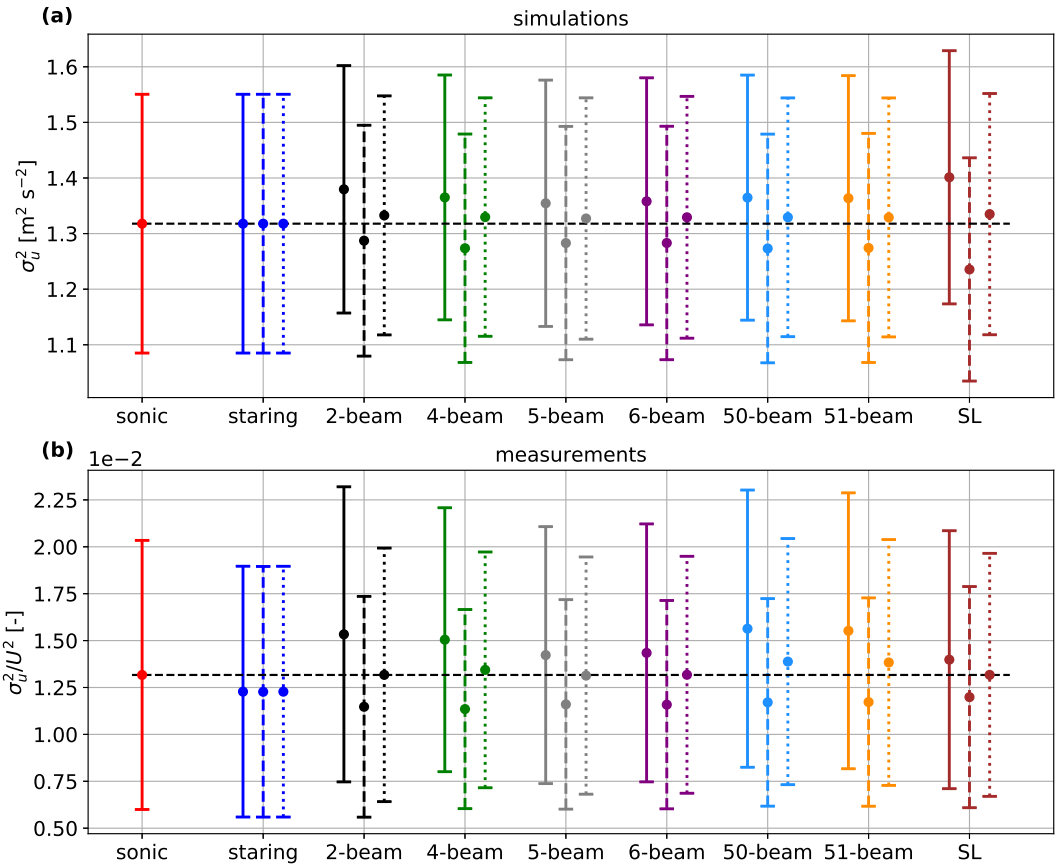

Figure 12. The along-wind variance derived from all considered lidars using the 'LSP-σ_u^2' method (solid lines), 'LSP-isotropy' method (dashed lines) and 'LSP-IEC' method (dotted lines). All lidars from simulations are assumed to have no probe volume and they measure at a single plane (Fig. 2).

in the simulations provides lower uncertainty than the SpinnerLidar despite having much fewer beams, as the SpinnerLidar's maximum opening angle is $\phi = 30°$. We observe the same trend when simulating the probe volume with a 6-beam pulsed system (not shown here). Possible reasons for the positive bias of the v- and w-variances seen from the simulation results are discussed in Section 5.

We study the dependence of the Reynolds stresses estimations on the increasing focus distance f_d for the 6-beam lidar based on numerical simulations. The setup has been shown in Fig. 4(b). We assume the lidar systems to be continuous-wave and pulsed, as shown in Fig. 14(a) and (b), respectively. All Reynolds stresses are computed using the centroid-derived radial velocity variances. Therefore, the estimated variances are attenuated by the probe volume and in general smaller than those from the sonic anemometer. For both types of lidar, we see that increasing the focus distance has negative effects on the estimation of all Reynolds stresses. The uncertainty increases due to the random error on the variances of the radial velocity;

	methods	staring	2-beam	4-beam	5-beam	6-beam	50-beam	51-beam	SL
	LSP-6Re	—	—	—	—	0	9.7	0	0.1
simulations	LSP-σ_u^2	0	4.7	3.6	2.8	3.0	3.6	3.5	6.3
(without probe volume)	LSP-isotropy	0	−2.3	−3.4	−2.6	−2.6	−3.4	−3.3	−6.2
	LSP-IEC	0	1.1	0.9	0.7	0.9	0.9	0.9	1.3
	LSP-6Re	—	—	—	—	−5.4	−23.9	−5.5	−5.6
measurements	LSP-σ_u^2	−6.8	16.4	14.3	8.0	8.9	18.7	17.9	6.2
(unfiltered variance)	LSP-isotropy	−6.8	−12.9	−13.8	−11.9	−12.0	−11.1	−11.0	−9.0
	LSP-IEC	−6.8	0	2.1	−0.3	0.1	5.4	5.0	0

Table 2. Relative error [%] of the mean values of the lidar-derived along-wind variance to the one from the sonic anemometer. The lidars' probe volumes are neglected in the simulations. Results from the simulations are computed using measurements at a single plane (same set up as Fig. 2). A negative value indicates that the along-wind variance is underestimated and vice-versa.

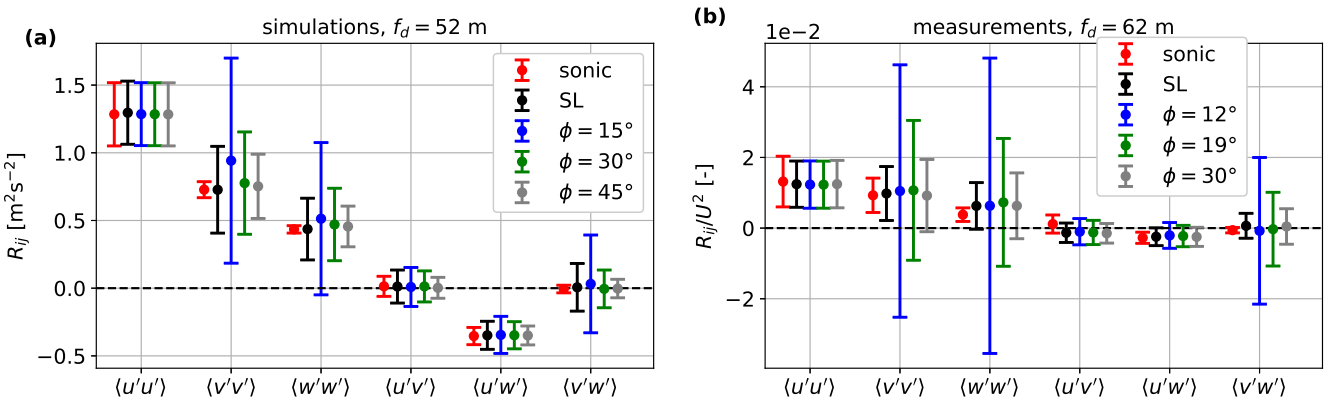

Figure 13. Dependence of the Reynolds stresses estimations on the increasing half-cone opening angle ϕ for the 6-beam lidar (single plane), the sonic anemometer and the SpinnerLidar ($\phi = 0$–$30°$). The probe volume in the simulations is assumed to be as in CW systems. All Reynolds stresses are computed using the unfiltered radial velocity variances.

they are less correlated when the lidar scans over a larger area. In the case of the CW system, the bias for the estimations increases with f_d due to its growing probe volume, while the bias is almost constant for the pulsed system, as expected. For the closest focus distance $f_d = 52$ m, the bias of the estimations from the pulsed system is evidently larger than those from the CW system, where the later system gives accurate estimations of all Reynolds stresses. We perform the same analysis with the 51-beam lidar and observe the same trends (not shown here).

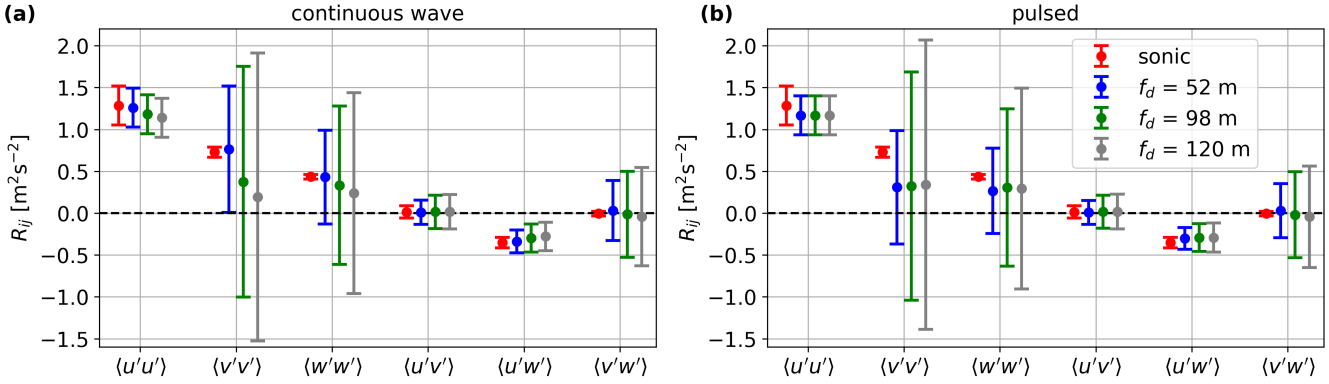

Figure 14. Dependence of the Reynolds stresses estimations on the increasing focus distance f_d for the 6-beam lidar (single plane, $\phi = 15°$), compared to those from the sonic anemometer. The probe volume in the simulations are assumed to be as in (a) a CW system, and (b) a pulsed system. All Reynolds stresses are computed using the centroid-derived (filtered) radial velocity variances.

5 Discussion

Results shown in Fig. 13 are from simulations that consider the CW lidar probe volume to mimic the lidar's behavior in the reality. Then, the Doppler radial velocity spectra are used to compute the 'unfiltered' velocity variances for both simulations and measurements. Compared to the estimations from the sonic anemometer, we observe positive biases of the lidar-retrieved v- and w- variances. The biases decreas with increasing the half-cone opening angle ϕ. The reason is that although the large matrix on the left side of Eq. (15) is not degenerate (i.e., its determinant is not zero) for a 6-beam lidar, the coefficients for R_{vv} and R_{ww} are very small (in the order of 10^{-3}) for $\phi = 15°$; the equation system is only balanced by overestimating both terms R_{vv} and R_{ww}. The coefficients are proportional to the value of the opening angle ϕ, so they increase to 10^{-2} in the case of $\phi = 30°$, and to 10^{-1} in the case of $\phi = 45°$, which explains why the biases are reduced with larger opening angles. The positive biases for R_{vv} and R_{ww} are slightly more evident in the simulations with probe volume compared to the case in which the probe volume is neglected (see Fig. 10 (a)), because the simulated radial velocity variances are different in the two scenarios.

As shown in Fig. 13, increasing the lidar opening angle improves the accuracy and uncertainty of R_{vv} and R_{ww} estimations. The uncertainty of σ_u^2 is not much influenced if the lidar has a central beam that always aligns with the mean wind, e.g. the six-, 51-beam lidars, and the SpinnerLidar. For nacelle lidars without a central beam, enlarging the opening angle brings higher

uncertainty to σ_u^2 estimation, which is a key parameter for assessing wind turbine loads (IEC, 2019). Therefore, the optimum opening angle for turbulence estimations depends on which Reynolds stress is of interest. In addition, for control applications, the large opening angle is beneficial for measuring wind directions, but sacrifices the accuracy of rotor-effective wind speed and wind shear estimations (Simley et al., 2018). The optimum opening angle is also very much relevant to the turbine's size.

In this work, we characterize turbulence in front of a small wind turbine at $1D$ and $1.2D$ in the simulations and the field experiment, respectively. Taylor's frozen turbulence hypothesis (and homogeneity) is assumed throughout our numerical simulations, because the wind evolution is not very relevant to turbulence statistics, but more to the rotor-effective wind speed estimations (Chen et al., 2021). Mann et al. (2018) showed that turbulence is slightly affected by the stagnation in front of the wind turbine rotor as it goes through the induction zone. The change of the low-frequency wind variation is related to the thrust coefficient of the wind turbine, but the main turbulence statistics do not change. In addition, the yaw misalignment of the wind turbine is not considered in this work. A small yaw misalignment (below 20°) does not affect much σ_u^2 estimations but increases the uncertainty of R_{vv} and R_{ww} estimations. For modern wind turbines with very large rotor disks, the single-point turbulence statistics do not represent well the inflow turbulence affecting the wind turbine. The least-square procedure cannot be used to characterize the inhomogeneous inflow. New methodologies, e.g., constrained simulations (Dimitrov and Natarajan, 2017; Conti et al., 2021), are needed to reconstruct the inhomogeneous wind field.

We show from both simulations and measurements that all six Reynolds stress components can be estimated accurately when using a nacelle multi-beam lidar. Although the spectral turbulence model used here (the Mann model), which is the basis of our simulated turbulence fields, assumes two of these components to be zero, namely $\langle u'v' \rangle$ and $\langle v'w' \rangle$, the methods and techniques introduced in this work enable us to estimate all components accurately. This is advantageous for the study of atmospheric flow over complex terrain and, particularly, in offshore conditions, where turbulence measurements are scarce and expensive, and where we rely very much on models to assess the site conditions that impact wind turbines. These models often assume relations between the turbulence components and/or use parametrizations of stresses/fluxes that are invalid due to the nature of the flow phenomena and the interaction between the waves and the wind field. For example, surface stresses over long-lasting waves can be highly misaligned with the vertical gradient of the horizontal wind; most parametrizations of the air-sea interaction assume such an alignment to estimate momentum fluxes within the marine boundary layer. Offshore nacelle lidars can therefore help us understanding phenomena that are otherwise difficult to assess with traditional anemometry used for offshore wind power development.

6 Conclusion and Outlook

This study investigated the dependence of the Reynolds stresses estimations on different number of beams, half-cone opening angles, focus distances, single or multiple measurement planes, and different types of the Doppler wind nacelle lidars using both numerical simulations and measurements. The considered lidar scanning patterns included the staring lidar (single beam), the 2-, 4-, 5-, 6-, 50-, 51-beam lidars and the SpinnerLidar, which reports 400 radial velocities with one scan. We assumed a homogeneous inflow turbulence (both for the simulations and measurements) and the Taylor's frozen turbulence (for the simu-

lations). The lidar-retrieved turbulence estimations were compared with those from a sonic anemometer at turbine hub height. Analysis of both numerical simulations and measurements showed that to estimate all the six Reynolds stresses accurately, a nacelle lidar system with at least six beams is required. Also, one of the beams of this system should have a different opening angle. Adding one central beam improves the estimations of the velocity components' variances. Measuring at multiple planes with the same beam orientations only reduces the uncertainty but not the bias in the reconstruction, if Taylor's frozen turbulence hypothesis is applied. All considered lidars can estimate the along-wind variance accurately by using the least-squares procedure and the assumption that the relations of the velocity components' variances are as suggested in the IEC standard. Also, the Doppler radial velocity spectra are needed for the accurate estimations. For both CW and pulsed lidars, increasing the opening angle reduces both the error and uncertainty of the estimations, while increasing the focus distance has opposite effects. In short, from all tested scanning strategies, a 6-beam CW lidar measuring at a close distance with a large opening angle gives the best estimations of all Reynolds stresses. The optimum value of the opening angle depends on the Reynolds stress term of interest and also the wind turbines' size. Further studies or experiments are needed to study the best opening angle of the 6-beam lidar for different applications.

In this work, the single-point turbulence statistics are estimated using the least-square procedure, which assumes homogeneity over the lidar scanning area. Wind turbines nowadays are often operating inside a wind farm or have large spans over the swept area. The assumption of homogeneous turbulence can be violated under those conditions. Therefore, further studies on the optimized lidar scanning strategy for turbulence estimation should consider the inhomogeneity of the inflow. Additionally, the proposed nacelle lidar scanning strategies can be used to study the wind evolution, the spatial correlations of turbulence and estimate multi-point statistics, which better characterize the inflow that interacts with the turbine than the hub height ones. The wind field reconstruction of the inhomogeneous wind fields can benefit from constrained simulations, which incorporate lidar measurements into three-dimensional turbulence wind fields. Future works could also consider the non-Gaussianity of turbulence (Liu et al., 2010; Schottler et al., 2017) and the scale-dependent anisotropy of wind fluctuations (Syed et al., 2023).

Data availability. Measurements from the SpinnerLidar are not publicly available due to a non-disclosure agreement between the authors and the provider of the data. Simulated nacelle lidar measurements are available upon requests.

Author contributions. All authors participated in the conceptualization and design of the work. WF and AS performed numerical simulations of nacelle lidars without probe volume. AS extended the simulations with lidar probe volume. WF conducted the analysis of field measurements and drafted the manuscript. AP and JM supported the whole analysis. All authors reviewed and edited the manuscript.

Competing interests. At least one of the (co-)authors is a member of the editorial board of Wind Energy Science. The authors have no other competing interests to declare.

Acknowledgements. The campaign was conducted as a part of the LIdar-assisted COntrol for RElidability IMprovement (LICOREIM) project at DTU Wind Energy. This study is funded by the European Union's Horizon 2020 research and innovation program under the Marie Sklodowska-Curie grant agreement No. 858358 (LIKE – Lidar Knowledge Europe, H2020-MSCA-ITN-2019).

References

Branlard, E., Pedersen, A. T., Mann, J., Angelou, N., Fischer, A., Mikkelsen, T., Harris, M., Slinger, C., and Montes, B. F.: Retrieving wind statistics from average spectrum of continuous-wave lidar, Atmospheric Measurement Techniques, 6, 1673–1683, https://doi.org/10.5194/amt-6-1673-2013, 2013.

Chen, Y., Schlipf, D., and Cheng, P. W.: Parameterization of wind evolution using lidar, Wind Energy Science, 6, 61–91, https://doi.org/10.5194/wes-6-61-2021, 2021.

Conti, D., Pettas, V., Dimitrov, N., and Peña, A.: Wind turbine load validation in wakes using wind field reconstruction techniques and nacelle lidar wind retrievals, Wind Energy Science, 6, 841–866, https://doi.org/10.5194/wes-6-841-2021, 2021.

Dimitrov, N. and Natarajan, A.: Application of simulated lidar scanning patterns to constrained Gaussian turbulence fields for load validation, Wind Energy, 20, 79–95, https://doi.org/10.1002/we.1992, 2017.

Dong, L., Lio, W. H., and Simley, E.: On turbulence models and lidar measurements for wind turbine control, Wind Energy Science, 6, 1491–1500, https://doi.org/10.5194/wes-6-1491-2021, 2021.

Eberhard, W. L., Cupp, R. E., and Healy, K. R.: Doppler lidar measurement of profiles of turbulence and momentum flux, Journal of Atmospheric and Oceanic Technology, 6, 809–819, https://doi.org/10.1175/1520-0426(1989)006<0809:DLMOPO>2.0.CO;2, 1989.

Fu, W., Peña, A., and Mann, J.: Turbulence statistics from three different nacelle lidars, Wind Energy Science, 7, 831–848, https://doi.org/10.5194/wes-7-831-2022, 2022a.

Fu, W., Sebastiani, A., Peña, A., and Mann, J.: Influence of nacelle-lidar scanning patterns on inflow turbulence characterization, Journal of Physics: Conference Series, 2265, 022 016, https://doi.org/10.1088/1742-6596/2265/2/022016, 2022b.

Gottschall, J. and Peinke, J.: How to improve the estimation of power curves for wind turbines, Environ. Res. Lett, 3, 15 005–7, https://doi.org/10.1088/1748-9326/3/1/015005, 2008.

Harris, M., Hand, M., and Wright, A.: Lidar for turbine control, National Renewable Energy Laboratory, Golden, CO, Report No. NREL/TP-500-39154, https://www.nrel.gov/docs/fy06osti/39154.pdf, 2006.

Held, D. P. and Mann, J.: Comparison of methods to derive radial wind speed from a continuous-wave coherent lidar Doppler spectrum, Atmospheric Measurement Techniques, 11, 6339–6350, https://doi.org/10.5194/amt-11-6339-2018, 2018.

IEC: IEC 61400-1. Wind turbines – Part 1: design guidelines, International standard, International Electrotechnical Commission, Geneva, Switzerland, https://standards.iteh.ai/catalog/standards/sist/3454e370-7ef2-468e-a074-7a5c1c6cb693/iec-61400-1-2019, 2019.

Kumer, V.-M., Reuder, J., Dorninger, M., Zauner, R., and Grubišić, V.: Turbulent kinetic energy estimates from profiling wind LiDAR measurements and their potential for wind energy applications, Renewable Energy, 99, 898–910, https://doi.org/10.1016/j.renene.2016.07.014, 2016.

Liu, L., Hu, F., Cheng, X. L., and Song, L. L.: Probability density functions of velocity increments in the atmospheric boundary layer, Boundary-Layer Meteorology, 134, 243–255, https://doi.org/10.1007/S10546-009-9441-Z/METRICS, 2010.

Mann, J.: The spatial structure of neutral atmospheric surface-layer turbulence, Journal of Fluid Mechanics, 273, 141–168, https://doi.org/10.1017/S0022112094001886, 1994.

Mann, J., Peña, A., Bingöl, F., Wagner, R., and Courtney, M. S.: Lidar scanning of momentum flux in and above the surface layer, Journal of Atmospheric and Oceanic Technology, 27, 959–976, https://doi.org/10.1175/2010JTECHA1389.1, 2010.

Mann, J., Penã, A., Troldborg, N., and Andersen, S. J.: How does turbulence change approaching a rotor?, Wind Energy Science, 3, 293–300, https://doi.org/10.5194/wes-3-293-2018, 2018.

Meyer Forsting, A. R., Troldborg, N., and Borraccino, A.: Modelling lidar volume-averaging and its significance to wind turbine wake measurements, Journal of Physics: Conference Series, 854, 012 014, https://doi.org/10.1088/1742-6596/854/1/012014, 2017.

Mikkelsen, T., Angelou, N., Hansen, K., Sjöholm, M., Harris, M., Slinger, C., Hadley, P., Scullion, R., Ellis, G., and Vives, G.: A spinner-integrated wind lidar for enhanced wind turbine control, Wind Energy, 16, 625–643, https://doi.org/10.1002/we.1564, 2013.

Newman, J. F., Klein, P. M., Wharton, S., Sathe, A., Bonin, T. A., Chilson, P. B., and Muschinski, A.: Evaluation of three lidar scanning strategies for turbulence measurements, Atmospheric Measurement Techniques, 9, 1993–2013, https://doi.org/10.5194/amt-9-1993-2016, 2016.

Peña, A., Hasager, C., Bay, Badger, M., Barthelmie, R. J., Bingöl, F., Cariou, J.-P., Emeis, S., Frandsen, S., Tronaes, Harris, M., and Karagali, I.: Remote Sensing for Wind Energy, DTU Wind Energy, 2015.

Peña, A., Floors, R., Sathe, A., Gryning, S. E., Wagner, R., Courtney, M. S., Larsén, X. G., Hahmann, A. N., and Hasager, C. B.: Ten Years of Boundary-Layer and Wind-Power Meteorology at Høvsøre, Denmark, Boundary-Layer Meteorology, 158, 1–26, https://doi.org/10.1007/s10546-015-0079-8, 2016.

Peña, A., Mann, J., and Dimitrov, N.: Turbulence characterization from a forward-looking nacelle lidar, Wind Energy Science, 2, 133–152, https://doi.org/10.5194/wes-2-133-2017, 2017.

Peña, A., Mann, J., and Thorsen, G.: SpinnerLidar measurements for the CCAV52, Tech. Rep. DTU Wind Energy E Vol. 0177, DTU Wind Energy, 2019.

Petersen, J. T., Kretz, A., and Mann, J.: Influence of transversal turbulence on lifetime predictions for a HAWT, in: Contributions from the Department of Meteorology and Wind Energy to the EWEC'94 Conference in Thessaloniki, Greece, p. 72, 1994.

Sathe, A. and Mann, J.: A review of turbulence measurements using ground-based wind lidars, Atmospheric Measurement Techniques, 6, 3147–3167, https://doi.org/10.5194/amt-6-3147-2013, 2013.

Sathe, A., Mann, J., Gottschall, J., and Courtney, M. S.: Can wind lidars measure turbulence?, Journal of Atmospheric and Oceanic Technology, 28, 853–868, https://doi.org/10.1175/JTECH-D-10-05004.1, 2011.

Sathe, A., Mann, J., Vasiljevic, N., and Lea, G.: A six-beam method to measure turbulence statistics using ground-based wind lidars, Atmospheric Measurement Techniques, 8, 729–740, https://doi.org/10.5194/amt-8-729-2015, 2015.

Schlipf, D., Fürst, H., Raach, S., and Haizmann, F.: Systems Engineering for Lidar-Assisted Control: A Sequential Approach, Journal of Physics: Conference Series, 1102, 012 014, https://doi.org/10.1088/1742-6596/1102/1/012014, 2018.

Schottler, J., Reinke, N., Hölling, A., Whale, J., Peinke, J., and Hölling, M.: On the impact of non-Gaussian wind statistics on wind turbines – an experimental approach, Wind Energy Science, 2, 1–13, https://doi.org/10.5194/wes-2-1-2017, 2017.

Simley, E., Fürst, H., Haizmann, F., and Schlipf, D.: Optimizing lidars for wind turbine control applications-Results from the IEA Wind Task 32 workshop, Remote Sensing, 10, https://doi.org/10.3390/rs10060863, 2018.

Smalikho, I. N. and Banakh, V. A.: Measurements of wind turbulence parameters by a conically scanning coherent Doppler lidar in the atmospheric boundary layer, Atmospheric Measurement Techniques, 10, 4191–4208, https://doi.org/10.5194/amt-10-4191-2017, 2017.

Sonnenschein, C. M. and Horrigan, F. A.: Signal-to-noise relationships for coaxial systems that heterodyne backscatter from the atmosphere, Applied Optics, 10, 1600–1604, https://doi.org/10.1364/AO.10.001600, 1971.

Syed, A. H., Mann, J., Platis, A., and Bange, J.: Turbulence structures and entrainment length scales in large offshore wind farms, Wind Energy Science, 8, 125–139, https://doi.org/10.5194/WES-8-125-2023, 2023.

Taylor, G. I.: The spectrum of turbulence, Proceedings of the Royal Society of London. Series A - Mathematical and Physical Sciences, 164, 476–490, https://doi.org/10.1098/rspa.1938.0032, 1938.

Wagner, R., Pedersen, T. F., Courtney, M., Antoniou, I., Davoust, S., and Rivera, R. L.: Power curve measurement with a nacelle mounted lidar, Wind Energy, 17, 1441–1453, https://doi.org/10.1002/we.1643, 2014.

Wagner, R., Courtney, M., Pedersen, T. F., and Davoust, S.: Uncertainty of power curve measurement with a two-beam nacelle mounted lidar, Wind Energy, 19, 1269–1287, https://doi.org/10.1002/we.1897, 2015.

Wyngaard, J.: Turbulence in the Atmosphere, Cambridge University Press, 2010.

Paper V: Wind turbine power performance characterization through aeroelastic simulations and virtual nacelle lidar measurements

Wind turbine power performance characterization through aeroelastic simulations and virtual nacelle lidar measurements

Wind turbine power performance characterization through aeroelastic simulations and virtual nacelle lidar measurements

Alessandro Sebastiani, Alfredo Peña and Niels Troldborg

Department of Wind Energy, Technical University of Denmark, Frederiksborgvej 399, 4000 Roskilde, Denmark

E-mail: aseb@dtu.dk

Abstract. The power performance of a wind turbine depends on several characteristics of the inflow, such as wind speed, turbulence and wind shear. Additionally, wind turbine control strategies affect the power performance of the wind turbines; under certain conditions one might want to, e.g., intentionally misalign the turbine with respect to the main wind direction. Here, we evaluate whether the accuracy in power performance evaluation can be improved by using multi-dimensional power curves in the form of multivariate polynomial regressions, which define the power output as function of wind speed, turbulence and yaw misalignment. The analysis is conducted on a dataset of virtual power performance measurements, which is generated through aeroelastic simulations combined with a simulator of nacelle lidar measurements. Results show that the multi-dimensional power curves can provide higher accuracy than those derived using the IEC standard for power curve measurements; the error in power prediction is nearly halved compared to that using the IEC standard power curve method. Additionally, we show that nacelle lidar measurements increase the accuracy of the multi-dimensional power curves when compared to using mast-based anemometer measurements.

1. Introduction

The first version of the IEC standard for power performance measurements described the power output of a wind turbine as function of only two flow characteristics: the air density and the mean wind speed at hub height [1]. However, studies have shown that wind turbine power performance is affected by other flow characteristics, such as atmospheric turbulence and wind shear [2; 3]. Because of the non-linearity of the power curve, the mean[1] power output depends on both the mean and the variance of the wind speed. Where the power curve is concave, e.g. for wind speeds slightly higher than the cut-in value, the mean power output increases with the wind speed variance. On the contrary, where the power curve is convex, e.g. for wind speeds slightly lower than the rated-value, the mean power output decreases with the wind speed variance. This expected behavior was confirmed by several studies through both simulations and measurements [2; 4; 5]. Additionally, neglecting the wind speed variation with height might result in a poor estimation of the kinetic energy flux through the rotor [3]. Therefore, in the most recent version of the IEC standard [6] for power performance measurements, both wind shear and atmospheric turbulence are considered. These additional flow characteristics increase the accuracy of the

[1] mean here refer to the average within a 10-min period

power performance assessment, resulting in more reliable power curves and less uncertainty in energy yield assessment (EYA).

Nevertheless, in order to guarantee an accurate EYA, it is crucial to account for flow inhomogeneities from the atmosphere-wind turbine interaction and evaluate their effect on the power performance. Previous studies used both parametric and non-parametric models to evaluate wind turbine power performance under different environmental conditions [7–9]. Recently, wake steering, which is a control strategy, introduced the need to evaluate the power performance of a wind turbine under yawed conditions, i.e. when the mean wind direction and the turbine rotor axis are misaligned [10]. Previous studies showed how to correct standard power curves for yaw misalignment [10; 11] in order to evaluate the effects of wake steering in EYA.

In this work, we evaluate whether the accuracy in power performance evaluation can be improved by using multi-variable power curves, which define the power output as function of wind speed, turbulence and yaw misalignment. The analysis is conducted on a dataset of power performance simulations. Specifically, numerical wind fields are generated with the turbulence spectral model of Mann [12], and the in-house aeroelastic code HAWC2 [13] is used to perform time-domain aeroelastic simulations. Additionally, we simulate measurements from a nacelle-mounted lidar to evaluate whether the accuracy of the new multi-variable power curve changes when using nacelle-mounted lidars instead of traditional mast-based anemometry.

This paper is organized as follows. The methodology is outlined in section 2, which describes the numerical wind fields in section 2.1, the lidar simulator in section 2.2 and the multi-dimensional power curves in section 2.3. Section 3 shows and discusses the accuracy of the multi-dimensional power curves. Conclusions are given in section 5.

2. Methodology

2.1. Generation of the dataset

The turbulence model by Mann is used to generate three-dimensional velocity fields $\mathbf{u}(\mathbf{x})$, with $\mathbf{u} = (u, v, w)$ being the along-wind, transverse, and vertical velocity components and $\mathbf{x} = (x, y, z)$ the spatial field. The wind fields are characterized by homogeneous frozen turbulence, with the wind speed fluctuations $\mathbf{u'} = (u', v', w')$ advected along the horizontal axis x. Therefore, assuming homogeneity and no vertical wind speed, the mean wind speed varies with height according to the chosen shear profile: $\mathbf{U} = (U(z), 0, 0)$. In case of no vertical shear, the mean wind speed is uniform in the (y, z) plane.

The turbulence fields are used as input to the HAWC2 aeroelastic simulations [13], which are performed with the Vestas V52 wind turbine, with a rotor diameter (D) of 52 m and a rated power of 900 kW. According to the IEC standard [6], power performance measurements are based on 10-min means of both wind speed and power output. Therefore, in order to get a 10-min mean power output from each aeroelastic simulation, all the wind fields have dimensions of ($U\,T$, 128 m, 128 m). We choose $T = 700$ s; the additional 100 s are needed to avoid the initial transient phase of the aeroelastic simulation, while the length of 128 m is used in both the vertical and lateral directions to ensure enough distance between the rotor and the edge of the turbulence field, avoiding possible bias due to the field periodicity [14].

We generate two different datasets, hereafter referred to as the synthetic and realistic dataset. The synthetic dataset is shaped in order to guarantee a data distribution that is convenient for the evaluation of the multi-dimensional power curves. On the other hand, the realistic dataset aims to replicate the data distribution that would be collected from a real wind turbine operating under optimal conditions. Both datasets present turbulence fields generated with the Mann-model length scale of $L = 29.4$ m and anisotropy of $\Gamma = 3.9$, while the other Mann-model parameter $\alpha\epsilon^{2/3}$ is varied to match the desired turbulence level. The synthetic dataset consists of 720 wind fields characterized by a uniform distribution of U between 6.5 and 12 m/s. Half

Table 1. Flow characteristics of the numerical wind fields in the different datasets. $[a, b]$ indicates a uniform or nearly uniform distribution between a and b. $N(\mu, \sigma)$ indicates a Gaussian distribution with μ and σ as mean and standard deviation, respectively. A single value indicates a constant over the whole dataset

Dataset	U [m/s]	L [m]	Γ	$\alpha\epsilon^{2/3}$ [$m^{4/3}$/s]	γ [°]	α	N
Synthetic (1st half)	[6.5, 12]	29.4	3.9	[0.005, 0.165]	0	0	360
Synthetic (2nd half)	[6.5, 12]	29.4	3.9	0.03	[−40,+40]	0	360
Realistic	[6, 14]	29.4	3.9	$N(0.06, 0.02)$	$N(0, 3)$	$N(0.15, 0.1)$	150

of this dataset (360 wind fields) presents a uniform turbulence distribution obtained by varying the $\alpha\epsilon^{2/3}$ parameter between 0.005 and 0.165 $m^{4/3}$/s and no yaw misalignment ($\gamma = 0°$). In the other half, turbulence is kept constant ($\alpha\epsilon = 0.03$ $m^{4/3}$/s) and γ is varied between ±40°. Additionally, all wind fields of the synthetic dataset have a uniform mean wind speed (no vertical shear). The realistic dataset consists of 150 wind fields characterized by sheared inflows and Gaussian distributions (μ representing the mean and σ the standard deviation) for $\alpha\epsilon^{2/3}$, γ and the shear exponent α ($\mu_{\alpha\epsilon^{2/3}} = 0.06\,m^{4/3}$/s, $\sigma_{\alpha\epsilon^{2/3}} = 0.02\,m^{4/3}$/s; $\mu_\gamma = 0°$, $\sigma_\gamma = 3°$; $\mu_\alpha = 0.15$, $\sigma_\alpha = 0.1$). The mean wind speed is varied between 6 and 14 m/s according to the wind speed distribution retrieved from wind-speed measurements on the west coast of Denmark [15].

In order to simulate the wind speed measurements close to a real power performance test, 10-min mean wind speeds are retrieved from the numerical wind fields from both virtual sonic anemometer (hereafter referred to as sonics) and nacelle-mounted lidar measurements. Specifically, we place one sonic anemometer at hub height and six more sonic anemometers along the vertical coordinate at distances of $\pm 6, \pm 14$ and ± 22 m from hub height. In this way, we obtain 10-min mean values of both power output and wind speed at seven different levels, similarly to a real power performance test where the wind speed is measured in front of an operating wind turbine.

2.2. Lidar simulations and wind-speed reconstruction

The lidar simulator scans the same velocity fields used as input to the aeroelastic simulations without considering the impact of the wind turbine, i.e., the induction zone in front of the rotor is not modelled. We simulate measurements from the DTU SpinnerLidar [16], which is a continuous-wave Doppler wind lidar that scans over the rose pattern shown in figure 1-a. Similar to [16], we assume that at the 400 locations of the rose pattern, shown as filled circles in figure 1, we obtain 400 averaged Doppler radial velocity spectra for each full scan. The system is set to generate a rose pattern every 2 s, so we get 300 Doppler spectra at each of the 400 scanning locations within a 10-min period. The SpinnerLidar is characterized by a laser wavelength of 1.565 μm and a lens aperture radius of 28 mm, which result in the weighting function φ shown in figure 1-b when the SpinnerLidar is focused at 1D in front of the rotor. In order to provide a good estimation of the probe-volume effect without getting out of the turbulence-box boundaries, we model the probe volume over a distance of 20 times the Rayleigh length Z_r, which is a lidar characteristic length defined by the laser wavelength, the lens radius and the focus distance. The portion of weighting function within $\pm 10\,Z_r$ around the focus point is highlighted in red in figure 1-b.

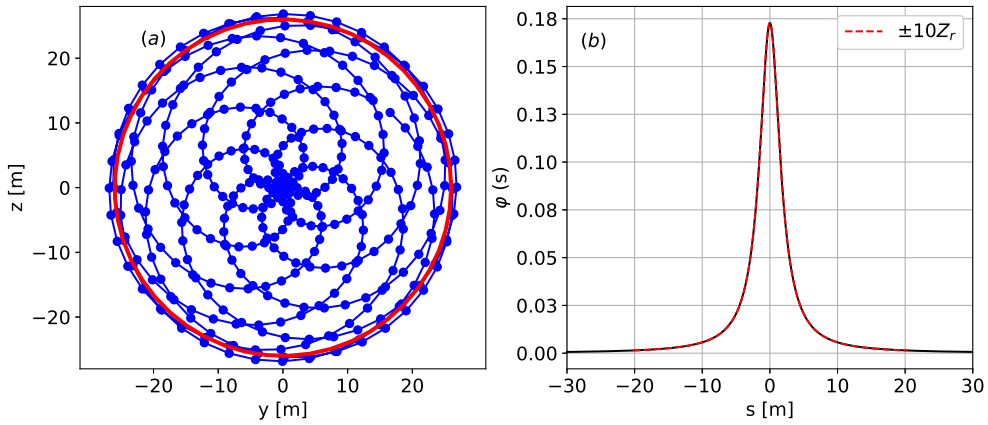

Figure 1. (*a*) Scanning configuration of the SpinnerLidar (*blue*) focused at 1D in front of the rotor (*red*). (*b*) Weighting function of the SpinnerLidar focused at 1D.

The simulated Doppler radial velocity spectrum is obtained as

$$S(v_r, t) = \int_{-10Z_r}^{10Z_r} \varphi(s) \cdot \delta(v_r - \mathbf{u}(s) \cdot \mathbf{n})\, \mathrm{d}s, \tag{1}$$

where s is the distance from the focus point along the lidar beam direction, v_r is the velocity component along the beam (radial velocity), $\mathbf{n}$ is the unit vector $\mathbf{n} = (n_x, n_y, n_z)$ along the beam direction and δ is the Dirac delta function. Equation 1 can be viewed as a weighted histogram distribution of v_r, which returns the weighted frequency of the considered value within the probe volume. We choose a discretization of 0.1 m/s for the histogram distribution in order to match the typical velocity resolution of a real lidar system. The measured radial velocity is then retrieved as the first statistical moment of the Doppler spectrum:

$$v_r(t) = \int_{-\infty}^{\infty} v_r \cdot S(v_r, t)\, \mathrm{d}v_r. \tag{2}$$

The radial velocity variance $\sigma_{v_r}^2$ is estimated as the second central moment of the ensemble averaged Doppler spectrum $\mathbf{S}(v_r) = \langle S(v_r, t) \rangle$ in order to avoid turbulence filtering caused by the probe-volume effect [17]:

$$\sigma_{v_r}^2 = \int_{-\infty}^{\infty} \mathbf{S}(v_r)(v_r - \bar{v}_r)^2\, \mathrm{d}v_r, \tag{3}$$

where $\bar{v}_r$ is the first moment of $\mathbf{S}(v_r)$. The virtual measurements of v_r and $\sigma_{v_r}^2$ are then used to reconstruct both the mean and variance of the wind speed over the 10-min interval.

In order to estimate the 10-min mean wind speed $\mathbf{U} = (U, V, W)$, the lidar beams are clustered in bins according to their height with a discretization of $\Delta z = 1$ m, so that the wind speed can be assumed as homogeneous within each bin despite of the wind shear. Consequently, the mean wind speed at each height $U(z)$ is retrieved by applying a least-square fit to all the beams within the same bin:

$$\Delta^2 = \int (\mathbf{n} \cdot \mathbf{U} - \langle v_r \rangle)^2 \mathrm{d}\mu, \tag{4}$$

where $\langle v_r \rangle$ is the ensemble average of the 300 radial velocities measured at each of the positions in the rose pattern during the 10-min period. Since the wind fields are homogeneous with regards

to turbulence, the Reynolds stress tensor $\mathbf{R}$ is assumed as uniform over the whole scanned area. Therefore, the Reynolds stresses $R_{ij} = \langle u_i' u_j' \rangle$ are retrieved by applying a least-square fit to all the beams:

$$\Delta^2 = \int (\mathbf{n} \cdot \mathbf{R}\mathbf{n} - \sigma_{v_r}^2)^2 \mathrm{d}\mu. \tag{5}$$

More details about the mean and turbulence reconstruction techniques can be found in [18].

2.3. Evaluation of the multi-dimensional power curves

After carrying out the HAWC2 simulations and scanning the wind fields with the virtual lidar, we get two datasets with 720 (synthetic dataset) and 150 (realistic dataset) observations of 6 attributes: U from both SpinnerLidar and sonics, the first Reynolds stress component $\langle u'u' \rangle = \sigma_u^2$ from both SpinnerLidar and sonics, $\cos(\gamma)$ and the 10-min mean power output P. The mean wind speed U is evaluated as the wind speed at hub height in the synthetic dataset, while in the realistic dataset, U is the rotor equivalent wind speed defined as in [3]. It should be noted that in cases of yaw misalignment $\gamma \neq 0°$, U measured by the SpinnerLidar represents the wind-speed component perpendicular to the rotor instead of the horizontal wind speed, as the nacelle-mounted lidar yaws with the turbine.

The two datasets are used to define three different multi-variable power curves: $P = P(U, \sigma_u^2)$, $P = P(U, \gamma)$ and $P = P(U, \sigma_u^2, \gamma)$, where U and σ_u^2 are measured from the SpinnerLidar or the sonics. The multi-variable power curves are modelled as multivariate polynomial regressions, whose input attributes consist of a polynomial combination of the original attributes with degree less than or equal to the specified degree β. For example, for the bivariate power curve $P = P(U, \sigma_u^2)$ with $\beta = 2$, we get the following polynomial expression: $y = c_1 + c_2 x_1 + c_3 x_2 + c_4 x_1^2 + c_5 x_2^2 + c_6 x_1 x_2$, where $y = P$, $x_1 = U$, $x_2 = \sigma_u^2$ and $c_1, .., c_6$ are the regression coefficients. When accounting for the yaw misalignment γ, the input attributes are $X = [U, \cos(\gamma)]$ and $X = [U, \sigma_u^2, \cos(\gamma)]$ for the bivariate and trivariate cases, respectively. For each multi-variable power curve, we evaluate nine values of β from the first to the ninth order.

Each regression model is tested through a K-fold cross-validation with K = 10: the dataset is randomly split into 10 sub-datasets (folds) presenting the same number of observations, and each fold is used as testing dataset, while the training dataset consists of the other nine folds. This results in training and testing the model ten times obtaining ten different test errors E_j, which are computed as the root mean square deviation between the estimated power output P^{est} and the reference value given by the aeroelastic simulations P, i.e., $E_j = \sqrt{\frac{1}{N} \sum_i (P_i^{est} - P_i)^2}$, where N is the number of observations in the testing fold. Models are evaluated by looking at the generalization error $\lambda = \frac{1}{10} \sum_j E_j$. This procedure ensures that the final error λ does not depend on how the dataset is split into training and testing sets, since the model is tested over all the observations.

3. Results

The accuracy of the multi-dimensional power curves is compared to that of the IEC standard power curve, which is defined according to the latest IEC standard [6]. In case the wind field is characterized by shear, we correct for the wind shear by using the rotor equivalent wind speed, while we do not apply any turbulence normalization. This is in line with the standard, as both wind-shear and turbulence corrections are recommended but not mandatory procedures [6].

When the synthetic dataset is used to define the power curves, all the multi-dimensional power curves are more accurate than the IEC standard power curve, as shown in figure 2-a. Both $P(U, \gamma)$ and $P(U, \gamma, \sigma_u^2)$ outperform the IEC standard due to the strong yaw misalignment that cannot be characterized by the standard power curve. Additionally, also the bivariate power curve $P(U, \sigma_u^2)$ provides higher accuracy than that using the IEC standard, showing the benefits of including turbulence to analyze the power output. For $P(U, \sigma_u^2)$, the SpinnerLidar is

much more accurate than the sonic, as the SpinnerLidar measures the wind-speed component perpendicular to the rotor despite the yaw misalignment. Between the two bivariate power curves, $P(U, \gamma)$ is the most accurate due to the cases of very large yaw misalignment (up to 40°), which make the correlation between P and γ stronger than that between P and σ_u^2. However, the highest accuracy is given by considering both γ and σ_u^2; compared to the IEC standard, the error is reduced by 79% and 80% for the sonic and the SpinnerLidar, respectively.

Figure 2 also shows how the generalization error changes with the degree of the polynomial regressions. As seen in the figure, the optimal value of β varies for the different power curves. For the three-dimensional power curves, λ strongly decreases up to $\beta = 3$, remains nearly constant for $3 \leq \beta \leq 5$ and quickly increases for $\beta \geq 6$, with the same trend for both SpinnerLidar and sonic. The bivariate regressions present a larger interval of nearly optimal values for β, with values of λ close to the minimum within $3 \leq \beta \leq 7$ and $3 \leq \beta \leq 9$ when considering σ_u^2 and γ, respectively.

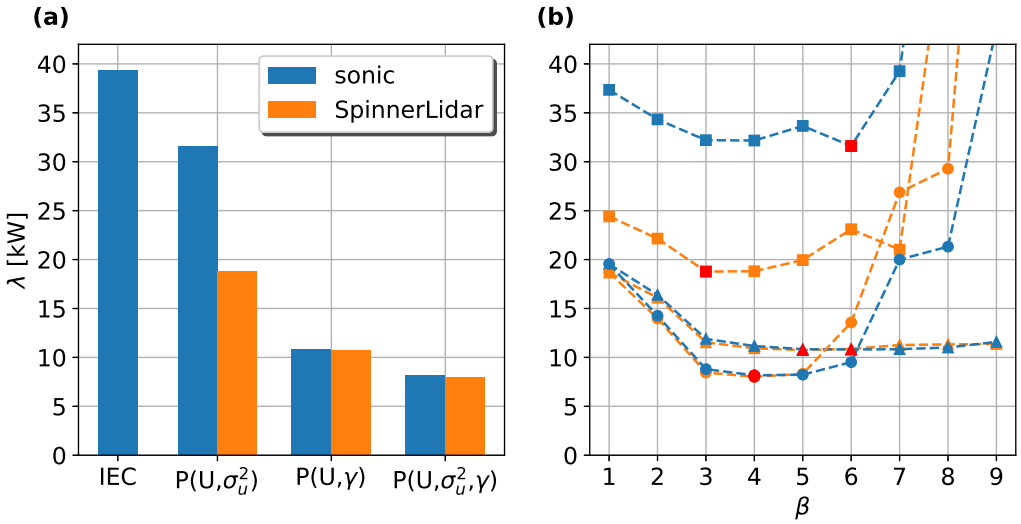

Figure 2. (a) Generalization error of power curves defined with the synthetic dataset when using the optimal β. (b) Variation of λ with the order of the polynomial regressions $P(U, \sigma_u^2)$ (*squares*), $P(U, \gamma)$ (*triangles*) and $P(U, \sigma_u^2, \gamma)$ (*circles*) based on sonic (*blue*) and SpinnerLidar (*orange*); optimal values are highlighted in red.

Figure 3 shows scatter plots of the power estimated by both the SpinnerLidar-based and the IEC power curves against the reference power given by the aeroelastic simulations for the synthetic dataset. Each scatter plot presents 720 points for both power curves since all the power values in the dataset are used for testing due to the cross validation. As shown in the figure, the multi-dimensional power curves provide a very good correlation between the estimated and reference power values without significant outliers, especially in the three-dimensional case.

When the realistic dataset is used to define the power curves, as shown in figure 4, only the bivariate regression $P(U, \sigma_u^2)$ is more accurate than that of the IEC standard. Similar to the results using the synthetic dataset, the SpinnerLidar provides higher accuracy than the sonic as the yaw misalignment is inherently accounted for. However, when γ is an input attribute to the regression, both the bivariate and trivariate regressions fail to outperform the IEC standard power curve for both sonic and SpinnerLidar measurements. This is due to the distribution of γ in the realistic dataset, which does not allow a proper training of the models.

When using the realistic dataset for training and testing, nearly all the multivariate

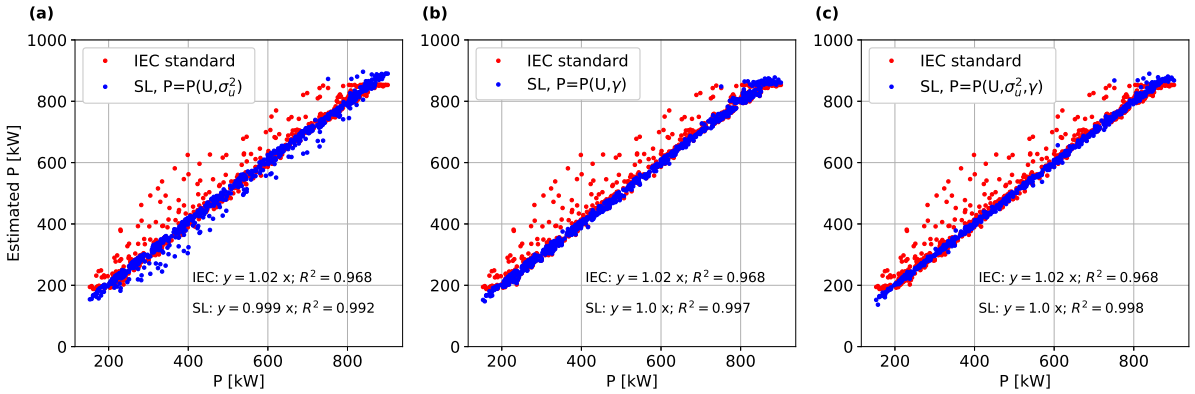

Figure 3. Scatter plots of the power estimated by both SpinnerLidar-based regressions and IEC standard power curve against the reference power for the synthetic dataset

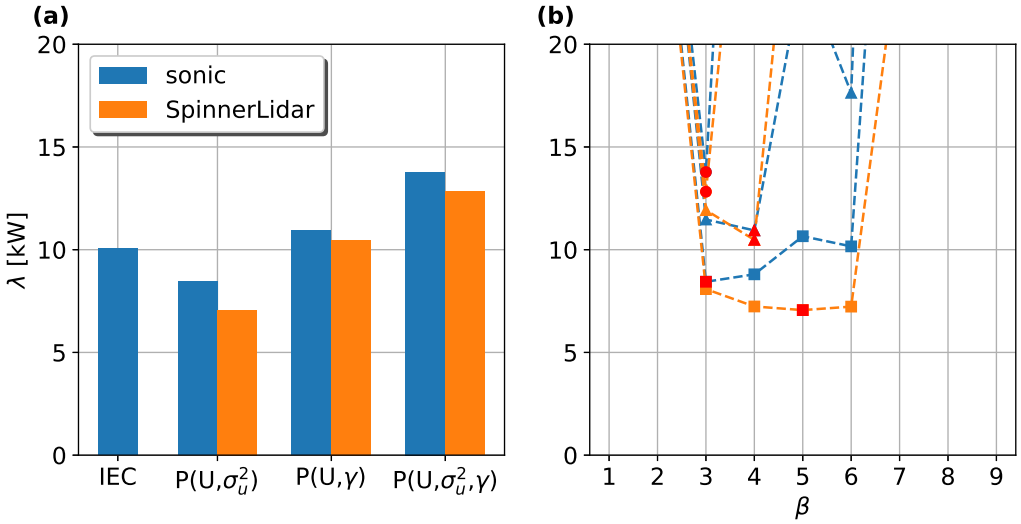

Figure 4. (*a*) Generalization error of power curves defined with the realistic dataset when using the optimal β. (*b*) Variation of λ with the order of the polynomial regressions $P(U, \sigma_u^2)$ (*squares*), $P(U, \gamma)$ (*triangles*) and $P(U, \sigma_u^2, \gamma)$ (*circles*) based on sonic (*blue*) and SpinnerLidar (*orange*); optimal values are highlighted in red.

regressions present the lowest error for $\beta = 3$ or $\beta = 4$, except for the SpinnerLidar-based $P(U, \sigma_u^2)$, which presents $\beta = 5$ as the optimal case. Additionally, for the three-dimensional case $P(U, \sigma_u^2, \gamma)$, λ quickly increases for $\beta > 3$ for both sonic- and SpinnerLidar-based power curves. Despite the higher mean error compared to the result of the IEC standard, figure 5 shows that the multi-dimensional power curves provide a reliable estimation of the power output, without resulting in large outliers.

Due to the differences in the results when analyzing the synthetic and realistic datasets, a third analysis is performed combining the two datasets. Specifically, all the multivariate polynomial regressions are trained on the synthetic dataset and tested on the realistic one. In this case, the models are evaluated based on the root mean square error instead of λ, since the models are only trained and tested once, without performing any cross-validation. As shown in figure 6, all the models including γ outperform the IEC standard power curve, with a clear

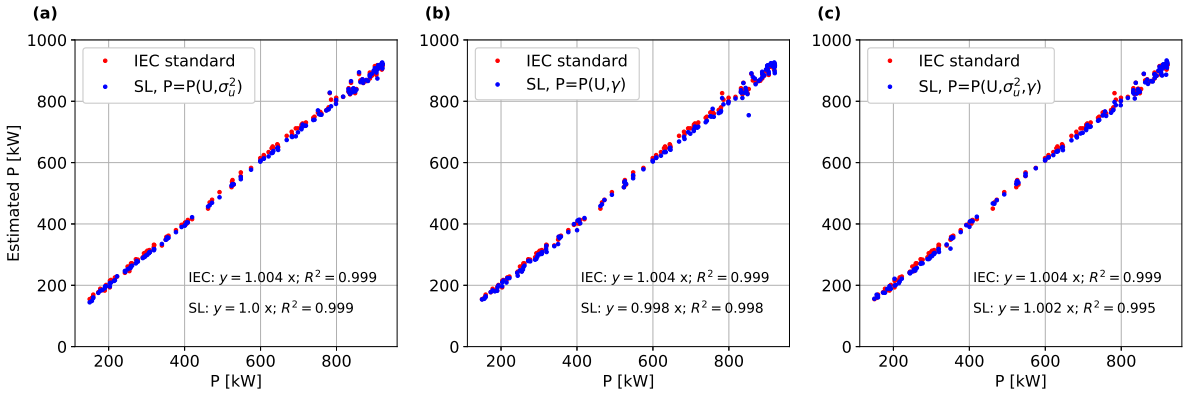

Figure 5. Scatter plots of the power estimated by both SpinnerLidar-based regressions and IEC standard power curve against the reference power for the realistic dataset

improvement compared to the case when the models are both trained and tested on the realistic dataset. This confirms that the realistic dataset is not suitable for training the models due to the low and non-uniformly distributed values of γ.

Furthermore, it should be noted that for the two-dimensional case $P(U, \sigma_u^2)$, only the SpinnerLidar outperforms the IEC standard, while the sonic provides an increase of the error. In this case, information about σ_u^2 does not benefit the power estimations; only when accounting for the yaw misalignment we observe the benefits. However, for both sonic and SpinnerLidar measurements, $P(U, \sigma_u^2, \gamma)$ outperforms $P(U, \gamma)$, showing that σ_u^2 adds valuable information to the model when γ is already known.

The three-dimensional power curve $P(U, \sigma_u^2, \gamma)$ provides the highest accuracy with an error of 7.2 kW and 6.4 kW for the sonic and the SpinnerLidar, respectively. When compared to the error of the IEC standard power curve (12.2 kW), this means a reduction of 41% and 48%. Differently from the case of figure 2, where the difference between sonics and SpinnerLidar is negligible, SpinnerLidar-based two-dimensional power curves perform better than those based on sonics. This is probably due to a better characterization of the wind shear and the kinetic energy flux throughout the rotor.

As shown in figure 6, the error of the three-dimensional power curve reaches the minimum for $\beta = 4$ and steeply increases for $\beta > 4$, further confirming the results in figure 2. Only when training the model with the realistic dataset, the trivariate regression presents $\beta = 3$ as the optimal case. However, that case can be neglected since the realistic dataset is not suitable to train the trivariate regression. In the two-dimensional cases $P(U, \sigma_u^2)$ and $P(U, \gamma)$, the error is nearly constant for a large number of degrees, similarly to the case of figure 2. Although it is not shown here, scatter plots for the case of figure 6 look similarly to those of figures 3 and 5, with very good correlation and without any outliers.

Figure 7 shows how the power output varies with σ_u^2 and γ according to the trivariate power curve $P = P(U, \sigma_u^2, \gamma)$ trained over the whole synthetic dataset and whose accuracy is shown in figure 6. In order to show the effect of the two variables σ_u^2 and γ, we use two different data distributions: in figures 7-(a,c), we have constant $\gamma = 0°$ and the same variation of U and σ_u^2 as in the synthetic dataset; in figures 7-(b,d), we have constant $\sigma_u^2 = 0.5\,\mathrm{m}^2/\mathrm{s}^2$ and the same variation of U and γ as in the synthetic dataset. As it can be seen in figures 7-(a,c), higher turbulence increases the power output for wind speed values close to cut-in, while it decreases the power output closely to the rated value. The yaw misalignment γ decreases the power output irrespective of the wind speed, as confirmed by figure 7-b. The effect seems to be the opposite

when looking at figure 7-*d*, as U represents the wind-speed component orthogonal to the rotor when using SpinnerLidar measurements. Consequently, in case of same U and different γ, higher γ means higher free-stream velocity. This effect on the power curve should not be misunderstood as a positive correlation between γ and P.

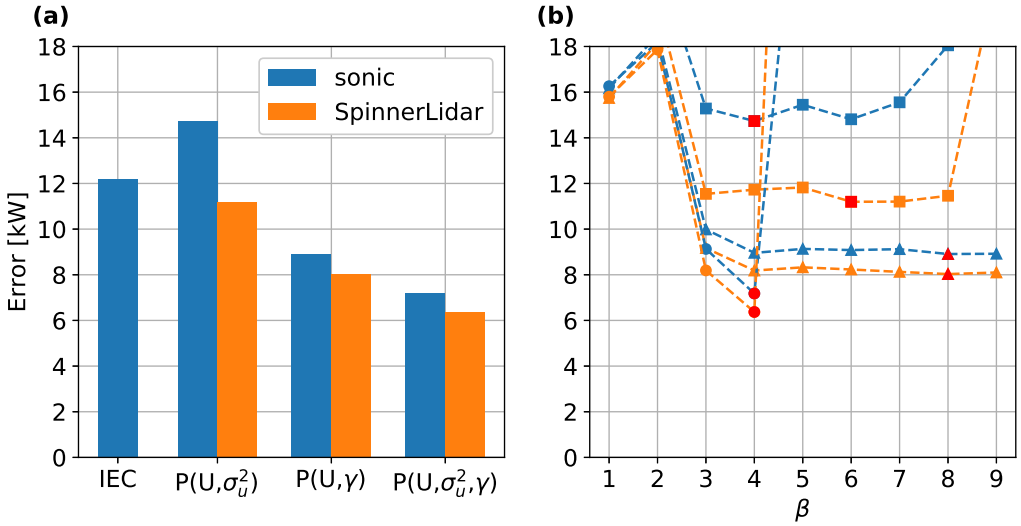

Figure 6. (*a*) Error of power curves trained on the synthetic dataset and tested on the realistic dataset when using the optimal β. (*b*) Variation of the error with the order of the polynomial regressions $P(U, \sigma_u^2)$ (*squares*), $P(U, \gamma)$ (*triangles*) and $P(U, \sigma_u^2, \gamma)$ (*circles*) based on sonic (*blue*) and SpinnerLidar (*orange*); optimal values are highlighted in red.

4. Discussion

Wind turbine power performance is modelled through multivariate power curves in the form of polynomial regressions, which present three input attributes: the mean wind speed U, the atmospheric turbulence evaluated as the wind speed variance σ_u^2 and the yaw misalignment γ. We do not include the shear exponent α as an input to the regressions as we account for the wind shear through the rotor equivalent wind speed. This likely gives similar accuracy to adding a 4^{th} term to the regression, without increasing the numerical complexity of the model. The evaluation of α as a 4^{th} input to the multivariate power curves could be part of the further development of this work.

The multivariate power curves are tested on a dataset consisting of virtual flow measurements. Therefore, one could question to which extent this approach would be affected by the uncertainties related to real field measurements. We are confident that the virtual flow measurements are a reliable and accurate representation of what we would get from field measurements, as long as these were conducted under nearly homogeneous conditions. In case of inhomogeneous conditions, the wind speed reconstruction described in section 2.2 would be unreliable, so that a different approach is needed to accurately retrieve U and σ_u^2 from the SpinnerLidar measurements v_r and $\sigma_{v_r}^2$. However, even when the assumption of homogeneity is rather crude, we expect the multivariate power curves to perform well. The difference is that the multivariate power curve will relate the power output to the lidar-derived characteristics rather than to the "true" flow characteristics. Additionally, when testing the multi-dimensional power curves with measurements out in the field, their accuracy might be challenged by the uncertainty in the estimation of the yaw misalignment, which is known in our virtual setup. Therefore,

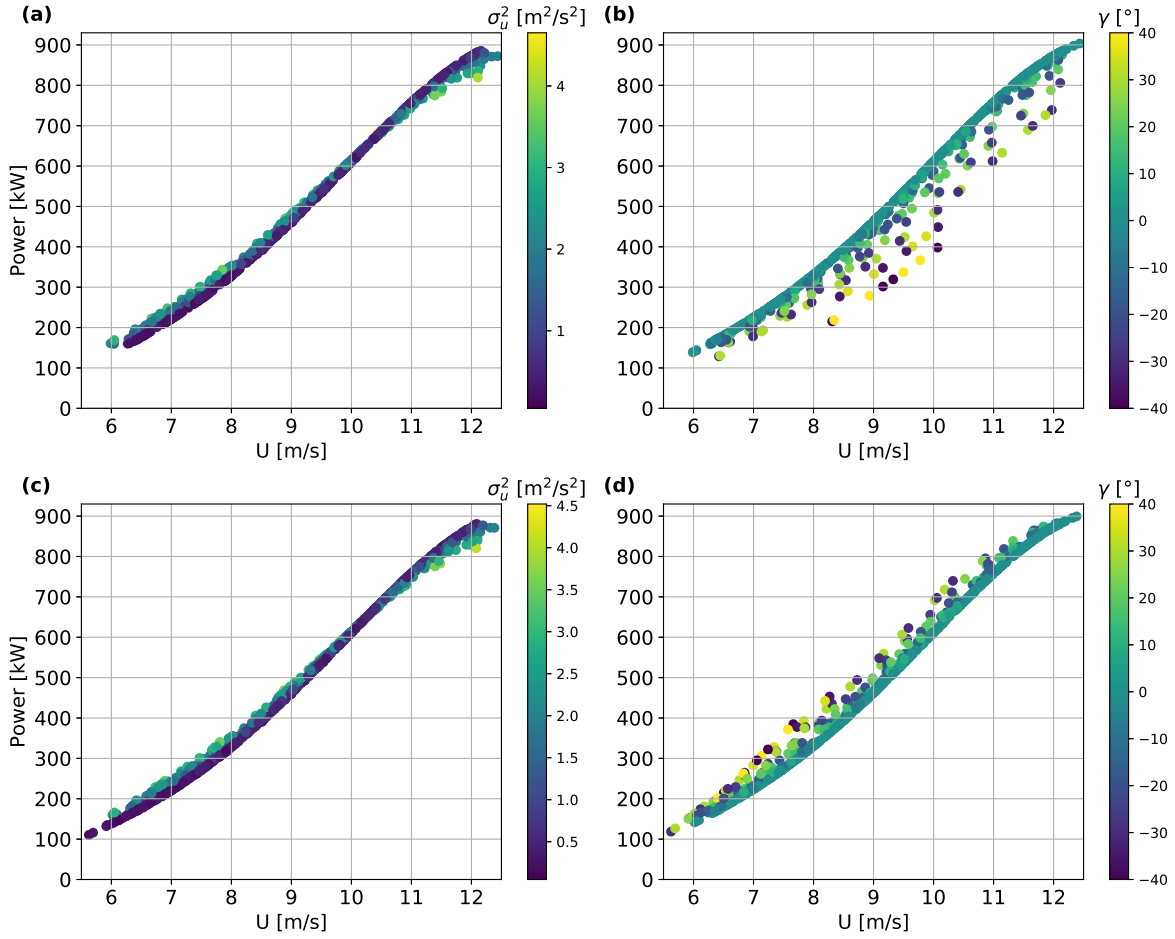

Figure 7. Power curves given by the trivariate regression $P = P(U, \sigma_u^2, \gamma)$ based on sonic (a, b) and SpinnerLidar (c, d) with $\gamma = 0°$ (a, c) and $\sigma_u^2 = 0.5\mathrm{m}^2/\mathrm{s}^2$ (b, d)

nacelle lidar measurements are needed to estimate the yaw misalignment more accurately than with, e.g., traditional nacelle-based wind vanes.

Testing the multivariate power curves under inhomogeneous conditions would be an interesting topic for future research. Additionally, it would be interesting to evaluate the necessary range of γ available in the training dataset in order to obtain accurate curves. Probably, in the synthetic dataset, we considered a larger γ interval ($\pm 40°$) than needed, while a larger standard deviation or more available data would make the realistic dataset suitable for training the model.

5. Conclusions

A methodology to evaluate power curves through aeroelastic simulations and virtual nacelle lidar measurements is outlined. Specifically, we test multi-dimensional power curves in the form of multivariate polynomial regressions, whose input attributes consist of the mean wind speed, the wind speed variance and the yaw misalignment. The mean wind speed is derived as either hub height wind speed or rotor equivalent wind speed, depending on whether the numerical wind fields are characterized by wind shear.

When properly trained, the multivariate polynomial regressions outperform the IEC standard

power curve. Specifically, when tested on a realistic dataset, which presents wind conditions similar to those of a test site on the west coast of Denmark, the trivariate power curve $P = P(U, \sigma_u^2, \gamma)$ predicts the power output with a 48% lower error than the IEC standard power curve. Additionally, the SpinnerLidar measurements increase the accuracy of the multi-dimensional power curve compared to mast-based sonic anemometers, due to a better characterization of the inflow to the rotor.

The optimal value for the degree of the polynomial expressions change depending on the input attributes, the dataset and the measuring device (mast-based anemometry or nacelle-mounted lidar). For the three-dimensional case $P(U, \sigma_u^2, \gamma)$, the minimum error is obtained with a polynomial expression of the 4^{th} order when using both the SpinnerLidar and the sonic measurements. However, a different optimal polynomial degree might be found using a different dataset.

Our results show that multi-dimensional power curves in the form of multivariate polynomial regressions can be a valuable alternative to the IEC standard power curve, with possible improvements in wind turbine power prediction and energy yield assessment.

This work should be extended by testing the same multi-dimensional power curves with either simulations of more realistic flow cases or measurements from a nacelle-mounted SpinnerLidar out in the field. Moreover, it would be interesting to test the same approach under inhomogeneous conditions, i.e. for wind turbines under waked conditions, where the gain in accuracy compared to the IEC standard power curve is expected to be much larger than what found in this work for homogeneous conditions.

Acknowledgement
This study is funded by the European Union's Horizon 2020 research and innovation program under the Marie Sklodowska-Curie grant agreement No. 858358 (LIKE – Lidar Knowledge Europe, H2020-MSCA-ITN-2019).

References

[1] IEC 2005 61400-12-1, power performance measurements of electricity producing wind, turbines

[2] Bardal L and Sætran L 2017 Influence of turbulence intensity on wind turbine power curves vol 137 pp 553–558

[3] Wagner R, Courtney M, Gottschall J and Lindelöw-Marsden P 2011 *Wind Energy* **14** 993–1004

[4] Clifton A and Wagner R 2014 Accounting for the effect of turbulence on wind turbine power curves vol 524

[5] Hedevang E 2014 *Wind Energy* **17** 173–195

[6] IEC 2017 61400-12-1, power performance measurements of electricity producing wind, turbines

[7] Bulaevskaya V, Wharton S, Clifton A, Qualley G and Miller W 2015 *Journal of Renewable and Sustainable Energy* **7**

[8] Clifton A, Kilcher L, Lundquist J and Fleming P 2013 *Environmental Research Letters* **8**

[9] Saint-Drenan Y M, Besseau R, Jansen M, Staffell I, Troccoli A, Dubus L, Schmidt J, Gruber K, Simões S and Heier S 2020 *Renewable Energy* **157** 754–768

[10] Fleming P, Annoni J, Shah J, Wang L, Ananthan S, Zhang Z, Hutchings K, Wang P, Chen W and Chen L 2017 *Wind Energy Science* **2** 229–239

[11] Gebraad P, Teeuwisse F, Van Wingerden J, Fleming P, Ruben S, Marden J and Pao L 2016 *Wind Energy* **19** 95–114

[12] Mann J 1994 *Journal of Fluid Mechanics* **273** 141–168

[13] Larsen T and Hansen A 2007 *How 2 HAWC2, the user's manual* (Risø National Laboratory) ISBN 978-87-550-3583-6

[14] Mann J 1998 *Probabilistic Engineering Mechanics* **13** 269–282

[15] Peña A, Floors R, Sathe A, Gryning S E, Wagner R, Courtney M S, Larsén X G, Hahmann A N and Hasager C B 2016 *Boundary-layer Meteorology]* **158** 1–26

[16] Peña A, Mann J and Rolighed Thorsen G 2019 *SpinnerLidar measurements for the CCAV52* (*DTU Wind Energy E* vol 0177) (Denmark: DTU Wind Energy) ISBN 978-87-93549-45-6

[17] Mann J, Peña A, Bingöl F, Wagner R and Courtney M 2010 *Journal of Atmospheric and Oceanic Technology* **27** 959–976

[18] Fu W, Peña A and Mann J 2021 *Wind Energy Science Discussions* **2021** 1–29

Paper VI: Numerical evaluation of multivariate power curves for wind turbines in wakes using nacelle lidars

Renewable Energy 202 (2023) 419–431

Contents lists available at ScienceDirect

Renewable Energy

journal homepage: www.elsevier.com/locate/renene

Numerical evaluation of multivariate power curves for wind turbines in wakes using nacelle lidars

Alessandro Sebastiani *, Alfredo Peña, Niels Troldborg

DTU Wind and Energy Systems, Technical University of Denmark, Frederiksborgvej 399, Roskilde, 4000, Denmark

ARTICLE INFO

Dataset link: https://doi.org/10.11583/DTU.20156714

Keywords:
Nacelle lidars
Power curves
Turbulence
Wakes
Multivariable regression

ABSTRACT

The IEC standards describe how to measure the power performance of an isolated wake-free wind turbine. However, most wind turbines operate under waked conditions for a substantial amount of time, calling for the need of a new methodology for power performance evaluation. We define multivariate power curves in the form of multivariate polynomial regressions, whose input variables are several wind speed and turbulence measurements retrieved with nacelle lidars. We use a dataset of synthetic power performance tests including both waked and wake-free conditions. The dataset is generated through aeroelastic simulations combined with both virtual nacelle lidars and the dynamic wake meandering model. A feature-selection algorithm is used to select the input variables among the available measurements, showing that the optimal model includes four input variables: three correspondent to wind speed and one to turbulence measures. Additionally, we give insights on the optimal nacelle-lidar scanning geometry needed to implement the multivariate power curve. Results show that the multivariate power curves predict the power output with accuracy of the same order under both waked and wake-free operation. For the in-wake cases, the accuracy is much higher than that of the IEC standard power curve, with an error reduction of up to 88%.

1. Introduction

For many years, the power output of a wind turbine was defined as function of two flow characteristics: the air density and the wind speed at hub height [1]. However, several studies have shown that additional variables should be considered when evaluating the power performance of a wind turbine, e.g. turbulence characteristics and vertical wind shear [2–4]. Clifton and Wagner [2] investigated the effect of atmospheric turbulence on the power output of a wind turbine through aeroelastic simulations and showed that turbulence and power are closely related for wind speeds just above the cut-in and just below the rated value. Specifically, the power output increases with turbulence around cut-in, while it decreases close to rated. The same effect was shown with measurements by Hedevang [5] and Bardal and Sætran [4]. Wagner et al. [3] evaluated the effect of the vertical wind shear on the power output. They showed that one single velocity measurement at hub height does not accurately estimate the kinetic energy flux through the rotor. Therefore, they introduced a methodology to increase the accuracy of the power curve by using wind speed measurements from several heights combined into one scalar quantity, the rotor equivalent wind speed.

Research on the effect of turbulence and vertical wind shear led to the revision of the International Electrotechnical Commission (IEC) standard for power performance testing. In the most recent version, both turbulence intensity and wind shear are included as variables to be considered when testing power curves [6]. However, the IEC standard power curves still provide a rather simplified evaluation of the power performance and require further improvements. One of the main issues, portrayed also in its newest edition, is that the IEC standard only describes the methodology to assess the power performance of an isolated, wake-free wind turbine. However, most wind turbines are currently clustered together within wind farms and operate under waked conditions for a substantial amount of time. This means that these wind turbines operate without an accurate indication of their power performance under their actual operating conditions. This is not only true for the waked wind turbines. Due to blockage effects, the performance of the non-waked wind turbines in a wind farm are also affected as shown by Sebastiani et al. [7]. Therefore, there is a need to implement an alternative methodology for power performance evaluation, which is reliable under waked conditions or complex inflow in general.

Several previous works have introduced alternative methods to model the power curve of a wind turbine. In some, the power output was modelled as function of the wind speed at hub height through both parametric and non-parametric models [8–11]. In others, the

* Corresponding author.
E-mail address: aseb@dtu.dk (A. Sebastiani).

https://doi.org/10.1016/j.renene.2022.11.081
Received 12 July 2022; Received in revised form 17 November 2022; Accepted 19 November 2022
Available online 23 November 2022

power performance was modelled through multivariate power curves accounting for several atmospheric variables, such as turbulence, vertical wind shear and wind veer [12–15]. Some other studies included control variables as the turbine's rotational speed and pitch angle of the blades [16,17]. Additionally, Sebastiani et al. [18] used trivariate power curves accounting for wind speed, turbulence and yaw misalignment. In many of these studies, only one wind speed measurement was considered [8–11,16,17], while others used wind speeds at several heights to characterize the vertical wind shear [12–15]. However, none of the studies included more than one wind speed measurement at the same height, which could be beneficial under waked conditions. Additionally, none of the available studies specifically focused on waked conditions.

In this work, we test multivariate power curves, which include several wind speed and turbulence measurements retrieved through nacelle-mounted lidars. To the best of our knowledge, this is the first evaluation of multivariate power curves in wakes using nacelle lidars. The main objective is to evaluate the power performance of a wind turbine with the same accuracy under both waked and free-standing conditions. We define multivariable power curves in the form of multivariate polynomial regressions, whose input variables are both wind speed and turbulence measurements at several locations in front of the rotor. We test several lidar configurations, with a varying number (from 6 to 400) of wind speed measurements. A feature-selection algorithm is used to select the optimal number of measurements needed to evaluate the power performance, as well as to give insights about the best measurement locations. The analysis is conducted on a dataset of synthetic power performance measurements, which is built with the combination of aeroelastic simulations and virtual nacelle lidar measurements. We use the dynamic wake meandering (DWM) model [19] to generate waked inflows and simulate power performance measurements in wake.

This paper is organized as follows. The methodology is outlined in Section 2, with descriptions of the homogeneous turbulent wind fields in Section 2.1, the DWM model in Section 2.2 and the lidar simulator in Section 2.3. In Section 2.4, we describe how the aeroelastic simulations are combined with the virtual lidars and the DWM model to generate a dataset of virtual power performance tests. The implementation of the multivariate power curves is described in Section 2.5. Results from the analysis for wake-free and waked conditions are shown in Sections 3.1 and 3.2, respectively. The combination of both conditions is shown in Section 3.3, while the optimal lidar scanning configuration is described in Section 3.4. Finally, discussion and conclusions are presented in Sections 4 and 5, respectively.

2. Methodology

We use the DTU in-house aeroelastic code HAWC2 [20] to perform aeroelastic simulations of the Vestas V52 wind turbine [21], which has a rated power of 850 kW and rotor diameter (D) of 52 m. Additionally, we implement a lidar simulator to retrieve virtual nacelle lidar measurements from the same turbulent wind fields, which are used as input to the aeroelastic simulations. The combination of the power output from the HAWC2 simulations and the virtual measurements from the lidar simulator results in a dataset of virtual power performance measurements. Specifically, the dataset is divided in two distinct parts, consisting of power performance measurements under homogeneous and waked conditions, respectively; the wake fields are simulated with the DWM model.

2.1. Turbulence spectral model

We use three-dimensional homogeneous turbulent wind fields generated with the turbulence spectral model by Mann [22], hereafter referred to as Mann model. The three-dimensional wind field is described by the vector field $\mathbf{u}(\mathbf{x})$, as time dependency is neglected because of the Taylor's frozen turbulence hypothesis. The velocity vector field $\mathbf{u} = (u, v, w)$ consists of the along-wind (u), transverse (v) and vertical (w) components, with the along-wind component aligned with the x direction of the right-hand coordinate system $\mathbf{x} = (x, y, z)$, as shown in Fig. 2. Assuming homogeneous turbulence and no vertical wind speed, the mean velocity field results in $\langle \mathbf{u}(\mathbf{x}) \rangle = (U(z), 0, 0)$, where the wind speed variation with height depends on the vertical shear.

The second-order statistics of the homogeneous three-dimensional wind field can be described with the spectral tensor $\boldsymbol{\Phi}(\mathbf{k})$, which is the Fourier transform of the covariance tensor $\mathbf{R}(\mathbf{r})$, where $\mathbf{r}$ is the separation vector and $\mathbf{k} = (k_1, k_2, k_3)$ is the vector field representing the wavenumbers along the (x, y, z) directions. The Mann model describes the spectral tensor $\boldsymbol{\Phi}$ as function of three parameters: $\alpha\epsilon^{2/3}$ is the product between the Kolmogorov constant α and the turbulent energy dissipation rate ϵ, Γ is a parameter related to the anisotropy of the turbulence field, and L is a length scale related to the size of the turbulence eddies.

In this work, all the three-dimensional turbulent wind fields are generated with $L = 29.4$ m and $\Gamma = 3.9$, which are the values suggested in the IEC standard [23], while $\alpha\epsilon^{2/3}$ is varied according to the desired level of atmospheric turbulence. All the wind fields have the maximum number of grid points allowed in HAWC2: $(N_x, N_y, N_z) = (8192, 64, 64)$.

2.2. Dynamic wake meandering model

The DWM model simulates wind turbine wakes in a time domain at a relatively low computational expense. It relies on Taylor's frozen turbulence assumption and consists of three elements: a model of the quasi-steady velocity deficit and its evolution downstream; a model of the wake meandering due to large-scale turbulence structures, and a model of the wake-generated turbulence [19].

The definition of the quasi-steady velocity deficit is strongly inspired by the work of Ainslie [24]. The wake deficit in the near-wake region (within 2–3D) is defined by the turbine's axial induction derived from blade element momentum (BEM) theory [19]. In the far-wake region (downstream distances larger than 2–3D), the wake evolution is described by the thin shear layer approximation of the rotationally symmetric Navier–Stokes (N–S) equations, with the pressure terms disregarded and an eddy viscosity term used for turbulence closure [19]. The eddy viscosity ν_t accounts for both atmospheric and shear layer generated turbulence through the formulation by Keck et al. [25]:

$$\nu_t = F_1\, k_1\, \mathrm{TI}_{amb} + F_2\, k_2 \max\left(\frac{R_w^2}{U_{\mathrm{hub}}\, R} \left| \frac{\partial U}{\partial R} \right| ; \frac{R_w}{R} \left(1 - \frac{U_{\min}}{U_{\mathrm{hub}}} \right) \right), \qquad (1)$$

where R_w is the wake radius, R is the rotor radius, TI_{amb} is the ambient turbulence intensity, $U_{\min}$ is the minimum wind speed in the wake and U_{hub} is the free-stream velocity at hub height. F_1 and F_2 are filter functions used to model the development of the turbulent stresses inside the wake. k_1 and k_2 are empirical constants. In our work, we use the HAWC2 default values for F_1, F_2, k_1 and k_2.

In the DWM model, the wake is assumed as a passive tracer driven by large-scale turbulence structures. Trujillo et al. [26] showed that the atmospheric turbulence structures responsible for the wake meandering are in the order of 2D and larger. Therefore, in the DWM model, the wake meandering is modelled by superimposing turbulence fluctuations with a cut-off frequency of $f_{cut} = \frac{U}{2D}$. Those turbulence fluctuations are modelled with a Mann-model generated turbulence box, which presents a discretization of $\Delta y = \Delta z = D$ and where the velocity vectors at each grid point represent the average over the grid cube.

In addition to the atmospheric turbulence and the apparent turbulence due to the meandering of the wake, additional turbulence is generated in the wake as a consequence of the velocity shear, as well as of trailing vortices generated at both tip and root of the blade. Wake-generated turbulence tends to be isotropic and characterized by smaller structures than atmospheric turbulence [27]. Therefore,

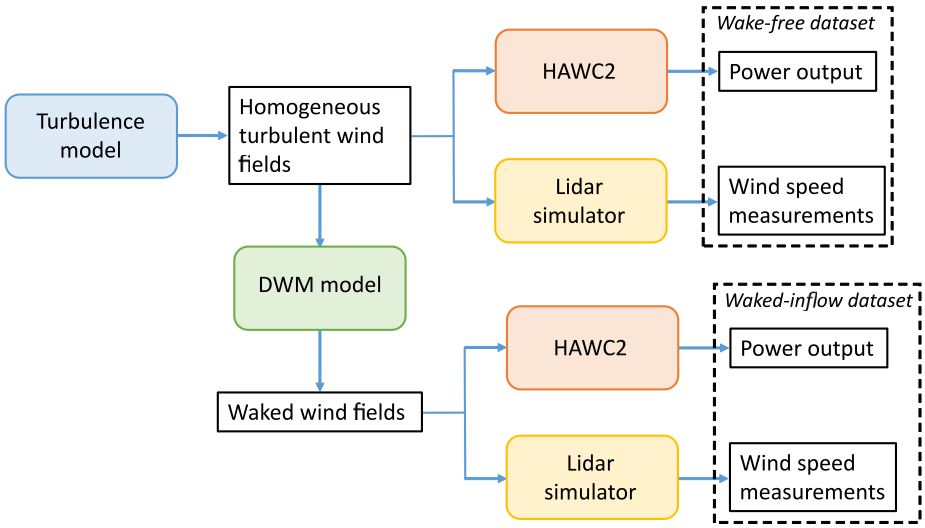

Fig. 1. Illustration of the numerical framework utilized to generate the dataset of virtual power performance measurements.

additional wake turbulence is modelled by super-imposing a Mann-model turbulence box generated with $\Gamma = 0$ and a length scale L which is 10% of the atmospheric turbulence length scale. Additionally, wake turbulence is purely mechanically generated and rather inhomogeneous. In the DWM, the inhomogeneity of wake-generated turbulence is modelled by scaling the wake turbulence box with the factor

$$K_{mt}(\hat{r}) = |1 - \hat{U}_{\text{def}}(\hat{r})|\, k_{m1} + \left|\frac{\partial \hat{U}_{\text{def}}(\hat{r})}{\partial \hat{r}}\right| k_{m2}, \tag{2}$$

where $\hat{U}_{\text{def}}$ is the axisymmetric wake velocity $U_{\text{def}} = U_{\text{amb}} - \Delta U$ nondimensionalized with U_{hub}. $\hat{r}$ is the radial distance normalized by the rotor radius. k_{m1} and k_{m2} are empirical constants [19]. We use the HAWC2 default values for both k_{m1} and k_{m2}.

The final three-dimensional velocity field is obtained through linear superposition of the quasi steady velocity deficit, the meandering turbulence and the wake-generated turbulence to the homogeneous ambient velocity field:

$$u_{\text{DWM}} = U_{\text{def}} + u'_{\text{amb}} + u'_{\text{meandering}} + K_{mt}\, u'_{\text{wake}} \tag{3}$$

2.3. Nacelle lidar simulator

We implement a lidar simulator to retrieve virtual nacelle lidar measurements from the same turbulent velocity fields used as input to the aeroelastic simulations. As shown in Fig. 2, the forward-looking lidar is located in the centre of the (y, z) plane and scans the inflow approaching the wind turbine. We simulate continuous-wave (CW) lidars using a typical weighting function $\varphi(s)$, which allows us to model the lidar probe-volume effect [28]:

$$\varphi(s) = \frac{1}{\pi}\,\frac{z_r}{z_r^2 + s^2}, \quad \text{with } z_r = \frac{\lambda\, f_d^2}{\pi\, r_b^2}, \tag{4}$$

where z_r is the Rayleigh length, λ is the laser wavelength, r_b is the lens aperture radius, f_d is the focus distance and s is the distance from the focus point along the lidar beam direction.

In this work, we assume $\lambda = 1565$ nm and $r_b = 28$ mm, which are common values among available CW lidars. In order to provide a realistic modelling of the probe-volume effect without requiring a critically large wind field, we model the weighting functions over distances of $\pm 6 z_r$ around the focus point, accounting for around 90% of the weight.

We test different scanning configurations, comprising both commercial and research lidars, as shown in Fig. 3. Specifically, we simulate the DTU SpinnerLidar [29], which retrieves 400 measurements every 2 s along the rose pattern of Fig. 3(a). Additionally, we simulate a 6-beam lidar and a circular scanning lidar. The 6-beam configuration is chosen as it is the optimal configuration for turbulence measurements [30], while the circular configuration is chosen as it is performed by one of the available commercial lidars for power performance tests. We also include a grid of 'sonic anemometers', which are able to retrieve the true wind and turbulence characteristics, without being affected by neither the volume averaging nor the method used to reconstruct the wind, as most lidars are.

The lidar virtual measurements consist in the retrieval of the Doppler radial velocity spectrum as

$$S(v_r, t) = \int_{s_{\min}}^{s_{\max}} \varphi(s)\,\delta(v_r - \mathbf{u}(s)\cdot\mathbf{n})\,\mathrm{d}s, \tag{5}$$

where v_r is the velocity component along the beam (radial velocity), $\mathbf{n} = (n_x, n_y, n_z)$ is the unit vector along the beam direction and δ is the Dirac delta function. Eq. (5) can be considered as a weighted histogram distribution of v_r within the probe volume. We use a discretization of 0.1 m/s for the histogram distribution in order to match the typical velocity resolution of a real lidar system. The measured radial velocity is the first statistical moment of the Doppler spectrum:

$$v_r(t) = \int_{-\infty}^{\infty} v_r S(v_r, t)\,\mathrm{d}v_r. \tag{6}$$

Here, the along-wind component u of the velocity vector is retrieved from the radial velocity by neglecting the contribution of both the transverse v and vertical w components:

$$u = \frac{v_r}{n_x}. \tag{7}$$

In order to get information about turbulence, the radial velocity variance $\sigma^2_{v_r}$ is obtained as the second central moment of the ensemble averaged Doppler spectrum $\mathbf{S}(v_r) = \langle S(v_r, t)\rangle$:

$$\sigma^2_{v_r} = \int_{-\infty}^{\infty} \mathbf{S}(v_r)\left(v_r - \bar{v}_r\right)^2 \mathrm{d}v_r, \tag{8}$$

where $\bar{v}_r$ is the first central moment of $\mathbf{S}(v_r)$, i.e., the mean radial velocity. This ensures that $\sigma^2_{v_r}$ is not affected by turbulence filtering due to the lidar spatial averaging [31].

When we face conditions in which the turbulent wind field is free of wakes, i.e., when the turbulent inflow is homogeneous, the components of the Reynolds stress tensor (variances and covariances of the velocity components) are estimated from the radial velocity variances $\sigma^2_{v_r}$ of the different lidar beams following the methodology described by Fu et al. [32].

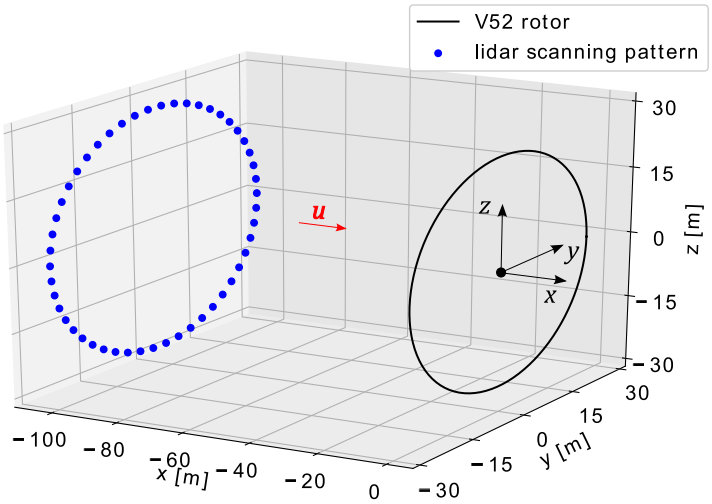

Fig. 2. Illustrative three-dimensional view of one of the simulated scanning patterns, the turbine rotor and the along-wind velocity component.

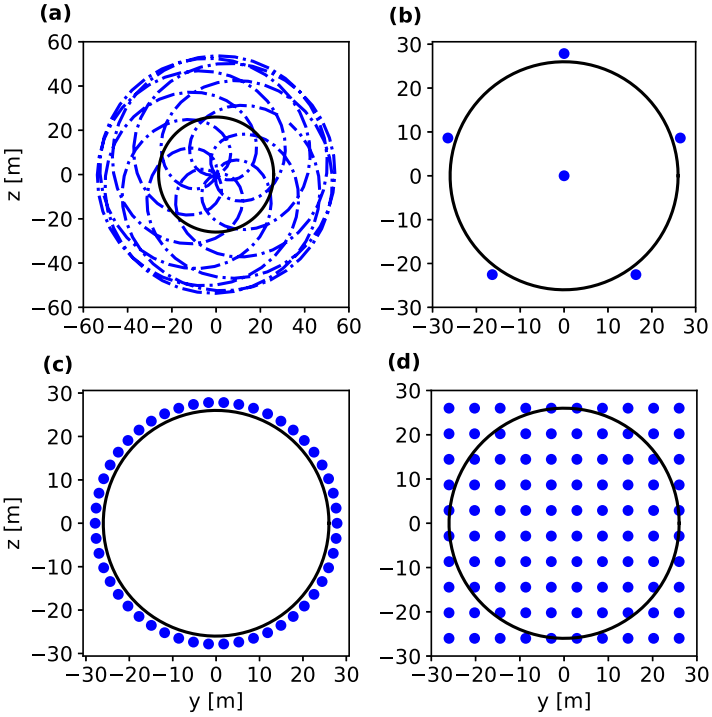

Fig. 3. Nacelle lidar scanning configurations: (*a*) SpinnerLidar focused at 2D; (*b*): 6-beam lidar focused at 2D; (*c*) circular scanning lidar focused at 2D; (*d*) grid of 'sonic anemometers'. The rotor is highlighted in *black*.

2.4. Generation of the dataset

As shown in Fig. 1, we combine HAWC2 with the DWM model and the lidar simulator to generate two datasets of virtual power performance tests: one consisting of wake-free homogeneous cases and the other of waked inflows, hereafter referred to as the wake-free and waked-inflow datasets. For the retrieval of 10-min statistics of both power output and wind characteristics, all the wind turbulent fields have dimensions of $(U_\infty T, 128\,\mathrm{m}, 128\,\mathrm{m})$, with $T = 700$ s. The additional 100 s are added to get 10-min statistics from the lidars, whose focus point is upstream of the rotor and that would otherwise be out of the turbulent field during the last few seconds of the simulation. The length of 128 m is chosen for both transverse and vertical directions so that we can account for a large portion of the weighting function. Additionally, some distance is needed between the rotor and the edge of the turbulence box in order to avoid possible biases due to field periodicity [33].

The wake-free dataset contains results from 620 10-min aeroelastic simulations characterized by uniform inflows (no shear). The wind speed varies uniformly within $[4, 14]$ m/s to cover the power curve from cut-in to rated values. The turbulent fields are characterized by $L = 29.4$ m, $\Gamma = 3.9$ and the parameter $\alpha\epsilon^{2/3}$ is nearly uniformly distributed within $[0.002, 0.25]$ $\mathrm{m}^{4/3}/\mathrm{s}$. The $\alpha\epsilon^{2/3}$ values are selected in order to get similar TI distributions at different wind speed ranges, with most values between 5% and 20%.

The waked-inflow dataset presents 864 10-min aeroelastic simulations characterized by waked conditions simulated with the DWM model. Three different wake conditions are included: 1/3 of the cases present a centred full wake, 1/3 a partial wake on the right side of the rotor ($\Delta y > 0$ m) and 1/3 a partial wake on the left side of the rotor

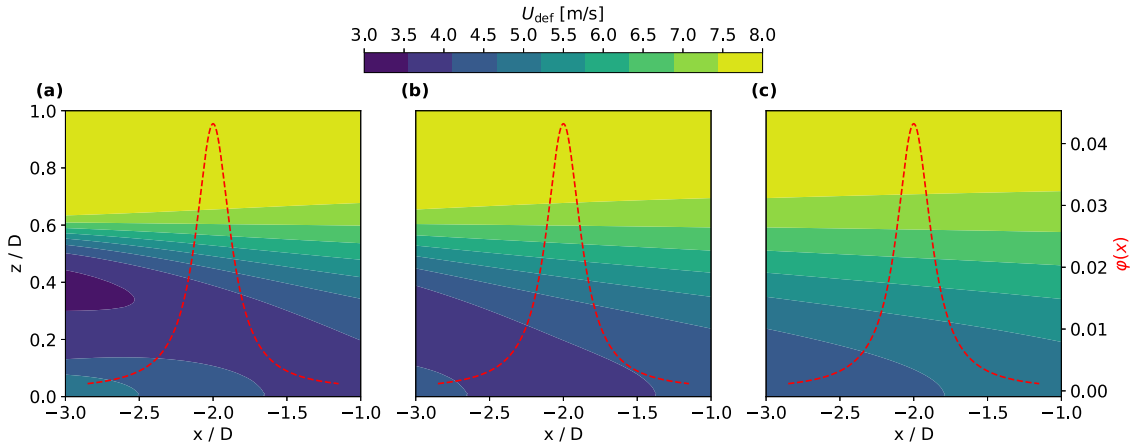

Fig. 4. Two-dimensional views of the quasi-steady velocity deficit in case of an upstream wake-generator rotor at $x = -5$D (*a*), $x = -6$D (*b*) and $x = -8$D (*c*), with a free-stream velocity of 8 m/s. The two-dimensional plane is obtained for $y = 0$ m. In red we show the weighting function of a CW lidar focused at $(x, y, z) = (-2\text{D}, 0, 0)$.

($\Delta y < 0$ m). For each condition, three different along-wind distances Δx are considered: 5D, 6D and 8D, with 96 simulations for each (Δx, Δy) case. Each of those sets of 96 simulations present a uniform distribution of free-stream velocities U_∞ within [6.5, 14] m/s and a nearly uniform distribution of TIs between 5% and 12%. As mentioned in Section 2.2, the waked field results from the superposition of three Mann-model generated turbulent fields. For all the waked fields in the dataset, the ambient turbulent field is generated with $L = 29.4$ m and $\Gamma = 3.9$, while $\alpha\epsilon^{2/3}$ is varied according to the desired level of atmospheric turbulence.

All turbulent wind fields used as input to the aeroelastic simulations are scanned with the lidar simulator to get a dataset of virtual power performance measurements, same as what we would get from a nacelle lidar mounted on an operating wind turbine. As mentioned in Section 2.3, we simulate the lidar scanning geometries illustrated in Fig. 3. For the in-wake cases, we account for the wake evolution inside the probe volume by calculating the quasi-steady velocity deficit at several downstream positions with an interspacing of $\Delta x = 0.1$D and linearly interpolating for the in-between locations. The wake meandering and the wake-generated turbulence are assumed as invariant with x. From Eq. (3), U_{def} varies with x, while all the other terms remain unchanged. As shown in Fig. 4, we need to account for the wake evolution in order to reliably represent the lidar measurements in wake, as it would be too unrealistic to consider one single profile $U_{\text{def}}(x, z)$ within the whole lidar probe volume.

2.5. Evaluation of the multivariate power curves

After performing the aeroelastic simulations and retrieving the virtual lidar measurements, both the wake-free and waked-inflow datasets are used to define multivariate power curves in the form of multivariable polynomial regressions. The input variables are combined into all possible polynomial combinations of degree less than or equal to the specified degree β. For example, for the case with three input variables $y = y(x_1, x_2, x_3)$ and $\beta = 2$, we get the following polynomial expression:

$$y = c_1 + c_2x_1 + c_3x_2 + c_4x_3 + c_5x_1^2 + c_6x_2^2 + c_7x_3^2 + c_8x_1x_2 + c_9x_1x_3 + c_{10}x_2x_3,$$

where $c_1, .., c_{10}$ are the coefficients of the polynomial regression.

In the wake-free homogeneous case, we consider two input variables and define the power output as function of the hub-height wind speed (U_{hub}) and atmospheric turbulence represented by the variance of the along-wind velocity component (σ_u^2): $P = P(U_{hub}, \sigma_u^2)$. This choice is based on the homogeneity of the inflow, which makes both U and σ_u^2 uniform over the whole (y, z) plane. For the SpinnerLidar, we use the methods described in Section 2.3 to derive U_{hub} and σ_u^2.

In the waked-inflow case, due to the strong inhomogeneity of the inflow, all the measured wind speed and turbulence values are considered as potential input variables to the polynomial regressions. When using lidar measurements, the wind speed U and the radial velocity variance $\sigma_{v_r}^2$ at each scanning location are considered, whereas U and σ_u^2 are considered when using the sonic anemometers. This difference is due to the difficulty in reconstructing σ_u^2 from $\sigma_{v_r}^2$ under inhomogeneous conditions. The input variables are then selected among the measured variables through a feature-selection process.

The feature selection is performed through a forward-selection algorithm. Starting with an empty model, variables are added one by one. At each step, each of the available variables is added to the existing model and the prediction error is calculated using nine values of $\beta = 1, 2, 3, \ldots, 9$. The variable providing the lowest error is selected and the selection continues until adding one more variable causes an increase of the prediction error due to overfitting. An illustration of the feature-selection process is shown in Fig. 5.

The prediction error given by each model is evaluated as a K-fold cross-validation with $K = 10$: the dataset is split into ten equally large folds, nine of which are used to train the model and the remaining one is used to test the model. This procedure is performed ten times using each of the folds as testing dataset and the final error, referred to as the generalization error λ, is evaluated as the average of the mean errors from the 10 folds: $\lambda = \frac{1}{10}\sum_j E_j$. The errors E_j are calculated with three different approaches in order to better compare the different models: the root mean square error (RMSE), the mean absolute error (MAE) and the mean absolute percentage error (MAPE). The cross-validation ensures that all observations in the dataset are used to test the model and the error does not depend on how we split into training and test sections.

If we evaluated the prediction accuracy on the 90% training data, the error would decrease with the number of features up to the maximum number of available features. However, this causes an overfitting over the training data with a larger error when testing the regression over the 10% testing data, as the model is too tightly related to the training data, causing less flexibility and larger errors when evaluating on the testing data. Therefore, there is an optimal number of features, which allows the most accurate modelling of the power-velocity relation without causing overfitting, which would enlarge the error as the number of features keep increasing.

3. Results

3.1. Wake-free dataset

For the wake-free dataset, only two variables are considered: the wind speed at hub height U_{hub} and the atmospheric turbulence (σ_u^2 at hub height), as the inflow is uniform and not much benefit is expected by measuring the wind speed at additional locations. In Fig. 6,

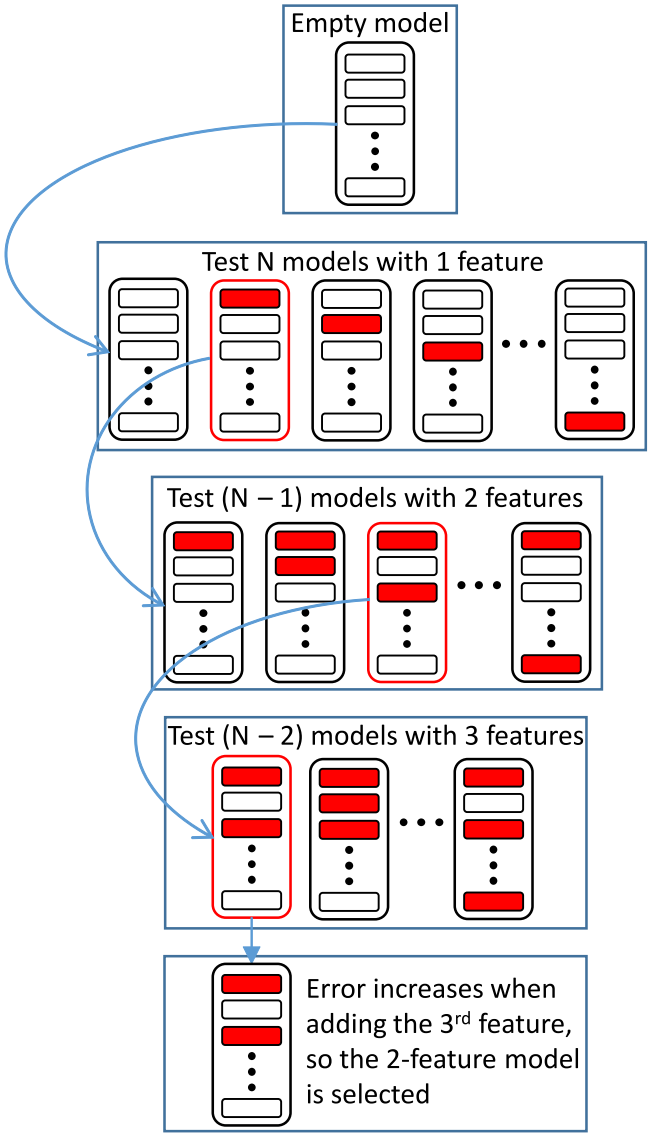

Fig. 5. Illustration of the feature-selection process in a case where two input variables are selected out of N available features.

the multivariate power curves are compared with the IEC standard power curve, which is defined using U_{hub} and without any turbulence normalization ($P = P_{\mathrm{IEC}}(U_{\mathrm{hub}})$). The multivariate power curve is more accurate than the IEC standard when using both SpinnerLidar and sonic anemometer velocity and turbulence measurements, with an error reduction of about 50% from the IEC standard power curve. The optimal polynomial order is $\beta = 7$ for both SpinnerLidar and sonic anemometer measurements. The scatter plots of Fig. 7 show the estimated power against the power predicted by the different power curves for all the 620 observations of the wake-free dataset. As illustrated, the multivariate power curves predict the power output quite accurately, without any significant outliers.

3.2. Waked-inflow dataset

When including the wake cases, the correlation between P and U_{hub} decreases, with higher scattered power curve plots, as shown in Fig. 8. Using the IEC standard power curve results in large errors in the evaluation of the power performance of a wind turbine in wake. Therefore, we use nacelle lidar measurements to define alternative multivariate power curves, which provide the same accuracy under wake and wake-free conditions.

We train the multivariate polynomial regressions by using SpinnerLidar measurements taken at 2D in front of the rotor for all the 864 cases in the waked-inflow dataset. The optimal number of features among the 800 available variables (400 measurements for both U and $\sigma^2_{v_r}$) and the optimal β are selected through the forward-selection algorithm combined with the $K = 10$-fold cross-validation. Fig. 9 shows the results of the feature selection, highlighting how the generalization error and the optimal degree change when increasing the number of input variables.

As shown in Fig. 9(a), four features are selected: three values of U and one of $\sigma^2_{v_r}$. When adding a fifth input variable, the error starts to increase and the feature-selection process stops. The input variables are selected approximately along a line passing through the rotor centre. This result agrees with the physics of wakes, which are generally characterized by a concentric velocity field. Finally, the optimal model is a 4th order polynomial with four input variables, giving an error reduction of 59% compared to the case of only one input variable.

We also use the waked-inflow dataset to train and test multivariate power curves based on measurements taken at 2D from the 6-beam lidar, the circular scanning lidar and the grid of sonic anemometers. Additionally, we also consider the case of a grid of sonic anemometers located exactly at the rotor, measuring the flow as if there was no turbine. Results of the forward-selection for those four cases are shown in Fig. 10. In all cases, either four or five features are selected, with three cases out of four including both wind speed and turbulence measurements. The grid of sonic anemometers at 2D is the only case that does not choose to use turbulence measurements. For both cases using the grid of sonic anemometers, the selected features come from measurements at different radial distances, similarly to the case using the SpinnerLidar measurements.

Fig. 11 shows the error variations related to the feature selection illustrated in Fig. 10. For the 6-beam case, the error drops 51% when adding the 2nd feature, and by 55% while including the 3rd and 4th features. For the circular scanning lidar, the five selected features provide an error reduction of 40% compared to the case of a single input. This shows the benefit of adding one measurement at a different radial distance, in analogy to the findings in Fu et al. [30] with regards to turbulence measurements with nacelle lidars. For the sonic anemometer grids, the feature selection provides error reductions of 57% and 52% when measuring at 2D and at the rotor, respectively. As expected, the error is lower when using measurements at the rotor plane, due to a better correlation between the inflow and the power output. As shown in Fig. 4, there might be strong velocity variations within a distance of $\Delta x = 2$D. Although not shown here, in all cases of Fig. 10, the feature selection results in polynomials of the 4th order ($\beta = 4$).

In Fig. 12, the generalization errors from the multivariate power curves are compared with those from the IEC standard power curve, which are also shown by the red line in Fig. 8. We use two different wind speed measurements as input to the relation $P = P_{IEC}(U)$: the wind speed at hub height (U_{hub}) and the rotor-averaged wind speed U_{rotor} estimated as the arithmetic mean of the wind speed values from all the sonic anemometers within the rotor area. As expected, results are more accurate when using U_{rotor} instead of U_{hub}, due to the strongly non-uniform inflow.

When considering only measurements at 2D, all the multivariate power curves outperform the IEC standard. Specifically, the SpinnerLidar provides the highest accuracy with a MAPE of 2.74%, while the circular configuration provides an error of 5.48%, which is larger than that from both the SpinnerLidar and the 6-beam lidar. The IEC power curve is less accurate with MAPE of 24.12% and 12.95% when using U_{hub} and U_{rotor}, respectively. The grid of sonic anemometers at 2D provide a MAPE of 3.43%, which demonstrates that accuracy does not necessarily increase when removing the lidar's probe-volume effect.

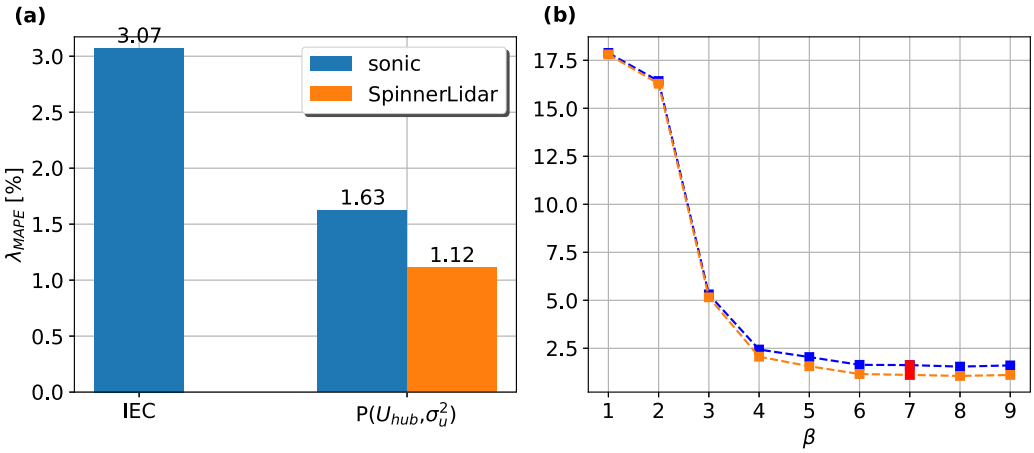

Fig. 6. (*a*) Generalization error in form of MAPE of power curves for the wake-free cases. (*b*) Variation of λ_{MAPE} with the order of the polynomial regressions based on sonic anemometer (*blue*) and SpinnerLidar (*orange*) measurements; optimal values are highlighted in red.

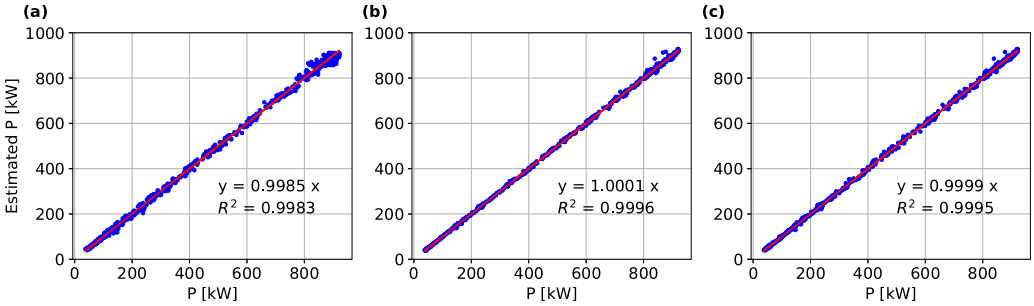

Fig. 7. Scatter plots of the power estimated by the IEC standard (*a*) and by the polynomial regression $P = P(U, \sigma_u^2)$ based on SpinnerLidar (*b*) and sonic anemometer (*c*) measurements in the wake-free cases. $y = x$ line is shown in *red*.

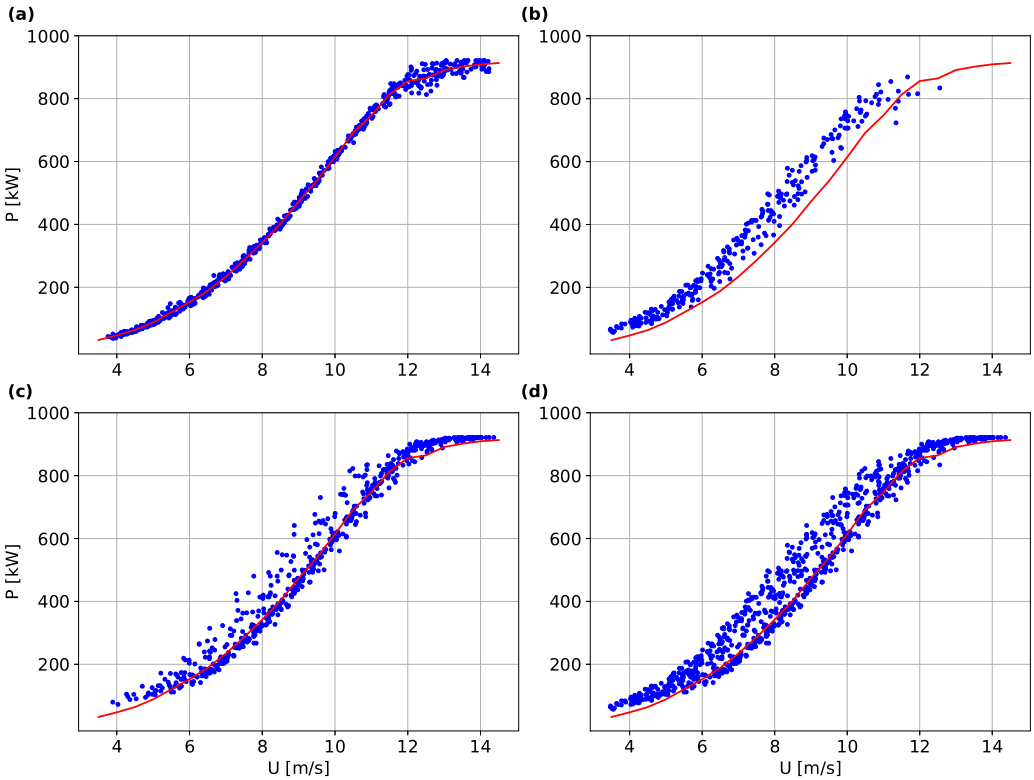

Fig. 8. IEC standard power curve (*red line*) and scattered power curves (*blue dots*) for cases including wake-free conditions (*a*), centred wakes (*b*), laterally-displaced wakes (*c*), and both centred and laterally-displaced wakes (*d*).

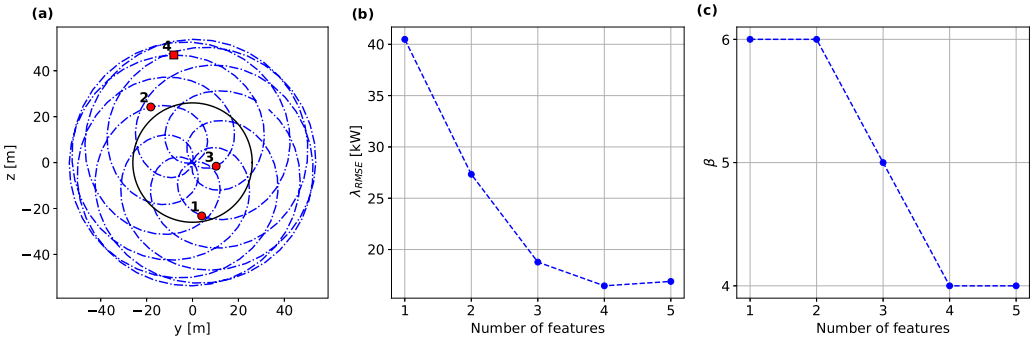

Fig. 9. (*a*) Scanning configuration of the SpinnerLidar (*blue*) with selected measurements (*red*) of U (*circles*) and $\sigma^2_{v_r}$ (*squares*) in the waked-inflow dataset; numbers indicate the selection order; rotor diameter is highlighted (*black*). (*b*) Variation of the generalization error with the number of selected-features. (*c*) Optimal degree for each model.

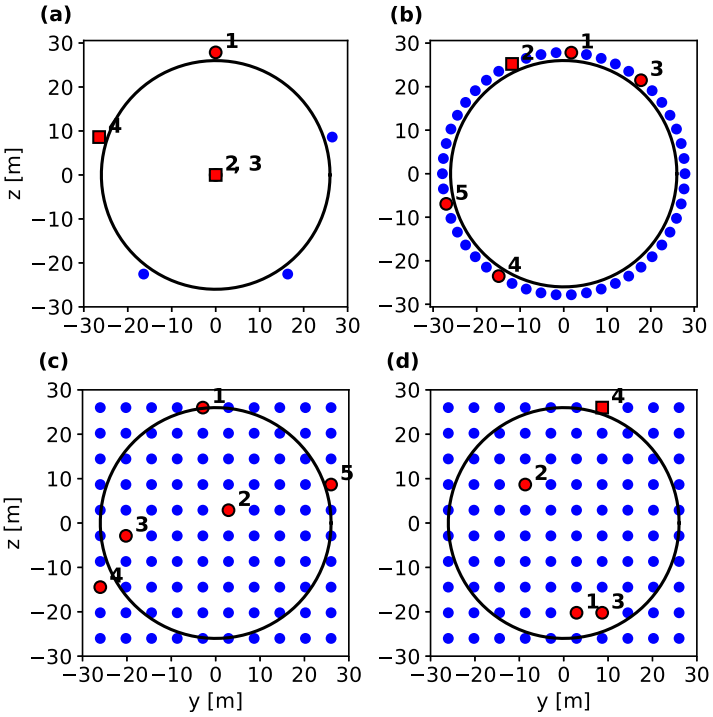

Fig. 10. Scanning configurations (*blue*) and selected measurements (*red*) of wind speed (*circles*) and turbulence (*squares*) in the waked-dataset: (*a*) 6-beam lidar focused at 2D; (*b*) circular scanning lidar focused at 2D; (*c*) grid of sonic anemometers at 2D; (*d*) grid of sonic anemometers at the rotor. Numbers indicate the selection order. The rotor diameter is highlighted (*black*).

The lower accuracy of the grid of sonic anemometers compared to the SpinnerLidar might be due to the smaller scanned area; thus it might be beneficial to measure outside of the rotor area. However, the lowest error (MAPE = 2.34%) appears for the grid of sonic anemometers located at the rotor, which shows the benefits of measuring close to the rotor. Similar findings are observed for the IEC power curves, which are more accurate when using wind speed measurements at the rotor position. However, even for the case of U_{rotor} evaluated at the rotor plane, the IEC power curve is less accurate than the multivariate power curves based on measurements at 2D from SpinnerLidar, 6-beam lidar and grid of sonic anemometers.

Table 1 shows all the generalization errors given by the cross-validation over the waked-inflow dataset. As shown in the table, the findings are the same for the MAPE and MAE metrics, whereas a small difference is observed for the RMSE. When using measurements at the rotor, the U_{rotor}-based IEC power curve provides the same RMSE of the grid of sonic anemometers at the rotor and lower RMSE than the SpinnerLidar. This is due to the RMSE giving a relatively high weight to larger errors, as the errors are squared before being averaged. Therefore, the grid of sonic anemometers and the SpinnerLidar give a few relatively large errors that make the RMSE increasing. However, it should be noted that this is the case only when the IEC power curve is based on measurements at the rotor plane. When using measurements at 2D, the multivariate power curves outperform the IEC power curve for all the error metrics.

The scatter plots of Fig. 13 show the estimated power against the power predicted by the different power curves for all the 864 observations of the waked-inflow dataset. As illustrated, the multivariate power curves predict the power output accurately. Specifically, we have intercept-free regression lines close to $y = 0.99\,x$ and determination coefficients close to $R^2 = 0.99$ for the SpinnerLidar, 6-beam and grid of sonic anemometer configurations, while the regression is less accurate when using the circular configuration. As illustrated in Figs. 13(a, b), the IEC power curves are less accurate than the multivariate power curves; the former tend to underestimate the power output, with regressions lines in the order of $y = 0.91\,x$ and $y = 0.95\,x$ for U_{hub} and U_{rotor}, respectively. Note that for both the 6-beam and circular lidar configurations, although their scatter is lower than that of the IEC power curve, a few strong outliers appear in Figs. 13 (d,e). These

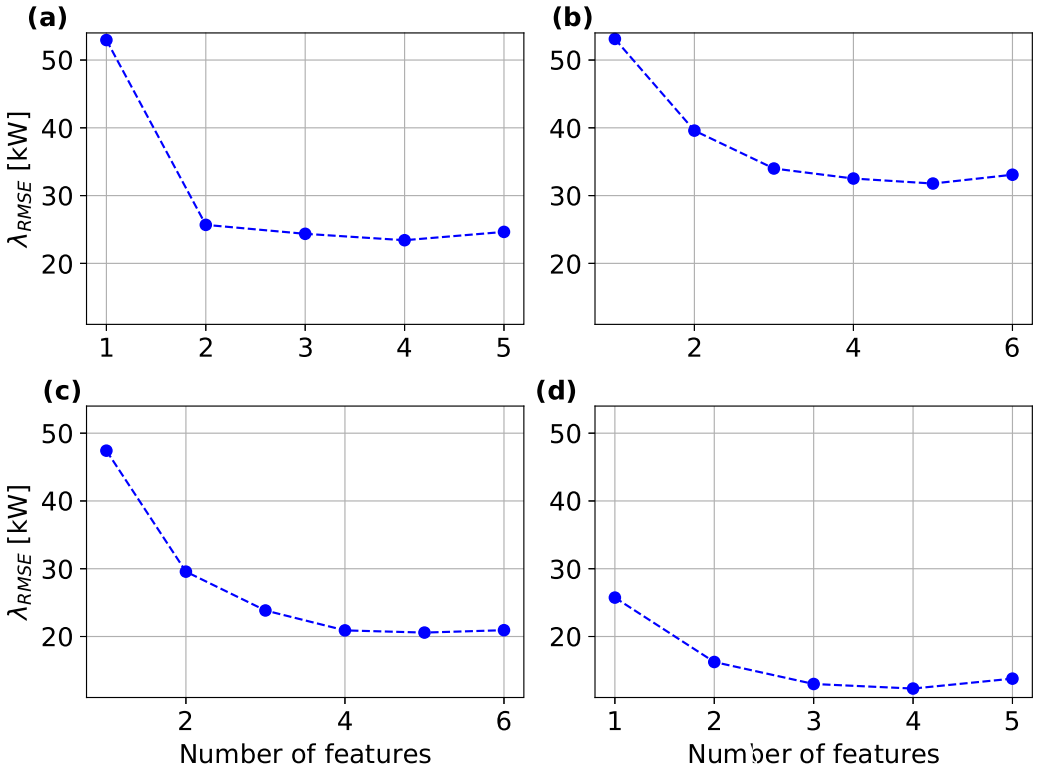

Fig. 11. Variation of the generalization error in the form of RMSE with the number of selected-features when using the waked-inflow dataset in the case of: (*a*) 6-beam lidar focused at 2D; (*b*) circular scanning lidar focused at 2D; (*c*) grid of sonic anemometers at 2D; (*d*) grid of sonic anemometers at the rotor.

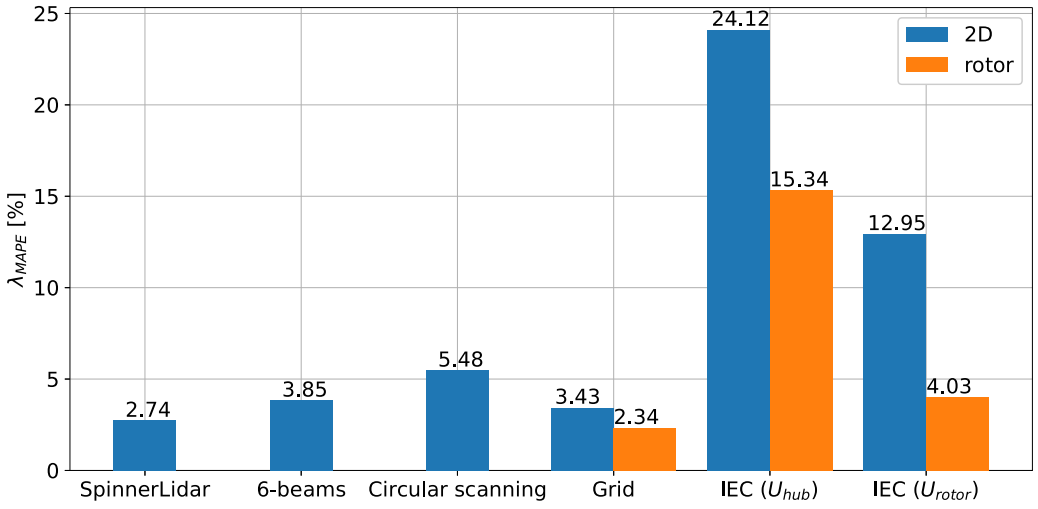

Fig. 12. Generalization error in the form of MAPE given by the optimal model for different configurations when trained and tested with the waked-inflow dataset.

Table 1
Generalization errors from the $K = 10$ cross-validation on the waked-inflow dataset with measurements retrieved both at the rotor and 2D upstream.

	2D						Rotor		
λ	SL	6-beam	Circular	Grid	IEC (U_{hub})	IEC (U_{rotor})	Grid	IEC (U_{hub})	IEC (U_{rotor})
RMSE [kW]	16.8	25.9	33.3	19.2	98.6	51.9	15.6	60.7	15.6
MAE [kW]	10.7	15.3	21.3	12.6	71.1	37.9	9.4	45.1	11.9
MAPE [%]	2.74	3.85	5.48	3.43	24.12	12.95	2.34	15.34	4.03

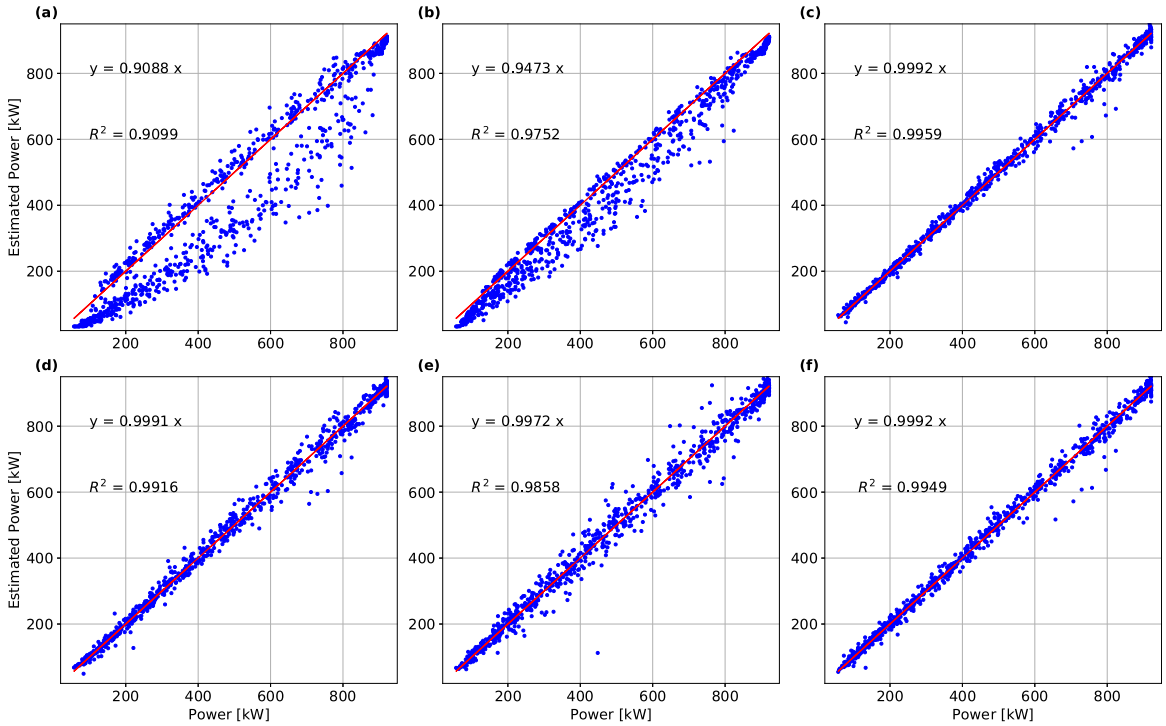

Fig. 13. Scatter plots of the estimated power against the real power output for different measurements at 2D in the waked-inflow dataset: (*a*) IEC-U_{hub}; (*b*) IEC-U_{rotor}; (*c*) SpinnerLidar; (*d*) 6-beam; (*e*) Circular; (*f*) Grid of sonic anemometers. $y = x$ line is shown in *red*.

two scanning patterns cannot fully evaluate the inflow under waked conditions.

3.3. Combining both datasets

Figs. 6 and 12 show that the multivariate power curves can accurately estimate the power output of a wind turbine under both waked and wake-free conditions. However, those results are obtained by training and testing the polynomial regressions on the single datasets separately, resulting in two different multivariate power curves for the homogeneous and waked conditions.

We want to evaluate whether it is possible to obtain a single multivariate power curve, which characterizes the wind turbine power output irrespective of knowing whether it is in wake or not. Therefore, we combine the two datasets (wake and wake-free) and, then, train and test a multivariate power curve through a $K = 10$-fold cross-validation over all the 1484 observations. We use measurements from the SpinnerLidar without the feature selection algorithm. We use $\beta = 4$, as it is the optimal value previously selected for the waked dataset, and the four input variables shown in Fig. 9(a), i.e. three wind speed and one turbulence measures taken along a line passing through the rotor centre. In this way, we can assess whether the results from the previous feature-selection are strongly dependent on the training dataset.

When using both datasets, the SpinnerLidar-based multivariate power curve is still accurate, as shown in Fig. 14(a). Compared to training with both datasets separately, the generalization error slightly increases to $\lambda_{\mathrm{MAPE}} = 2.86\%$ only.

Furthermore, in order to assess the flexibility of the regression model and its dependence on the training dataset, we use a new dataset to test the SpinnerLidar-based multivariate power curve. Specifically, we use the combination of wake-free and waked-inflow datasets to define the power curve, which is then tested on a new dataset consisting of 192 observations characterized by wakes from either two or three upstream rotors, with a spacing of 6D between them. Distributions for the wind speed and atmospheric turbulence are the same as in the waked-inflow dataset. Here, we do not perform the cross-validation, as we use the entire combined dataset to train the regression model, which is then used to predict the power output of all the 192 observations in the testing dataset. As shown in Fig. 14(b), the power prediction is very accurate, with a MAPE = 3.42%. The model performs accurately when tested on conditions that are not included in the training dataset; this shows that overfitting is avoided.

3.4. Optimal scanning configuration

The feature selection suggests a common trend for all the measurement configurations: as shown in Fig. 9, the features are selected along a line passing through the rotor centre. Additionally, results using the 6-beam lidar are more accurate than those using the circular configuration, which demonstrates the need for measurements at different radial distances.

In order to test the robustness of the optimal configuration suggested by the results of Figs. 9 and 10, we evaluate how the accuracy of the multivariate power curves changes for different input variables. Specifically, we focus on the SpinnerLidar and use the same polynomial order ($\beta = 4$) and number of features (three wind speed and one turbulence measurements), but selected at different locations. We evaluate how the error changes when we select features along a line through the rotor centre rotated of an azimuth angle θ with respect to the optimal case of Fig. 9. Additionally, we perform the same analysis, but on features over the same radius.

The selected features for each rotation are shown in Fig. 15(a) and the related errors in Fig. 15(b). The error does not vary substantially with the rotations, increasing up to $\lambda_{MAPE} = 4.1\%$. On the contrary, the accuracy strongly decreases when we select the features along a circular path. As shown in Fig. 15(c,d), errors are generally large and strongly dependent on the radius of the circular path, varying from 5.95% to 19.74%. Starting from $R = 7$ m, the error decreases for larger values of R, reaching a minimum at around 3/4 of the rotor radius ($R = 20$ m), and increasing again for circular paths outside the rotor area.

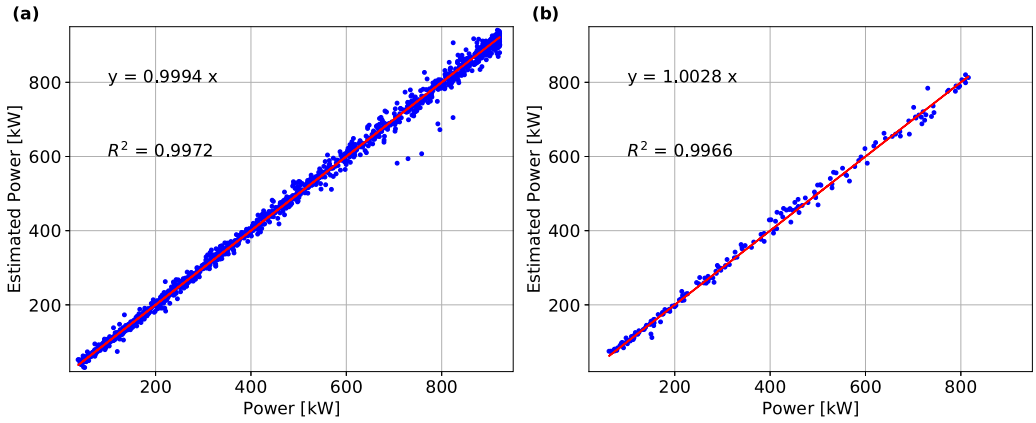

Fig. 14. Scatter plots of the estimated power against the real power output for all the observations of the combined dataset (a) and the multiple-wakes case (b). The power is estimated with the SpinnerLidar-based multivariate power curve. $y = x$ line is shown in *red*.

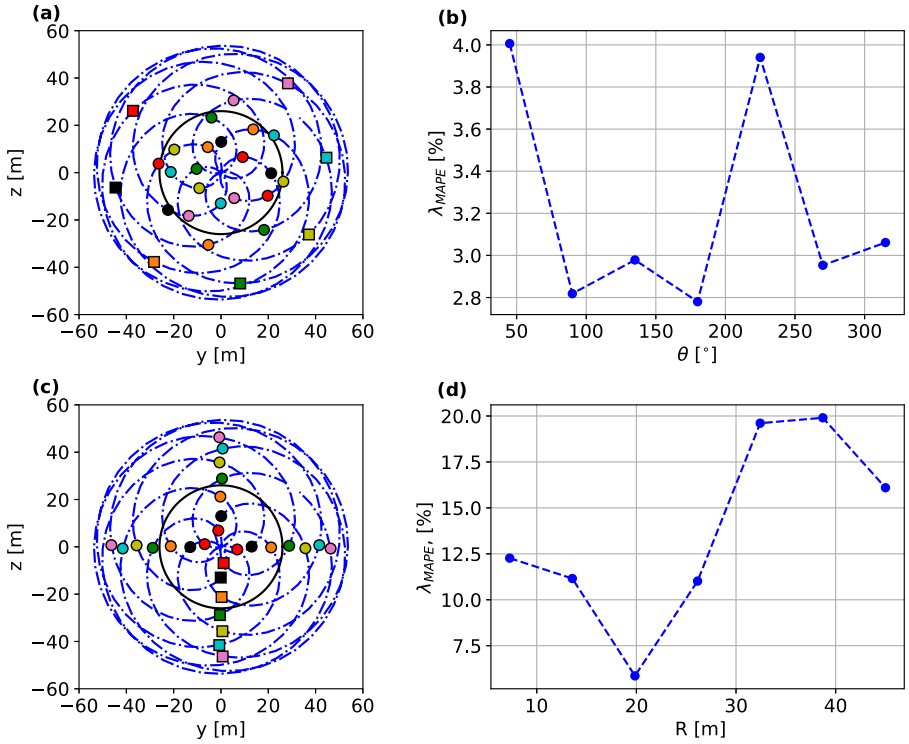

Fig. 15. Variation of the generalization error with the selected features. (a, b): Selected features obtained by rotating the optimal locations of an azimuth angle θ. (c, d): Selected features along circular patterns at different radii R.

4. Discussion

4.1. Alternative power curve measurements

We show that the accuracy of the IEC standard power curve under waked conditions increases when measuring closer to the rotor and when using the rotor-averaged wind speed as reference. Therefore, when using the IEC standard power curve in combination with engineering wake models for energy yield assessment, the rotor-averaged wind speed should be used instead of a single measurement at hub height. This aspect is often underestimated when evaluating engineering wake models, where the details are normally put into the modelling of the wakes and not much attention is paid to the wind-to-power conversion [34–36].

In our study, when combining the DWM model with the IEC standard power curve, the power output is predicted with a MAPE of 15.34% and 4.03% when using U_{hub} and U_{rotor}, respectively. However, these errors are obtained with velocity measurements at the rotor plane. When using measurements at 2D in front of the rotor, as suggested by the IEC standard [6], the error using the IEC standard power curve is much larger (up to 24.12%). Therefore, under inhomogeneous and complex flows, the wind speed should be measured at several locations and as close as possible to the rotor to minimize the errors in predicting power output.

When measuring close to the rotor, e.g. at 1D, one might argue that the wind speed measurements should be corrected for the induction in order to get the free-stream velocity. The need for such correction is a consequence of defining wind turbine power curves as a relation between the power output and the free-stream velocity, which is generally defined as the wind speed measured at the turbine location without the turbine being there. However, wind measurements out of the induction zone are a valid estimation of the free-stream velocity only under few specific conditions, e.g. for an isolated turbine in flat terrain, which do not coincide with the operating conditions of most

wind turbines. Therefore, in this work, we develop a power curve, which relates the power output to a number of characteristics of the inflow without assuming that the velocity measurements correspond to the 'true' free-stream velocity.

We use nacelle lidars to measure the inflow characteristics, as they currently are the most capable systems for measuring the wind speed impacting the rotor. The idea is to develop power curves, which relate the power output of the wind turbine to a number of inflow conditions and wind characteristics measured by the lidar rather than to the free-stream velocity. Such power curves would give a reliable estimation of the power output independently of the operating conditions, whereas the IEC standard power curve is reliable only under restricted conditions.

In this work, we propose data-driven power curves in the form of multivariate polynomial regressions based on nacelle lidar measurements, showing that they can reliably evaluate the power performance of a wind turbine under waked conditions. This approach could be replicated with field data by mounting a lidar on the nacelle of a wind turbine, which operates under both waked and free-standing conditions. However, it should be noted that in our simulations, wakes are the only source of flow complexity. Out in the field, inhomogeneity and flow complexity can be caused by a number of factors, such as terrain effects and turbulence conditions. Therefore, more complex methods than multivariate polynomial regressions might be needed to develop power curves that are reliable under both waked and wake-free operation.

4.2. Scanning configurations

All the feature selection processes result in four or five features selected for the optimal model. However, when five features are selected, the use of the 5th selected feature results in small error reductions (2.2% and 1.5% for the circular configuration and the grid of sonic anemometers, respectively). These results suggest that four is the optimal number of features. But where we should retrieve these four features? Results from the feature selection in Figs. 9 and 10 show that it is beneficial to retrieve the measurements along a line through the rotor centre and that measurements at similar radial distances should be avoided. Results in Fig. 15(a,b) further confirm the benefits in measuring along such a line, showing that the accuracy does not change much with the azimuth orientation of the measurements. This is expected due to the shape of the velocity deficit of turbine wakes. By measuring on a radial line, we can estimate the wake radius and the portion of the rotor in wake.

The deficiencies of the circular configuration are confirmed by the results of Fig. 15(c,d). The error is generally large and strongly dependent on the radius of the scanning path. Note how the error is high for a very small radius, it decreases as the radius grows up to about the size of the rotor radius, where it reaches a minimum before increasing again. If the lidar performs such a scanning configuration, the highest accuracy of the multivariate power curve results when scanning at the rotor. When scanning on either a very small or very large circular path, an accurate estimation of the velocity field within the rotor area cannot be achieved.

When using the SpinnerLidar measurements, as shown in Fig. 9(a), the selected features are located both inside and outside of the rotor area, showing that measurements outside the rotor area might be beneficial to evaluate the power performance in wake, as they allow a better characterization of the inflow to the rotor. However, if one had to choose between two configurations presenting all features either inside or outside the rotor area, we expect the error to be larger when using features outside the rotor area. This is because of the order of selection of the features by the feature-selection algorithm, which selects a measurement within the rotor area as first selected feature and one just outside the rotor area as second. Additionally, the circular configurations of Fig. 15(c,d) give the lowest error when using measurements within the rotor area (R = 20 m), suggesting once more that features selected within the rotor area are likely to give a more accurate estimation of the power performance than those outside of the rotor.

5. Conclusions

Alternative wind turbine power curves are implemented in the form of multivariable polynomial regressions, whose input variables consist of several wind speed and turbulence measurements retrieved using nacelle lidars. The power curves are tested on a dataset of synthetic power performance measurements, which is generated through the combination of aeroelastic simulations with virtual nacelle lidar measurements. Additionally, power performance measurements in wake are simulated with the DWM model.

Our results show that nacelle lidars can be used to characterize the power performance of a wind turbine under waked conditions with an accuracy of the same order as that in wake-free operation. Specifically, when using measurements from the SpinnerLidar, we obtain MAPE of 1.12% and 2.74% under homogeneous and waked conditions, respectively. These errors are much lower than those from the IEC standard power curve: 3.07% and 24.12% for homogeneous and waked conditions, respectively, i.e., an error reduction of 88% for the waked inflow cases. Furthermore, under waked conditions, the MAPE from IEC standard power curve is reduced to 4.03% when using a rotor-averaged wind speed at the rotor position.

We test several nacelle lidar configurations, which measure the wind speed at a different number of locations arranged along different patterns. A feature-selection algorithm is used to select the input variables among the available measurements, showing the benefit to measure wind characteristics at more than one location. We find error reductions of more than 50% compared to the case of a univariate polynomial regression using one single wind speed measurement. Additionally, the feature selection shows the importance in measuring turbulence, which is selected as an input variable for all the lidar configurations and for one of the two grid of sonic anemometers.

The optimal multivariate power curve consists of a multivariable polynomial regression of the 4th order with four input variables: three wind speed and one turbulence measurements from different locations. Those measurements should be arranged along a line passing through the rotor centre rather than on a circular pattern to better capture the radial velocity gradient of the waked flow.

Our methodology for power performance evaluation is not largely affected by the lidar probe volume averaging, as the accuracy does not increase when using measurements from virtual sonic anemometers. Additionally, we show that accuracy in power curve measurements increases when measuring closer to the rotor due to wake evolution.

This research might be extended by testing the same approach with field measurements from nacelle lidars within wind farms. Additionally, further numerical investigations including wind turbine induction and wind evolution can be important for future studies.

CRediT authorship contribution statement

Alessandro Sebastiani: Conceptualization, Methodology, Software, Formal analysis, Investigation, Writing – original draft. **Alfredo Peña:** Conceptualization, Methodology, Writing – review & editing, Supervision. **Niels Troldborg:** Conceptualization, Methodology, Writing – review & editing, Supervision.

Declaration of competing interest

The authors declare that they have no known competing financial interests or personal relationships that could have appeared to influence the work reported in this paper.

Data availability

Datasets related to this article can be found at https://doi.org/10.11583/DTU.20156714.

Acknowledgements

We would like to thank Jennifer Marie Rinker for developing the HAWC2 model of the V52 wind turbine.

This work has received funding from the European Union Horizon 2020 through the Innovation Training Network Marie Skłodowska-Curie Actions: Lidar Knowledge Europe (LIKE) [grant number 858358].

References

[1] IEC, 61400-12-1, Power performance measurements of electricity producing wind turbines, 2005.
[2] A. Clifton, R. Wagner, Accounting for the effect of turbulence on wind turbine power curves, J. Phys. Conf. Ser. 524 (1) (2014) http://dx.doi.org/10.1088/1742-6596/524/1/012109.
[3] R. Wagner, M. Courtney, J. Gottschall, P. Lindelöw-Marsden, Accounting for the speed shear in wind turbine power performance measurement, Wind Energy 14 (8) (2011) 993–1004, http://dx.doi.org/10.1002/we.509.
[4] L. Bardal, L. Sætran, Influence of turbulence intensity on wind turbine power curves, Energy Procedia 137 (2017) 553–558, http://dx.doi.org/10.1016/j.egypro.2017.10.384.
[5] E. Hedevang, Wind turbine power curves incorporating turbulence intensity, Wind Energy 17 (2) (2014) 173–195, http://dx.doi.org/10.1002/we.1566.
[6] IEC, 61400-12-1, Power performance measurements of electricity producing wind turbines, 2017.
[7] A. Sebastiani, A. Peña, N. Troldborg, A. Meyer Forsting, Evaluation of the global-blockage effect on power performance through simulations and measurements, Wind Energy Sci. 7 (2) (2022) 875–886, http://dx.doi.org/10.5194/wes-7-875-2022.
[8] M. Marčiukaitis, I. Žutautaitė, L. Martišauskas, B. Jokšas, G. Gecevičius, A. Sfetsos, Non-linear regression model for wind turbine power curve, Renew. Energy 113 (2017) 732–741, http://dx.doi.org/10.1016/j.renene.2017.06.039.
[9] E. Taslimi-Renani, M. Modiri-Delshad, M. Elias, N. Rahim, Development of an enhanced parametric model for wind turbine power curve, Appl. Energy 177 (2016) 544–552, http://dx.doi.org/10.1016/j.apenergy.2016.05.124.
[10] J. Gottschall, J. Peinke, How to improve the estimation of power curves for wind turbines, Environ. Res. Lett. 3 (1) (2008) http://dx.doi.org/10.1088/1748-9326/3/1/015005.
[11] B. Manobel, F. Sehnke, J.A. Lazzús, I. Salfate, M. Felder, S. Montecinos, Wind turbine power curve modeling based on Gaussian processes and artificial neural networks, Renew. Energy 125 (2018) 1015–1020, http://dx.doi.org/10.1016/j.renene.2018.02.081.
[12] F. Pelletier, C. Masson, A. Tahan, Wind turbine power curve modelling using artificial neural network, Renew. Energy 89 (2016) 207–214, http://dx.doi.org/10.1016/j.renene.2015.11.065.
[13] Y.-M. Saint-Drenan, R. Besseau, M. Jansen, I. Staffell, A. Troccoli, L. Dubus, J. Schmidt, K. Gruber, S.G. Simoes, S. Heier, A parametric model for wind turbine power curves incorporating environmental conditions, Renew. Energy 157 (2020) 754–768, http://dx.doi.org/10.1016/j.renene.2020.04.123.
[14] V. Bulaevskaya, S. Wharton, A. Clifton, G. Qualley, W.O. Miller, Wind power curve modeling in complex terrain using statistical models, J. Renew. Sustain. Energy 7 (1) (2015) http://dx.doi.org/10.1063/1.4904430.
[15] A. Clifton, L. Kilcher, J.K. Lundquist, P. Fleming, Using machine learning to predict wind turbine power output, Environ. Res. Lett. 8 (2) (2013) http://dx.doi.org/10.1088/1748-9326/8/2/024009.
[16] O. Janssens, N. Noppe, C. Devriendt, R. Van de Walle, S. Van Hoecke, Data-driven multivariate power curve modeling of offshore wind turbines, Eng. Appl. Artif. Intell. 55 (2016) 331–338, http://dx.doi.org/10.1016/j.engappai.2016.08.003.
[17] D. Astolfi, R. Pandit, Multivariate wind turbine power curve model based on data clustering and polynomial LASSO regression, Appl. Sci. 12 (1) (2022) http://dx.doi.org/10.3390/app12010072.
[18] A. Sebastiani, A. Peña, N. Troldborg, Wind turbine power performance characterization through aeroelastic simulations and virtual nacelle lidar measurements, J. Phys. Conf. Ser. 2265 (2) (2022) 022059, http://dx.doi.org/10.1088/1742-6596/2265/2/022059.
[19] H. Aagaard Madsen, G. Larsen, T. Larsen, N. Troldborg, R. Mikkelsen, Calibration and validation of the dynamic wake meandering model for implementation in an aeroelastic code, J. Solar Energy Eng. 132 (4) (2010) http://dx.doi.org/10.1115/1.4002555, 041014 (14 pages).
[20] T. Larsen, A. Hansen, How 2 HAWC2, the user's manual, 2007.
[21] J.M. Rinker, M.H. Hansen, T.J. Larsen, Calibrating a wind turbine model using diverse datasets, in: SCIENCE of MAKING TORQUE from WIND (TORQUE 2018), J. Phys. Conf. Ser. 1037 (2018) http://dx.doi.org/10.1088/1742-6596/1037/6/062026.
[22] J. Mann, The spatial structure of neutral atmospheric surface-layer turbulence, J. Fluid Mech. 273 (1994) 141–168.
[23] IEC, 61400-1, Wind turbines – Part 1: design guidelines, fourth, 2019.
[24] J. Ainslie, Calculating the flowfield in the wake of wind turbines, J. Wind Eng. Ind. Aerodyn. 27 (1-3) (1988) 213–224, http://dx.doi.org/10.1016/0167-6105(88)90037-2.
[25] R.-E. Keck, D. Veldkamp, H. Aagaard Madsen, G. Larsen, Implementation of a mixing length turbulence formulation into the dynamic wake meandering model, J. Solar Energy Eng. 134 (2) (2012) 021012, http://dx.doi.org/10.1115/1.4006038.
[26] J.-J. Trujillo, F. Bingöl, G. Larsen, J. Mann, M. Kühn, Light detection and ranging measurements of wake dynamics. Part II: two-dimensional scanning, Wind Energy 14 (1) (2011) 61–75, http://dx.doi.org/10.1002/we.402.
[27] H. Aagaard Madsen, G. Larsen, K. Thomsen, Wake Flow Characteristics in Low Ambient Turbulence Conditions, Copenhagen Offshore Wind, 2005.
[28] C.M. Sonnenschein, F.A. Horrigan, Signal-to-noise relationships for coaxial systems that heterodyne backscatter from the atmosphere, Appl. Opt. 10 (1971) 1600–1604.
[29] A. Peña, J. Mann, G. Rolighed Thorsen, SpinnerLidar Measurements for the CCAV52, Vol. 0177, DTU Wind Energy, Denmark, 2019.
[30] W. Fu, A. Sebastiani, A. Peña, J. Mann, Influence of nacelle-lidar scanning patterns on inflow turbulence characterization, J. Phys. Conf. Ser. 2265 (2) (2022) 022016, http://dx.doi.org/10.1088/1742-6596/2265/2/022016.
[31] J. Mann, A. Peña, F. Bingöl, R. Wagner, M. Courtney, Lidar scanning of momentum flux in and above the atmospheric surface layer, J. Atmos. Ocean. Technol. 27 (6) (2010) 959–976, http://dx.doi.org/10.1175/2010JTECHA1389.1.
[32] W. Fu, A. Peña, J. Mann, Turbulence statistics from three different nacelle lidars, Wind Energy Sci. 7 (2) (2022) 831–848, http://dx.doi.org/10.5194/wes-7-831-2022.
[33] J. Mann, Wind field simulation, Probab. Eng. Mech. 13 (1998) 269–282.
[34] A. Niayifar, F. Porte-Agel, Analytical modeling of wind farms: A new approach for power prediction, Energies 9 (9) (2016) http://dx.doi.org/10.3390/en9090741.
[35] N.G. Nygaard, S.T. Steen, L. Poulsen, J.G. Pedersen, Modelling cluster wakes and wind farm blockage, J. Phys. Conf. Ser. 1618 (2020) http://dx.doi.org/10.1088/1742-6596/1618/6/062072.
[36] T. Gögmen, P. van der Laan, P.-E. Réthoré, A. Peña, G. Larsen, S. Ott, Wind turbine wake models developed at the Technical University of Denmark: A review, Renew. Sustain. Energy Rev. 60 (2016) 752–769, http://dx.doi.org/10.1016/j.rser.2016.01.113.

Paper VII: Wind turbine power curve modelling in wake using measurements from a hub-mounted lidar

Wind turbine power curve modelling in wake using measurements from a hub-mounted lidar

Alessandro Sebastiani[a], Nikolas Angelou[a], Alfredo Peña[a]

[a]*DTU Wind and Energy systems, Technical University of Denmark, Frederiksborgvej 399, Roskilde, 4000, Denmark*

Abstract

Most wind turbines are installed inside wind farms, where they usually operate under waked inflow conditions during their life-time. Because of those strongly inhomogeneous inflow conditions, the power performance of a waked wind turbine cannot be assessed by following the IEC standard procedure. Thus, new methods are needed to evaluate the power performance of a waked wind turbine. In this work, we investigate the accuracy of a multivariate power curve acquired through a polynomial regression, whose input variables are wind speed and turbulence measurements retrieved upstream of the turbine rotor. For this purpose, we use measurements from the SpinnerLidar, a continuous-wave, scanning Doppler lidar measuring along a rosette pattern. The SpinnerLidar was mounted in the spinner of a Neg Micon 80 wind turbine within an onshore wind farm in western Denmark. The input variables are selected among the available lidar measurements with a feature-selection algorithm, resulting in seven input variables for the optimal case: six wind speed and one turbulence measurements. The multivariate power curve is tested and compared with IEC-similar power curves under both waked and wake-free conditions. Results show that the multivariate power curve is more accurate than the IEC-similar power curves, with error reductions up to 65.3% in the estimated power output. Additionally, we test the impact of the lidar scanning configuration, showing that a circular scanning lidar, centered at the hub height, is suitable to implement the multivariate power curve when the diameter of the scanning pattern is approximately equal to 0.9 rotor diameters.

Keywords: lidar, power curve, wake, multivariable regression

1. Introduction

The standard procedure to measure the power curve of a wind turbine is described in the standard by the International Electrotechnical Commission (IEC) [1]. The IEC standard describes how to measure the power performance of a wake-free wind turbine, whose performance is supposedly not affected by neighbouring wind turbines [1]. However, most wind turbines operate inside wind farms, where they often stand in the wake of upstream turbines. In those cases the IEC power curve cannot be used to reliably evaluate their power performance. Thus, most operating wind turbines do not have an indication of their expected power performance under actual operating conditions. Therefore, alternative procedures to the IEC standard are needed to conduct the performance monitoring of operating wind turbines.

Previous studies have introduced alternative data-driven power curves in order to improve the evaluation of the wind turbine power performance relatively to the IEC power curve [2]. Those works introduced both parametric and non-parametric power curve models, which can be catalogued according to the input variables [3]. In some models, the hub-height wind speed measured with a nacelle-mounted cup is the only input variable to the power curve [4, 5, 6, 7, 8]. However, since the wind turbine power output is function of several flow characteristics [9, 10], uni-variate power curves were outperformed by models which account for additional features of the inflow, such as turbulence, vertical wind shear and vertical wind veer [11, 12, 13, 14, 15]. Additionally, the accuracy of data-driven power curves has been further improved by including control-related variables, such as yaw misalignment, rotor's rotational speed and blades' pitch angles [16, 17, 18, 19].

In the available studies, power curves were modelled using either nacelle-mounted anemometry or ground-based instruments located close to the turbine, i.e. meteorological masts and ground-based lidars. Not much attention has been paid to power curve modelling using nacelle-mounted lidars, which are able to characterize the inflow to the turbine independently of both the turbine location and the operating conditions. Nacelle lidars have been successfully used to measure flow characteristics, such as turbulence [e.g. 20, 21], vertical wind shear [e.g. 22, 23] and wake dynamics [e.g. 24, 25]. However, their potential for power performance assessment is still quite unexplored. Sebastiani et al. [26] numerically evaluated multivariate power curves based on virtual nacelle lidar measurements through aeroelastic simulations in wake, finding error reductions up to 88% relatively to the IEC power curve.

In this work, we aim to validate the numerical findings of Sebastiani et al. [26]. We use measurements from a wind lidar mounted in the hub of a Neg Micon 80 wind turbine installed in the onshore wind farm in Tjæreborg, western Denmark. The wind lidar is the DTU SpinnerLidar [27, 28, 29], which is used to characterize the inflow to the turbine under both waked and wake-free conditions.

The wake field studies that have been conducted so far have been based on observations from downwind looking nacelle lidars [24, 30, 31, 32, 25, 33]. Thus, there is a lack of measurements from upwind looking nacelle lidars mounted on waked turbines. Therefore, the Spinnerlidar measurements, along with the turbine Supervisory Control and Data Acquisition (SCADA) data, form a state-of-the-art dataset for evaluating the power performance of a waked wind turbine. Additionally, since the SpinnerLidar provides a full picture of the inflow to the turbine, this dataset can be used to test several lidar scanning patterns by selecting measurements along particular trajectories, following the same approach as in Fu et al. [34].

We investigate a multivariate power curve in the form of polynomial regressions whose input variables can be several wind speed and turbulence measurements retrieved with the SpinnerLidar. Together with the multivariate power curve, we test two IEC-similar power curves implemented using either hub height wind speed or rotor effective wind speed estimates based on the SpinnerLidar measurements. Additionally, we used the SpinnerLidar measurements for wake detection in order to select wake-free time intervals for the development of the IEC-similar power curves.

This paper is organized as follows. The methodology is presented in Sect. 2, which contains the description of the field campaign (Sect. 2.1), the processing of the SpinnerLidar Doppler spectra (Sect. 2.2), the wind field reconstruction methods used to retrieved wind characteristics from the lidar measurements (Sect. 2.3), the filtering of the turbine data (Sect. 2.4) and the methods to implement and test the power curves (Sect. 2.5). The results of this study are presented in Sect. 3. In specific, Sect. 3.1 shows the wake-detection method, while the results from testing the power curves are shown in Sect.s 3.2 and 3.3. The optimal scanning configuration is investigated in Sect.s 3.4. Discussion and conclusions are reported in Sect. 4 and 5, respectively.

2. Methodology

2.1. Field campaign set-up

Measurements were retrieved within an onshore wind farm with eight Neg Micon (NM) 80 2.3 MW wind turbines, with rotor diameter (D) of 80 m and hub height of 59 m. The dataset covers a period of nine days from 02-09-2012 to 11-09-2012, and the site is located in Tjæreborg, western Denmark. A similar campaign was conducted at the same site with a simpler circular scanning lidar installed in the spinner of the same wind turbine[35]. As shown in Fig. 1, the SpinnerLidar is mounted on turbine T2, measuring under both waked and wake-free conditions depending on the wind direction. Operating SCADA data were additionally available from the turbine T2, including measurements from both a cup anemometer and a wind vane mounted on the turbine nacelle. The measurements have been preliminary analyzed by Kapp [36], who compared the SpinnerLidar measurements at hub height with measurements from both the nacelle-mounted cup anemometer and the ultrasonic anemometer mounted on a meteorological mast installed at the site.

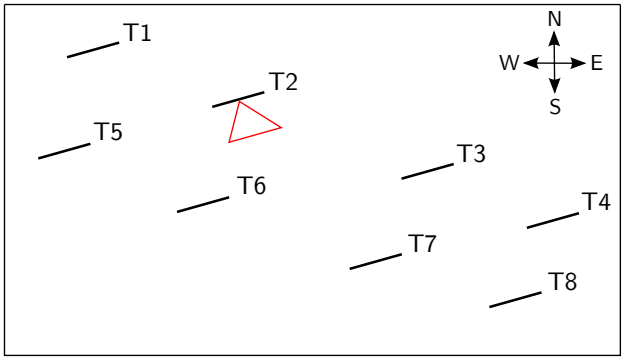

Figure 1: Schematics of the wind farm layout.

The SpinnerLidar consists of a continuous-wave (cw) Doppler lidar equipped with a scanner-head that consists of two rotating optical prisms. The prisms rotate with a fixed velocity ratio of 13:7 and each deflects the line-of-sight of the lidar by 15°. Due to this characteristics the trajectory of the line-of-sight follows a rosette pattern with an opening angle from 0° to 30°. Furthermore, the SpinnerLidar can adjust mechanically the measuring distance and

thus the measuring configuration can include one or more measuring distances that in practice can range between 10 m and up to 200 m from the instrument. More technical details can be found in the patent description [37, 27, 29].

In this field campaign, the SpinnerLidar was mounted in the rotating spinner of the turbine and it was focused to measure at 100 m, i.e. 1.25 D, upstream of the turbine. Due to the prisms' configuration and the tilt of the rotor, measurements were not retrieved within a plane parallel to the rotor, but they were distributed over a distance of around 20 m along the x-axis, as shown in Fig. 2-(b). The lidar system was set to cover the rosette pattern of Fig. 2-(a) within 10 s with a sampling frequency of 100 Hz. Since the SpinnerLidar was mounted in the rotating spinner of the turbine, the scanning pattern of Fig. 2-(a) was rotating together with the rotor. Therefore, over longer periods, measurements were retrieved across all the rotor swept area, as shown in Fig 2-(c) for a measurement period of 1 min.

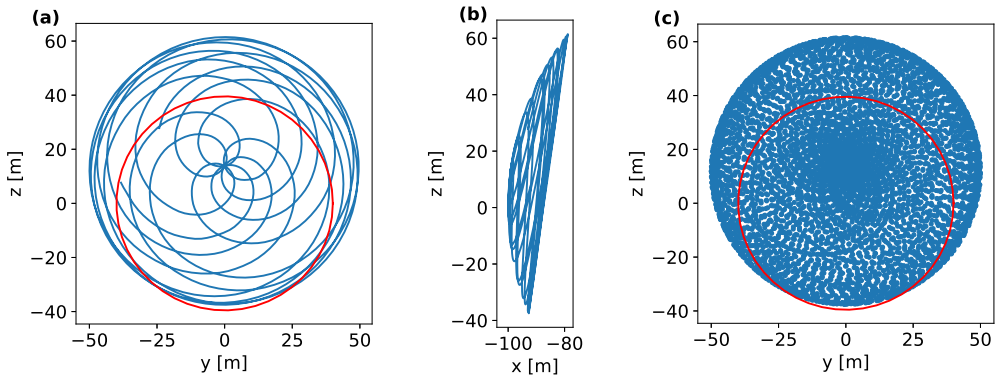

Figure 2: Scanning pattern covered by the SpinnerLidar every 10 s (a, b) and locations of measurements retrieved during 1 min (c). The red line indicates the rotor diameter.

2.2. SpinnerLidar data processing

The SpinnerLidar Doppler spectra cover a frequency bandwidth of 50 MHz divided in 256 bins. Since the laser wavelength is $\lambda = 1.565$ μm, the radial velocity measurements cover the interval 0-39 m/s with a resolution of 0.15 m/s. The first step in the processing of the raw Doppler spectra is the

removal of the background noise. For this purpose, two spectra are obtained as the median spectra from all the raw Doppler spectra retrieved during two different 10-min intervals, and the background spectrum is defined by taking the lower value between the two median spectra for each frequency bin. The two selected 10-min intervals are chosen in order to obtain two median spectra with peaks corresponding to different radial velocities, as shown in Fig 3-(a), so that the spectra peaks are not considered in the background noise. Each spectrum is then flattened by dividing with the background noise as shown in Fig. 3-(b) for one single Doppler spectrum.

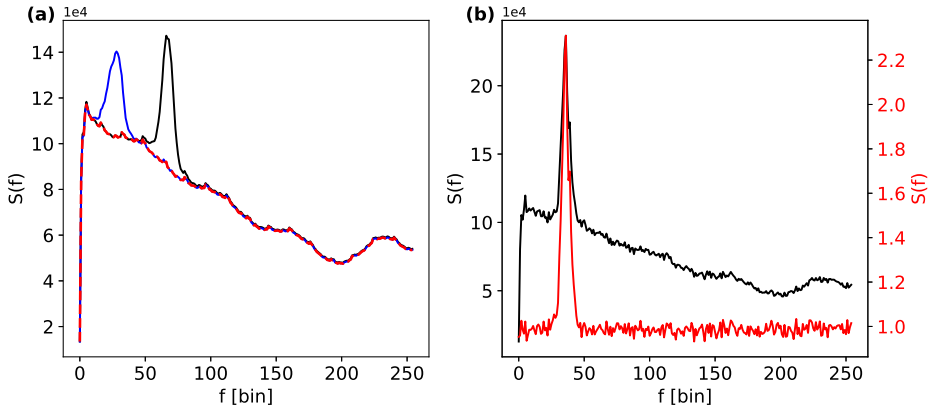

Figure 3: (a): Background spectrum (*red* dashed line) obtained from the two median spectra (*blue* and *black* solid lines). (b): Raw Doppler spectrum (*black*) and the corresponding flattened spectrum (*red*).

Once all Doppler spectra are flattened, special attention is paid to the spectra retrieved in the centre of the scanning pattern. Several of those spectra are characterized by high energy at low frequency, and it is difficult to detect the wind induced Doppler peak. This low frequency noise is related to reflections from the top window of the SpinnerLidar [29, 38]. In general, we found that the energy in the first frequency bin is highly correlated with the energy in the remaining bins, with a decrease in the correlation for the bins presenting the wind-related Doppler shift. Figure 4-(a) shows the correlation coefficient between the spectrum values $S(f_i)$ and $S(f_1)$ for two different 10-min intervals. The correlation coefficients are obtained using values from all the spectra within the considered 10-min interval. Due to the high correlation, for each i^{th} frequency bin, the relation between $S(f_i)$ and $S(f_1)$ can be modelled with a linear least-square regression using the 10-min

interval which shows the highest correlation for that specific i^{th} bin among the two intervals shown in Fig. 4-(a). This is done in order to avoid using wind-affected correlations. Then, the linear regressions are used to normalize the central-beam spectra which have their maximum value in either the 1^{st} or 2^{nd} frequency bin. This is done in order to both filter the spectra and also avoid removing large amounts of measurements. As shown in Fig. 4-(b) for one central-beam spectrum from the 20120910-00:00 time interval, the readability of the spectrum substantially increases after normalizing with the values given by the regression coefficient combined with the $S(f_1)$ value of the spectrum.

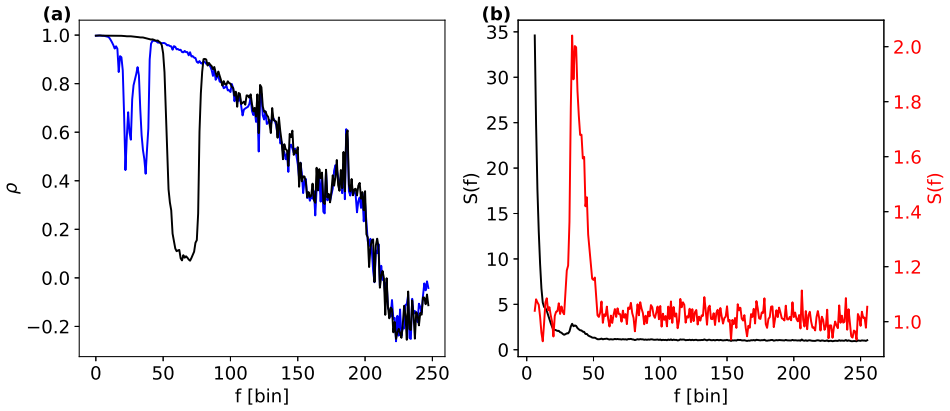

Figure 4: (a): Correlation coefficient (ρ) between $S(f_i)$ and $S(f_1)$ from two different time intervals. 20120904-00:00 (*blue*) and 20120904-08:40 (*black*). (b): Central-beam flattened Doppler spectrum before (*black*) and after (*red*) normalizing with the regression values.

In order to finally get rid of the noise, spectra are further normalized by the value obtained as the mean plus five times the standard deviation of the values within the last 50 bins ($v_r > 31.48$ m/s). To further clean from noise at low frequency, values of the first six bins ($v_r < 0.6$ m/s) are manually set to zero. To further clean from peaks which are not related to wind, spectra are grouped in bins every 10 consecutive spectra and the median spectrum for each bin is retrieved. Then, spectra values are manually set to zero where the median spectrum is zero excluding values at the sides of the peak up to 1 m/s from the edge of the median spectrum.

Since the lidar rotates in the turbine spinner, the location of the lidar scanner head is monitored with two accelerometers which are used to retrieve the measurement locations. In order to retrieve the wind velocity, the

Doppler spectra acquired over the scanned (y, z) plane are gathered in grid square 3 m x 3 m cells. Subsequently, 10-min ensemble average spectra are calculated by averaging all Doppler spectra retrieved within the same cell during a 10-min interval. Then, the 10-min mean radial velocity $\langle v_r \rangle$ is obtained as the median value of the ensemble average spectrum $\langle S(v_r) \rangle$, while the radial velocity variance $\sigma^2_{v_r}$ is estimated as the second statistical central moment of the ensemble spectrum

$$\sigma^2_{v_r,\mathrm{unf}} = \int_{-\infty}^{\infty} \langle S(v_r) \rangle \, (v_r - \langle v_r \rangle)^2 \mathrm{d}v_r \tag{1}$$

in order to avoid turbulence filtering due to the lidar spatial averaging, as shown in [39]. Only grid cells containing at least 30 Doppler spectra are considered for the estimation of both $\langle v_r \rangle$ and $\sigma^2_{v_r}$.

2.3. Wind field reconstruction

The wind velocity vector field is defined as $\mathbf{u} = (u, v, w)$ within the right-handed coordinate system (x, y, z) of Fig. 2, where the x direction is aligned with the rotor axis. Due to the strong inhomogeneity of the waked flow field, most wind field reconstruction methods cannot be applied to retrieve either two or three components of the wind velocity vector. Therefore, by neglecting the yaw misalignment between the rotor axis and the wind direction and assuming no lateral nor vertical mean components ($V = W = 0$), the mean wind speed is estimated as $U = \langle v_r \rangle \, / \, \langle n_x \rangle$, where $\langle n_x \rangle$ is obtained as the average of the $x-$axis components of the beam unit vectors $\mathbf{n} = (n_x, n_y, n_z)$ within the grid cell. Information about turbulence is retrieved in the form of $\sigma^2_{v_r}$ as the strongly inhomogeneous conditions leave no margin for the reconstruction of the along-wind component variance σ^2_u. Figure 8 shows the mean wind speed U and the radial velocity variance $\sigma^2_{v_r}$ measured across the scanned area during the 10-min interval 20120911-06:10.

As it can be seen in Fig. 8-(a), turbine T2 is in the wake of an upwind turbine during the considered time interval, with wind speed variation from 6.4 m/s to 15.4 m/s within the scanned area. There is good agreement between the spatial distribution of the wind speed and turbulence estimations, as the largest turbulence values are measured at the wake boundary, where higher turbulence is expected due to the mechanically-produced turbulence associated with the strong radial velocity shear.

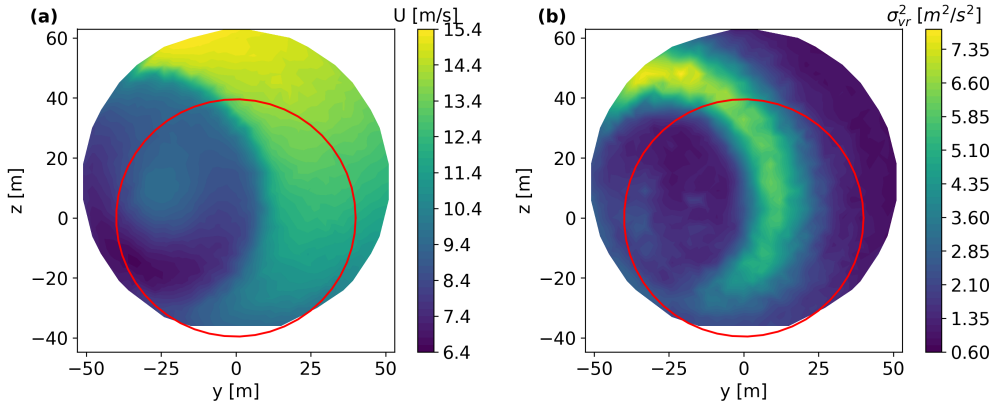

Figure 5: Mean wind speed (a) and radial velocity variance (b) across the scanned area from the 10-min interval 20120911-06:10

2.4. Turbine data filtering

The wind speed is never above the rated value during the measurement period, so that the turbine is expected to operate at its maximum aerodynamic efficiency with a blade pitch angle equal to $\beta \approx 0°$. However, some 10-min intervals are characterized by power curtailment and large β. In order to define unbiased power curves, 10-min intervals are discarded when either $\beta > 2°$ or the 10-min mean power output P is lower than 5 kW. In Fig. 6, the 10-min mean power values are plotted against the mean wind speed measured by the nacelle-mounted cup and the discarded time intervals are highlighted in red.

2.5. Power curve modelling

We use the SpinnerLidar measurements to define multivariate power curves in the form of multivariable polynomial regressions, whose input variables consist of wind speed (U) and turbulence (σ_{v_r}) measurements. The polynomial regression consists of all the possible polynomial combinations of the input variables with degree lower or equal to a specified degree α. For example, in the case of three input variables $y = y(x_1, x_2, x_3)$ and degree $\alpha = 2$, we would get the following polynomial expression

$$y = c_0 + c_1x_1 + c_2x_2 + c_3x_3 + c_4x_1x_2 + c_5x_2x_3 + c_6x_1x_3 + c_7x_1^2 + c_8x_2^2 + c_9x_3^2, \quad (2)$$

where $c_0, .., c_8$ are the regression coefficients.

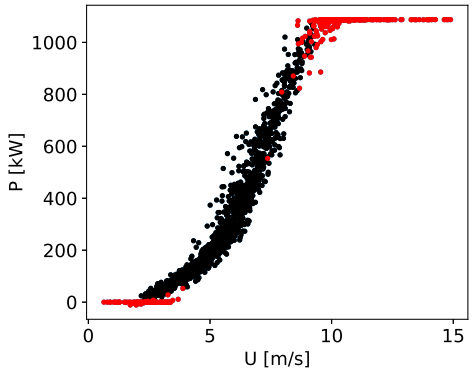

Figure 6: Scatter plot of 10-min mean power output against 10-min mean wind speed at hub height measured by the nacelle-mounted cup. Discarded time intervals ($\beta > 2° \,|P < 5$ kW) are highlighted in red.

The values of U and σ_{v_r} from all the grid cells are considered as potential input variables to the polynomial regressions. Therefore, a feature-selection process is implemented to select the input variables among the available measurements. Specifically, a forward-selection algorithm is utilized for the feature selection. The process starts with an empty model and iteratively selects the variable that give the lowest error in power prediction among the available ones. Six different degrees are tested at each step ($\alpha = 1, .., 6$) and the one giving the lowest error is selected. This selection process is repeated until adding one more variable causes an increase of the error due to overfitting.

At each step of the selection process, the prediction error is evaluated through a K-fold cross-validation with $K = 5$: the dataset is split into 5 equally large subsets, 4 of which are used to train the model and 1 is used to test the model. This process is repeated 5 times, with a different subset reserved for validation each time. The model performance is quantified with the generalization error λ, i.e. the average of the mean errors from the 5 folds: $\lambda = \frac{1}{5}\sum_j E_j$. The error E_j is evaluated as the root mean square error (RMSE). The cross-validation helps to prevent overfitting of the regressions, as all the observations, i.e. the 10-min intervals, in the dataset are used to test the model and the accuracy does not depend on how we split into train and test sections.

In order to implement the forward-selection algorithm, all observations in the dataset must contain the same variables. However, for each 10-min

period, we only consider grid cells with at least 30 Doppler spectra, resulting in different number of measurements among the observations. Therefore, we need to select a group of grid cells available in all the 10-min intervals which are used to define and test the multivariate power curves. A trade-off is made between maximizing the number of observations and the available cells within each observation, resulting in a dataset, hereafter referred to as the testing dataset, of 759 observations with 712 cells whose locations are shown in Fig. 7.

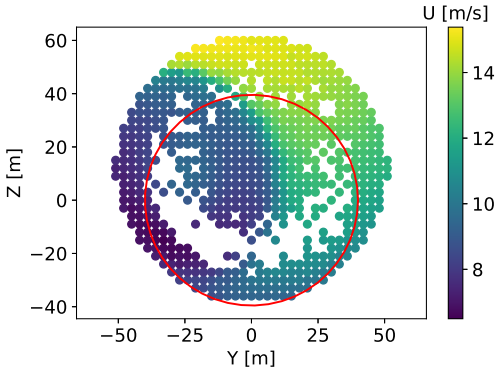

Figure 7: Mean wind speed during the time interval 20120911-06:10 at the 712 cells used to define the multivariate power curves. The rotor diameter is highlighted in *red*.

In addition to the multivariate power curves, we implement IEC-similar power curves by applying the IEC binning method with either the hub-height wind speed (U_{hub}) and the rotor effective wind speed (U_{REWS}) given by the SpinnerLidar measurements:

$$U_{\text{REWS}} = \frac{1}{\pi R^2} \iint_A U(y,z)\,\mathrm{d}y\,\mathrm{d}z,$$

where A is the rotor area and R is the rotor radius. We refer to these curves as IEC-similar as the utilized wind speed measurements are not IEC-compliant since they are retrieved 1.25 D upstream of the rotor and the wind direction is not known. However, we define the IEC-similar power curves using only time intervals when the turbine is not in wake according to a wake-detection method based on the SpinnerLidar measurements.

All the implemented power curves are tested with a K-fold cross-validation with $K = 5$ using the 759 observations available for the multivariate power

curves. Two error metrics are used to test the power curves: the RMSE and the mean absolute percentage error (MAPE):

$$\text{RMSE} = \sqrt{\frac{\sum_{i=1}^{N}(P_i - \hat{P}_i)^2}{N}}$$

$$\text{MAPE} = \frac{100}{N}\sum_{i=1}^{N}\left|\frac{P_i - \hat{P}_i}{P_i}\right|,$$

where N is the number of observations in the dataset and $\hat{P}$ is the estimated power output.

3. Results

3.1. Wake detection

The IEC-similar power curves are defined using time intervals when the wind turbine is not in wake. Since information about the wind direction is not available, a wake detection method is implemented using the SpinnerLidar measurements. Specifically, for each of the 759 available 10-minute intervals, a 2$^{\text{nd}}$ order Gaussian function is fitted to the 10-min mean v_r values measured by the SpinnerLidar across the $y-z$ plane. In the free-wake cases, as shown in Fig. 8-(a), the v_r values follow quite accurately a Gaussian distribution, but without perfect $y-$axis symmetry due to the vertical wind shear. Under waked operation, as shown in Fig. 8-(b), the v_r values do not resemble a Gaussian distribution. Therefore, the agreement between the measured v_r and the reconstructed values $v_{r,G}$ given by the Gaussian function is higher for wake-free intervals than under waked-conditions.

A threshold of 3.5% is empirically chosen for the MAPE between the measured and reconstructed values: $E_{\text{fit}} = 100/N\sum_1^N(v_r - v_r^G)/v_r$, where N is the number of available grid cells for the considered time interval. The wind turbine is considered to operate in wake-free conditions when $E_{\text{fit}} < 3.5\%$ and under waked conditions otherwise. This results in 494 time intervals in wake and 265 time intervals under waked operation.

Figure 9 shows the agreement between the wind speed measured by the Spinnerlidar at hub height, i.e. cell located at $y = 0$ and $z = 0$, and by the nacelle-mounted cup during the 265 wake-free intervals. As it can be seen in Fig 9, the SpinnerLidar slightly overestimates U_{hub} relatively to the nacelle-mounted cup. The discrepancy between the two instrument can be due to

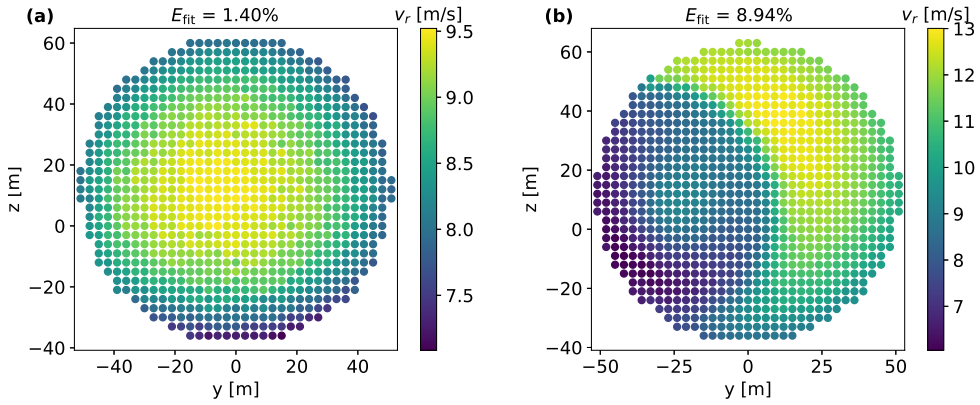

Figure 8: Radial velocity values v_r and error of the Gaussian fit (E_{fit}) under wake-free (a) and waked (b) conditions.

several reasons, such as wrong calibration of the nacelle transfer function or flow distortion caused by the rotor and the nacelle upstream of the cup anemometer. In general, nacelle cup anemometers do not provide reliable estimations of the wind speed and we do not use the results from Fig. 9 to assess the accuracy of the SpinnerLidar measurements, but rather as a validation of the wake detection process.

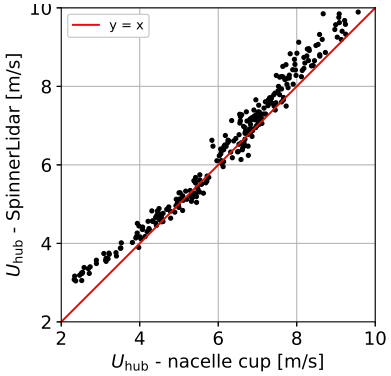

Figure 9: Hub height 10-minute wind speeds (U_{hub}) given by the SpinnerLidar against the ones measured by the nacelle-mounted cup.

3.2. IEC-similar power curves

The 265 wake-free observations are used to define the IEC-similar power curves using either the hub-height wind speed (U_{hub}) or the rotor effective wind speed (U_{REWS}). In both cases, the wind speed measurements are retrieved with the SpinnerLidar. Following the IEC standard [1], 10-min mean values are grouped in bins every 0.5 m/s, and only bins containing at least 3 values are considered. The resulting power curves are shown in Fig. 10 together with the 265 10-minute power-velocity values.

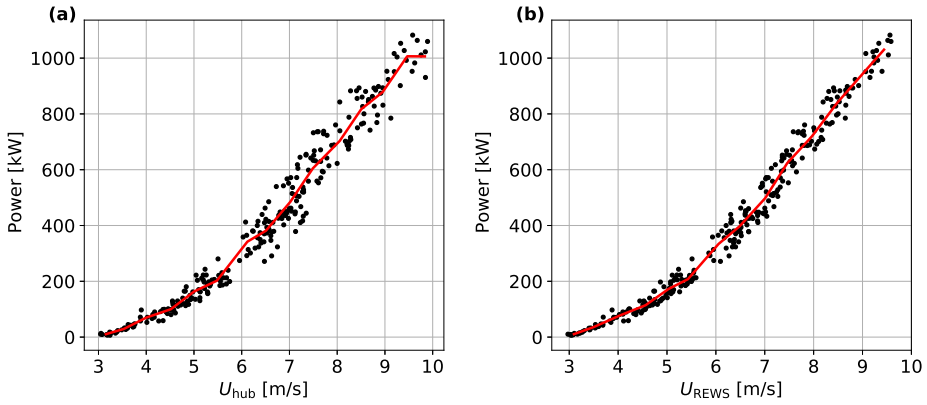

Figure 10: Scatter plot of the 10-min mean power output against the hub-height wind speed (*a*) and the rotor effective wind speed (*b*) given by the SpinnerLidar and the related power curves obtained with the IEC binning method (*red*).

As it can be seen in Fig. 10-(a), the IEC-similar power curve covers the wind speed interval 3-10 m/s when using U_{hub}. The power output is underestimated for $U_{\mathrm{hub}} = 10$ m/s, and the estimation would be more reliable if more data was available. However, since there are at least three 10-min intervals in the 10 m/s bin, the estimation is reliable according to the IEC standard, and we include this bin in the power curve to show the potential shortcomings of the IEC standard. Fig. 10-(b) shows the IEC-similar power curve using U_{REWS}. This covers the interval 3-9.5 m/s and it is characterized by less scattering than when using U_{hub}, as U_{REWS} is estimated using wind speed measurements across the whole rotor swept area, accounting for the spatial variations of the wind kinetic energy flux due to, e.g., vertical wind shear or yaw misalignment.

Both IEC-similar power curves are tested through cross-validation using the testing dataset. However, we consider only time intervals with both U_{hub}

and U_{REWS} within the corresponding available bins showed in Fig.s 10-(a) and 10-(b), resulting in 704 available observations. The IEC-similar predict the power output with MAPE of 27.6% and 16.2% when using U_{hub} and U_{REWS}, respectively. As it can be seen by comparing Fig.s 11-(a) and 11-(a), the evaluation of the power performance is more accurate when using U_{REWS}, resulting in fewer outliers and higher correlation between the predicted and true power output values.

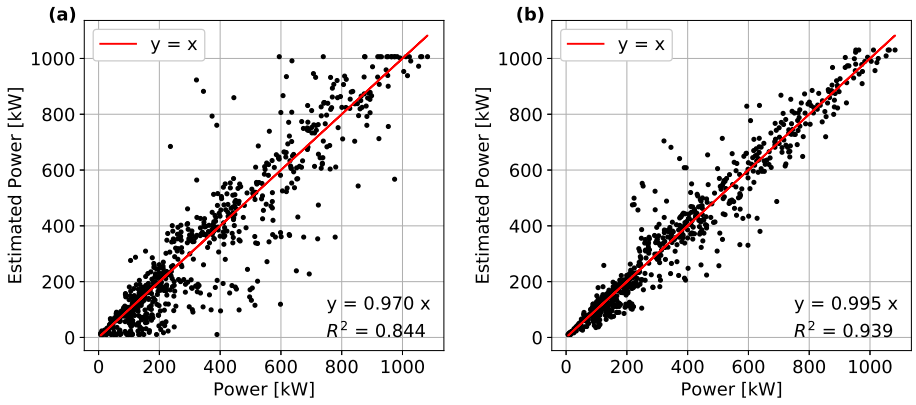

Figure 11: Scatter plot between true and predicted power output using the IEC-similar power curves with U_{hub} (a) and U_{REWS} (b).

3.3. Multivariate power curve

The feature-selection process is used to obtain the optimal number of input variables for the multivariate power curve among the 1424 available variables (712 measurements of both U and σ_{v_r}). During the feature-selection process, the optimal degree α is also selected among the six tested values. The optimal multivariate power curve is the polynomial expression with 9 input variables (6 values of U and 3 of σ_{v_r}) and $\alpha = 2$. The location of the selected features is shown in Fig 12-(a), where the selected variables are indicated with red circles and red squares corresponding to U and $\sigma^2_{v_r}$, respectively. Fig. 12-(b) shows the generalization error obtained at each step of the feature-selection process. The error steeply decreases up to the 6^{th} selected feature, it flattens when increasing above the 7^{th} feature and it increases when adding the 10^{th} feature. So, we only use the first 7 selected features, as the 8^{th} and 9^{th} do not substantially increase the performance of

the model. When four or more variables are included in the model, $\alpha = 2$ is the polynomial degree which provides the best performance of the model, as shown in Fig. 12-(c).

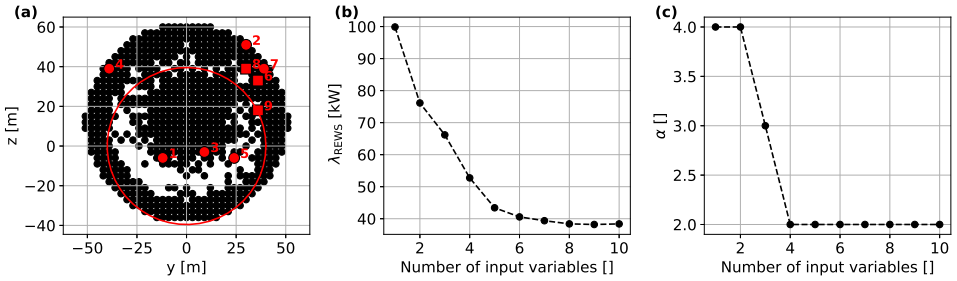

Figure 12: (*a*): Available SpinnerLidar measurements (*black*) with selected measurements (*red*) of U (*circles*) and $\sigma^2_{v_r}$ (*squares*); *red* numbers indicate the selection order; rotor diameter is highlighted (*red* line). (*b*): Variation of the generalization error with the number of selected features. (*c*): Variation of the optimal degree with the number of selected features.

As it can be seen in Fig. 12-(a), selected features include both wind speed and turbulence measurements. One turbulence measurement is also available among the first 7 selected features, which are responsible for a large portion of the error reduction. This is in agreement with the numerical results of Sebastiani et al. [26], further confirming the benefit of including turbulence measurements in the evaluation of the wind turbine power performance.

The results from the feature-selection process show that the wind turbine power performance is more accurately evaluated when including more than one single wind speed measurement. Specifically, as shown in Fig. 12-(b), the power output is predicted with a RMSE of 99.9 kW and 39.3 kW when using one and seven input variables, respectively. This means that an error reduction of 60.6% is provided by the additional 6 features. When evaluating the multivariate power curve in terms of MAPE, the optimal case gives an error of $\lambda_{\mathrm{MAPE}} = 12.2\%$. Table 1 shows the generalization error given by the multivariate power curve and the two IEC-similar curves. Specifically, compared to the U_{hub}-based power curve, the multivariate power curves provides error reductions of 65.3% and 55.6% in terms of RMSE and MAPE, respectively. Relatively to the U_{REWS}-based power curve, error reductions of 41.2% and 24.5% in terms of RMSE and MAPE, respectively.

Results from Fig. 12 and Table 1 show that the multivariate power curve provides an overall reliable evaluation of the wind turbine power performance,

Table 1: Generalization errors from the $K = 5$ cross-validation on the testing dataset

λ	IEC-similar (U_{hub})	IEC-similar (U_{REWS})	Multivariate
MAPE [%]	27.6	16.2	12.2
RMSE [kW]	113.4	67.2	39.3

with low average errors in power output predictions. Fig. 13 shows the scatter plot between the true power output and the values estimated by the multivariate power curve for all the observations in the testing dataset. As it can be seen in Fig. 13, the scatter plot provides a fitted linear regression with slope of 0.992 and coefficient of determination of $R^2 = 0.975$, meaning that the multivariate power curve provides a both accurate and precise estimation of the power output, with clear improvement compared to the results of the IEC-similar power curves shown in Fig.s 11-(a) and 11-(b).

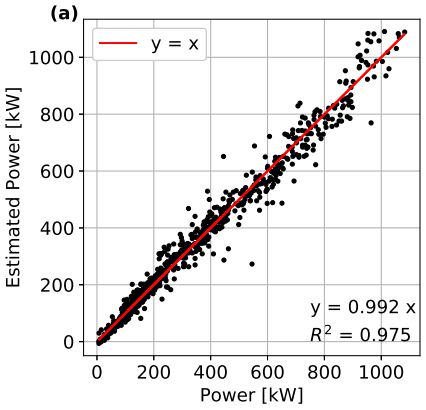

Figure 13: Scatter plot between true and predicted power output using the multivariate power curve with 7 input variables and $\alpha = 2$.

3.4. Optimal scanning configuration

In order to test the robustness of the optimal configuration given by the feature selection and shown in Fig. 12-(a), we evaluate the variation in accuracy when using different input variables to the multivariate power curve. We evaluate how the error changes when using the same degree $\alpha = 2$ and selecting the same number of features rotated of an azimuth angle θ relatively to the optimal case of Fig. 12. As it can be seen in Fig. 14-(b),

the error varies with θ up to 25.3%, i.e. around twice the optimal error of 12.2%. This is in agreement with the numerical findings from Sebastiani et al. [26]. However, in their numerical results, there was larger difference in accuracy between the multivariate and IEC power curves, so that even when doubling its error, the multivariate power curve still provided a large improvement compared to the IEC power curve. In our case, when rotating the selected features of θ, the power estimation is slightly more accurate than the U_{hub}-based curve and less accurate than the U_{REWS}-based curve.

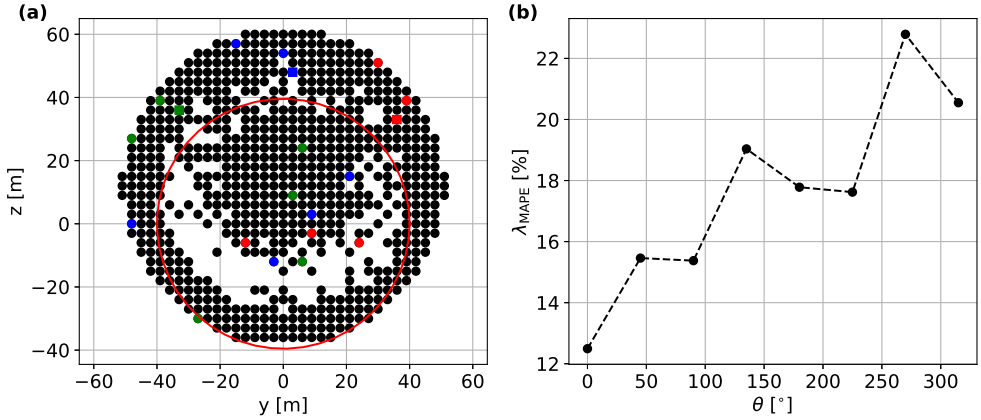

Figure 14: (a): Optimal features (red) and features selected with roations of $\theta = 45°$ ($blue$) and $\theta = 90°$ ($green$). (b): Variation of the generalization error with the azimuth angle θ.

The accuracy of the multivariate power curve is highly dependent on the selected features. As shown in Fig. 14, when applying small variations in the selected features, the error in power output estimation increases, getting close to that of the IEC-similar power curve. Since the optimal features are strongly related to the location of the turbine in the farm and the wind direction distribution during the test, they might be different for other turbines in the wind farm. Therefore, the multivariate power curve might be inaccurate when measuring the wind characteristics at the locations obtained as the optimal ones for another turbine.

In order to define a more flexible lidar scanning configuration, which could be used independently of the turbine location, we test the multivariate power curve using measurements along a circular pattern. We test 13 different configurations with 7 measurements (6 U and 1 $\sigma^2_{v_r}$) along circular patterns

with diameters from 0.2 D to 1.4 D. As shown in Fig. 15-(a), the circular scanning lidars are simulated by selecting SpinnerLidar measurements along the circular patterns. Fig. 15 shows the errors in power prediction given by the multivariate power curves using the 7 measurements along the circular pattern and $\alpha = 2$. Starting with the smallest diameter, the error decreases as the diameter of the scanning configuration increases up to a minimum at 0.9 D. then, the error increases when further enlarging the scanning pattern.

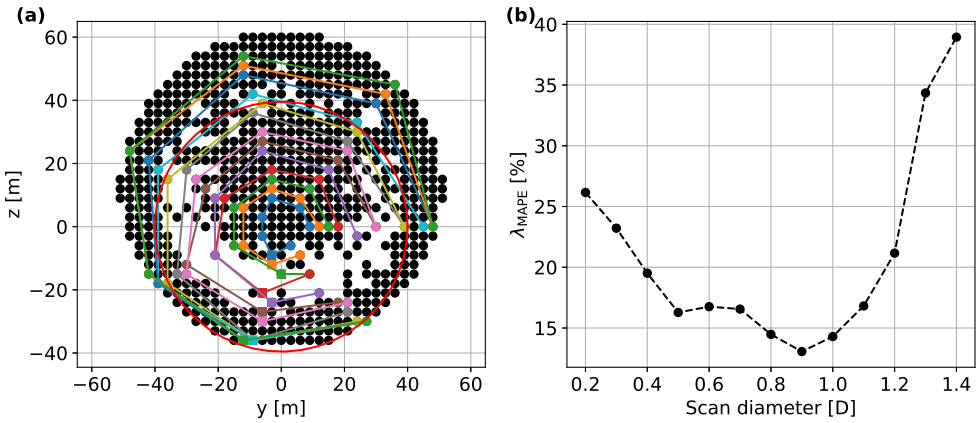

Figure 15: (*a*): Optimal features (*red*) and features selected with roations of $\theta = 45°$ (*blue*) and $\theta = 90°$ (*green*). (*b*): Variation of the generalization error with the azimuth angle θ.

In the case of a circular scanning lidar with a 0.9 D diameter, the multivariate power curves estimate the power output with MAPE of 13.1%. That is 7.4 % higher than when using the optimally selected features, but 52.5% and 19.1% lower than with the U_{hub}- and U_{REWS}-based IEC-similar power curves, respectively. Additionally, the power output estimation is also quite accurate when the scanning configuration has a diameter of either 0.8 D or 1 D, with MAPE of 14.5% and 14.3%, respectively. Therefore, the circular scanning configuration is suitable to evaluate the turbine power performance with the multivariate power curve as long as it is characterized by the correct diameter. This is in agreement with the numerical results from Sebastiani et al. [26], who showed good accuracy of the multivariate power curves when using a circular scanning lidar with a diameter of ≈ 0.8 D.

4. Discussion

Our results show that multivariate power curves in the form of polynomial regressions are more accurate than the IEC binning method based on either the hub-height wind speed or the rotor effective wind speed. Specifically, the rotor effective wind speed is usually used to apply the IEC power curve in combination with engineering wake models when conducting energy yield analyses (EYA). A lot of attention has been paid to improve engineering wake models in the estimation of the flow field, but a considerable portion of the error in EYA is due to the conversion of the available wind flow in power output. Therefore, EYA could benefit from the utilization of the multivariate power curves for the conversion from wind speed to power. As shown in this work, the multivariate power curve is more accurate than the IEC in predicting the power output of a waked wind turbine using information of the inflow provided by a Doppler lidar installed in the spinner.

The multivariate power curve could be also used to improve the accuracy in monitoring the wind turbine power performance, as well as to conduct production validation tests, i.e. assessing whether the turbines are producing at a level consistent with their theoretical power curve. Nacelle lidars are becoming more and more common within the wind energy industry, as they can be used for several applications such as lidar assisted control, load assessment and wake steering-based wind farm control.

Results from this work show the benefits of mounting the lidar in the turbine hub relatively to more traditional nacelle-mounted lidars. With a hub-mounted lidar, since the scanning pattern rotates together with the turbine, a larger portion of the rotor swept area is covered relatively to a nacelle-mounted lidar with the same scanning configuration.

5. Conclusions

Multivariate wind turbine power curves are defined in the form of multivariable polynomial regressions, whose input variables are several wind speed and turbulence measurements retrieved by the DTU SpinnerLidar mounted in the turbine hub. The multivariate power curves are defined and tested under both waked and wake-free conditions with measurements retrieved at the onshore wind farm in Tjæreborg (Denmark). The multivariate power curves are compared with IEC-similar power curves implemented using the IEC binning method.

The IEC-similar power curves are defined using wake-free measurements only. These are selected using a wake-detection method based on the SpinnerLidar measurements. Additionally, we show a procedure to process the lidar Doppler spectra in order to retrieve both wind speed and turbulence measurements.

Our results show that the multivariate power curves provide a more accurate evaluation of the wind turbine power performance than the IEC binning method. Specifically, when using the multivariate power curve, the error in power output estimation is reduced by 65.3% and 41.2% relatively to the U_{hub}- and U_{REWS}-based IEC-similar power curves, respectively.

The input variables to the multivariate power curve are selected among all the available SpinnerLidar measurements with a feature-selection process based on a forward-selection algorithm. The optimal power curve consists of polynomial regressions of the 2^{nd} order and 7 input variables (6 wind speed and 1 turbulence measurements). The accuracy of the multivariate power curve substantially varies when changing the input variables, highlighting the uniqueness of the optimal configuration.

In order to provide a robust method to apply the multivariate power curve in different cases without changing the lidar measurement locations, circular scanning configurations are tested by selecting SpinnerLidar measurements along circular patterns. Results show good accuracy of the multivariate power curves when the scanning pattern diameter is around 0.9 D, with error reductions of 52.5% and 19.1% relatively to the U_{hub}- and U_{REWS}-based IEC-similar power curves, respectively.

This work shows that the Tjæreborg dataset is suitable for studies focused on the evaluation of the wind turbine power performance under waked conditions. This research could be extended by testing more complex machine learning algorithms to model the wind turbine power performance using the SpinnerLidar measurements. Additionally, the multivariate power curves should be tested for applications such as power forecasting and annual energy production estimations.

Acknowledgements

Professor Torben Mikkelsen and Senior Researcher Mikael Sjöholm from the Section of Meteorology and Remote Sensing of the Wind Energy department of DTU are acknowledged for designing and conducting the field campaign. The field campaign was supported by the Danish Advanced Technol-

ogy Foundation: Grant 049-2009-3: *Integration of Wind LIDAR's In Wind Turbines for Improved Productivity and Control*. The analysis of the measurements and the research work presented in this article has received funding from the European Union Horizon 2020 through the Innovation Training Network Marie Skłodowska-Curie Actions: Lidar Knowledge Europe (LIKE) [grant number 858358].

Data Availability

Datasets can be found at https://10.11583/DTU.22182403

References

[1] IEC, 61400-12-1, power performance measurements of electricity producing wind turbines, 2017.

[2] Y. Wang, Q. Hu, L. Li, A. M. Foley, D. Srinivasan, Approaches to wind power curve modeling: A review and discussion, Renewable and Sustainable Energy Reviews 116 (2019). doi:10.1016/j.rser.2019.109422.

[3] M. Lydia, S. S. Kumar, A. I. Selvakumar, G. E. Prem Kumar, A comprehensive review on wind turbine power curve modeling techniques, Renewable and Sustainable Energy Reviews 30 (2014) 452 – 460. doi:10.1016/j.rser.2013.10.030.

[4] J. Gottschall, J. Peinke, How to improve the estimation of power curves for wind turbines, Environmental Research Letters 3 (2008). doi:10.1088/1748-9326/3/1/015005.

[5] E. Taslimi-Renani, M. Modiri-Delshad, M. Elias, N. Rahim, Development of an enhanced parametric model for wind turbine power curve, Applied Energy 177 (2016) 544–552. doi:10.1016/j.apenergy.2016.05.124.

[6] M. Marčiukaitis, I. Žutautaitė, L. Martišauskas, B. Jokšas, G. Gecevičius, A. Sfetsos, Non-linear regression model for wind turbine power curve, Renewable Energy 113 (2017) 732 – 741. doi:10.1016/j.renene.2017.06.039.

[7] B. Manobel, F. Sehnke, J. A. Lazzús, I. Salfate, M. Felder, S. Montecinos, Wind turbine power curve modeling based on gaussian processes and artificial neural networks, Renewable Energy 125 (2018) 1015–1020. doi:https://doi.org/10.1016/j.renene.2018.02.081.

[8] K. Xu, J. Yan, H. Zhang, H. Zhang, S. Han, Y. Liu, Quantile based probabilistic wind turbine power curve model, Applied Energy 296 (2021). doi:10.1016/j.apenergy.2021.116913.

[9] R. Wagner, M. Courtney, J. Gottschall, P. Lindelöw-Marsden, Accounting for the speed shear in wind turbine power performance measurement, Wind Energy 14 (2011) 993–1004. doi:10.1002/we.509.

[10] J. Sumner, C. Masson, Influence of Atmospheric Stability on Wind Turbine Power Performance Curves, Journal of Solar Energy Engineering 128 (2006) 531–538. doi:10.1115/1.2347714.

[11] R. Pandit, D. Infield, M. Penas, Accounting for environmental conditions in data-driven wind turbine power models, IEEE Transactions on Sustainable Energy (2022) 1–10. doi:10.1109/TSTE.2022.3204453.

[12] Y.-M. Saint-Drenan, R. Besseau, M. Jansen, I. Staffell, A. Troccoli, L. Dubus, J. Schmidt, K. Gruber, S. G. Simoes, S. Heier, A parametric model for wind turbine power curves incorporating environmental conditions, RENEWABLE ENERGY 157 (2020) 754–768. doi:10.1016/j.renene.2020.04.123.

[13] V. Bulaevskaya, S. Wharton, A. Clifton, G. Qualley, W. O. Miller, Wind power curve modeling in complex terrain using statistical models, Journal of Renewable and Sustainable Energy 7 (2015). doi:10.1063/1.4904430.

[14] A. Clifton, L. Kilcher, J. K. Lundquist, P. Fleming, Using machine learning to predict wind turbine power output, Environmental Research Letters 8 (2013). doi:10.1088/1748-9326/8/2/024009.

[15] A. Clifton, R. Wagner, Accounting for the effect of turbulence on wind turbine power curves, Journal of Physics: Conference Series 524 (2014). doi:10.1088/1742-6596/524/1/012109.

[16] F. Pelletier, C. Masson, A. Tahan, Wind turbine power curve modelling using artificial neural network, Renewable Energy 89 (2016) 207–214. doi:10.1016/j.renene.2015.11.065.

[17] A. Sebastiani, A. Peña, N. Troldborg, Wind turbine power performance characterization through aeroelastic simulations and virtual nacelle lidar measurements, Journal of Physics: Conference Series 2265 (2022) 022059. doi:10.1088/1742-6596/2265/2/022059.

[18] O. Janssens, N. Noppe, C. Devriendt, R. Van de Walle, S. Van Hoecke, Data-driven multivariate power curve modeling of offshore wind turbines, Engineering Applications of Artificial Intelligence 55 (2016) 331 – 338. doi:10.1016/j.engappai.2016.08.003.

[19] D. Astolfi, R. Pandit, Multivariate wind turbine power curve model based on data clustering and polynomial lasso regression, Applied Sciences (Switzerland) 12 (2022). doi:10.3390/app12010072.

[20] A. Peña, J. Mann, N. Dimitrov, Turbulence characterization from a forward-looking nacelle lidar, Wind Energy Science 2 (2017) 133–152. doi:10.5194/wes-2-133-2017.

[21] W. Fu, A. Peña, J. Mann, Turbulence statistics from three different nacelle lidars, Wind Energy Science 7 (2022) 831–848. doi:10.5194/wes-7-831-2022.

[22] A. Borraccino, D. Schlipf, F. Haizmann, R. Wagner, Wind field reconstruction from nacelle-mounted lidars short range measurements, Wind Energy Science 2 (2017) 269–283. doi:10.5194/wes-2017-10.

[23] J. Medley, W. Barker, M. Harris, M. Pitter, C. Slinger, T. Mikkelsen, M. Sjöholm, Evaluation of wind flow with a nacelle-mounted, continuous wave wind lidar (2014). URL: `http://www.ewea.org/annual2014/`.

[24] J.-J. Trujillo, F. Bingöl, G. Larsen, J. Mann, M. Kühn, Light detection and ranging measurements of wake dynamics. part ii: two-dimensional scanning, Wind Energy 14 (2011) 61–75. doi:10.1002/we.402.

[25] D. Conti, N. Dimitrov, A. Peña, T. Herges, Probabilistic estimation of the dynamic wake meandering model parameters using spinnerlidar-derived wake characteristics, Wind Energy Science 6 (2021) 1117–1142. doi:10.5194/wes-6-1117-2021.

[26] A. Sebastiani, A. Peña, N. Troldborg, Numerical evaluation of multivariate power curves for wind turbines in wakes using nacelle lidars, Renewable Energy 202 (2023) 419–431. doi:https://doi.org/10.1016/j.renene.2022.11.081.

[27] M. Sjöholm, A. T. Pedersen, N. Angelou, F. F. Abari, T. Mikkelsen, M. Harris, C. Slinger, S. Kapp, Full two-dimensional rotor plane inflow measurements by a spinner-integrated wind lidar, in: European Wind Energy Association Conference, 2013.

[28] A. Peña, J. Mann, G. Rolighed Thorsen, SpinnerLidar measurements for the CCAV52, volume 0177, DTU Wind Energy, Denmark, 2019.

[29] N. Angelou, M. Sjöholm, Data Reliability Enhancement for Wind-Turbine-Mounted Lidars, Remote Sensing 14 (2022). URL: https://www.mdpi.com/2072-4292/14/13/3225. doi:10.3390/rs14133225.

[30] E. Machefaux, G. Larsen, N. Troldborg, K. Hansen, N. Angelou, T. Mikkelsen, J. Mann, Investigation of wake interaction using full-scale lidar measurements and large eddy simulation: Investigation of wake interaction using full-scale lidar measurements and les, Wind Energy 19 (2016) 1535–1551. doi:10.1002/we.1936.

[31] T. Herges, D. Maniaci, B. Naughton, T. Mikkelsen, M. Sjöholm, High resolution wind turbine wake measurements with a scanning lidar: Paper 854 (2017). doi:10.1088/1742-6596/854/1/012021.

[32] D. Trabucchi, J.-J. Trujillo, M. Kühn, Nacelle-based lidar measurements for the calibration of a wake model at different offshore operating conditions, Energy Procedia 137 (2017) 77–88. doi:https://doi.org/10.1016/j.egypro.2017.10.335, 14th Deep Sea Offshore Wind RD Conference, EERA DeepWind'2017.

[33] I. Sood, E. Simon, A. Vitsas, B. Blockmans, G. C. Larsen, J. Meyers, Comparison of large eddy simulations against measurements from the lillgrund offshore wind farm, Wind Energy Science 7 (2022) 2469–2489. doi:10.5194/wes-7-2469-2022.

[34] W. Fu, A. Sebastiani, A. Peña, J. Mann, Dependence of turbulence estimations on nacelle-lidar scanning strategies, Wind Energy Science Discussions 2022 (2022) 1–21. doi:10.5194/wes-2022-85.

[35] T. Mikkelsen, N. Angelou, K. Hansen, M. Sjöholm, M. Harris, C. Slinger, P. Hadley, R. Scullion, G. Ellis, G. Vives, A spinner-integrated wind lidar for enhanced wind turbine control, Wind Energy 16 (2013) 625–643. doi:10.1002/we.1564.

[36] S. Kapp, Lidar-based reconstruction of wind fields and application for wind turbine control, Ph.D. thesis (2017).

[37] T. Mikkelsen, J. Mann, M. Nielsen, Rotating prism scanning device and method for scanning, 2011. EP 2304489.

[38] K. A. Brown, T. G. Herges, High-fidelity retrieval from instantaneous line-of-sight returns of nacelle-mounted lidar including supervised machine learning, Atmospheric Measurement Techniques 15 (2022) 7211–7234. URL: https://amt.copernicus.org/articles/15/7211/2022/. doi:10.5194/amt-15-7211-2022.

[39] J. Mann, A. Peña, F. Bingöl, R. Wagner, M. Courtney, Lidar scanning of momentum flux in and above the atmospheric surface layer, Journal of Atmospheric and Oceanic Technology 27 (2010) 959 – 976. doi:10.1175/2010JTECHA1389.1.